University of Trento

Department of Physics

Doctoral Degree in Physics

Final Thesis

LISA Pathfinder noise performance results: disturbances in the sub-mHz frequency band and projection to LISA

Supervisor:
Prof. Stefano Vitale

Candidate:
Eleonora Castelli

Doctoral cycle XXXII

Abstract

The LISA Pathfinder ESA mission was concluded on July 18th, 2017, after 18 months of operations as one of the most successful ESA missions ever. It was launched on December 3rd, 2015 with the purpose of assessing the feasibility of geodesic motion of two free-falling test masses at the level required by LISA, the first space-based gravitational wave observatory programmed for launch in 2034. This was achieved by measuring the relative acceleration between free-falling test masses with a sensitivity several orders of magnitude better than any other present or future mission. In addition to this, LISA Pathfinder constituted an advanced technological test for the flight hardware of the LISA mission.

In this thesis work I will illustrate the detail of the experimental results obtained in the course of the mission, whose best performance was published in February 2018, and discuss their consequences for LISA. I will, in particular, describe in some detail a series of observations for which a definitive physical model is still lacking.

I will then discuss possible explanations with the aim to reduce the number of available interpretations, and in order to lay the basis for a feasible on-ground experimental campaign in view of LISA.

Contents

Contents **3**

1 Introduction **6**
1.1 Gravitational waves detection principles in the context of LISA and LISA Pathfinder 9

2 LISA Pathfinder **17**
2.1 LISA Pathfinder instrument hardware 19
2.1.1 The Gravity Reference Sensor 20
2.1.2 Optical Metrology Subsystem 22
2.1.3 Drag-Free and Attitude Control System 23
2.1.4 Drag Free Propulsion System 25
2.2 System dynamics 25
2.3 LISA Pathfinder as a tester for LISA requirements 28
2.3.1 Requirements and expected noise model at launch . . . 29

I Experimental results from LISA Pathfinder **32**

3 Differential acceleration noise between free falling test-masses **38**
3.1 Correction of inertial effects 38
3.2 LPF noise performance along the mission 42
3.3 Low frequency noise 47
3.3.1 Brownian noise plateau 47
3.3.2 Low frequency branch 49
3.4 Comparison with noise models 55
3.4.1 LPF modeled noise sources 56
3.5 Excess power in the low frequency noise 60

4 Differential acceleration along angular degrees of freedom **65**
4.1 Cross-correlation between translational and angular acceleration noise 69
4.2 Expected torque noise 71
4.2.1 Angular actuation noise 71
4.2.2 Brownian noise along angular degrees of freedom 72
4.3 Comparison with results 73

5 Spurious signals in acceleration noise data **75**
5.1 Phenomenology 76
5.1.1 Spurious signals occurrence 78
5.2 Glitches detection and fit 80
5.3 Statistics of the spurious events 85
5.3.1 Time of arrival t_0 85
5.3.2 Transferred impulse per unit mass Δv 87
5.3.3 Amplitude and duration of the glitches 91
5.4 Torque associated to glitches 96

II Discussion **99**

6 Sources of low frequency excess noise **101**
6.1 Non-thermal pressure fluctuations 101
6.2 Gravitational noise from mass loss inside the SC 102
6.2.1 Mass loss from depletion of propellant tanks 102
6.2.2 Mass leakage from SC elements 106
6.3 Brownian noise from extra dissipation 108

7 Physical origin of the glitches **111**
7.1 One-sided glitches as outgassing phenomena 111
7.2 Two-sided glitches 117

8 Conclusions **119**

Appendixes **120**

A Spectral estimation with minimum correlation frequency selection and Bayesian error estimate **122**
A.1 Low frequency excess noise 126

B List of all differential acceleration noise runs **128**

C LISA Pathfinder experimental results **132**
C.1 Noise performance 132
C.2 Low frequency excess noise 139
C.3 Angular differential acceleration 146
C.4 Cross correlation of differential angular acceleration with translational differential acceleration 159

D List of all detected spurious signals in acceleration data **171**

Acknowledgements **190**

Bibliography **194**

1 Introduction

The quest for gravitational waves has been subjected to a boost since the detection, by the LIGO-Virgo array of ground-based interferometers, of gravitational signals coming from various kind of sources, such as black-hole black-hole (BH-BH) and neutron-star neutron-star (NS-NS) mergers [1, 2].

The large-scale experiments designed for the gravitational investigation of the universe are increasing in number and in the years to come will cover the various ends of the gravitational spectrum, illustrated in Figure 1.1: from very low frequencies Pulsar Timing Arrays (PTA), to low frequencies space-based detectors as the Laser Interferometer Space Antenna (LISA) [3], to higher frequencies cryogenic terrestrial detectors like KAGRA [4] AdvLIGO+ [5] and AdvVirgo [6].

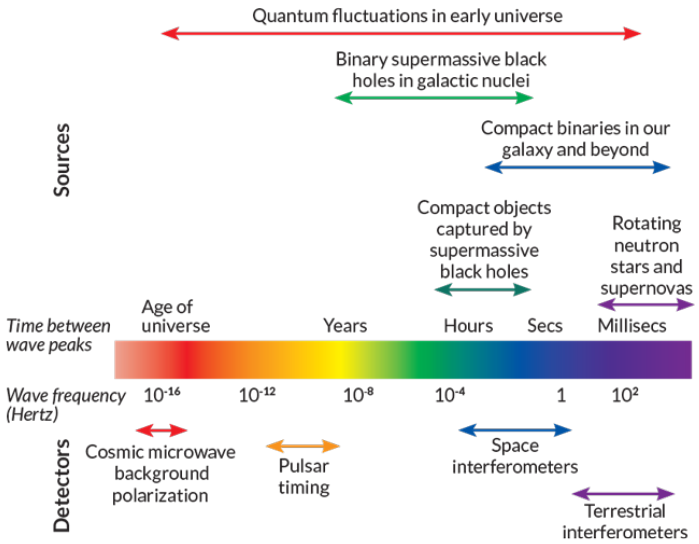

Figure 1.1: Gravitational frequency spectrum with pictorial representation of frequency bands of interest for the various physical sources of gravitational waves, together with the respective detectors. Space-base gravitational wave detectors like LISA, are sensitive in the frequency band between 0.1 mHz to 1 Hz. (Adapted from `https://lisa.nasa.gov/`)

The space-based gravitational wave detector, LISA, is a large class mission that has been officially selected by the European Space Agency (ESA) with nominal launch date set to 2034.

It is going to be the first gravitational wave observatory completely space-based, and it therefore is going to be sensitive to gravitational waves in

a frequency band that allows to detect astrophysical phenomena not yet detectable, such as Massive Black-Holes (MBH) and exotic compact binaries. Moreover, flying a space-based GW detector would allow for joint detection of gravitational signals together with ground-based detectors [7].

LISA also constitutes a pioneering technological challenge, as it is an interferometric constellation whose elements are three separate spacecrafts, each carrying two independent scientific payloads communicating separately with the other two satellites via a high coherence laser-interferometric link.

The initial concept of the LISA mission dates back to mid 1980s, with a mission proposed by the Joint Institute for Laboratory Astrophysics in the Unites States of America with the tentative name of Laser Antenna for Gravitational-radiation Observation in Space (LAGOS) [8, 9]. This first idea was already referring to a triangular constellation of three spacecrafts flying around the Sun, with only two interferometric arms established between the parent and the children spacecrafts.

In the course of the 1990s the mission focus moved to Europe, where the LISA project started shaping first as a six-spacecraft constellation [10], culminating then to the concept of a triple interferometric link among three identical spacecrafts in 1998 [11]. By that time, the collaboration between ESA and NASA had been started via the LISA Study Team and a technology demonstration mission had been programmed for launch in 2002, with the name of European LISA Technology demonstration satellite (ELITE). The launch date for LISA was initially set to 2008.

During the first decade of the 2000s, the mission encountered several major delays and cancellation risks and was eventually included inside ESA's Cosmic Vision program in a rescaled version [12]. In the course of this decade the mission was renamed to New Gravitational Observatory evolved LISA (NGO eLISA), and it would have consisted of two interferometric links established among three spacecrafts located at the vertexes of a 1 million km side triangle.

The technology demonstration mission original design was also subjected to various modifications until its final design became stable [13, 14], and was launched on December 3rd, 2015 with the name of LISA Pathfinder (LPF). Pathfinder had the twofold role of being both a technological test for the LISA scientific hardware, and the proof of concept that geodesic motion is possible at the unprecedented levels required by LISA.

LPF technological hardware, the LISA Technology Package (LTP) [15], has been designed to be as close as possible to the LISA design, in order to demonstrate the feasibility of LISA requirements from LPF noise measurements.

The various elements of the LTP have been designed and built by the research groups involved in the LPF collaboration [13], spread among European countries and institutions and the United States.

Its nominal science objective was the assessment of the relative acceleration of two freely falling test-masses (TM), with a precision of a few orders of magnitude better than any other performed or planned mission so far. This has translated into the measurement of the noise level of the TMs relative acceleration, which turned out to be quieter than budgeted.

LPF first published results [16], showed that the noise level reached on-board the spacecraft was already several times better than the original requirements. The final noise performance of Pathfinder [17], reached in February 2017, exceeded the requirements for LISA and turned out being a very promising result for the era of gravitational wave discoveries below the mHz threshold, paving the way for the follow-up large scale mission.

Thanks to the success achieved by the LPF mission, the LISA original design of Figure 1.2 with three 2.5 million km interferometric arms was reinstated, and was finalized in the proposal submitted to ESA at the beginning of 2017 [3]. The proposal was then selected to be ESA's class-L3 mission in June 2017, just before the end of LPF 18-months mission extension.

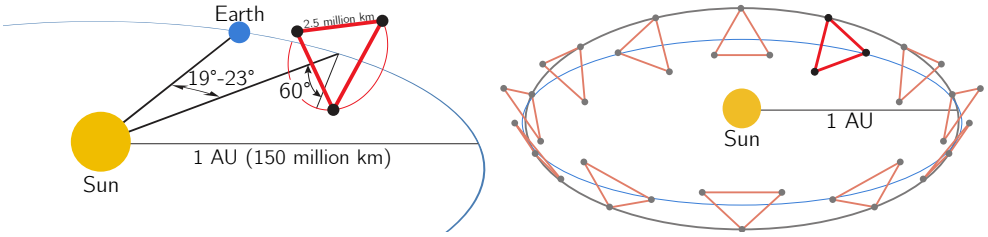

Figure 1.2: LISA orbital scheme. Left: The spacecraft triangular constellation with 2.5 millionkm arms is located behind the Earth at a distance of about $19° \div 20°$, inclined of $60°$ with respect to the ecliptic plane. The orbital radius is ~ 1 AU. Right: Representation of motion of LISA revolutionizing around the Sun; the blue line stands for the ecliptic plane, while the gray solid line pictures the motion of one of the three spacecrafts. (Adapted from [3])

1.1 Gravitational waves detection principles in the context of LISA and LISA Pathfinder

Although LISA is not the main focus of this work, it establishes the framework in which the LISA Pathfinder mission was performed: in the following I am going to provide a summary of the LISA mission and the theory behind gravitational waves detection in space, only for scopes connected to this work discussion.

Gravitational waves will serve as experimental probe to investigate the universe through the vibrations of space-time itself, as they are emitted by the motion of accelerating masses in space-time, so that cosmological occurrences that were unobserved until now can be detected.

The gravitational wave detectors working principle is the same both on ground and in space, that is, the tidal deformation of space-time induced by a passing gravitational wave can be detected via laser interferometry. On ground this is achieved with a network of 3-4 km-long Michelson interferometers, with different spatial orientations and different locations (LIGO Livingstone, LIGO Hanford and Virgo).

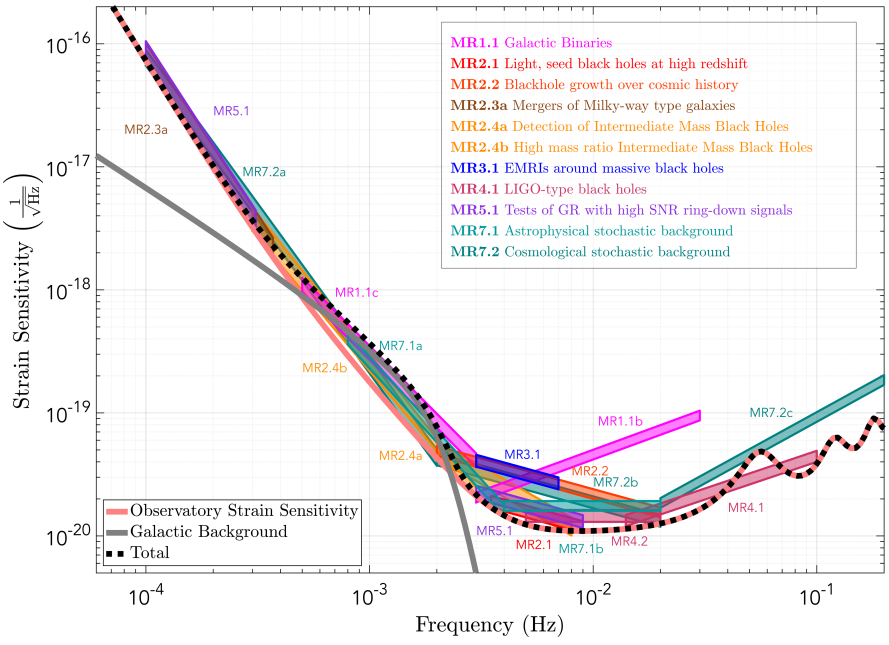

Figure 1.3: LISA strain sensitivity curve, plotted against the galactic background and the regions of the spectrum where the several phenomenons are detectable (Adapted from [3]).

LISA, now in the middle of its Phase A study, is going to investigate the gravitational spectrum in the frequency band ranging from 20 µHz to 1 Hz, which is populated with various different GW sources related to astrophysical dynamics and the limits of General Relativity, as depicted in the sensitivity curve of Figure 1.3.

LISA will act as an isotropic full-sky observatory its sensitivity, meaning that it is going to be sensitive to every signal above its noise level.Among the physical phenomena that will be available to LISA, one can list massive black holes (MBH) mergers, compact binary systems, evolution of galactic nuclei and stochastic background signals from the early epochs of the universe.

In order to follow the same operating principle of the terrestrial interferometers, LISA will use laser interferometry to measure the phase shift between laser beam propagating between test bodies, thus detecting any change in their relative distance caused by space-time perturbations.

The vertexes of the triangular interferometer arms are constituted by free-falling TMs, to suppress the non-gravitational forces that could affect the space-time deformation measurement caused by the GW passage. Each of the two inertial reference TMs will then communicate with one of the TMs located on the distant spacecrafts, as is pictured in the schematic representation of Figure 1.4.

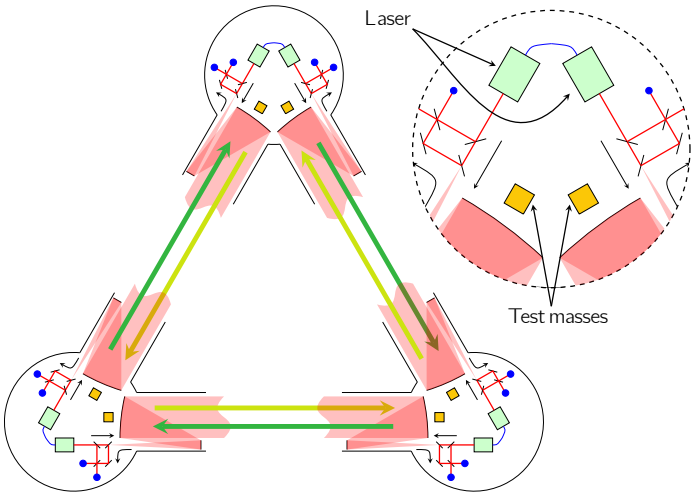

Figure 1.4: LISA constellation of three identical spacecrafts: each one is depicted with a schematic representation of the payload (laser interferometer and free-falling TM), and the laser links connecting two TMs. (Adapted from [3])

The practical implementation of the experiment does not exactly resemble the one of the terrestrial Michelson interferometers: the spacecrafts are linked

by a continuous interferometric scheme, which reminds of the Doppler tracking of satellites.

Each LISA spacecraft will send two outgoing laser signals to the other SCs, receiving back two incoming beams phase-locked to the reference laser located on-board. The phase replica of the signal is then sent back to its original SC, and the phase difference to the local laser is measured.

The basic measurement of each LISA link is constituted by the phase comparison between the beam received from a distant spacecraft and the one of the local laser. Such measurement is however dominated by orders of magnitude by phase noise, and in order to suppress it, the measurements from different links are time-delayed and then added or subtracted in a combination.

With the proper choice of delays one can show that, while the GW signal is not canceled, the phase noise of each laser at a given time enters in the combination twice, but with opposite signs, and is thus suppressed. The calculation of delays requires thus the knowledge of the beam propagation time.

This technique is named Time Delay Interferometry (TDI), and can be used to synthesize Michelson-like interferometers with the 3 SCs and two interferometric laser connections on each arm. It is possible to establish three independent TDI combinations that allow the measurement of gravitational signals: two of them actually resemble independent Michelson interferometers, simultaneously sensitive to GWs in both polarizations, while the third configuration (called Sagnac) is insensitive to GWs and can be used to characterize the instrument noise background.

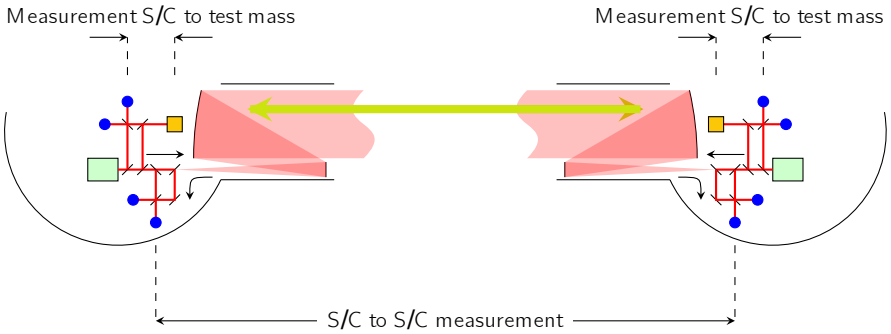

Figure 1.5: Measurement of TM-TM distance broken up in three separate contributions. (Adapted from [18])

The evaluation of distance between TMs is split into three separate contributions, as depicted in Figure 1.5: one long-distance connection between

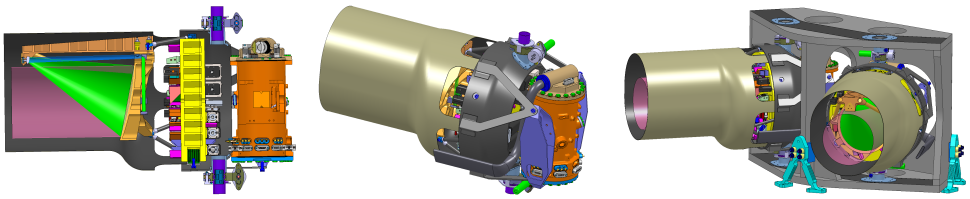

Figure 1.6: 3D industrial rendering of the conceptual design for a two-payload assembly to be mounted inside a single spacecraft. Left: sectioned view of a single payload cylinder containing the laser telescope (green) and vacuum enclosure of the GRS. Center: external view of a single payload assembly. Right: Complete view of the two-payload assembly inserted in their common frame. (Adapted from [3], courtesy of Airbus)

the two spacecrafts, precisely between the two interferometer optical benches fixed on the SC, and two local measurements occurring inside the satellites, between the optical bench and its belonging TM.

The part of the measurement that occurs inside the spacecrafts is related to TMs and their surrounding hardware, constituting the hardware core of the experiment. Since the TMs play the role of endpoints for the interferometric laser arms, they need to be kept undisturbed and thus maintained in an environment clean of force disturbances that could be confused with the effect of gravitational radiation. Hence, each TM is going to be hosted in a separate payload, resulting in a total number of two payloads per spacecraft.

The conceptual design under study during the LISA Mission Phase A is the one depicted in Figure 1.6, with two identical cylindrical assemblies mounted on a common frame that allows them to rotate in order to keep the LISA constellation in place.

A single payload unit consists therefore of several different elements: an optical assembly, which comprehends the Optical Bench Interferometer (OBI), the telescope and the TM enclosing system, the GRS; a reference laser system; a phase-meter; a drag-free control system. The structure is schematically depicted in Figure 1.7.

The drag-free control system regulates the µN thrusters following the TMs motion, in order to keep the spacecraft centered on the TMs without applying any disturbances along the interferometer axes and rotate it as needed to maintain the beam alignment with the receiving spacecraft.

Due to the complicated dynamics of such system, the x position of the TMs relative to the SC is measured by the interferometer, while the other degrees of freedom are read out electrostatically by the Electrode Housing (EH), the

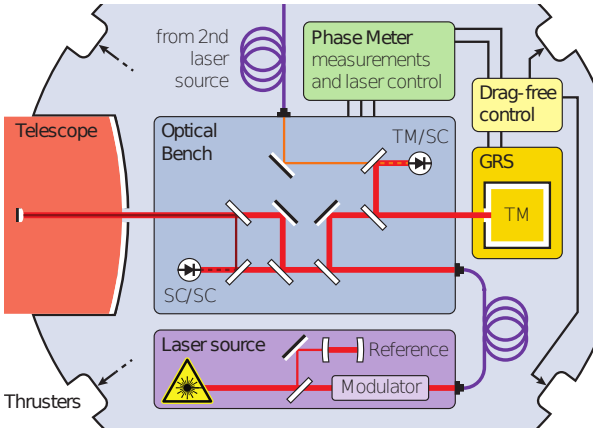

Figure 1.7: Schematic view of the LISA payload with its components: the TM enclosed in the GRS, the DFACS, the laser source, the optical assembly and the telescope. (Adapted from [19])

hollow molybdenum structure with electrode walls surrounding each TM.

The free-falling TM and its EH together with the release and lock mechanism take the name of Gravity Reference Sensor (GRS), an apparatus whose role is to enclose the TM, act as geodesic reference and receive the laser beam in order to perform the optical measurement. The GRS design remains unvaried from the one used on-board LPF and is thoroughly described in section §2.1.1.

The Optical Bench Interferometer is a solid block of Zerodur™ ceramic glass, the same used in LPF [20], with fused silica glasses and beam-splitters as components bonded to the bench through a technique called hydroxide-catalysis bonding [21].

The different measurement partitions of Figure 1.5 are performed by different interferometers built on the optical bench: the SC-SC separation is detected by the science interferometer, with the local laser source acting as reference, while the incoming distant beam is collected through the telescope and is directed to the interferometer optics.

The high-quality 30 cm aperture telescope is needed for the collection of incoming laser beam, and should not introduce additional wavefront aberrations during transmission of the laser beam to the distant spacecraft.

The local part of the measurement is instead realized by the TM interferometer: since both the reference and probing beams are located on the optical bench, the TM acts as a mirror and reflects the impacting beam onto the bench.

The phase-meter is implemented after the science interferometer photodetector and it detects the phase difference between the signal coming from

the distant spacecraft and the local on-board oscillator. This is done by digitizing the photo-detector output at 50 MHz in order to overcome the Nyquist frequency of the science signal, which is also dominated by annual variations of the Doppler frequency which go up to 20 MHz, and then processing the digital signal in a FPGA in order to recover its phase and frequency.

The limiting noise sources for the LISA range are therefore going to be the single TM acceleration noise at low frequencies (below ~ 3 mHz), due to the inability of completely isolating the TMs from external disturbances, and the laser phase noise at high frequencies (above ~ 10 mHz).

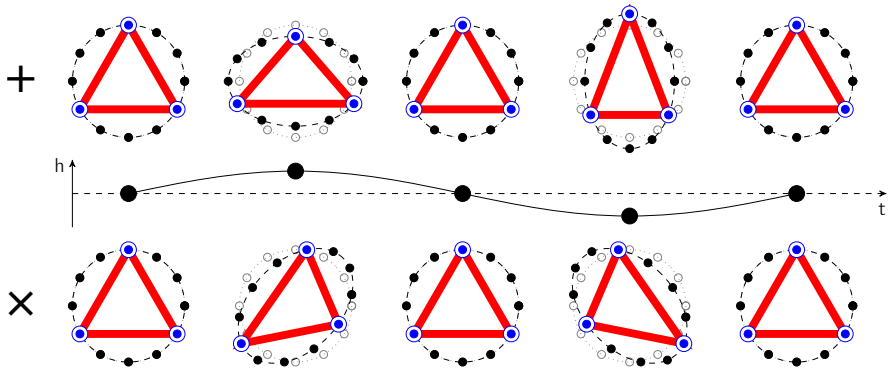

Figure 1.8: Graphic representation of the LISA constellation deformation due to passing GW in the + or × polarization. (Adapted from [18])

LISA will therefore have the sensitivity to detect a passing gravitational wave causing a time-dependent frequency shift in the laser beams connecting the two endpoint free-falling TMs in each arm, that are behaving as free-falling observers in space-time.

If the two observers are at rest, they move along geodesics and their separation distance L is subject only to changes in the metric tensor, as the ones occurring in the case of a passing gravitational wave. Moreover, LISA peculiar triangular configuration will guarantee sensitivity to incoming gravitational waves in different polarizations, as depicted in Figure 1.8.

A single LISA arm can be approximated with two test particles at rest, or free falling observers, exchanging a light beam with initial frequency $\nu_0 = c/\lambda$. The space-time curvature caused by a passing GW with generic amplitude h will modulate the frequency of the beam measured by free falling observers, resulting in a frequency shift $\delta\nu = \nu_{\rm em} - \nu_{\rm rec}$, that is

$$\delta\nu = \nu_{\rm em}(t-T) - \nu_{\rm rec}(t) = \nu_0 \left(h_{\rm em}(t-T) - h_{\rm rec}(t)\right), \tag{1.1}$$

where T is the propagation delay time between the emitter and the receiver.

The frequency shift (1.1) is time-modulated with the time derivative, given by

$$\frac{\mathrm{d}}{\mathrm{d}t}\left[\delta\nu\right] = \nu_0(\dot{h}_{\mathrm{em}}(t-T) - \dot{h}_{\mathrm{rec}}(t)). \tag{1.2}$$

Frequency modulation between the free-falling observers may also occur in the absence of any space-time curvature h if each free-falling observer is subjected to acceleration relative to its own inertial frame. Thus, spurious forces $f_{\mathrm{em,rec}}$ acting respectively on the emitting and receiving observers will generate a frequency derivative

$$\frac{\mathrm{d}}{\mathrm{d}t}\left[\delta\nu\right] = \frac{\nu_0}{c}\frac{f_{\mathrm{em}} - f_{\mathrm{rec}}}{m}. \tag{1.3}$$

Doppler frequency shift is both produced by deformation of the metric tensor due to passing gravitational signals and external forces acting on free-falling test masses.

The passing gravitational wave and the presence of forces that accelerate the observers relative to their own inertial frame, once combined together, give for the mutual acceleration between free-falling observers

$$\frac{\mathrm{d}}{\mathrm{d}t}\left[\delta\nu\right] = \nu_0(\dot{h}_{\mathrm{em}} - \dot{h}_{\mathrm{rec}}) + \frac{\nu_0}{c}\underbrace{\frac{f_{\mathrm{em}} - f_{\mathrm{rec}}}{m}}_{\Delta g}, \tag{1.4}$$

where Δg represents the differential force per unit mass acting on the free-falling observers.

The noise contribution to frequency shift modulation of the accelerating force (1.3) can be quantified by calculating the Power Spectral Density (PSD) of the processes, that is

$$\left|\frac{c}{\nu_0}\right|^2 S_{\frac{\mathrm{d}}{\mathrm{d}t}\left[\delta\nu\right]}(\omega) = S_{\Delta g}(\omega). \tag{1.5}$$

Thus, acceleration noise is superimposed to the interferometer readout noise. This is usually expressed as noise in detected beam phase $\delta\theta$. To compare this with the contribution of the acceleration noise, one can recall that

$$S_{\frac{\mathrm{d}}{\mathrm{d}t}\left[\delta\nu\right]}(\omega) = \omega^2 S_{\delta\theta}(\omega), \tag{1.6}$$

which allows to transform the frequency modulation noise into a phase shift noise. The acceleration noise can then be converted into and effective phase noise, that is

$$\left|\frac{c}{\nu_0}\right|^2 \omega^2 S_{\delta\theta}(\omega) = S_{\Delta g}(\omega), \tag{1.7}$$

$$\left|\frac{c}{\nu_0}\right|^2 S_{\delta\theta}(\omega) = \frac{S_{\Delta g}(\omega)}{\omega^2}. \tag{1.8}$$

The aforementioned equation implies that the observer acceleration noise $S_{\Delta g}$ contribute to phase shift noise $S_{\delta\theta}$, a contribution that becomes prominent in the lower frequency part of the spectrum, since the ω^{-2} behavior dominates.

This evaluation of the free-falling observer acceleration noise clarifies the importance of assessing the contribution of the single TM acceleration noise in the LISA interferometric link connection, and consequently justifies the investigation of low frequency acceleration noise, highlighting the foremost importance of a precursory mission like LPF.

The LISA sensitivity noise model of Figure 1.3 clearly shows the amount of sources that become available in the sub-mHz part of the spectrum. As seen in (1.8) sensitivity in the low frequency part of the spectrum is limited by the single TM acceleration noise, whose Amplitude Spectral Density (ASD) requirement for LISA is set to be

$$S_{\mathrm{acc}}^{1/2}(f) = 3\sqrt{1+\left(\frac{0.4\,\mathrm{mHz}}{f}\right)^2}\sqrt{1+\left(\frac{f}{8\,\mathrm{mHz}}\right)^4}\,\mathrm{fm\ s^{-2}Hz^{-1/2}}. \tag{1.9}$$

The aim of this thesis is the detailed discussion of the LISA Pathfinder noise performance results obtained in the course of the whole mission. With respect to the last noise performance published works [17], here I am going to illustrate the evolution of LPF performance together with the results of the analysis that still remain unexplained.

This work will therefore presents in much deeper detail the experimental results behind the published performance, including the analysis of additional observables and data, and more sophisticated data analysis methods. Based on that I will discuss the possible physical interpretations of such observations, significantly narrowing down their number, with the aim of paving the way to a campaign of laboratory test that may finally consolidate the performance model for LISA.

2 LISA Pathfinder

As stated in the Introduction §1, the main purpose of LISA Pathfinder was to assess the quality of geodesic motion between two nominally free-falling test bodies in space-time by measuring their parasitic differential acceleration, Δg, which is the most important scientific product of the mission.

To perform such measurement, the LPF apparatus is built as schematized in Figure 2.1: the basic design is constituted by three orbiting bodies, two interferometrically linked test-masses with no mechanical contact with the surrounding environment, which constituted by the enclosing spacecraft and the measuring hardware.

A local inertial reference frame is established on-board LPF by putting one of the two TMs in pure free-fall motion, with no applied force. Once in flight, only the first TM is completely free-falling along all translational degrees of freedom, while the other one is actuated since the spacecraft exerts static gravitational DC-forces that would otherwise cause the second TM to drift away.

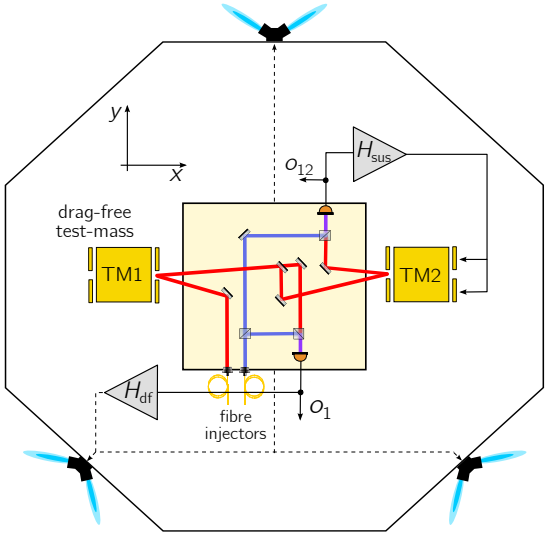

Figure 2.1: Schematic representation of LISA Pathfinder experimental apparatus. The two TMs are enclosed within their Electrode Housings (EH) and interferometrically linked along the drag-free sensitive x-axis. The Optical Bench mounts two interferometers, one to perform measurements (red) and one for reference (blue). Two feedback loops $H_{\rm sus}$ and $H_{\rm df}$ are fed with the differential displacement o_{12} and the TM1 position o_1 readouts respectively, in order to actuate TM2 and the µN thrusters to keep the system centered on TM1. (Adapted from [22] and [16])

The spacecraft follows TM1 by sensing its position $o_1(t)$ and feeding it back to the micro-Newton thrusters via the drag-free control loop $H_{\rm df}$, forcing the repositioning of the spacecraft itself.

TM2 is instead forced to follow the drag-free TM1 through the electrostatic suspension control loop $H_{\rm sus}$, which regulates the capacitive actuators located around the TM, exerting an actuation force to maintain the TM-TM separation distance fixed. The spacecraft will in turn rotate around the y and z axes to keep TM2 centered inside its EH.

However, the closed-loop measurement presents some shortcomings, due to the fact that the second TM needs to follow the motion of the first one. The most relevant is the underestimation of $\Delta g \simeq \Delta a = a_2 - a_1$, which makes it necessary to subtract the forces commanded to TMs $f_{\rm c}$ in order to retrieve the correct value of the differential acceleration

$$\Delta g = a_2 - a_1 - \frac{f_{\rm c}}{m}, \tag{2.1}$$

with m mass of the TMs. Δg can be more specifically identified with the difference in force per unit mass between the two free-falling TMs along their conjoining sensitive axis, due to all sources except for the commanded feedback force, as it is described in Chapter §3.

The ASD of Δg, $S_{\Delta g}^{1/2}$, accounts for the system performance noise level, whose requirement for LISA Pathfinder is given by

$$S_{\Delta g}^{1/2}(f) \leq 30\sqrt{1+\left(\frac{f}{3\,\mathrm{mHz}}\right)^2}\,\mathrm{fms}^{-2}\mathrm{Hz}^{-1/2}, \tag{2.2}$$

holding in the measurement bandwidth from 1 mHz to 30 mHz.

The LPF noise performance ASD requirements are depicted in Figure 2.2 in comparison with the LISA acceleration ASD requirements (1.9). The LPF scientific payload showed only minor changes with respect to the original LISA design and the relaxation in both amplitude and frequency range for the performance requirements (2.2) was needed only to keep the mission costs low: by all means LPF served as technological test for the LISA measurement apparatus.

LPF also traveled closer to Earth with respect to the designed LISA orbit of Figure 1.2, but to a location with similar gravitational environment: it orbited around the first Lagrangian point L1, that is, the location at which the rotation of the satellite results to be synchronous with the Earth rotation and its orbital period is equal to the Earth's one.

Beside their orbits, the biggest difference between LISA and LPF regarding the apparatus design is the reduction from a triangular SC constellation to a

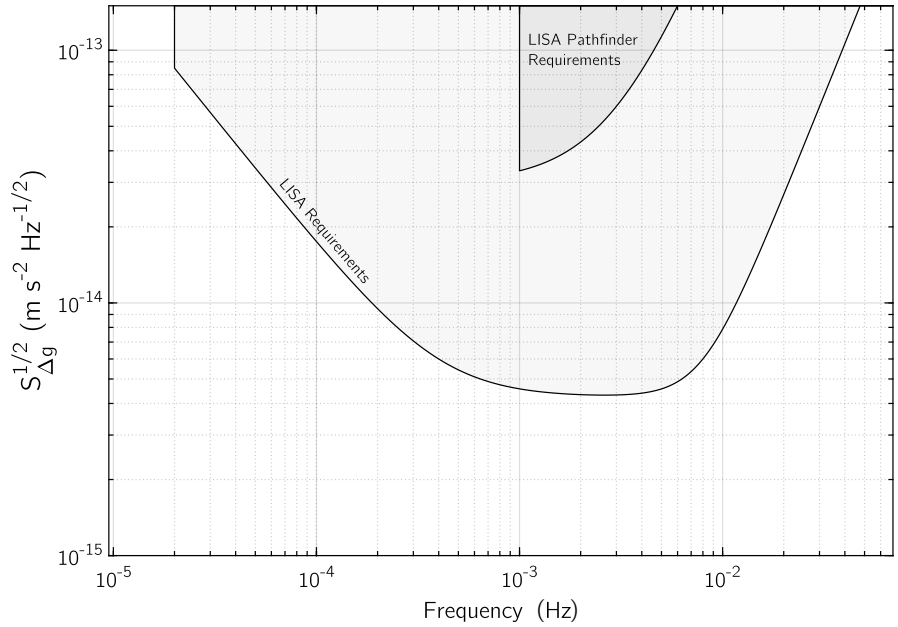

Figure 2.2: Comparison of the LISA Pathfinder ASD requirements (2.2) with respect to the LISA acceleration noise requirements (1.9).

single spacecraft configuration. The TM-TM interferometer was enclosed within a single satellite, meaning that the laser arm was shrunk from 2.5×10^6 km to about 38 cm, becoming insensitive to passing GW.

2.1 LISA Pathfinder instrument hardware

The LPF system configuration will be described in the following sections in more detail, where the various components of the scientific payload are outlined.

All the elements of the flight hardware are common between LISA and LPF and take the name of LISA Technology Package (LTP), a technological apparatus consisting of two Gravity Reference Sensors (GRS), the Drag Free Attitude and Control System (DFACS), the Optical Metrology Subsystem (OMS) and the Data Management Unit (DMU). The LTP elements have a fixed position on the satellite and from a dynamics point of view are considered to be part of the spacecraft.

As in the LISA payload, each two TMs with its EH is part of a single GRS, while the Optical Bench Interferometer is included in the OMS, accounting for all the interferometers and optical components on-board.

The two aforementioned control loops, $H_{\rm df}$ and $H_{\rm sus}$ belong to the DFACS, the apparatus regulating the displacements and attitudes applied to maintain the experimental configuration, while the DMU has the role of transmitting telemetry data to the on-board computer and interfacing the various LTP components.

2.1.1 The Gravity Reference Sensor

The GRS purpose is to track the TMs motion by measuring the change in capacitance caused by a displacement of the TM inside the EH, which in turn induces a voltage variation. It is then necessary to apply an electrostatic potential to counteract the static gravitational forces that could cause the TM to drift away and impact on the housing.

The output signal of this motion sensor is the driving input for the drag-free control loop, which regulates then the SC motion along y and z, since the x direction is controlled by the interferometer output.

The GRS apparatus that flew on LPF is the same that is going to fly on LISA. The TMs are two gold-coated gold-platinum alloy cubes, in the proportions of 73% Au and 27% Pt, with nominal masses $m = (1.928 \pm 0.001)$ kg and side $l = (46.000 \pm 0.005)$ mm.

The choice of the TM materials is due to their very high density and low magnetic susceptibility $\chi_{\rm m} \simeq 10^{-5}$, fundamental in order to keep the magnetic disturbances as low as possible on the spacecraft: because of this all the magnetic components of the LTP are kept at minimum.

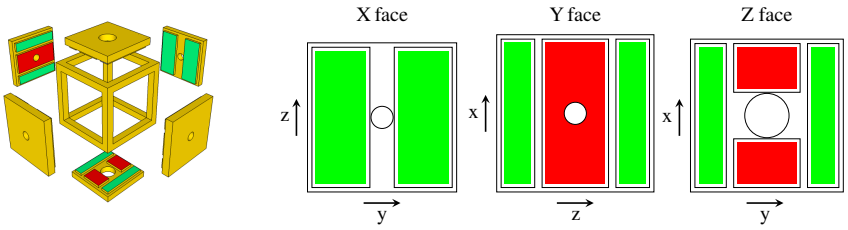

Figure 2.3: Left: Representation of the electrode housing enclosing the TM. Right: Depiction of the different electrodes configuration for the x, y and z facets.

The TMs are surrounded by a set of gold-coated molybdenum electrodes placed in the inside walls of the EH and isolated from ground through a set of sapphire spacers, as depicted in Figure 2.3. The gaps d between the masses

and the electrodes vary depending on the degrees of freedom as

$$\begin{aligned} d_x &= 4\,\text{mm}, \\ d_y &= 2.9\,\text{mm}, \\ d_z &= 3.5\,\text{mm}, \end{aligned} \tag{2.3}$$

chosen in order to get the widest possible gaps, while preserving the necessary displacement sensitivity and electrostatic actuation authority.

Moreover, the TMs with their EHs are located inside of a vacuum chamber, which is vented to the outside of the satellite by means of a ventilation hose, since the pressure inside the spacecraft is $\sim$2 orders of magnitude higher than the required level of 10^{-5} Pa, due to constant outgassing of the satellite components.

Since the TMs are not grounded, it was necessary to use a technique to remove the charge accumulated from cosmic rays impacting them without establishing any contact: this is performed via UV light discharging, where the TMs or the electrodes are shone with ultraviolet light coming from Hg discharge lamps. In order to properly discharge the TMs, the accumulated charge is evaluated by applying a known voltage to the electrodes and measuring the resulting force on the TMs.

The discharge can then occur in two different modes of operation. On one hand one there is a rapid discharge mode, which implies an interruption of the acceleration measurement, a charge measurement and a subsequent maximum intensity discharge via UV light. On the other hand there is a continuous discharge mode, which happens with low intensity light during the science measurement run and prevents the charge to build up on the mass.

Another important element of the GRS is the launch-lock mechanism, which is composed by three different actuators and is used to immobilize the TMs during the launch phase, to release them once the spacecraft reached L1 and to regrab them if needed when performing diagnostics operations. Several TMs regrab operations were successfully realized in the course of the mission, and the system always recovered the previous performance once the masses were released.

The first lock stage is the one applied during the spacecraft launch, where the TMs were blocked on the cube vertexes by a set of eight hydraulic fingers which apply a 1200 N force, to avoid damage due to the launch stress. There is then a second stage, during which two plungers are used to break the adhesion between the mass and the launch lock and reposition the TM within the electrode housing, acting only on the $+z$ and $-z$ faces. A third release stage

makes use of a pin that breaks the adhesion between the TM and the plunger, in order to put the TM in free-fall condition without perturbing its motion.

2.1.2 Optical Metrology Subsystem

The OMS is the ensemble of all the optical components of the LTP, and its role is to perform the interferometric readout of the TMs displacements at any time. It consists of the reference laser unit, the laser modulator, the optical bench interferometer and the phase-meter.

An high stability Nd:YAG non-planar ring oscillator laser with 35 mW power and 1064 nm wavelength is the so called reference laser unit, and it is the same oscillator that will be used for the LISA mission.

The non-planarity of the laser is realized through a slight rotation of the direction of light polarization at every round trip, diminishing of the optical losses in the output beam and leading therefore to high stability of the laser.

The laser source is coupled to a single mode fiber and then fed to the laser modulator: here the beam is split into two separate paths which are then shifted in frequency by an Acousto-Optic Modulator (AOM). The heterodyne frequency difference is $f_{\mathrm{het}} = 2\,\mathrm{kHz}$ with the AOM frequencies at 80 MHz and $80\,\mathrm{MHz} \pm f_{\mathrm{het}}$.

These two modulated beams are then directed to the interferometer on the Optical Bench Interferometer, which, as in LISA, was a solid ($200 \times 212 \times 22.5$) mm block of Zerodur™ ceramic glass where all the optical components have been silicate bonded to the plate using the hydroxide-catalysis technique, in order to suppress the mechanical drift of the optical components.

On the OBI, the two beams reflected by the various beam splitters and mirrors form four different Mach-Zehnder heterodyne interferometers, as illustrated in Figure 2.4. The relative displacement between TMs and two rotation angles are provided by the $o_{12}(t)$ interferometer, while the $o_1(t)$ interferometer measures the relative position and rotation angles of TM1 with respect to the SC. This kind of interferometer could be used as is for the local LISA interferometer.

The two remaining interferometers are the *frequency interferometer*, which detects the laser frequency fluctuations and is used to correct for laser variations, and the *reference interferometer*, which instead measures the interferometric noise floor of the system.

The laser beams are then collected by the photo-diodes, whose signals are in turn sent to the phase-meter, which samples the signal at 100 Hz and

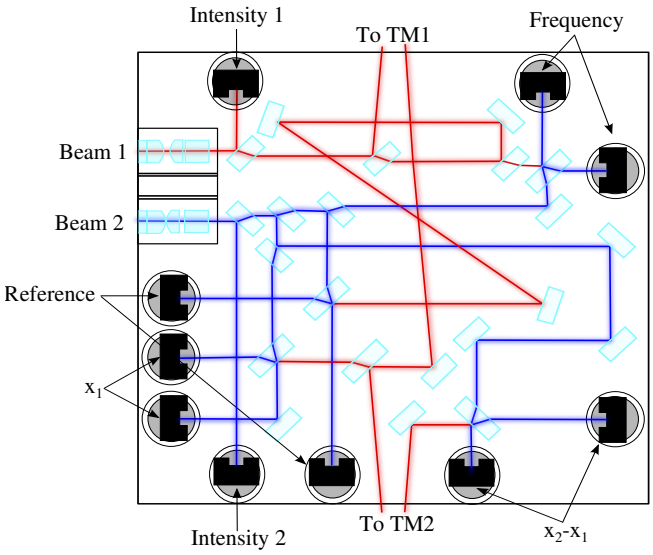

Figure 2.4: Schematic representation of the optical bench: the two different laser sources (red and blue) constitute the four separate interferometers and are detected by the photo-diodes, pictured in black. (Adapted from [20])

performs a Fourier transform of the data to estimate the phase of the signal at f_{het}.

The signals o_1 and o_{12} from the two science interferometers are instead used to detect the TMs displacements and alignments along the x-axis, in order to reposition the TMs with respect to the interferometer. In the end the data are downsampled at 10 Hz by the Data Management Unit (DMU) before being transmitted to the on-board computer.

2.1.3 Drag-Free and Attitude Control System

As stated above, the DFACS is responsible of maintaining the experimental configuration of the system with one drag-free TM and the other one electrostatically suspended. This is achieved by sensing and actuating the position of the TMs and by controlling the spacecraft dynamics.

Actually, there are several different modes of operation, that can be used for the characterization of several different physical quantities during the science operations. The one described below is called *Science Mode 1*, which constitutes the baseline mode to measure the differential acceleration noise.

In Science Mode 1 the controller acts on, and aims at keeping constant, a total number of 15 degrees of freedom, which are detailed in the following:

- the x_1 coordinate of TM1 relative to the SC reference frame, whose driving signal is the o_1 interferometer output, and the actuator is constituted by the set of µN thruster that push the SC to follow TM1;

- the TM relative coordinate $x_{12} = x_2 - x_1$, which is driven by o_{12} and the relative actuator consists of the the proper set of electrodes that electrostatically push TM2 to follow TM1;

- the ϕ and η rotations of both TM relative to the SC, depicted in Figure 2.5, exerted by the proper interferometer outputs actuated electrostatically;

- the θ rotation of TM2, pictured in Figure 2.5, relative to the SC, whose drive signal is the electrostatic rotation sensor and actuation is electrostatic too;

- the relative y- and z-motion of both TMs relative to the SC, which follows a more sophisticated scheme. The drive signals are the proper electrostatic displacement sensors along y, z for both TMs. At frequencies $\geq 1\,\mathrm{mHz}$ such coordinates are *drag-free*: the controller acts on the µN-thrusters, rotating and pushing the SC to follow both TMs, such that they both stay at fixed positions within the SC.

  However, the absolute orientation of the SC relative to the celestial frame at lower frequencies is measured by two autonomous star-trackers, and the proper set of electrostatic forces is applied firstly to the TMs along y and z, to force the line joining them, and then the SC, to maintain the desired orientation relative to the celestial frame. Such orientation is chosen to keep at all times the SC solar panel pointing the Sun and the communication antenna pointing the Earth;

- the θ rotation of TM1 relative to the SC, which follows the same logic of y and z, uses electrostatic sensing, and acts both on thruster and on electrostatics.

The performance requested to these controllers depends on the degree of freedom: x_1 was constrained to be less than $5\,\mathrm{nm\,Hz^{-1/2}}$ above $1\,\mathrm{mHz}$ (and same for the other translational degrees of freedom), while for x_{12} the controller was to be maintained at $\mathrm{pm\,Hz^{-1/2}}$ value and the angular jitter, instead, needed to be less than $\mathrm{mrad\,Hz^{-1/2}}$.

2.1.4 Drag Free Propulsion System

The Drag Free Propulsion System (DFPS) of LPF is a direct heritage from the GAIA mission [23] and via the signals coming from the DFAC controls the three sets of four cold gas µN thrusters, mounted symmetrically on the spacecraft at 120° as shown in Figure 2.1.

The DFPS is constituted by three modules: the feed module, the thruster assembly and the electronics. The first one modulates the cold N_2 gas pressure coming from the propellant tanks through a mechanical pressure valve, which serves as high pressure monitor and low pressure regulator at the same time.

The gas is then delivered to the µN thruster assembly, at operational pressure reduced with respect to the regulating stage, which provides insulation from the previous module while exerting the propulsion commanded by the DFACS, needed to maintain the SC on its orbit.

The last component of the DFPS is the electronics, which has the role of checking and controlling the functioning of the previous two modules. It constitutes the interface with the SC and the DMU, controls the mechanical elements of the feed module, monitors the thrust provided by the thruster assembly and checks any possible failure in the propulsion system.

2.2 System dynamics

Thanks to the nm level jitter, small relative to the mm gap separation $d_{x,y,z}$, and to the low level of the expected forces, in the closed loop LPF configuration the equations of motion for the system can be linearized around their working point. In particular static force fields can be expanded to first order in the TM coordinates.

The force couplings between SC and TMs can then be modeled as springlike constants, the stiffnesses, and the angular expressions are either linearized or small enough to be second-order contributions.

Hence, the LPF spacecraft and the two TMs can be modeled by the system depicted in Figure 2.5. In the following TM1 will always referred to as the drag-free TM, while TM2 will be referred to as the actuated TM, but the roles of the two TMs are actually interchangeable.

The dynamics of the LPF system is thus expressed by a system of linearized

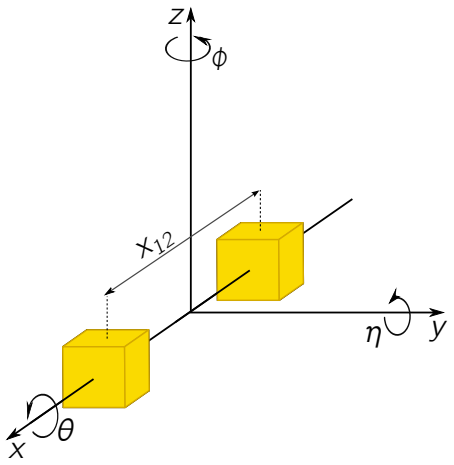

Figure 2.5: TMs are linked along the x-axis, and the frame origin is taken at the center of their separation distance x_{12}. The d.o.f. here depicted are detected either optically (x, η, φ) or capacitively (y, z, θ).

differential equation, whose time-domain form is given by

$$m\ddot{x}_1 + m\ddot{x}_{\mathrm{SC}} + m\omega_1^2 x_1 = f_1, \tag{2.4}$$

$$m\ddot{x}_2 + m\ddot{x}_{\mathrm{SC}} + m\omega_2^2 x_2 = f_2 + f_{\mathrm{c}}, \tag{2.5}$$

$$m_{\mathrm{SC}}\ddot{x}_{\mathrm{SC}} - m\omega_1^2 x_1 - m\omega_2^2 x_2 = f_{\mathrm{SC}} - f_{\mathrm{c}} + f_{\mathrm{c,SC}}, \tag{2.6}$$

where the TMs have nominally identical mass $m_1 = m_2 \equiv m$ and the time dependence of the quantities has been omitted for readability purposes.

The $\omega_i^2 x_i$ terms represent the force due to position dependent fields with $-\omega_i^2$ as the force gradient. f_1, f_2, and f_{SC} are the external forces felt by the TMs and SC, and f_{c} and $f_{\mathrm{c,SC}}$ are the commanded forces applied by the DFACS in order to actuate TMs and SC respectively. The absolute position of the SC in the third equation of (2.6) is determined with respect to the celestial frame J2000.

The main objective of the experiment, the differential parasitic force $f_2 - f_1$, can then be derived by subtracting (2.4) from (2.5), giving

$$\ddot{x}_2 - \ddot{x}_1 + \omega_2^2 x_2 - \omega_1^2 x_1 = \frac{f_2 - f_1 + f_{\mathrm{c}}}{m}, \tag{2.7}$$

which can be rewritten as

$$\ddot{x}_{12} + \omega_2^2 x_{12} + \Delta\omega^2 x_1 - \frac{f_{\mathrm{c}}}{m} = \frac{f_2 - f_1}{m}, \tag{2.8}$$

by defining the differential coordinate as $x_{12} = x_2 - x_1$ and the differential quadratic stiffness as $\Delta\omega^2 = \omega_2^2 - \omega_1^2$.

In such small signal approximation, interferometers signals are affected by just additive noise so that

$$o_1 = x_1 + n_1, \tag{2.9}$$

$$o_{12} = x_{12} + n_{12}. \tag{2.10}$$

Replacing coordinates $x_{12,1}$ with signals $o_{12,1}$ and writing the sum of all noisy terms as $n_{\rm tot}$, (2.8) becomes

$$\ddot{o}_{12} + \omega_2^2 o_{12} + \Delta\omega^2 o_1 - \frac{f_{\rm c}}{m} + n_{\rm tot} = \frac{f_2 - f_1}{m}. \tag{2.11}$$

It must be said that that nominal commanded forces $f_{\rm c}$ do not coincide with real applied force. To a first approximation they differ for any random force generated in the actuator, which is, however. included in the disturbance $f_2 - f_1$, but may also be affected by calibration error and delays between the software command to the actuator and the actual application of the force.

As the main objective of the experiment is the differential parasitic force $f_2 - f_1$, one can then construct the differential acceleration between the TMs along the conjoining x-axis, Δg as the differential force per unit mass, giving

$$\Delta g(t) = \ddot{o}_{12}(t) + \omega_2^2 o_{12}(t) + \Delta\omega^2 o_1(t) - g_{\rm c}(t) + n_{\rm tot}(t), \tag{2.12}$$

where $g_{\rm c}$ are the commanded forces per unit mass.

In the course of the mission, the LPF dynamic model has been carefully calibrated via the injection of signals in the system and the evaluation of the system response [24]. Taking into account the model calibration, the differential acceleration Δg can be rewritten as by

$$\Delta g(t) = \ddot{o}_{12}(t) - g_{\rm c}(t) + \omega_{2,\rm tot}^2 o_{12}(t) + \Delta\omega_{\rm tot}^2 o_1(t) - \delta_{{\rm ifo},k}\ddot{o}_1(t), \tag{2.13}$$

which can be extended by expanding the commanded forces per unit mass as

$$\begin{aligned} \Delta g(t) = \ddot{o}_{12}(t) - \lambda_2 \frac{f_{\rm c,2}}{m}(t - \tau_2) + \lambda_1 \frac{f_{\rm c,1}}{m}(t - \tau_1) \\ + \omega_{2,\rm tot}^2 o_{12}(t) + \Delta\omega_{\rm tot}^2 o_1(t) - \delta_{\rm ifo}\ddot{o}_1(t). \end{aligned} \tag{2.14}$$

In the above expression (2.14) the used quantities are:

- the two nominally identical TM masses are $m = 1.928(1)\,\mathrm{kg}$;
- the commanded forces per unit mass acting on the two TMs are modeled as a single term $g_{\rm c}(t)$:

$$g_{\rm c}(t) = \lambda_2 \frac{f_{\rm c,2}\,(t - \tau_2)}{m} - \lambda_1 \frac{f_{\rm c,1}\,(t - \tau_1)}{m}; \tag{2.15}$$

- the stiffnesses $\omega^2_{j,\mathrm{tot}}$ express the coupling to relative motion on-board the SC, depend on the actuation configuration used on the satellite and have been estimated *a-posteriori* [24] from the background stiffness ω^2_j,

$$\omega^2_{j,\mathrm{tot}} = \omega_j + \alpha_{o_j} F_{\max} + \alpha_{\phi_j} N_{\max}; \tag{2.16}$$

- $\delta_{\mathrm{IFO},k}$ is a cross-coupling term that depends on the different epochs of the spacecraft.

The model (2.14) can be furtherly extended by linearizing the commanded force per unit mass (2.15), resulting in

$$\begin{aligned} \Delta g(t) = \ddot{o}_{12}(t) &- \lambda_2 \frac{f_{\mathrm{c},2}(t)}{m} - C_2 \frac{\dot{f}_{\mathrm{c},2}(t)}{m} \\ &+ \lambda_1 \frac{f_{\mathrm{c},1}(t)}{m} + C_1 \frac{\dot{f}_{\mathrm{c},1}(t)}{m} \\ &+ \omega_2^2 o_{12}(t) + \Delta\omega_{12}^2 o_1(t) - \delta_{\mathrm{ifo}} \ddot{o}_1(t), \end{aligned} \tag{2.17}$$

where $C_j \equiv \lambda_j \tau_j$ are the linearized delay coefficients and $j = 1, 2$ refer to the TMs indexing. The results of the parameter estimation used in the generation of the experimental products of the mission can be retrieved in [24].

The time-series $\Delta g(t)$ expressed by (2.17) constitutes the fundamental scientific product of the mission, that is the pure residual differential acceleration between the TMs along the sensitive axis.

The noise performance analysis has been carried out on what are referred to as noise-only measurements, that is, measurements of $\Delta g(t)$ during which no other experiment is performed on the SC, in order to estimate the residual differential acceleration only due to parasitic forces.

2.3 LISA Pathfinder as a tester for LISA requirements

The first limitation to the measurement of parasitic forces stems form the fact that TMs are tracked by a laser interferometer with pm resolution. This set a high frequency limit to the ability to resolve true accelerations above the interferometer readout noise, which in the original design had to fulfill the requirement [25]

$$S^{1/2}_{\mathrm{IFO,req}} = 4.3 \left(\frac{f}{30\,\mathrm{mHz}}\right)^2 \mathrm{pm\,Hz^{-1/2}}. \tag{2.18}$$

Another complication arisen in LPF that will not affect LISA is the correlation of noise sources located on-board the spacecraft: TMs located in the same apparatus are subjected to common disturbances, as noise of magnetic and thermal origin, and these contributions could be correlated in such a way that could lead to underestimation of the noise level on the spacecraft.

Instead, correlated noise sources in LISA may only be of astrophysical origin, like fluctuations in the interplanetary magnetic field, charged particles flux and solar radiation pressure are due to the coupling to the Sun.

This drawback is mitigated by the intrinsic differences between the TMs: even though they are built with the same physical properties, there are some intrinsic differences in their susceptibility values, and their responses to thermal and magnetic disturbances are thus mismatched.

Coupling to the gravitational field gradient is also different in LPF relative to LISA. Contrarily to LPF, in LISA the two TMs located at the ends of an interferometric link are coupled to two different SCs. However, in both missions this effect can be subtracted from the data by estimating the gradients $\omega_{j,\mathrm{tot}}$ with dedicated calibration experiment and correcting the data as discussed in previous Section §2.2.

2.3.1 Requirements and expected noise model at launch

The noise sources affecting the LPF performance have been evaluated prior to the course of the mission, and have been accounted in the expected noise model for the mission. The detailed description of the Pathfinder noise contributions, together with their quantitative estimate, will be given in Section 3.4.

Here it is only depicted the noise performance Best Estimate before launch, accounting for the three prominent contribution to the noise model and pictured in Figure 2.6. In the plot, the noise contributions are indicated with their Best Estimate (BE) value allocated before the mission launch [25].

These terms establish the expected noise performance behaviour in all working conditions, and can be ascribed to three main effects, among the many that have been modeled:

- electrostatic actuation noise caused by the TMs-applied voltages, impacting at low frequencies, whose pre-launch requirement was

$$S^{1/2}_{\mathrm{act,BE}}(f) = 10.1 \left(\frac{1\,\mathrm{mHz}}{f}\right) \mathrm{fm\,s^{-2}\,Hz^{-1/2}}, \tag{2.19}$$

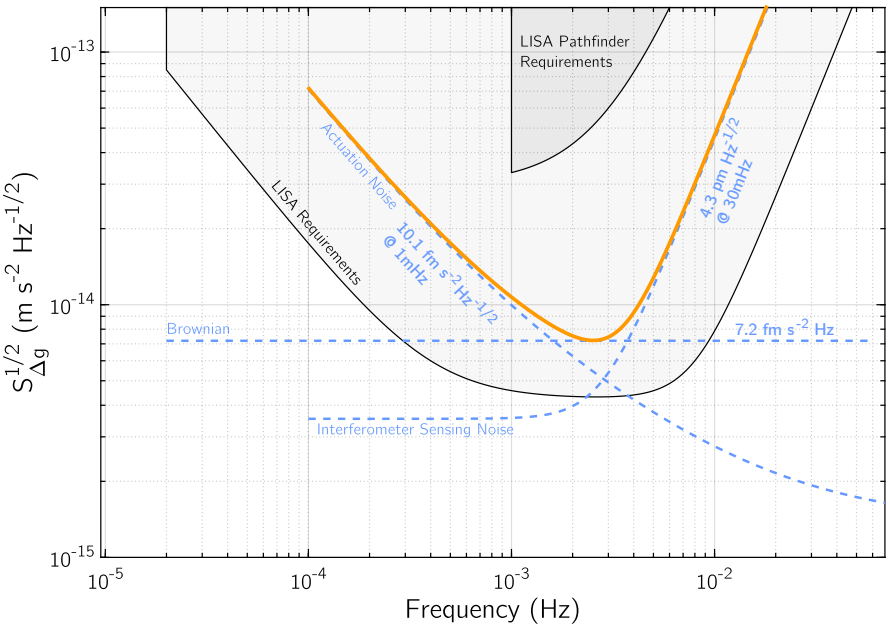

Figure 2.6: LISA Pathfinder Best Estimate noise performance curve (orange), depicted as sum of the interferometer sensing, actuation and Brownian noise levels modeled before launch. The three noise sources are illustrated with their respective Best Estimate values.

- Brownian white noise due to residual gas inside the system, acting on all the noise spectrum, with pre-launch best estimate being

$$S_{\mathrm{B,BE}}^{1/2} = 7.2 \text{ fm s}^{-2} \text{ Hz}^{-1/2}. \tag{2.20}$$

- interferometer sensing fluctuations, relevant at higher frequencies, with pre-launch requirement set by (2.18).

These three terms establish the expected noise performance behaviour in all working conditions, as depicted in Figure 2.6 showing the contributions of the interferometer sensing, actuation and Brownian noise sources with the values allocated as Best Estimate before LPF launch.

On the first day of operations, March 1st, 2016, the noise performance of the mission was the one illustrated in Figure 2.7, retracing the actuation (2.19) and Brownian (2.20) allocated noise level, and notably improving the interferometer predicted contribution (2.18).

Moreover, as the compensation of the gravitational imbalance was much better than expected, allowing to reduce the actuation voltages and therefore the actuation noise at low frequency: this led to an improvement of the

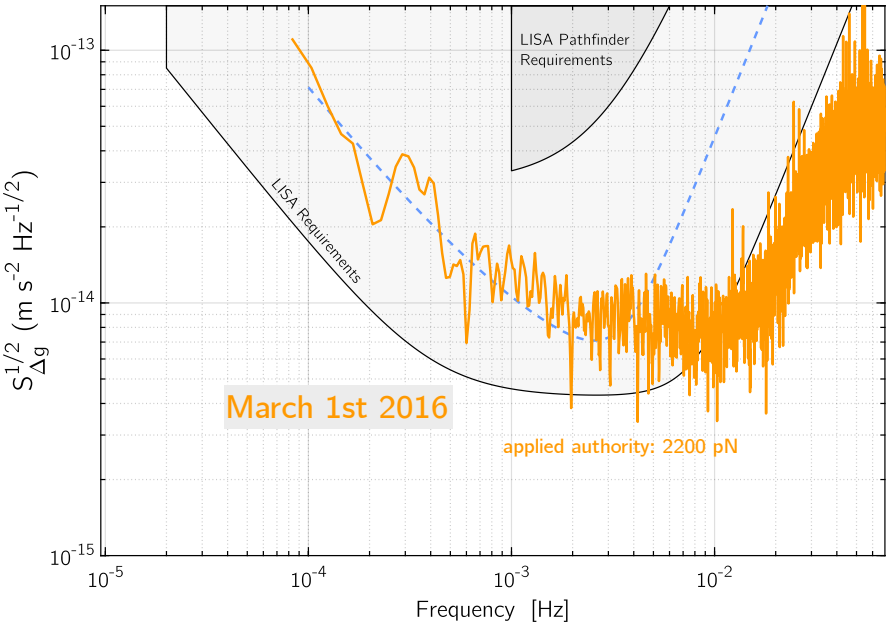

Figure 2.7: Noise spectrum for the Δg measurement performed on the first days of operations between March 1st, 2016 and March 3rd, 2016 (orange data), compared to the Best Estimate noise model of Figure 2.6 (dashed light blue line). The initial applied authority on TM2 was $F_{x2} = 2200\,\mathrm{pN}$, and was then reduced in the course of operations.

performance down to a level that we did not expect to reach during the mission, whose analysis is the subject of the following Part §I.

Part I

Experimental results from LISA Pathfinder

In the following chapters, I will provide a thorough discussion of the LISA Pathfinder experimental results obtained in the course of the mission, with the extent of widening the landscape provided by the noise performance results published after the conclusion of the mission.

This thesis constitutes therefore the long write-up of [17], and a substantial part of the analysis performed in this work contributed to the aforementioned publication.

The noise performance of LPF has been evaluated via the assessment of the differential parasitic acceleration Δg between the two free-falling TMs inside the SC, as seen in Section §2.2. The outcome of the LPF experimental results and this work original contributions are illustrated in this Part, and will be organized as follows.

- The differential acceleration noise spectrum of LPF is found to be subjected to inertial dynamical effects connected to the spacecraft motion, as the action of centrifugal and Euler forces due to the SC rotation and the coupling of the SC motion to the interferometer readout. The contribution of these features to the noise performance has been estimated with the available telemetry data and the differential acceleration noise has subsequently been corrected for their effect, as described in Section §3.1.

- Once purged from the inertial dynamical effects, the differential acceleration noise performance is therefore evaluated in in comparison with the expected noise model and with particular attention to the low frequency noise behavior, being the main focus of my work and a limiting noise source for the LISA sensitivity. This original analysis is carried out in Chapter §3.3.

- In order to better investigate the low frequency noise performance, in Chapter §4 I performed the needed analysis to assess the presence of correlation at low frequency between the differential acceleration noise $\Delta\gamma$ in the angular degrees of freedom and the translational differential acceleration Δg.

- The differential parasitic acceleration time-series $\Delta g(t)$ has also been found to be affected by spurious force signals of unknown nature, which are distributed along the course of the whole mission and are illustrated in Chapter §5. The investigation of these signals is a completely original contribution: they have been individually fitted and subtracted from

the data leaving no residual noise, allowing to separate them from the analysis of the noise performance features.

- The detailed description of the employed statistical analysis techniques for spectral estimation, which have been developed in a partially original fashion are going to be presented in Appendices A.

In conclusion, my personal contributions to the comprehension of LPF experimental results are: the analysis of noise features arising from the acceleration noise performance, the torque noise analysis in comparison with the differential acceleration noise, the statistical analysis of the spurious signals arising in the noise, and the partial modification of the spectral estimation techniques applied to data.

During the mission, there have been measurement sessions in which forces and various signals have been applied, in order to calibrate the experiment. The noise-only measurements, instead, have been characterized by not applying any external stimulus and by maintaining stable operating conditions. Actuation stability was achieved by reducing the applied actuation voltages, while temperature stability was passively established by the thermal design, with no active T control system.

The noise performance experimental results taken into account in this work are a selection of twelve noise-only runs with duration that ranges from a minimum of almost 3 up to 18 uninterrupted days. The analysis of noise runs with a duration of $\sim 3\,\mathrm{d}$ allows to reach the lowest frequency portion ($\geq 20\,\mu\mathrm{Hz}$) of the noise spectrum, and to guarantee the highest possible number of averaging segments in the spectrum estimation.

The noise runs under analysis were acquired between March 2016 and June 2017, over the course of 16 months, during which several engineering and science maneuvers took place on the satellite.

- For starter, in the course of the whole mission the system control was handed to NASA four times, during which they performed Space Technology 7 Disturbance Reduction System (ST7-DRS) operations [26], in order to test colloidal gas thrusters.

- In addition to this, the TMs were re-grabbed via the launch-lock mechanism and the spacecraft entered the so called *LPF safe mode* for a total of five times during science operations.

- At the beginning of April 2017, $\sim 500\,\mathrm{d}$ after launch, a deorbiting procedure was executed to push LPF outside of its equilibrium orbit and

prepare it for dismissal: it started on April 6th, 2017 and concluded on April 11th, 2017 at `19:40:00`. The deorbiting procedure was realized simultaneously to the fifth *LPF safe mode*.

- The fourth NASA handout period started on April 12th, 2017 at `16:00:00`, just after deorbiting, and the ST7-DRS testing phase ended on April 29th, 2017 at `17:35:00`, when the system control was handed back to ESA. After the end of NASA operations, the DRS packets have been permanently shut down.

The main operating conditions of the twelve noise runs under consideration are listed in Table 2.1. They have been measured in the actuation configuration minimizing low frequency noise (`URLA` and `UURLA`), while the majority of the noise measurement acquired during operations have been taken with different actuation configurations.

The average working temperature of the apparatus has also been recorded for the twelve noise runs, to account for the history of the T evolution in the course of the mission. In Chapter 3 I will also refer to the lowest temperature noise runs taken at $< 2\,^{\circ}\mathrm{C}$, for comparison on some peculiar aspects of the analysis.

The first cool-down occurred on January 23rd, 2017 and brought temperature from $T \simeq 22\,^{\circ}\mathrm{C}$ down to $T_{\mathrm{low}} \simeq 12\,^{\circ}\mathrm{C}$ (417 days after launch), while the second and last one occurred on April 29th, 2017 (513 days after launch) immediately after getting back control of the satellite from NASA. During the second cool-down temperature was lowered down to $T_0 < 2\,^{\circ}\mathrm{C}$: only an upper limit can be put on T_0, being its value outside the temperature diagnostics subsystem working range [27].

The cool-down to T_0 furtherly lowered the Brownian noise level, but simultaneously led to a sharp increase of the spurious signals occurrence rate, which made the noise measurements at this temperature unusable for the sake of estimating the differential acceleration noise performance. The Brownian level at T_0 was then estimated on Δg data segments free from spurious events, which will be detailedly discussed in Chapter §5.

The apparatus was kept at $\sim T_0$ between May 3rd, 2017 and May 12th, 2017, with the temperature $T_{\mathrm{low}} \simeq 11\,^{\circ}\mathrm{C}$ eventually restored on May 15, 2017 [27]. The spacecraft temperature was brought back to $T \simeq 22\,^{\circ}\mathrm{C}$ on May 20th: with the rising of T, the rate of spurious events affecting Δg also went back to the levels of before the cool-down.

Table 2.1: List of twelve noise-only runs acquired during LPF operations that have a time duration over three days. Noise runs with indexes #17, #39, #42 and #74 are additional with respect to [17].

Run	Start time	Stop time	Duration (d)	Authority configuration	Average temperature (°C)
6	2016-03-21 01:59:10	2016-03-26 07:59:45	5.3	URLA	22
9	2016-04-04 00:00:00	2016-04-13 07:59:45	9.3	UURLA	22
17	2016-05-16 00:00:00	2016-05-16 11:36:00	3.2	UURLA	22
39	2016-06-19 13:00:00	2016-06-24 08:00:00	4.8	UURLA	22
42	2016-07-17 12:00:00	2016-07-2012 06:00:00	2.7	UURLA	22
43	2016-07-24 17:00:00	2016-07-30 00:00:00	5.3	UURLA	22
59	2016-11-16 11:05:00	2016-11-26 08:00:00	9.9	UURLA	22
61	2016-12-26 07:59:30	2017-01-13 19:58:00	18.5	UURLA	22
66	2017-02-14 01:59:50’	2017-02-27 09:53:30	13.3	UURLA	11
74	2017-05-18 18:24:46	2017-05-23 02:00:00	4.3	UURLA	11
75	2017-05-29 13:55:10	2017-06-05 08:00:00	6.8	UURLA	22
76	2017-06-08 12:00:45	2017-06-17 01:42:31	8.6	UURLA	22

3 Differential acceleration noise between free falling test-masses

As anticipated in the previous Chapter §2, the time-series of pure residual differential acceleration between the TMs along the sensitive axis $\Delta g(t)$ is the fundamental scientific product of the mission and is expressed by (2.17).

However, additional effects impacting on $\Delta g(t)$ need to be taken into account when estimating the TMs residual differential acceleration from telemetry data, since the LPF spacecraft cannot be safely approximated to a perfectly aligned system located inside an inertial reference frame.

These inertial effects originating from the rotation of the SC are not relevant for LISA: in LPF the SC attitude control was of the order of $\sim$ mrad $\mathrm{Hz}^{-1/2}$, while in LISA is expected to be at some tens of nrad $\mathrm{Hz}^{-1/2}$. The suppression of disturbances present only in the LPF experimental apparatus allows to focus on the analysis and characterization of the other disturbances which are of interest for LISA.

3.1 Correction of inertial effects

There are two categories of inertial effects that impact only on LPF:

- the interferometer picks up other degrees of freedom besides the separating distance between the TMs, δg_{sc}. The main resulting effect is the leakage of the angular motion of the SC in the in the estimate of $\ddot{x}_{12}$, an effect relevant above $\sim 10\,\mathrm{mHz}$;
- Euler and centrifugal forces due to the SC rotation, $g_{\mathrm{rot}}(t)$. These directly impact the critical frequency band below $\sim 1\,\mathrm{mHz}$

The interferometer rotational pickup does not affect the differential acceleration measurement itself, and its suppression may almost be considered somewhat aesthetic. Its correction is obtained rather straightforwardly by fitting and subtracting the proper sensor outputs in the post-processing phase. Nevertheless, applying the correction consents to properly characterize only the physical disturbances relevant for LISA.

The former inertial contribution, δg_{sc}, accounts for the misalignments among TMs, GRS and spacecraft, whose two main effects are illustrated schematically in Figure 3.1: the translational misalignment of the TM with

respect to the interferometer axis and the rotational misalignment of the TM with respect to its Center of Rotation (CoR).

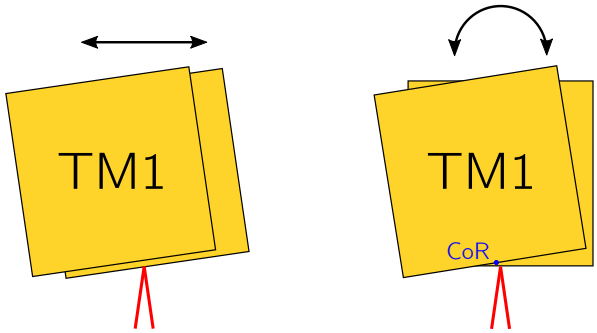

Figure 3.1: Schematic depiction of the misalignment between TMs, GRS and spacecraft that give rise to the inertial contribution $\delta g_{\rm sc}$(Adapted from [28])

The impact of this coupling on the LPF noise performance mainly results in an amplitude *bump* towards the higher frequency part $20 \div 200\,\mathrm{mHz}$ of the noise spectrum $S_{\Delta g}^{1/2}$ (light-blue curve of Figure 3.3).

This quantity strongly depends on rotation or displacement of the TMs along the non-sensitive axes y, z, ϕ, η, in the form of

$$\delta g_{\rm sc}(t) = b_1 \ddot{\overline{\phi}}(t) + b_2 \ddot{\overline{\eta}}(t) + b_3 \ddot{\overline{y}}(t) + b_4 \ddot{\overline{z}}(t) + b_5 \overline{y}(t) + b_6 \overline{z}(t), \tag{3.1}$$

a model that is currently being improved [28] to take into account all the actual coupling effects on the apparatus.

The rotational effects $g_{\rm rot}(t)$ of (3.7) due to the angular jitter of the rotating spacecraft frame are divided in two different contributions

$$g_{\rm rot}(t) \equiv g_{\dot{\Omega}}(t) + g_{\Omega}(t), \tag{3.2}$$

that is, the centrifugal forces due to the rotation of the spacecraft $g_{\Omega}(t)$ and the Euler forces due to the rotational acceleration of the spacecraft $g_{\dot{\Omega}}(t)$, where $\Omega(t)$ constitutes the satellite angular velocity. $\Omega(t)$ is the sum of a part subjected to secular variation, estimated via the star-trackers located on the SC, and in-band fluctuations, estimated from the average TM torque applied along y and z.

The centrifugal term g_{Ω} is included in the green curve of Figure 3.3 and enters the dynamics of LPF as the rotation of the spacecraft exerts a centrifugal force on the TMs, as depicted in Figure 3.2a.

The centrifugal correction is therefore given by

$$\begin{aligned} g_{\Omega} &= -\left(\Omega_{\phi}^2 + \Omega_{\eta}^2\right)(x_2 - x_1), \\ &= -\left(\Omega_{\phi}^2 + \Omega_{\eta}^2\right) d, \end{aligned} \tag{3.3}$$

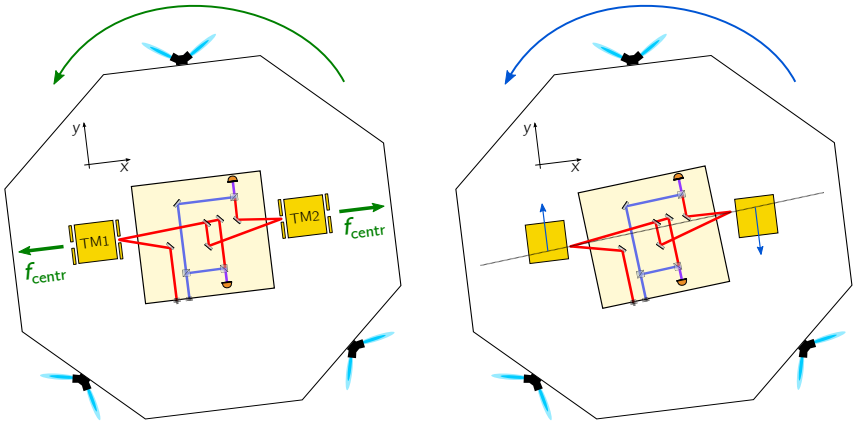

(a) Schematic depiction of the centrifugal force acting on the TMs and generating g_Ω.

(b) Schematic depiction of the Euler force acting on the TMs and exerting $g_{\dot\Omega}$.

Figure 3.2: Schematic depiction of the inertial rotational effects acting on the spacecraft.

where $d = x_2 - x_1$ separation distance between the TM along the sensitive x-axis and the time dependence of all quantities is tacit for readability purposes.

The Euler force term dependent on $\dot\Omega$ is non-zero in the case of a mismatch of the TM conjoining axis along the y and z directions, as depicted in Figure 3.2b and its effect on the noise performance is pictured as the the yellow curve of Figure 3.3. The evaluation of the $g_{\dot\Omega}$ term is carried out by measuring the TM torques caused by the SC rotation on the ϕ and η degrees of freedom, resulting into

$$\begin{aligned} g_{\dot\Omega} &= \left(\cancel{\Omega_\eta \Omega_\theta} - \dot\Omega_\phi\right)(y_2 - y_1) + \left(\dot\Omega_\eta - \cancel{\Omega_\phi \Omega_\theta}\right)(z_2 - z_1), \\ &= -\dot\Omega_\phi\ \delta y + \dot\Omega_\eta\ \delta z, \\ &= \left(-\frac{N_\phi}{I_{zz}}\delta\phi + \frac{N_\eta}{I_{yy}}\delta\eta\right) d, \end{aligned} \tag{3.4}$$

where the Ω^2 terms in the y, z mismatch channels are negligible and the rotational acceleration terms $\dot\Omega_{\phi,\eta}$ have been rewritten as

$$\dot\Omega\delta y = \frac{N_\phi}{I_{zz}}\delta y = d\ \frac{N_\phi}{I_{zz}}\delta\phi, \tag{3.5}$$

$$\dot\Omega\delta z = \frac{N_\eta}{I_{yy}}\delta z = d\ \frac{N_\eta}{I_{yy}}\delta\eta, \tag{3.6}$$

in terms of the applied torques $N_{\phi,\eta}$ on the TMs, moments of inertia $I_{yy,zz}$ and respective angular misalignments $\delta\phi = \delta y/d, \delta\eta = \delta z/d$.

The suppression of the centrifugal effect $g_\Omega(t)$ of expression (3.3) is performed in the post-processing phase by evaluating the contribution for each run, separately. The Euler term (3.4) is instead evaluated via a global fit to groups of runs, according to three various operation periods established on the SC, as indicated in [24].

The impact of non-inertialities on Δg can be assessed by rewriting the inertial differential acceleration as

$$\Delta g'(t) \equiv \Delta g(t) + \delta g_{\rm sc}(t) + \underbrace{g_\Omega(t) + g_{\dot\Omega}(t)}_{g_{\rm rot}(t)} . \tag{3.7}$$

The inertial contributions in $\Delta g'$ can be estimated and subtracted separately to recover the clean sensitive axis differential acceleration $\Delta g' \equiv \Delta g$, and their distinct effects are noticeable in the noise spectra of the residual differential acceleration $S^{1/2}_{\Delta g}$, depicted in Figure 3.3 for the best performance noise run of February 2017, published in [17].

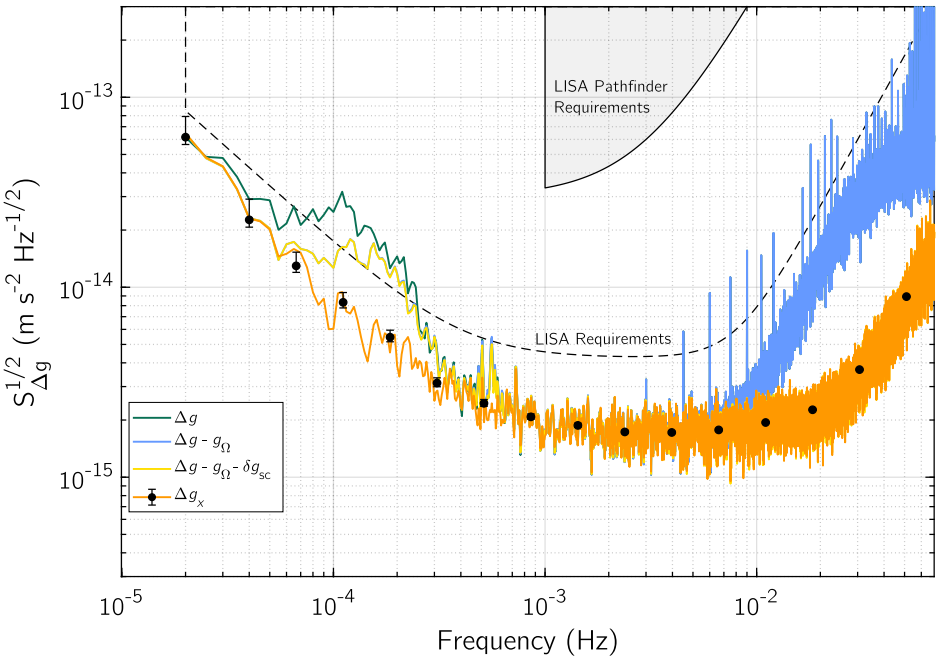

Figure 3.3: ASD of one uninterrupted stretch of data measured in February 2017 published in [17]. The continuous lines refer to the ASD calculated via the Welch periodogram method, while the points correspond to the Bayesian ASD estimate described in Appendix §A.

In the plot, the noise spectrum contains different features that are progressively suppressed with the subtraction of the various inertial terms in (3.7) and

the ASD of Δg is evaluated using two different methods. The continuous lines represent the ASD evaluated via the classical Welch periodogram method [29], also referred to as Weighted Overlapping Segment Average (WOSA) method, while the black points refer to a partially original ASD estimation technique with minimum correlation frequency selection and Bayesian error bars estimation, which is going to be discussed in theoretical detail in Appendix A.

3.2 LPF noise performance along the mission

The orange curve and black points of Figure 3.3 establish therefore the noise spectrum of LPF after the subtraction of inertial effects. Beyond the correction of inertial effects, the data pictured in the plot also account for the subtraction of spurious signal occurrences, which are detailedly described in Chapter §5.

The spurious signals effect on the noise performance can be appreciated in Figure 5.2, where a comparison is held between the ASD of $\Delta g(t)$ data corrected for the inertial effects, but before and after the subtraction of the spurious signals.

Once the differential acceleration data $\Delta g(t)$ are purged also from the effect of the spurious signals, a common structure can be found for all noise-only runs spectra, that is, an high frequency ascent, a white-noise plateau and a low frequency rising.

The detailed depiction of the ASD of the noise-only $\Delta g(t)$ measurements of Table 2.1 is provided in Figure 3.4, where for clarity it is reported only the Bayesian estimation of the ASD, whose theoretical derivation is illustrated in Appendix A.

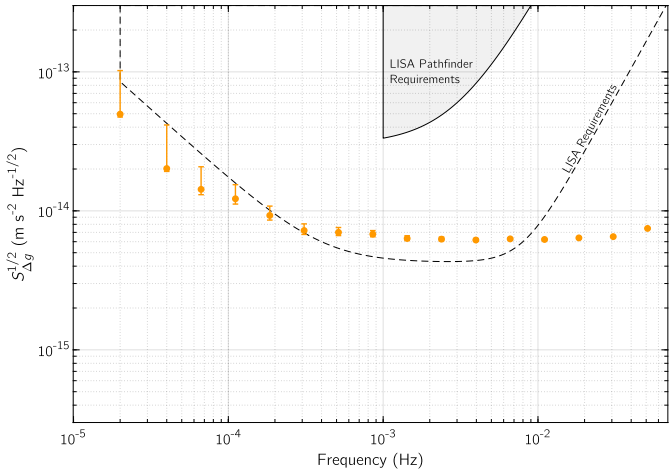

(a) Noise performance of run #6

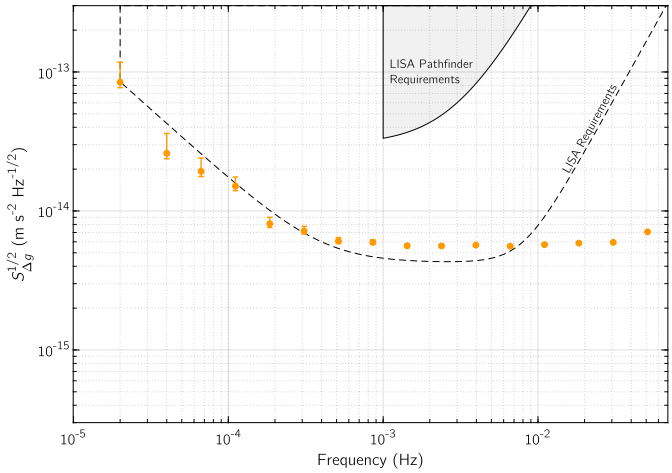

(b) Noise performance of run #9

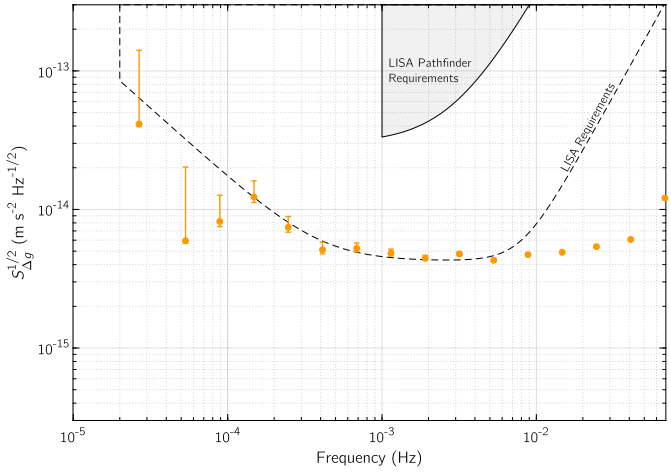

(c) Noise performance of run #17

Figure 3.4: ASD of the noise-only runs of Table 2.1.

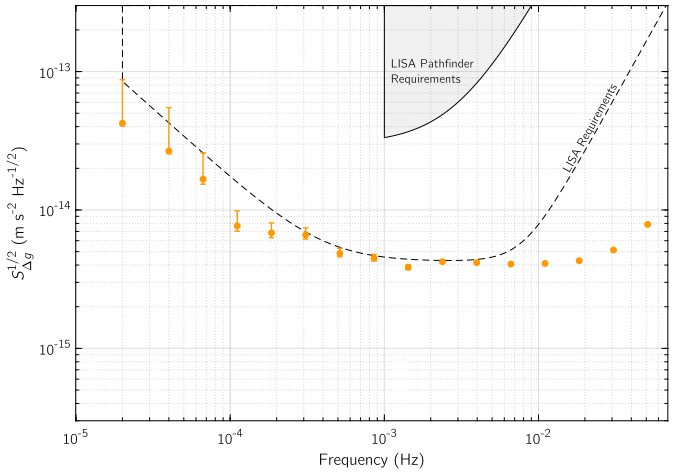

(d) Noise performance of run #39

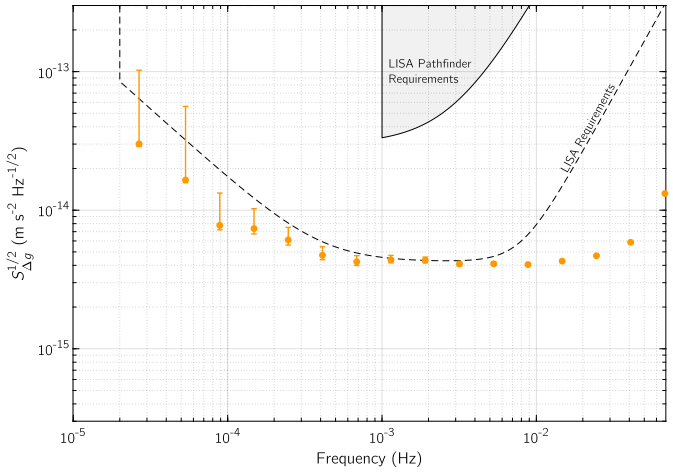

(e) Noise performance of run #42

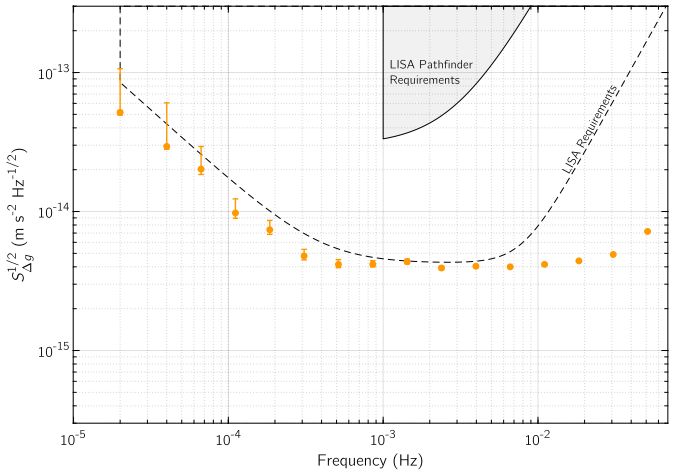

(f) Noise performance of run #43

Figure 3.4: ASD of the noise-only runs of Table 2.1.

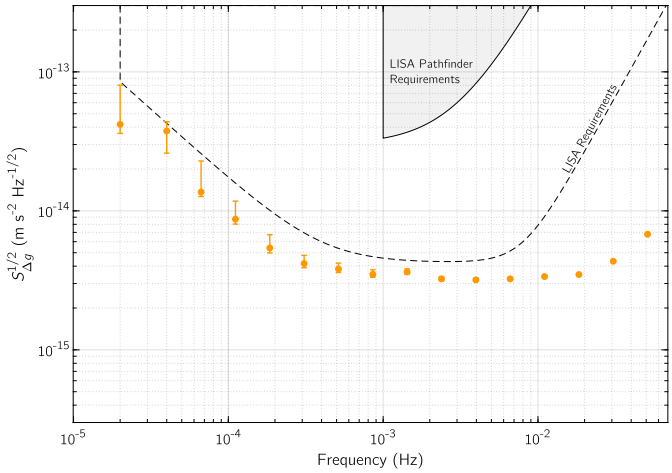

(g) Noise performance of run #59

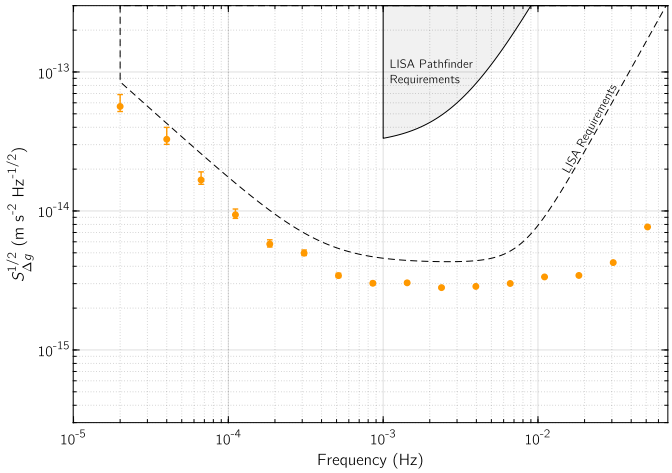

(h) Noise performance of run #61

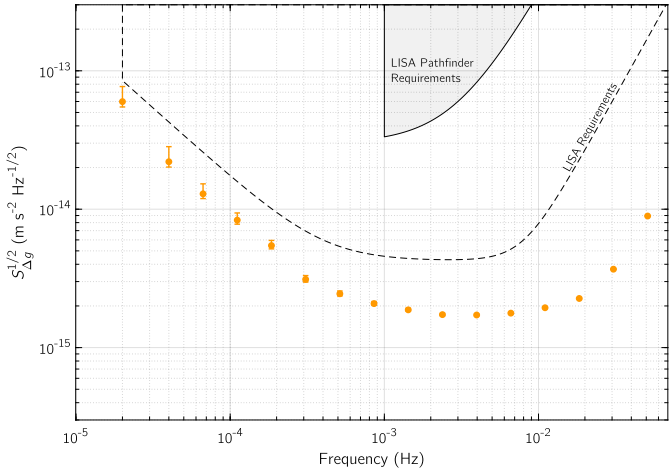

(i) Noise performance of run #66

Figure 3.4: ASD of the noise-only runs of Table 2.1.

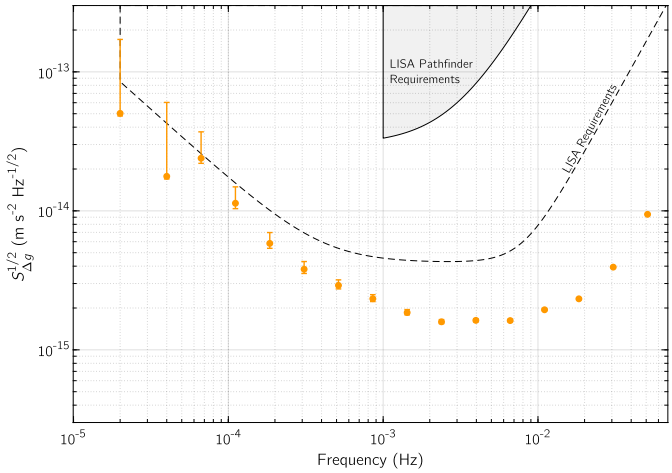

(j) Noise performance of run #74

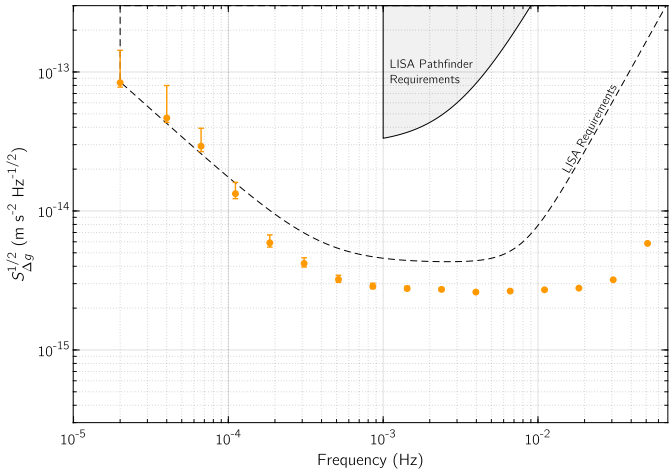

(k) Noise performance of run #75

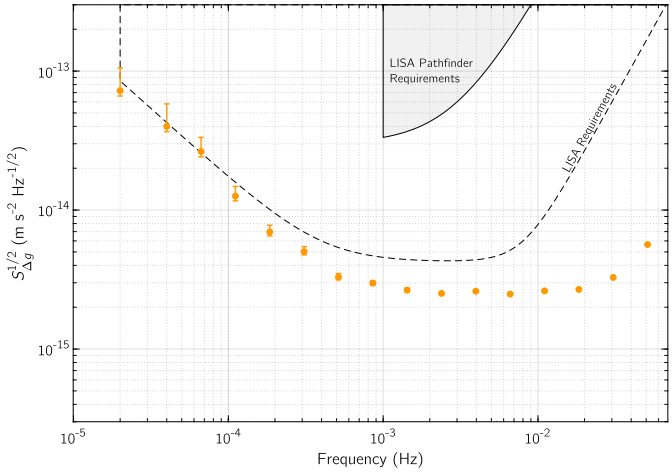

(l) Noise performance of run #76

Figure 3.4: ASD of the noise-only runs of Table 2.1.

3.3 Low frequency noise

As anticipated in previous Chapters §1 and §2, the emphasis of this work is on the white and low frequency parts of the spectrum, that is, in the mHz band and lower. The high frequency ascent of the noise spectrum is attributable mainly to interferometer sensing noise and is not going to be as relevant in LISA as it was in LPF measurements.

The low frequency part of the spectrum shows a rather consistent behaviour for all runs: a branch following a power-law at the lowest frequencies, merging into a flat plateau at frequencies above 1 mHz. The value of the plateau depends on the epoch of the run and on its temperature, while the power-law branch is nearly independent of the run epoch and condition. The two features are analyzed in the following.

3.3.1 Brownian noise plateau

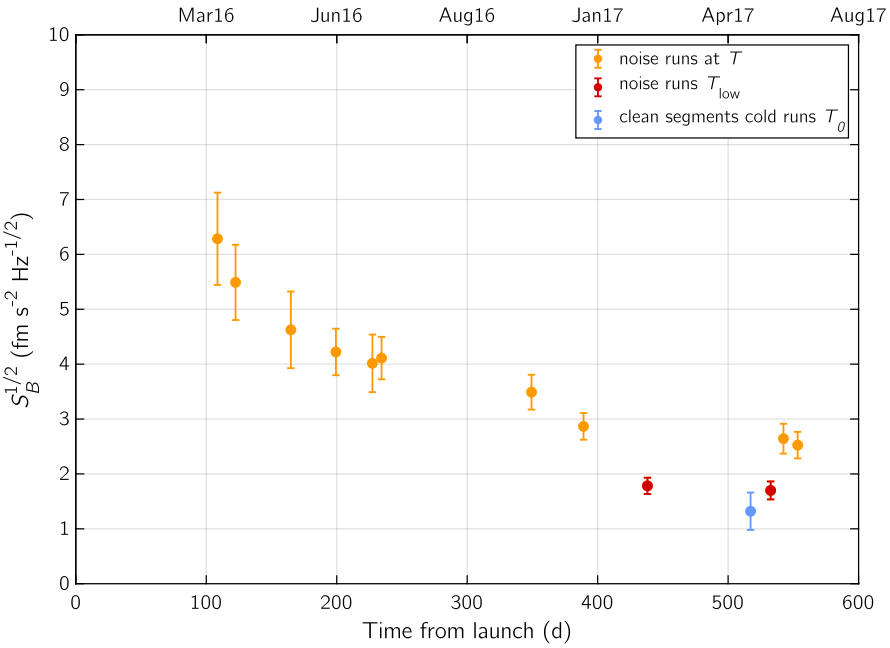

Figure 3.5: Evolution of the Brownian noise level evaluated in the frequency range $2 \div 4\,\mathrm{mHz}$ as a function of the days elapsed from launch. Each point represents a different noise-only run. Orange points refer to data measured at $T = 22\,^{\circ}\mathrm{C}$, red dots refer to the noise runs taken at $T_{\mathrm{low}} = 11\,^{\circ}\mathrm{C}$. The single blue dot represents the Brownian measured during the undisturbed segments of the cold noise runs at $T_0 < 2\,^{\circ}\mathrm{C}$, measured in May 2017.

The frequency independent plateau in the Δg spectra is confidently ascribed to Brownian noise due to residual gas pressure surrounding the TMs.

This attribution is motivated by the following reasons.

- The PSD of Brownian noise from viscous damping is indeed frequency independent.

- The observed noise level depends on the time from launch. This is shown in Figure 3.5, where the plateau values for the twelve noise runs have been evaluated by averaging the noise spectra between 2 mHz and 4 mHz and are reported as a function of the days elapsed from launch.

  The observed time evolution of the Brownian noise is consistent with the decrease of pressure within the GRS expected from the continuous venting to the outer space.

  In addition to this, the noise level was subjected to further decrease in correspondence of the two cool-downs executed on-board, down to T_{low} and then to T_0, highlighted in the plot with red and blue points.

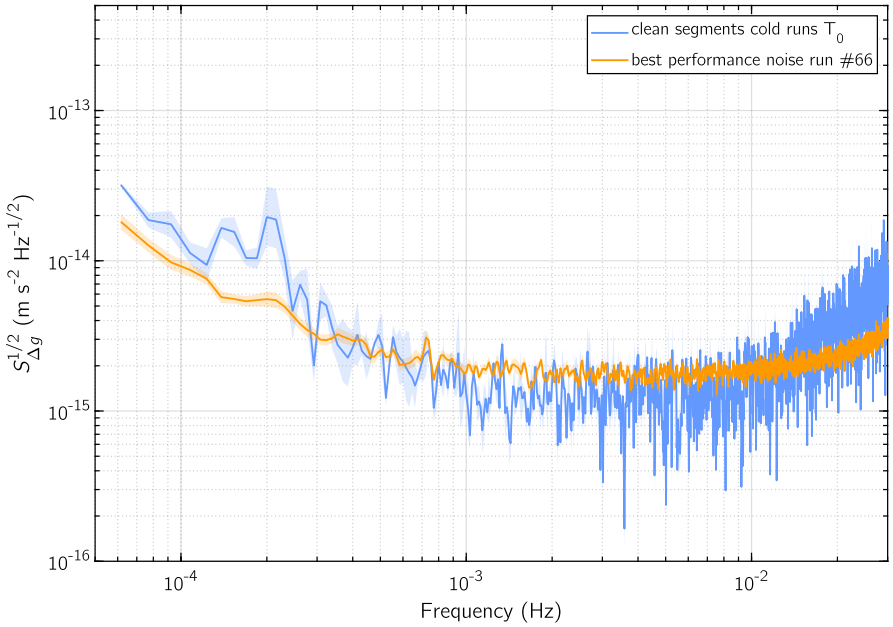

Figure 3.6: Comparison among Brownian levels of the best performance noise run of February 2017 and the Brownian level of the segments free from glitches (Chapter §5) of the noise runs measured at T_0.

In Figure 3.6 the spectrum of the best performance noise run #66 of February 2017, taken at T_{low}, is plotted against the spectrum of the clean

noise segments of the T_0 noise runs, for frequencies between 0.1 mHz and 60 mHz.

In the plot, a decrease in the Brownian noise level can be appreciated from $1.78 \pm 0.15\,\mathrm{fm\ s^{-2}Hz^{-1/2}}$ (3.16) down to $1.3 \pm 0.3\,\mathrm{fm\,s^{-2}\,Hz^{-1/2}}$ (3.17) in the T_0 noise runs. Such decrease is consistent with the lowering of pressure due to the decreased thermally activated outgassing within the GRS.

3.3.2 Low frequency branch

3.3.2.1 Decorrelation of the effect of temperature

An obvious candidate source for low-frequency noise are temperature fluctuations. In order to isolate the low frequency behavior from temperature-related phenomena, differential acceleration data have been decorrelated from the effect of the temperature T_{EH} internal to the EH. The temperature readout is provided by a total of eight thermometers located on the EH (four per each TM), and allow estimation of the absolute temperature $\overline{T}$ on each TM, as

$$\overline{T}_1(t) = \frac{\sum_{i=1}^{4} T_i(t)}{4} \tag{3.8}$$

$$\overline{T}_2(t) = \frac{\sum_{i=5}^{8} T_i(t)}{4}. \tag{3.9}$$

The correction for the absolute temperature fluctuations, when applied to $\Delta g(t)$, gives as final product

$$\Delta g_{T\mathrm{dec}}(t) = \Delta g(t) - \alpha_1 \overline{T}_1(t) - \alpha_2 \overline{T}_2(t), \tag{3.10}$$

where $\alpha_{1,2}$ are the absolute T decorrelation parameters for the two TMs. The parameters α_1 and α_2 obtained through the fit are listed in Table 3.1 and are found to be compatible with the ones obtained in independent EH thermal modulation experiments [30]. In what follows, the differential acceleration time-series under analysis have all been decorrelated for the effect of absolute temperature.

The absolute temperature decorrelation affects the noise spectrum $S_{\Delta g}^{1/2}$ only on the lowest frequency bin, and its effect diminishes progressively with time with the same behavior of the Brownian noise depicted in Figure 3.5, as does the internal pressure on-board the satellite.

The dedicated experiments aforementioned have shown that, during the early stages of the operations, the residual temperature dependence was an

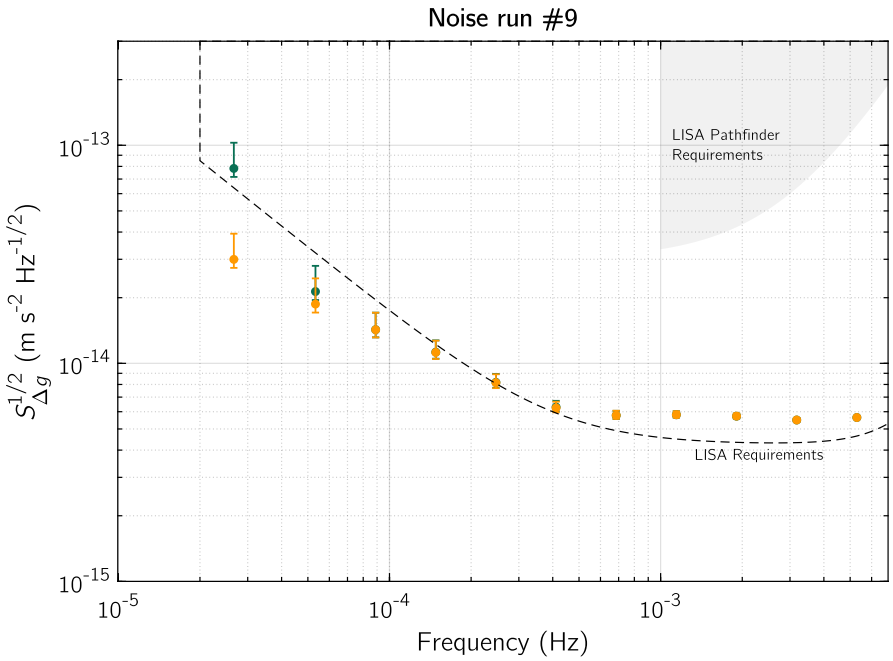

(a) Noise run #9 of April 2016.

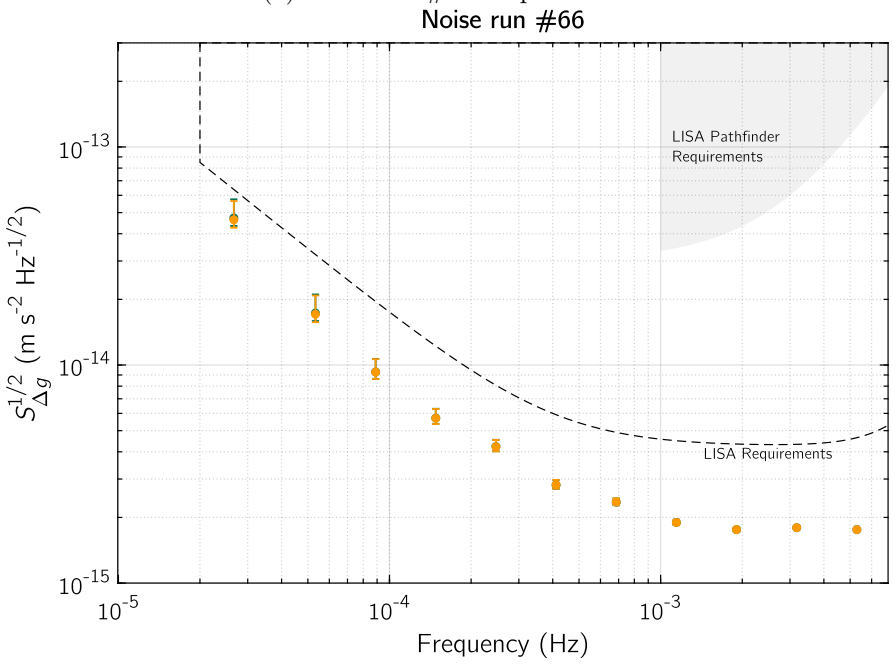

(b) Noise run #66 of February 2017.

Figure 3.7: Comparison among $S_{\Delta g}^{1/2}$ and $S_{\Delta g_{T\mathrm{dec}}}^{1/2}$.

Table 3.1: Absolute temperature decorrelation parameters $\alpha_{1,2}$ for the twelve noise runs of Table 2.1. The only relevant ones are the parameters for runs #6, #9, #17, #42 and #74.

Run	α_1 (pm s^{-2} °C^{-1})	α_2 (pm s^{-2} °C^{-1})
6	6.9 ± 0.9	-2.8 ± 0.7
9	4.7 ± 0.9	-1.7 ± 0.8
17	3.9 ± 0.5	-1.9 ± 0.4
39	3.7 ± 1.2	-1.4 ± 0.8
42	1.5 ± 0.3	-0.7 ± 0.2
43	2.3 ± 1.3	-0.5 ± 0.8
59	0.1 ± 0.2	0.5 ± 0.4
61	0.8 ± 0.4	-0.5 ± 0.3
66	0.5 ± 0.5	-0.5 ± 0.5
74	1.4 ± 0.6	-1.7 ± 0.4
75	0.2 ± 1.1	-0.9 ± 0.7
76	0.2 ± 0.8	-0.1 ± 0.6

effect of temperature driven outgassing with comparatively high pressure. As seen in Table 3.1, such comparatively large temperature coefficient decayed in time along with the suppression of the outgassing, leaving a small, time-dependent coefficient fully compatible with the gravitational field modulation due to local distortion in the GRS.

Thus, these temperature effects can be kept negligible within LISA noise budget, provided the temperature stability and the pressure condition obtained in LPF can be reproduced. The rest of the analysis is going to be focused on temperature decorrelated data.

3.3.2.2 Low frequency noise behavior

The low frequency noise behavior can be separated from the experimental noise spectrum for T decorrelated data $S^{1/2}_{\Delta g, T\mathrm{dec}}$ by marginalizing the run-dependent Brownian noise, according to the statistical procedure described in Appendix §A.1.

The results are reported in Figure 3.8, depicted together with the ASD of the low frequency noise term of all noise measurements under analysis. For consistency purposes, the low frequency noise spectra have been estimated by choosing the lowest common frequency to all the twelve noise runs, that is $f_0 = 27\,\mu\mathrm{Hz}$.

The data in Figure 3.8 are consistent with a global fit to the power law

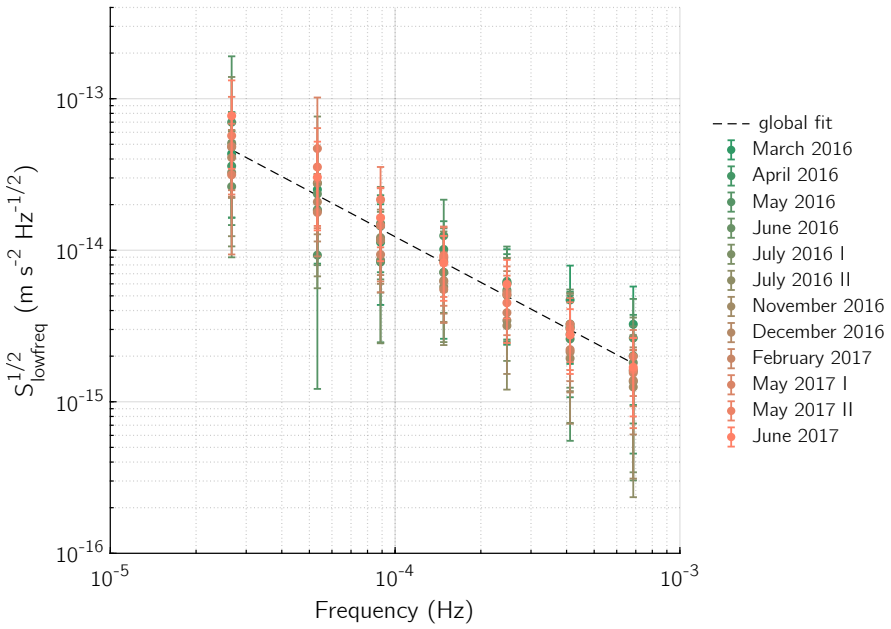

Figure 3.8: Low frequency noise behavior in ASD obtained after marginalizing the Brownian contribution. Here the results are depicted for the twelve noise-only runs listed in Table 2.1. The dashed line represents the global fit to the power law $A\ f^{-n}$ with parameters given by (3.11).

$A\ f^{-n}$ with

$$\begin{aligned} &n = 2.0 \pm 0.2, \\ &A = (1.8 \pm 0.3) \times 10^{-36}\ \mathrm{m^2 s^{-4} Hz^{n-1}}. \end{aligned} \tag{3.11}$$

If one assumes that the real model for the low frequency noise S_{lowfreq} is given by

$$S_{\text{lowfreq}}(f_j) = \frac{A}{f_j^2}, \tag{3.12}$$

for each frequency bin f_j, the global fit gives

$$A^{1/2}_{(n=2)} = (1.2 \pm 0.7) \times 10^{-18} \mathrm{m\ s^{-2} Hz^{1/2}}, \tag{3.13}$$

which corresponds to the dashed line of Figure 3.8.

The fit quality improves by fitting individually $S_{\text{lowfreq},k}(f)$ per each noise run k. This also allows to trace any residual dependencies of the low frequency tail from the physical conditions in which the various runs were performed, allowing to extract additional information by analyzing the history of the low frequency noise slope $A_k^{1/2}$ along the course of the mission.

The time evolution of the low frequency noise is depicted in Figure 3.9, where the slope values $A_k^{1/2}$ are together with the history of engineering and scientific operations occurred on LPF.

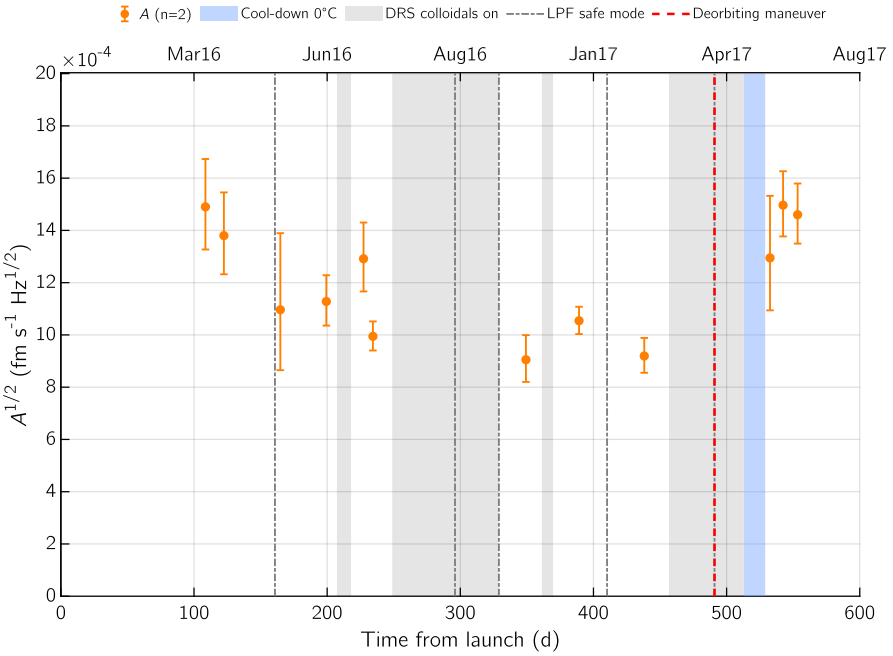

Figure 3.9: Evolution of the slope of model (3.12) run by run (orange points). The vertical gray dash-dotted lines indicate LPF safe mode activation, that is, TMs regrab operations, while the light gray bands are the NASA ST7-DRS operating periods. In April 2017, the deorbiting maneuver (red dashed line) is simultaneous to a TMs regrab and is immediately followed by the system cool-down to T_0 (blue shaded band).

On the vertical axis of Figure 3.9, the slope $A^{1/2}$ is depicted for T decorrelated $\Delta g_{T\mathrm{dec}}$ time-series (orange points). Data show a barely significant decreasing trend up to April 2017, $\sim 500\,\mathrm{d}$ after launch, while the last three points, taken right after the deorbiting maneuver and the cool-down to T_0 and referring to to noise runs #74, #75 and #76 of Table 2.1, show a small but significant increase in the $A^{1/2}$ value, interrupting the decreasing trend of previous measurements.

The individual fit to the f^{-2} behavior (3.12) highlights therefore the existing differences in slope and shape among of the various noise runs. Hence, to avoid depending too much on the details of the low frequency spectrum shape of the single noise run, a good indicator would be a quantity independent of the specific fitting model used.

Such figure of merit is the the numerical integral Δg_{tot} of the low frequency noise spectrum $S^{1/2}_{\mathrm{lowfreq}}$ over the frequency band from $27\,\mu\mathrm{Hz}$ to $1\,\mathrm{mHz}$ for the

twelve noise under analysis. The time evolution of this quantity is depicted in Figure 3.10, again together with the history of engineering and scientific maneuvers executed on LPF.

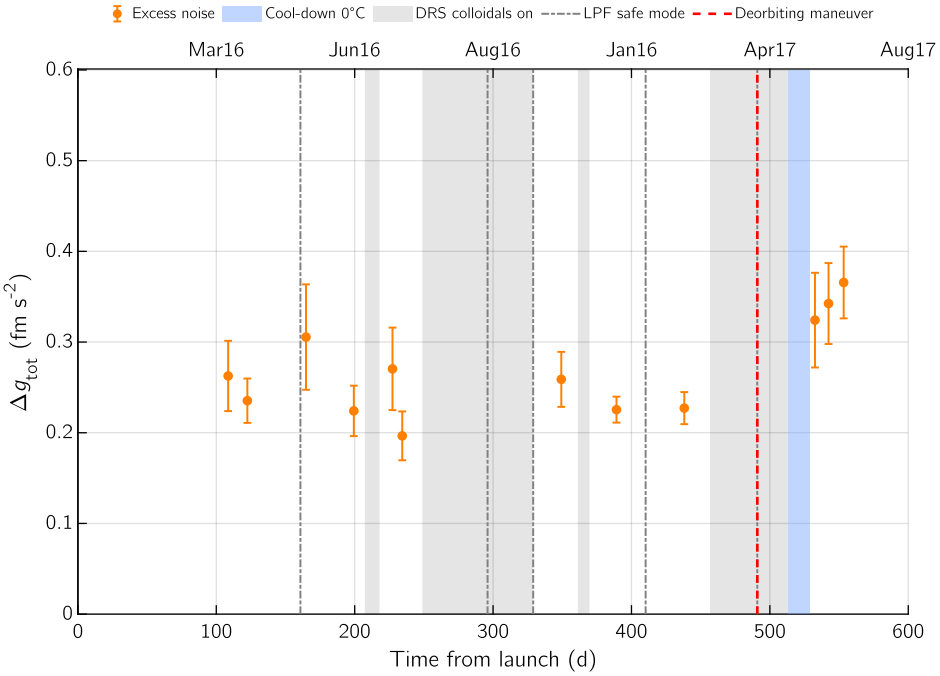

Figure 3.10: Numerical integral over the frequency domain of low frequency noise $\Delta g_{\rm tot}$, run by run (orange points). The vertical gray dash-dotted lines indicate LPF safe mode activation, that is, TMs regrab operations, while the light gray bands are the NASA ST7-DRS operating periods. In April 2017, the deorbiting maneuver (red dashed line) is simultaneous to a TMs regrab and is immediately followed by the system cool-down to T_0 (blue shaded band).

For comparison, the analysis has been performed both on $S^{1/2}_{\Delta g}$ data containing the effect of temperature (green points) and for T decorrelated $S^{1/2}_{\Delta g, T\rm dec}$ noise spectra (orange points).

As anticipated, the effect of the T decorrelation (3.10) is more evident in the first noise runs, becoming less and less important in the course of the operations up to February 2017.

The low frequency spectrum integral $\Delta g_{\rm tot}$ looks remarkably stable along the course of the mission, up until the series of engineering and scientific operations put into place between April and May 2017.

Again, the three noise runs acquired after the deorbiting maneuver and the cool-down to T_0 appear to belong to a different group of measurements: they show very little compatibility with the other data and depart from the noise

stability of the runs up to before April 2017.

3.4 Comparison with noise models

In this section the observed noise ASD is compared to the one expected on the basis of the best physical model we currently have. The various noise sources within such model depend on parameters that were expected to vary in the course of the mission, and were therefore measured in dedicated experiments performed as close as possible to the noise runs.

The measured ASD $S_{\Delta g}^{1/2}$ of run #66 of February 2017, the best performance noise run achieved during LPF operations, is depicted in anticipation of the content of this section in Figure 3.11, compared with the total modeled noise for that measurement, detailed with the description of the various noise contributions, in Subsection 3.4.1.

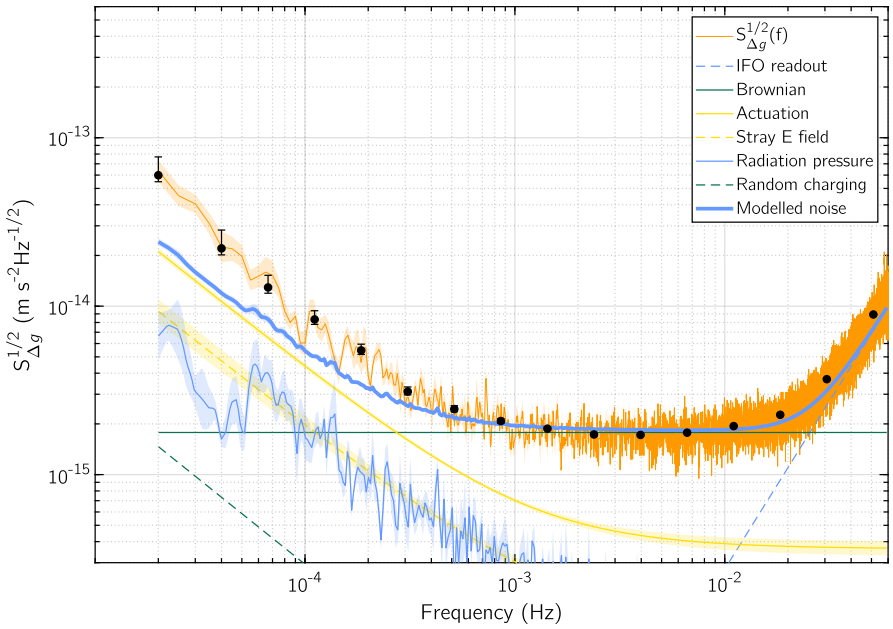

Figure 3.11: Noise budget of the LPF mission, referred to the uninterrupted noise run measured in February 2017 and published in [17]. The black dashed line refers to the LISA requirements, the orange data is the ASD of the February run calculated with the Welch periodogram method and the black points constitute the ASD estimated with the method expressed in Appendix §A.

The figure also anticipates that the noise spectrum shows a quite consistent correspondence to the expected performance (3.14) down to $\sim 1\,\mathrm{mHz}$, where

instead the low frequency behavior departs from the modeled noise and an excess power tail becomes evident with respect to the expected noise.

The excess power at low frequency appears with similar shape in all the noise-only runs under analysis, which are the ones with a long enough duration to reach 20 µHz in ASD, and is consistent over the course of the whole mission. The noise spectra of all the twelve noise runs of Table 2.1 compared to their respective modeled noise level are depicted in Appendix §C.1.

3.4.1 LPF modeled noise sources

The expected full noise model is given by

$$S^{1/2}_{\mathrm{mod},k}(f) = \sqrt{S_{\mathrm{act}}(f) + S_{\mathrm{B},k} + S_{\mathrm{IFO}}(f) + S_{\mathrm{stray}}(f) + S_{\mathrm{rand}}(f) + S_{\mathrm{las}}(f)}, \tag{3.14}$$

whose prominent contributions are the three effects used to evaluate the Best Estimate performance before launch [25]: electrostatic actuation noise $S_{\mathrm{act}}(f)$ caused by the TMs-applied voltages, Brownian white noise $S_{\mathrm{B},k}$ due to residual gas inside the system and interferometer sensing noise $S_{\mathrm{IFO}}(f)$, which acts only at high frequency.

As the noise performance improved, additional fainter perturbation sources have been estimated and the most energetic among them are the fluctuations due to stray electric fields $S_{\mathrm{stray}}(f)$, random charging noise $S_{\mathrm{rand}}(f)$ and laser radiation pressure fluctuations $S_{\mathrm{laser}}(f)$ [25].

The noise performance model presented here does not include pressure effects that are not correlated with temperature, the remaining gravitational noise and the effect of amplitude-modulated high frequency magnetic field.

3.4.1.1 Actuation noise

Actuation voltages are constantly applied to the TMs via the electrodes located on the EH (Figure 2.3), exerting thus constant forces and torques on the translational x, y, z and rotational ϕ, η, θ degrees of freedom of each TMs, in order to maintain them centered within the GRS and on the sensitive x-axis (oriented according to the convention illustrated in Figure 2.5).

Amplitude fluctuations in the applied voltages would produce a force noise proportional to the amplitude of the control force exerted by the actuation voltages, therefore depending on the actual values of the applied authorities. In the course of operations nine different set of authorities were applied to the TMs, and are summarized in Table 3.2.

Table 3.2: List of authorities used during operations. All scientific measurements used to estimate the noise performance of LISA Pathfinder have been realized in `URLA` and `UURLA` mode. The units for forces are pN for forces F and pN m for torques N.

authority	F_{x1} (pN)	F_{x2} (pN)	$N_{\theta 1}$ (pNm)	$N_{\theta 2}$ (pNm)	F_{y1}	F_{y2}	$N_{\eta 1}$	$N_{\eta 2}$	F_{z1}	F_{z2}	$N_{\phi 1}$	$N_{\phi 2}$
`UURLA`	0	50	4	4	1000	1000	4	4	500	500	1.5	1
`URLA`	0	50	16.37	16.37	3670	3670	13.32	13.32	5820	5820	1.5	1
`RLA`	0	200	16.37	16.37	3670	3670	13.32	13.32	5820	5820	3	3
`RED`	0	600	16.37	16.37	3670	3670	13.32	13.32	5820	5820	3	3
`NOM`	0	2200	16.37	16.37	3670	3670	13.32	13.32	5820	5820	10	11
`BIG`	5000	5000	16.37	16.37	3670	3670	13.32	13.32	5820	5820	10	11
`DURLA`	0	100	4	4	0	2000	4	4	0	500	1.5	1
`BIGPlus`	5000	5000	16.37	16.37	3670	3670	13.32	13.32	5820	5820	10	11
`LargePhi`	0	2200	16.37	16.37	3670	3670	13.32	13.32	5820	5820	60	60

The best noise performance value of the actuation noise in ASD [31] is given by

$$S_{\rm act}^{1/2}(f) = (5.05 \pm 0.19) \left(\frac{0.1\,\mathrm{mHz}}{f}\right) \text{ fm s}^{-2}\text{ Hz}^{-1/2}, \tag{3.15}$$

and is pictured as the continuous yellow line in Figure 3.11, where is the most important contribution at low frequency.

The actuation configuration of the noise measurement acquired on the first day of operations and plotted in Figure 2.7 is the `NOM` configuration of Table 3.2, while the twelve noise runs under analysis have been taken in the `URLA` and `UURLA`, to ensure the minimum impact of actuation on the Δg noise. The actuation configurations employed in every noise run are listed in Appendix B.

3.4.1.2 Brownian noise

Brownian noise arises from motion of residual gas present inside the LTP and is a white noise source impacting the noise performance at all frequencies. The force noise from gas damping was estimated before launch by taking into account torsion pendulum dedicated experiments and simulations [32], with attention to the structure of gaps around TMs in the GRS.

In the course of operations, the LTP was subjected to constant venting to space to reduce the pressure inside the vacuum chamber due to residual gas as much as possible, down to $\sim 10^{-5}$Pa. The Brownian level has then been estimated for every noise measurement by fitting the white noise floor of $S_{\Delta g}^{1/2}$ between 2 mHz and 4 mHz.

The Brownian best noise performance value of in ASD is therefore given by

$$S_{\mathrm{B},k=66}^{1/2} = (1.78 \pm 0.15) \text{ fm s}^{-2}\text{ Hz}^{-1/2}. \tag{3.16}$$

It must be said though that the noise runs taken at T_0 show that this noise level could be in principle be lowered even further down to

$$S_{\mathrm{B},T_0}^{1/2} = (1.3 \pm 0.3) \text{ fm s}^{-2}\text{ Hz}^{-1/2}. \tag{3.17}$$

3.4.1.3 Interferometer sensing noise

Interferometer sensing noise is the limiting noise source above ~ 10 mHz and accounts for all sources of phase noise which do not result from motion of the TMs. Among these are included

- sources connected to the interferometer readout, such as phase-meter noise, photon shot noise and FEE photodiode noise;
- noise sources due to the absolute phase difference between the measurement and reference interferometers, causing phase noise and laser amplitude noise;
- laser frequency noise coupling via the arm-length mismatch in the measurement interferometer.

The interferometer sensing noise best performance value

$$S_{\mathrm{IFO}}^{1/2}(f) = 9 \left(\frac{f}{1\,\mathrm{mHz}} \right)^2 \mathrm{fm\ s^2\ Hz^{-1/2}}, \tag{3.18}$$

only relevant at higher frequencies $f > 10\,\mathrm{mHz}$.

3.4.1.4 Low frequency fluctuation in average stray electrostatic fields

Low frequency fluctuations in average stray electrostatic fields arise from the interaction of TM charge with the residual effective DC potential bias applied on a single GRS electrode, which explains the residual sensitivity of the electrodes to a change in the TM charge.

Therefore, the presence of a non-zero residual charge on the TM would couple to the effective potential on the surface of single x-axis electrode, giving rise to a noisy force acting on the TM. The surface effect is companioned by fluctuations in the electrode potential generated by the Front End Electronics actuation, which will add to the stray voltages.

Furthermore, from the interaction between the average stray electrostatic field and the TM charge also originates a force noise from random TM charging, caused from the incoming charged particles shot noise, which will be discussed in the following section.

Low frequency fluctuations in average stray electrostatic fields result in an acceleration noise with a f^{-1} behaviour in ASD, that is

$$S_{\mathrm{stray}}^{1/2}(f) = (1.98 \pm 0.25) \left(\frac{0.1\,\mathrm{mHz}}{f} \right) \mathrm{fm\ s^{-2}\ Hz^{-1/2}}, \tag{3.19}$$

illustrated in Figure 3.11 as the dashed yellow line.

3.4.1.5 Random TM charging

The random TM charging, caused by incoming cosmic rays, will generate a f^{-2} force noise in power, proportional to the applied DC bias on the TM [33]

$$\begin{aligned} S_{\text{rand}}(f) &= S_q(f) \left(\frac{\mathrm{d}C_x}{\mathrm{d}x} \frac{\Delta x}{C_{\text{tot}} M} \right)^2 \\ &= \frac{2e^2 \lambda_{\text{eff}}}{4\pi^2 f^2} \left(\frac{\mathrm{d}C_x}{\mathrm{d}x} \frac{\Delta x}{C_{\text{tot}} M} \right)^2, \end{aligned} \tag{3.20}$$

where e is the elementary charge, λ_{eff} effective single charge event rate (for Poisson shot noise), C_x is the x-electrode capacitance and Δx is the effective potential on a single electrode.

This results in a best noise performance ASD given by the dashed green line in Figure 3.11 with value

$$S^{1/2}_{\text{rand}}(f) = 0.03 \left(\frac{1\,\text{mHz}}{f} \right) \text{fm s}^{-2}\text{Hz}^{-1/2}. \tag{3.21}$$

3.4.1.6 Laser radiation pressure

Laser radiation pressure generates an acceleration noise that is proportional in power to the incident laser power on the TM and to the in-band relative intensity noise, which is estimated via a power monitor photodiode on the optical bench.

The laser radiation pressure noise contribution is evaluated using the normalized laser power detected on the quadrant diodes, and is in fact depicted as the noisy thin blue line in Figure 3.11.

3.5 Excess power in the low frequency noise

The excess power can be evaluated run by run via the ASD of the low frequency noise term (3.12) $S^{1/2}_{\text{lowfreq}}(f)$, with respect to the LPF expected low frequency noise performance

$$S^{1/2}_{\text{lf,mod}}(f) = \sqrt{S_{\text{act}}(f) + S_{\text{stray}}(f) + S_{\text{rand}}(f) + S_{\text{las}}(f)}, \tag{3.22}$$

obtained as a modification of (3.14).

The evaluation of the low frequency noise behavior $S^{1/2}_{\text{lowfreq}}(f)$ for the best performance noise run #66 is illustrated in Figure 3.12, compared with its expected low frequency noise performance $S^{1/2}_{\text{lf,mod}}(f)$. The estimation of the

excess noise at low frequency with respect to the expected noise performance for all the twelve noise runs under investigation is illustrated in Appendix C.2 .

The modeled noise (3.22) can be fit to an inverse power of frequency behavior, as for the low frequency branch of $S_{\Delta g, T\mathrm{dec}}(f)$,

$$\frac{A_{\mathrm{noise}}}{f^{n_{\mathrm{noise}}}}, \tag{3.23}$$

which results in $n_{\mathrm{noise}} = 1.76 \pm 0.03$, compatible within 2σ with the global fit parameter of (3.11), $n = 2.0 \pm 0.2$.

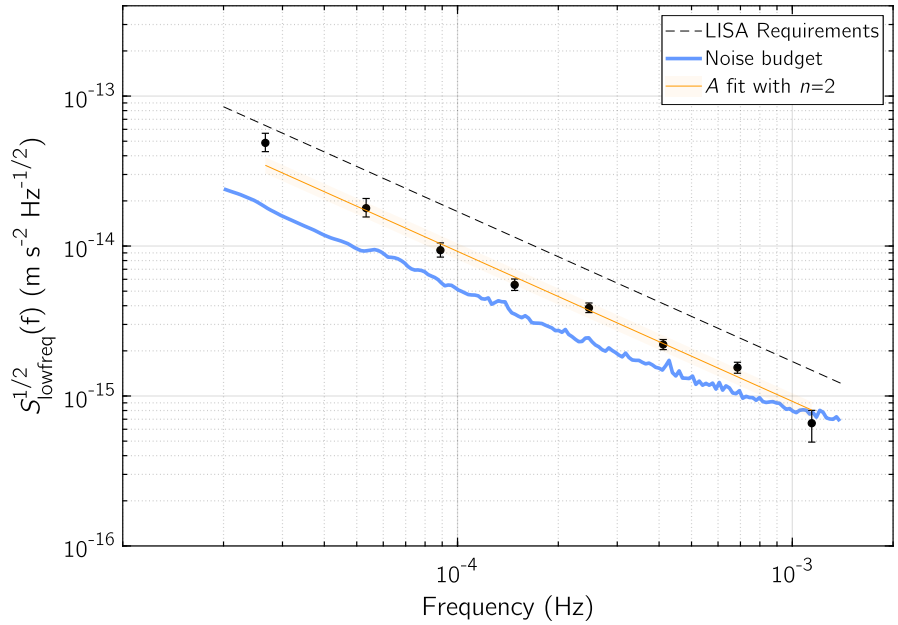

Figure 3.12: ASD of low frequency noise behavior $S_{\mathrm{lowfreq}}(f)$ compared to the modeled expected noise (thick blue line) for the best performance noise run of February 2017, run #66. The dashed black line represents the LISA acceleration noise requirement (1.9), while the orange line is the f^{-2} fit to the ASD data used to estimate the slope A.

The difference in the excess power at low frequency for the three last noise runs acquired after the engineering maneuvers of April and May 2017 can be observed in Figure 3.13, where it is depicted the comparison between the MCMC grand average of $S^{1/2}_{\mathrm{lowfreq}}$ measured in runs taken before (orange points) and after (black points). As in previous Section §3.3, all the noise run data have been decorrelated from the effect of temperature inside the EH.

The behavior of the excess noise in measurement runs acquired after the deorbiting maneuver is affected by a visible increase in the noise level at the lower frequencies $20\,\mu\mathrm{Hz} \leq f \leq 100\,\mu\mathrm{Hz}$. Instead, by looking at the MCMC

grand average of the three noise runs taken after April 2017, a systematic excess power can be detected in the lowest three frequency bins with respect to the common excess noise of the noise runs up to February 2017.

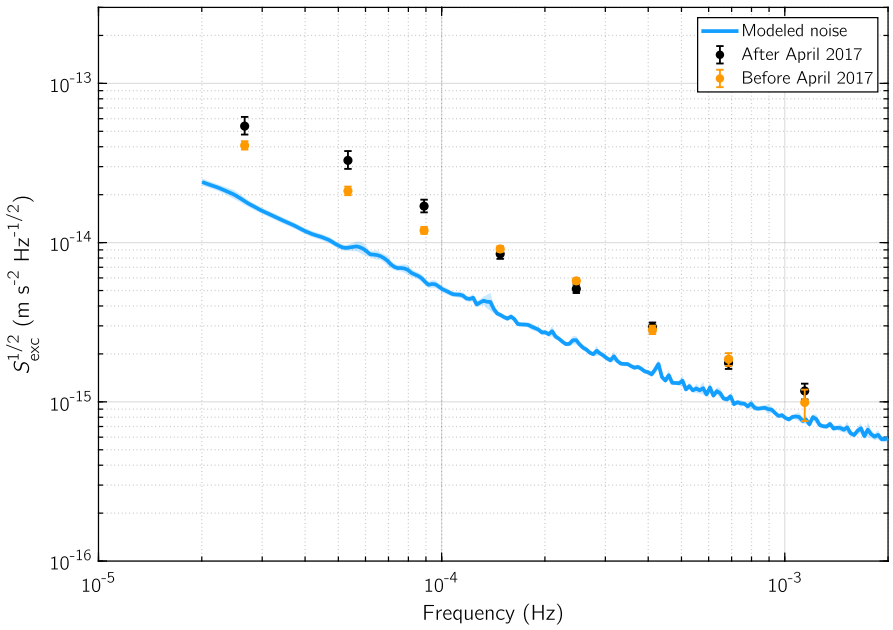

Figure 3.13: Monte Carlo Markov Chain (MCMC) evaluation of the excess noise for three groups of noise runs: nine noise-only runs measured before the deorbiting maneuver of April 2017 and the system cool-down of May 2017 and three noise-only runs measured after that.

Additional information about the excess power with respect to the modeled performance (3.22) can be provided also by the plot of the numerical integral Δg_{tot} of the low frequency noise.

The modified plot of Δg_{tot} is illustrated in Figure 3.14 for T decorrelated data and is integrated with the numerical integrals of the best performance modeled noise and the common low frequency noise behavior for noise runs taken before April 2017 of Figure 3.13.

For what concerns the excess power in the low frequency noise, the last three noise runs appear therefore to belong to a different group of measurements, as they show very little compatibility with the other data. Their low frequency ASD behavior is characterized by a bump the lowest frequency bins for $27\,\mu\text{Hz} \leq f \leq 200\,\mu\text{Hz}$, and their time evolution appears to depart from the increasingly stabilizing trend of the noise runs from before April 2017, both for the low frequency noise slope $A^{1/2}$ and for the numerical integral over the frequency domain Δg_{tot}.

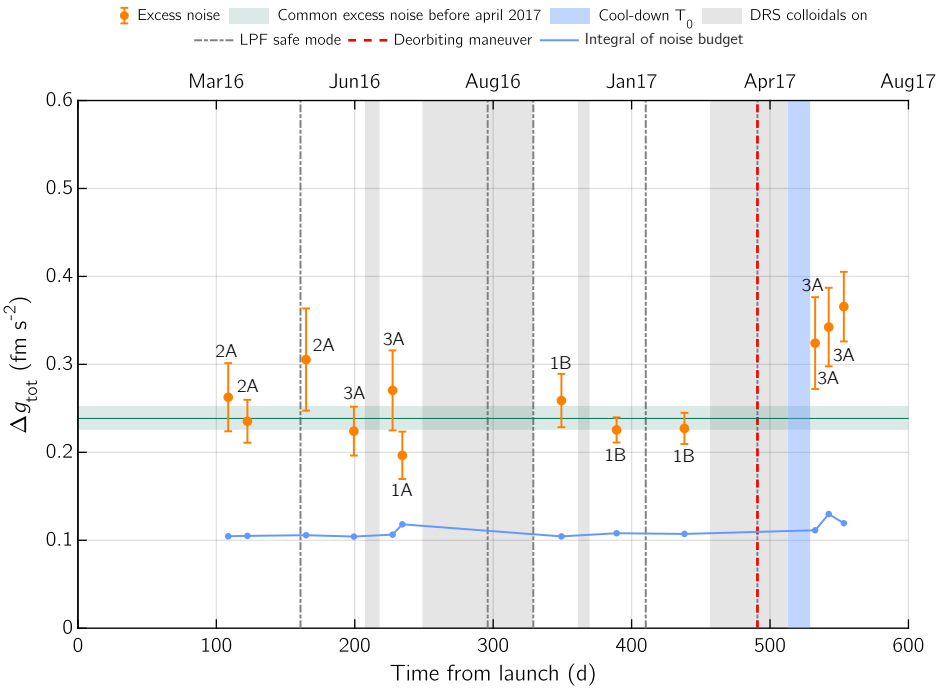

Figure 3.14: Numerical integral over the frequency domain of low frequency excess noise, run by run (orange points). The green horizontal band represents the same integration performed over the MCMC excess noise grand average of the noise runs acquired before April 2017. The blue line is the numerical integral of the noise budget for the every noise run.

In previous works [17] the change in the excess noise behavior was tentatively ascribed to the specific propellant feed branch used for those data runs, labeled as `3A` in Figures 3.9, 3.10 and 3.14: this hypothesis was excluded altogether with the addition of the June 2016 #39 and the first July 2016 #42 noise run, taken on the same propellant branch and showing a lower excess slope value.

Notice that the excess noise is independent of the operating temperature both for the runs before deorbiting/cool down and for those after it.

The excess noise at low frequency is also found to be independent of the pressure around the TM: while the Brownian noise, proportional to pressure, keeps decreasing, and decreases in steps by decreasing the temperature, the excess ones stay constant or jumps to a new value with no change in pressure.

Finally we notice that a significant mechanical stress is expected to be associated to the cool-down to T_0. At least one sudden event of stress relaxation, with large steps in all the coordinate of the TMs was detected during the run and supports such an expectation.

The discussion of experimental results regarding the low frequency noise

behavior is presented in Part §II, where some possible sources for the excess power at low frequency are quantitatively estimated.

4 Differential acceleration along angular degrees of freedom

In order to narrow down the set of possible sources of the observed excess in Δg low frequency noise, it has been investigated the presence of any torque on the TMs associated to S_{lowfreq}.

If, for instance, the noise was originating in a localized source of force $\boldsymbol{F}$ off-centered and normal with respect to the TM, such force would exert a torque $N = rF$, with r the relevant arm-length. An example for this kind of force might be a noisy voltage exerted by a single electrode on the TM x-face, in which case $r \simeq 1\,\mathrm{cm}$.

The excess force noise would then manifest in two ways: a corresponding excess should be detectable in the torque noise, and some degree of correlation between torque and force should be visible. The torque per unit moment of inertia γ would then be

$$\gamma = \frac{Fr}{I} = \frac{6Fr}{mR^2} = \frac{6r}{R^2}\, g. \tag{4.1}$$

Thus, a noisy force per unit mass g would convert into a noisy γ with a conversion arm

$$b = \frac{6r}{R^2}, \tag{4.2}$$

and such torque will have only components along z and y, which should then manifest as correlated torque noise along those axes.

In LPF the angular readout of the TM rotation around y and z is interferometric, with comparatively high sensitivity. However, in order to detect small torques one needs to get rid of the large angular acceleration of the SC relative to the TMs. This is achieved by looking at the differential angular motion, as it is done to measure the translational acceleration along x.

Then, in order to evaluate the cross-correlation between the translational $\Delta g(t)$ and rotational differential acceleration $\Delta\gamma(t)$, the angular time-series was built with a model similar to the translational one (2.14) for the rotational degrees of freedom ϕ and η.

These are the only two degrees of freedom that induce a non-orthogonal motion to x and whose differential readout is available with enough sensitivity and is sufficiently isolated from the spacecraft motion.

The $\Delta\gamma(t)$ time series for the ϕ angle (and likewise for η) is estimated from

$$\begin{aligned}\Delta\gamma_\phi = \ddot{\phi}_2 - \ddot{\phi}_1 - (\omega^2_{\phi 1}\phi_1 - \omega^2_{\phi 2}\phi_2) \\ + G_{\phi_1}\frac{N_{\phi_1}}{I_{zz}} - G_{\phi_2}\frac{N_{\phi_2}}{I_{zz}} + C_{N\phi_1}\frac{\dot{N}_{\phi_1}}{I_{zz}} - C_{N\phi_2}\frac{\dot{N}_{\phi_2}}{I_{zz}},\end{aligned} \tag{4.3}$$

where ω^2 represent the stiffnesses, G are gains multiplying the torques N per unit moment of inertia I, and C_N are delays proportional to the first time-derivatives of the torques.

However, the angular differential acceleration (4.3) shows a coupling to the common mode of torques $N^{\mathrm{CM}}_{\phi,\eta}$ and the common mode of the angles $\phi^{\mathrm{CM}}, \eta^{\mathrm{CM}}$, coming from the correction to the average shift between the angle readout of the two interferometers of the LTP.

Needing a correction for these coupling effects, the torque common mode between $N_{\phi 1}$ and $N_{\phi 2}$ (or $N_{\eta 1,\eta 2}$) is given by

$$N^{\mathrm{CM}}_{\phi} \equiv \overline{N}_{\phi} = \frac{N_{\phi 1} + N_{\phi 2}}{2I_z}, \tag{4.4}$$

$$N^{\mathrm{CM}}_{\eta} \equiv \overline{N}_{\eta} = \frac{N_{\eta 1} + N_{\eta 2}}{2I_y}, \tag{4.5}$$

while the correction of the common mode coupling to ϕ (and likewise for η) requires the two following quantities

$$\overline{\phi} = \frac{\phi^{\mathrm{IFO}}_1 + \phi^{\mathrm{IFO}}_1}{2} \tag{4.6}$$

$$\overline{\omega}^2_{\phi\phi} = \frac{\omega^2_{\phi_1} + \omega^2_{\phi_2}}{2}, \tag{4.7}$$

where $\phi^{\mathrm{IFO}}_{1,2}$ is the interferometric readout of the angle position.

The common-mode decorrelated angular differential acceleration $\Delta\gamma^{\mathrm{dec}}(t)$ is then obtained via

$$\Delta\gamma^{\mathrm{dec}}_{\phi}(t) = \Delta\gamma_{\phi}(t) - \lambda_{\phi}\overline{N}_{\phi}(t) - \alpha_{\phi}\left(\ddot{\overline{\phi}}(t) + \overline{\omega}^2_{\phi\phi}(t)\overline{\phi}(t)\right), \tag{4.8}$$

$$\Delta\gamma^{\mathrm{dec}}_{\eta}(t) = \Delta\gamma_{\eta}(t) - \lambda_{\eta}\overline{N}_{\eta}(t) - \alpha_{\eta}\left(\ddot{\overline{\eta}}(t) + \overline{\omega}^2_{\eta\eta}(t)\overline{\eta}(t)\right), \tag{4.9}$$

where $\lambda_{\phi,\eta}$ and $\alpha_{\phi,\eta}$ represent the decorrelation parameters and are indicated in Table 4.1.

The power spectra of the decorrelated angular differential acceleration $\Delta\gamma^{\mathrm{dec}}(t)$, both for the ϕ and η angles are depicted in Figure 4.1 for the best performance noise run #66 of February 2017, while those for the remaining runs are reported in Appendix §C.3.

Table 4.1: Angular common mode decorrelation parameters for the parameters $\lambda_{\phi,\eta}$ and $\alpha_{\phi,\eta}$ of equations (4.8)-(4.9).

Run	λ_ϕ	σ_{λ_ϕ}	α_ϕ	σ_{α_ϕ}	λ_η	σ_{λ_η}	α_η	σ_{α_η}
6	−0.019	0.002	0.0270	0.0008	0.0009	0.0007	−0.0182	0.0004
9	−0.0084	0.0002	0.0261	0.0005	0.0049	0.0005	−0.0205	0.0002
17	−0.0060	0.0003	0.0192	0.0007	0.0024	0.0005	−0.0286	0.0004
39	−0.0086	0.0003	0.022	0.001	0.0041	0.0005	−0.0334	0.0006
42	−0.0066	0.0004	0.0214	0.0007	0.004	0.001	−0.0306	0.0009
43	−0.0099	0.0004	0.0216	0.0006	0.0083	0.0008	−0.042	0.002
59	−0.0052	0.0003	0.0210	0.0006	0.0053	0.0005	−0.0241	0.0003
61	−0.0091	0.0002	0.0258	0.0009	0.0046	0.0002	−0.0218	0.0005
66	−0.0122	0.0002	0.0181	0.0005	0.0014	0.0003	−0.0279	0.0006
74	−0.0068	0.0004	0.0176	0.0008	0.0013	0.0006	−0.0169	0.0007
75	−0.0083	0.0003	0.023	0.001	0.0085	0.0005	−0.0253	0.0005
76	−0.0111	0.0002	0.0269	0.0009	0.0049	0.0003	−0.0217	0.0004

To account for the excess with respect to the modeled torque noise, in Figure 4.2 we report the experimental $S_{\Delta\gamma_\phi}$ value at $f_\phi^{\mathrm{B}} \simeq 0.7\,\mathrm{mHz}$, as a function of the epoch, together with its expected value. Around f_ϕ^{B} the spectrum reaches its minimum.

Before proceeding further and discuss the comparison to the expected noise model in Section §4.3, let us compare these results for $\Delta\gamma$ with Δg in search for correlation, as is described in the following Section §4.1.

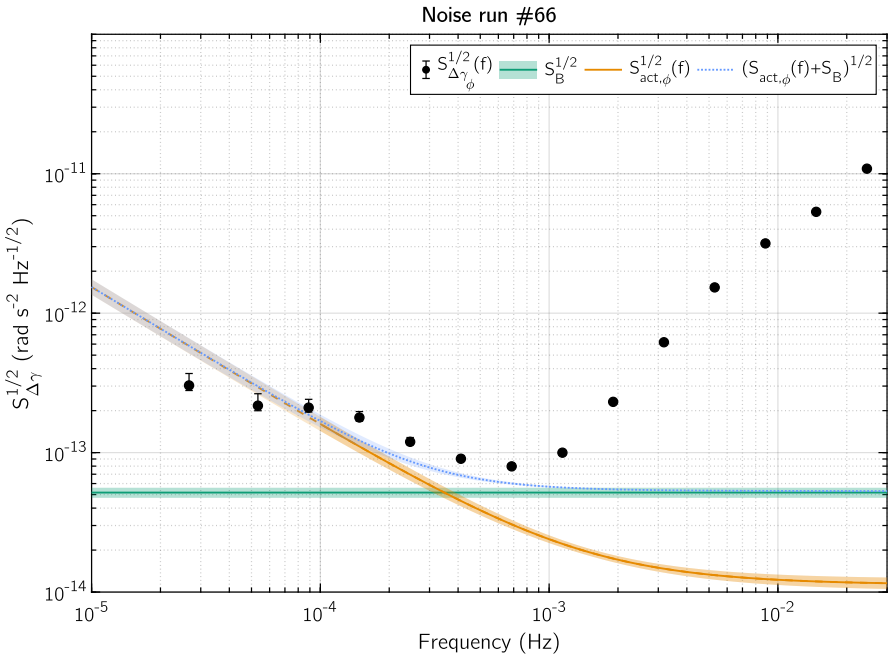

(a) ϕ channel

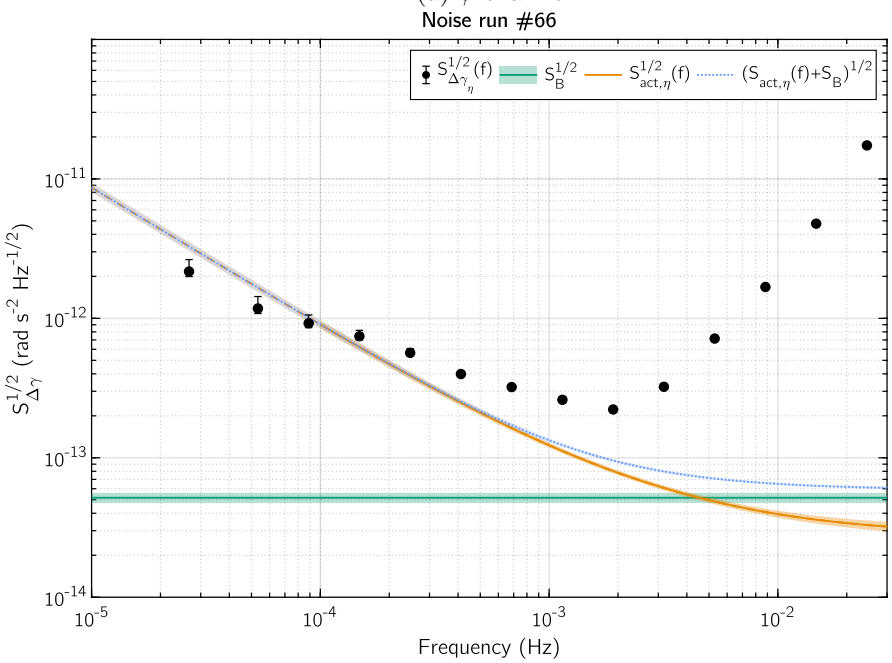

(b) η channel

Figure 4.1: ASD of the angular differential acceleration $S^{1/2}_{\Delta\gamma}$ of the best performance noise run published in [17] for the two angular degrees of freedom ϕ and η. The angular actuation noise $S^{1/2}_{\mathrm{act}}(f)$ is the continuous orange line down to 0.1 mHz, while its extension at lower frequencies is dashed. The angular Brownian noise $S^{1/2}_{\mathrm{B}}$ is the green line, and their sum $S_{\Delta\gamma,k}(f)$ is the blue dotted curve.

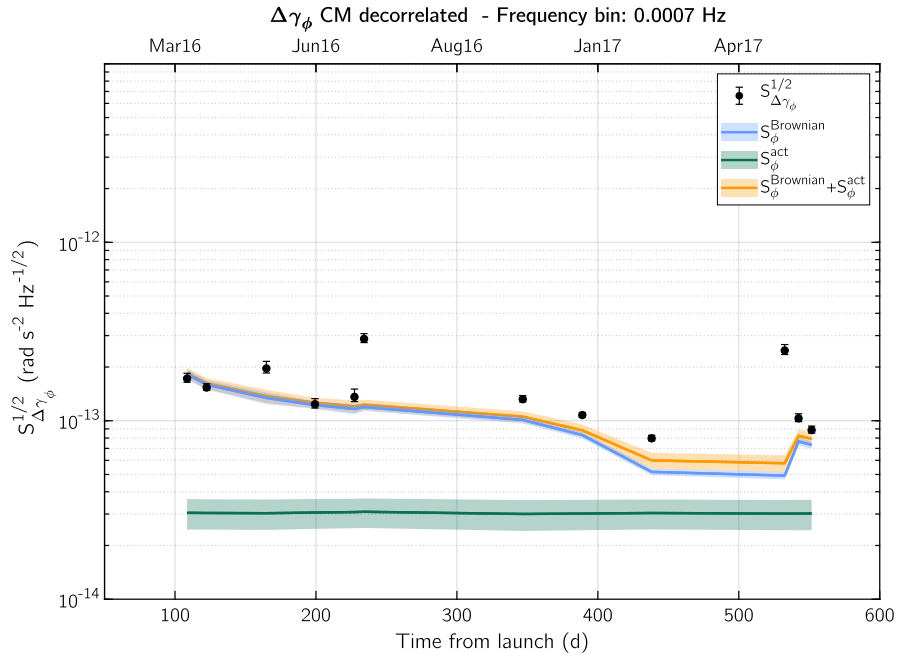

Figure 4.2: Comparison among the experimental value $\min S^{1/2}_{\Delta\gamma_\phi}$ at $f^{\mathrm{B}}_{\phi} = 0.7\,\mathrm{mHz}$, the expected angular Brownian noise $S^{\mathrm{B}}_{\phi,k}$, the budgeted actuation noise $S^{\mathrm{act}}_{\phi}(f^{\mathrm{B}}_{\phi})$ and their sum $S^{\mathrm{white}}_{\phi,k}(f^{\mathrm{B}}_{\phi})$ for each of the twelve noise-only runs. Error-bars are 1σ for all physical quantities.

4.1 Cross-correlation between translational and angular acceleration noise

Once that the angular counterpart of the differential acceleration has been established as (4.8) and (4.9), the presence of any correlation between the time-series of Δg and $\Delta\gamma^{\mathrm{dec}}_{\phi,\eta}$ can be assessed in order to understand if the excess power in the lower frequency part of the noise spectrum $S_{\Delta g}$ is caused by spectral leakage from angular degrees of freedom.

The correlation between zero-mean stochastic processes whose spectra are calculated through the WOSA method [29], can be calculated by estimating the Magnitude Squared (MS) cross-coherence spectrum $|\rho(f)|$ of the two processes [34].

The MS cross-coherence is defined as

$$|\rho(f)|^2 = \frac{|S_{\Delta g,\Delta\gamma}|^2}{S_{\Delta g} S_{\Delta\gamma}}, \tag{4.10}$$

where $S_{\Delta g,\Delta\gamma}$ is the power cross-spectrum of the two processes.

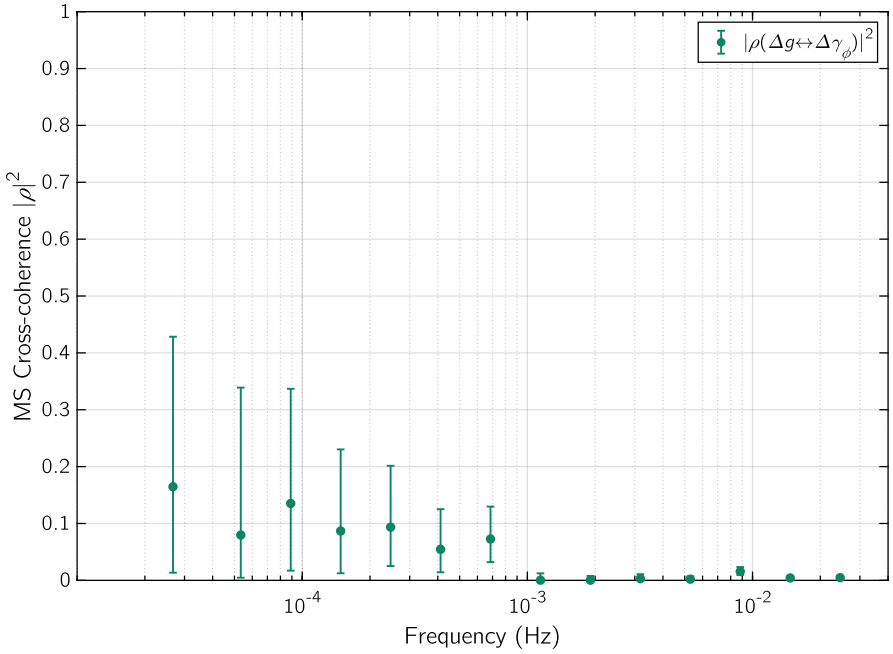

(a) ϕ channel.

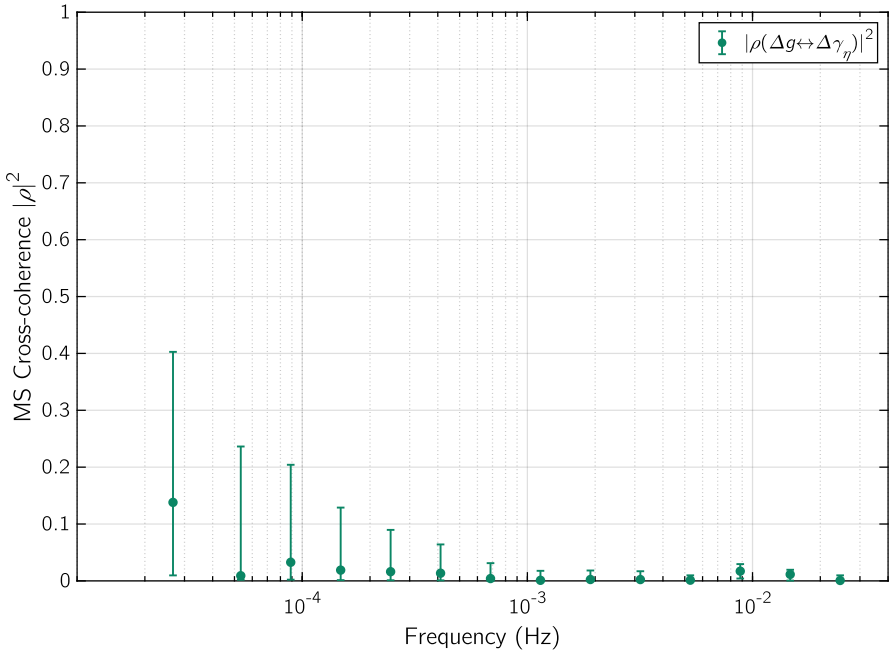

(b) η channel.

Figure 4.3: Magnitude squared cross-correlation spectra $|\rho(f)|^2$ of the translational to angular differential acceleration $\Delta g \leftrightarrow \Delta\gamma$ of the best performance noise run published in [17].

Since the ASD spectra for the time-series under analysis is estimated through the modification of the WOSA method illustrated in §A, the cross-coherence estimation is naturally extended from (4.10) to the Bayesian estimation technique for minimally correlated frequency bins.

The cross-coherence spectra $|\rho(f)|^2$ for the correlation between $S_{\Delta g}$ and the angular differential acceleration spectra $S_{\Delta\gamma_\phi}$ and $S_{\Delta\gamma_\eta}$ are shown in Figure 4.3 for the best performance noise run #66 of February 2017, while those for the other runs under analysis are reported in Appendix §C.4.

4.2 Expected torque noise

In Figure 4.1 it is reported for comparison the current best estimate of the expected torque noise. We expect the leading contributions to the torque noise along ϕ and η to be actuation noise along those degrees of freedom and Brownian noise.

In our simplified model, the torque ASD in run k is the sum of the two contributions

$$S_{\Delta\gamma,k}(f) = S^{\mathrm{act}}_{\Delta\gamma}(f) + S^{\mathrm{B}}_{\Delta\gamma,k}. \tag{4.11}$$

where $S^{\mathrm{act}}_{\Delta\gamma}(f)$ and $S^{\mathrm{B}}_{\Delta\gamma,k}$ are the angular actuation noise and Brownian noise respectively. The actuation noise is described in the next Section §4.2.1, while the angular Brownian noise derivation is described in Section §4.2.2.

4.2.1 Angular actuation noise

Actuation torque noise is modeled analogously to the force one: it depends on the various actuation settings (maximum authorities listed in Table 3.2), that in turn depend on the single noise run.

The prediction of the models are reported for each noise run in the respective plot in Appendix §C.3. However, it must be said that the model prediction for $S_{\mathrm{act},\phi}$ is based on a set of experiments performed in orbit [31], which were limited to frequencies higher than 0.1 mHz.

Therefore, the three lowest frequency points of the differential angular acceleration noise spectrum $S^{1/2}_{\Delta\gamma}$ may not be explained with the current actuation model, and its extension down to 27 µHz is depicted with a dashed line.

In addition to this, dedicated experiments were not performed for the actuation model on the η channel, for which an extrapolation from the ϕ

prediction was performed. Again, the model is reliable only down to 0.1 mHz, and its extension at lower frequencies is depicted with a dashed line.

The extrapolated model allows to only get a grasp of the actuation noise contribution for the η angle, although the real actuation noise model for η is confidently compatible with the extrapolated one depicted in Figure C.6l within a factor 2.

4.2.2 Brownian noise along angular degrees of freedom

The relationship between the angular and translational acceleration noise due to Brownian motion can be exploited by examining how their noise spectra are related to noise generated by torques and forces respectively, expressed by the relations

$$S_N = \frac{I^2}{2} S_{\Delta\gamma}, \tag{4.12}$$

$$S_F = \frac{M^2}{2} S_{\Delta g}. \tag{4.13}$$

At the same time, torque and force noise arise from rotational and translational gas damping via the Nyquist theorem, that is

$$S_N = 4k_{\mathrm{B}}T\beta_{\mathrm{rot}}, \tag{4.14}$$

$$S_F = 4k_{\mathrm{B}}T\beta_{\mathrm{tr}}, \tag{4.15}$$

where the gas damping coefficients $\beta_{\mathrm{rot,tr}}$ are known from torsion pendulum experiments [32] both for a 4-TMs pendulum and for a single-TM pendulum enclosed in a GRS housing

$$\beta_{4\mathrm{TM}} = 4(r^2\beta_{\mathrm{tr}}^{\infty} + \beta_{\mathrm{rot}}), \tag{4.16}$$

$$\beta_{1\mathrm{TM}}^{\mathrm{GRS}} = \beta_{\mathrm{rot}}. \tag{4.17}$$

The gas damping coefficient can be easily estimated for a LISA Pathfinder TM, starting from the computational simulations [32] of its pressure dependence along ϕ, $\beta_\phi(p)$. This allows to combine (4.12)-(4.13), giving for the ratio of expressions (4.16)-(4.17),

$$\frac{r^2\beta_{\mathrm{tr}}^{\infty} + \cancel{\beta_{\mathrm{rot}}}}{\beta_{\mathrm{rot}}} \simeq \frac{\left.\frac{\partial\beta}{\partial p}\right|_{\mathrm{GRS}}}{\left.\frac{\partial\beta}{\partial p}\right|_{1\mathrm{TM}}} = \frac{5.7\times10^{-6}\,\mathrm{m^3s}}{4.8\times10^{-8}\,\mathrm{m^3s}} \sim 118. \tag{4.18}$$

Taking into account the cubic TMs of LPF, the final result is

$$S_N \simeq S_F \frac{r^2}{118} \tag{4.19}$$

$$S_{\Delta\gamma} \simeq \frac{r^2}{118}\frac{2}{I^2}\frac{M^2}{2}S_{\Delta g} = \frac{36}{118}\frac{r^2}{R^4}S_{\Delta g}, \tag{4.20}$$

which allows the conversion of displacement Brownian noise $S^{\mathrm{B}}_{\Delta g}$ into angular Brownian noise along ϕ, $S^{\mathrm{B}}_{\Delta\gamma_\phi}$. As for the actuation noise model, the same angular Brownian noise level has been assumed to hold also for η, since dedicated simulations were not available.

4.3 Comparison with results

At the lowest frequencies the predicted torque noise model is compatible or even larger than the observed values for all noise runs illustrated in Appendix §C.4: this occasional overestimate is not surprising as the prediction is based on some amount of extrapolation.

Only at frequencies above $\sim 0.1\,\mathrm{mHz}$ we observe a definite excess over the model, which is more pronounced for $S_{\Delta\gamma_\eta}$: a systematic power excess is visible in the η channel with respect to ϕ, up to a factor ~ 5 in some of the measurements.

Being the torque noise model for η derived from ϕ measurements, in the following we are going to compare observations to the model only for $\Delta\gamma_\phi$.

The presence of excess noise in the angular spectra $S_{\Delta\gamma_\phi}$ depends on the single noise run and does not show a stable behavior, as is clear from Figure 4.2. The lack of a consistent excess at the lowest frequencies puts therefore an upper limit to the amount of torque associated to the excess Δg noise at those same frequencies.

To better discuss such upper limit we have investigated the spectral cross-coherence between $\Delta\gamma$ and Δg. A significant degree of correlation $|\rho(f)|^2$ between Δg and $\Delta\gamma$ is occasionally present, and is marginal at lower frequencies for most noise runs under analysis.

In some noise runs, the presence of correlation at higher frequencies $\sim 10\,\mathrm{mHz}$ is connected to cross-talk with the SC motion. The presence of correlation is in any case dependent on the single noise run, and does not manifest systematically.

It is interesting to discuss the meaning of (4.10) in the classical case in which

$$\Delta g(t) = \Delta g_0(t) + \alpha \Delta g_{\mathrm{exc}}(t), \tag{4.21}$$

with Δg_0 independent of $\Delta g_{\rm exc}$. The PSD is then

$$S_{\Delta g}(\omega) = S_{\Delta g_0}(\omega) + \alpha^2 \; S_{\Delta g_{\rm exc}}(\omega), \tag{4.22}$$

and the fraction of the total PSD of Δg which is due to $\Delta g_{\rm exc}$, in power, is given by

$$|\rho(\omega)|^2 = \frac{\alpha^2 S_{\Delta g,{\rm exc}}(\omega)}{S_{\Delta g}(\omega)}. \tag{4.23}$$

A frequency independent plateau can be identified in the lowest frequency bins of Figure 4.3a, which corresponds then to a correlated fraction $\alpha^2 \; S_{\Delta g_{\rm exc}}$ of the noise PSD $S_{\Delta g}$ given by

$$\alpha^2 = 0.097, \quad \text{with } 2\sigma \text{ confidence interval } \left[0.032; 0.182\right]. \tag{4.24}$$

This implies that the correlated fraction of the excess noise at low frequency is at most 18% in power with a 95% probability. Hence, it is reasonable to assume that correlation effects visible in $|\rho(f)|^2$ are not connected to the excess noise at low frequency in Δg.

This is therefore in contrast with the hypothesis of a common process accelerating the TM both along translational and angular degrees of freedom, giving rise to excess noise in both Δg and $\Delta\gamma$.

5 Spurious signals in acceleration noise data

As anticipated at the beginning of Part §I, the differential parasitic acceleration per unit mass $\Delta g(t)$ has been found to be affected by spurious force signals of unknown nature, impacting on the LPF noise performance and limiting its sensitivity. This kind of spurious impulses, depicted in Figure 5.1, were referred to as *glitches* during LPF operations, and are distributed along the course of the whole mission.

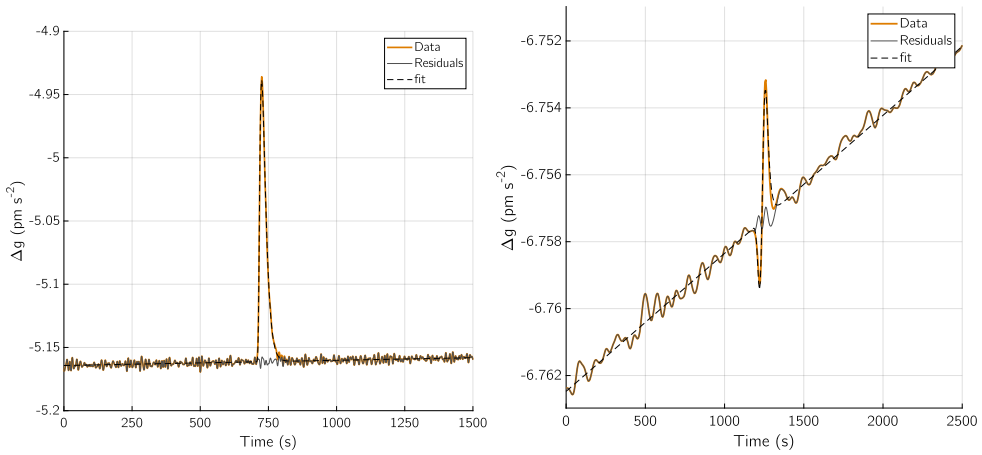

Figure 5.1: Two glitches detected in the lowpassed data from the best performance noise run of February 2017 published in [17]. The events are shown here as they appear in the original lowpassed $\Delta g(t)$ data, with the presence of the DC noise background. The noise data are plotted together with the fit performed to subtract the events and the noise residuals. Left: one-sided signal. Right: two-sided signal.

The glitches effect on the noise performance can be appreciated in Figure 5.2, where a comparison is held between the ASD of $\Delta g(t)$ data corrected for the non-inertial effects, but before and after the subtraction of the glitches.

In the plot, the effect of the glitches on the noise spectrum becomes evident at frequencies $f \lesssim 10\,\mathrm{mHz}$, with a white noise plateau in the mHz regime and a low frequency noise tail below $\sim 300\,\mu\mathrm{Hz}$. The glitches visibly impact $S_{\Delta g}^{1/2}$ only in the case of noise runs containing multiple glitch occurrences with an high total transferred impulse, as the one depicted here.

Reducing their impact on the noise spectrum of $\Delta g(t)$ requires to individually identify, fit and subtract the glitches from the data, in order to obtain a clean differential acceleration noise $S_{\Delta g}$.

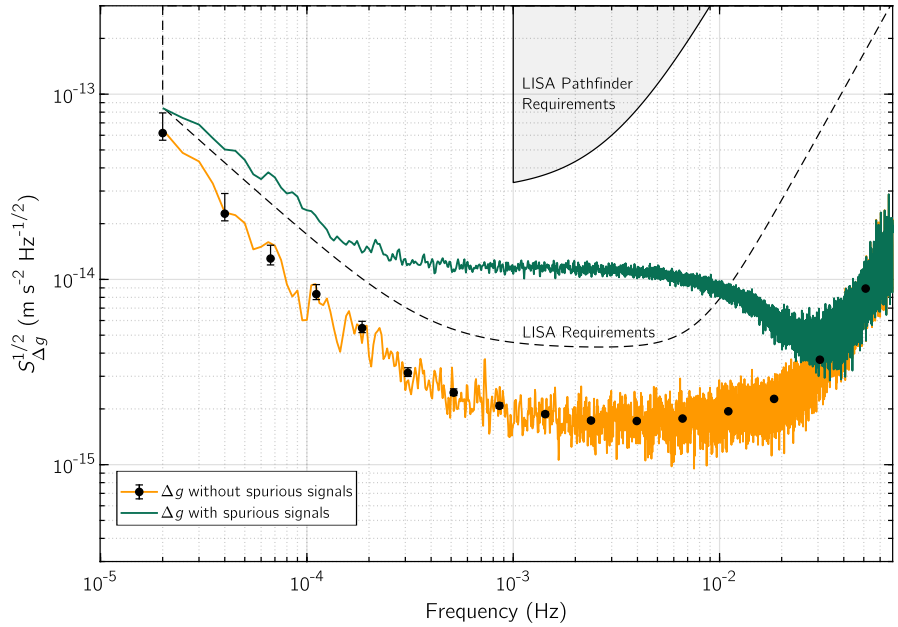

Figure 5.2: Comparison of ASD of the best performance noise run of February 2017, before (green) and after (orange) subtraction of the spurious signal identified in the time series.

After subtraction, no residual noise is left in $\Delta g(t)$ data: the comparison between the noise spectrum evaluated by subtracting the events and the one obtained by cutting them out are compatible within the uncertainties, apart for fluctuations due to numerical differences.

5.1 Phenomenology

Due to the high frequency noise component, the glitches only emerge from $\Delta g(t)$ after the application of a lowpass filter on time-series data, and manifest as force per unit mass signals well defined in time, which average back to zero and impress no net change in force to the TM.

Two exemplifying events, occurred during the two-weeks best performance noise run #66 of February 2017, are depicted in Figure 5.1.

The two glitches of in the plot represent the two different families of signals detected in the data, and they can be distinguished as follows:

1. one-sided signals, the most numerous ones, illustrated in the left-hand panel;

2. oscillating two-sided signals, a minority, pictured in the right-hand panel.

Glitches in $\Delta g(t)$ time-series may originate in two ways: they may either consist of true force glitches acting on the TM, or they could be spurious features superimposed to the interferometer output appearing in the noise term n_{12} of equation (2.10).

The two cases may be in principle be discriminated by comparing data of the differential interferometric readout time-series $o_{12}(t)$ to the differential electrostatic position readout

$$o_{12}^{\mathrm{GRS}}(t) = x_2(t) - x_1(t) + n_{12}^{\mathrm{GRS}}, \tag{5.1}$$

where $x_2(t)$ and $x_1(t)$ are the TMs coordinates and n_{12}^{GRS} is the electrostatic noise term.

In Figure 5.3 we show an example of a rather energetic glitch in $\Delta g(t)$ where the motion of the TM is detected by both $o_{12}(t)$ and $o_{12}^{\mathrm{GRS}}(t)$. Unfortunately, for less energetic glitches, the GRS electrostatic readout is not sensitive enough.

The spurious signal impulse occurring in the lowpassed $\Delta g(t)$ data is depicted on the left-hand side vertical axis, while the time-series of the interferometric and electrostatic differential position readouts, $o_{12}(t)$ and $o_{12}^{\mathrm{GRS}}(t)$, are displayed on the right-hand side vertical axis, which pictures displacement.

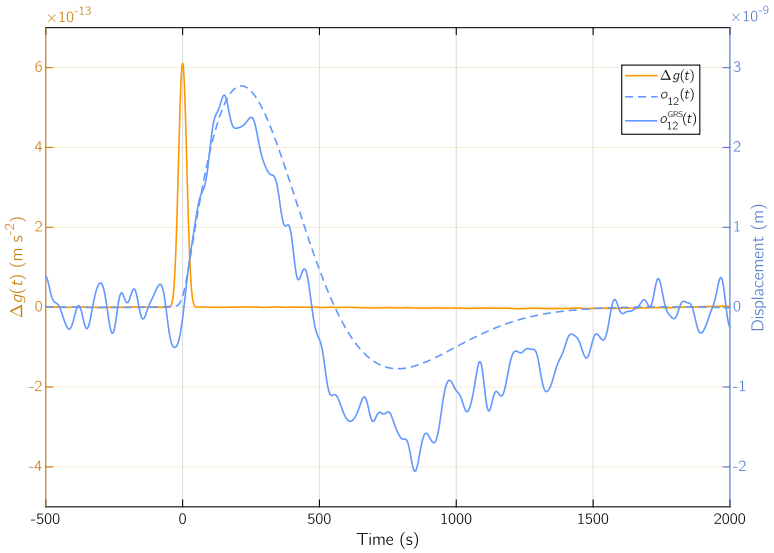

Figure 5.3: Visibility of a spurious signal occurrence from the noise run #61 of December 2016. The left-hand side vertical axis (orange) shows $\Delta g(t)$ lowpassed time-series, while the right-hand side vertical axis (light-blue) shows the response in the $o_{12}(t)$ and $o_{12}^{\mathrm{GRS}}(t)$ data.

The three time-series in the plot have been lowpassed with a Blackman-Harris window of 100 s duration and a 4-th order polynomial has been subtracted from the background, using a 300 s stretch of data at the beginning and at the end of the 2500 s total data stretch.

Since $\Delta g(t)$ (2.13) is a quantity derived from the second-order time derivative of the differential coordinate x_{12}, the expected response of the differential position readout channels should recall the filtered double integral of the spurious impulse, that is a ramp convolved with the 100 s Blackman Harris filter function.

Hence, if the signal response had not been detectable in the $x_{12}(t)$ time-series then it would have been caused by a noise source not connected to the TMs displacement. Instead, being the response to the glitch visible both in $o_{12}(t)$ and in $o_{12}^{\mathrm{GRS}}(t)$, the signal is qualified as caused by a TMs displacement mechanism.

In correspondence of the very energetic spurious signal time of arrival at $t = 0$ s, a few nm displacement is felt by the TMs differential dynamics, and is then brought back to zero by the electrostatic suspension control loop. The detectability of the displacement in the differential position readout channels, both interferometric and electrostatic, qualifies these events as manifestation of pure force signals acting on the TMs differential position.

In the case of two-sided events the shape of the expected response of the differential position readout channels $o_{12}(t)$ and $o_{12}^{\mathrm{GRS}}(t)$ should again recall the filtered double integral of the spurious signal, which has the shape of the derivative of a Dirac's delta function. The $o_{12}(t)$ and $o_{12}^{\mathrm{GRS}}(t)$ response should then recall the convolution between a step function and the Blackman-Harris filter, but it appears that the differential position readout channels don't have the sensitivity needed to detect such response, being the two-sided signals faint and very rare.

5.1.1 Spurious signals occurrence

The total number of glitches detected during the twelve long noise-only runs listed in Table 2.1 is of 57 occurrences, insufficient to perform statistical considerations on the glitches incidence and distribution. To counteract this, the data set was extended by taking into account the glitches occurring in all the available $\Delta g(t)$ time-series measured during ESA operations, in order to access a wider set of data spread over eighteen months of operations and varied actuation configurations.

These account also for quiet short noise segments occurring before or after programmed experiments and noise-only runs measured far from the operating conditions for LPF. The list of all $\Delta g(t)$ runs with their respective authority configuration is listed in Appendix B.

Glitches have been detected in a total number of 39 out of 80 $\Delta g(t)$ data segments, which immediately appeared to fall into two separate categories.

The first one is constituted by 108 events occurring in the 35 runs taken at temperatures $T \simeq 22\,^{\circ}\mathrm{C}$ and $T_{\mathrm{low}} \simeq 11\,^{\circ}\mathrm{C}$, spreading along all operations and with no significant differences in the glitch occurrence rate.

The latter is formed by 405 events detected in the course of about 10 days, in the 4 $\Delta g(t)$ runs measured during the system cool-down to $T_0 < 2\,^{\circ}\mathrm{C}$ occurred between April 29th, 2017 and May 12th, 2017, when the glitch occurrence rate increased of a factor ~ 35.

Because of the extraordinarily high number of spurious occurrences during the T_0 cool-down noise runs, the glitches have been analyzed by maintaining the two data sets separated. In the following, events from ambient-T and T_{low} runs are marked as *ordinary*, in comparison with *cold* glitches from T_0 measurement runs.

Moreover, several glitches from the cold runs manifest as superimposed signals, as it is depicted in Figure 5.4, making a complete subtraction of all events not attainable for measurements taken during the cool-down to T_0: the result of the fit is therefore relevant only for the statistical investigation of the glitches phenomenon and not for the evaluation of LPF noise performance.

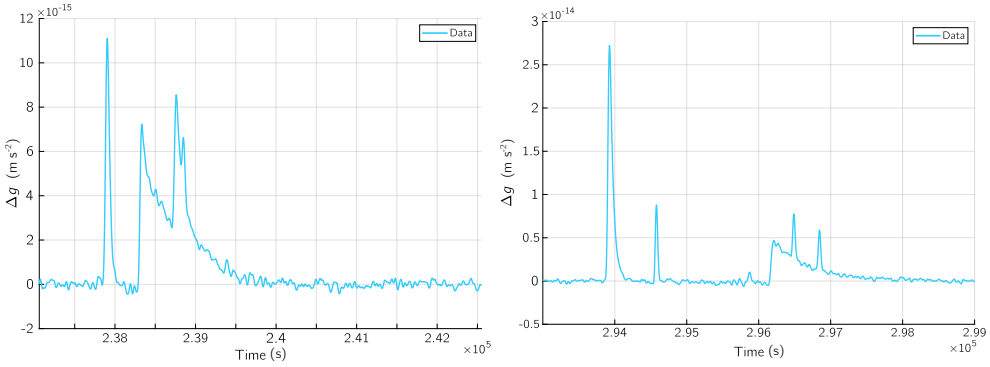

Figure 5.4: Example of spurious signal superimposed occurrences from noise run #71.

Nevertheless, one can perform a partial subtraction of glitches in the cold noise runs and evaluate the noise spectrum $S^{1/2}_{\Delta g,T_0}(f)$ on the longest available data segments free from glitches, after the subtraction of as much events as possible, in order to compare its performance to the one of ordinary runs.

After bringing the temperature back to $T_{\rm low}$ and later to $T \simeq 22\,^{\circ}\mathrm{C}$, the rate of the signals went back to the same level as before the cool-down. One could thus presume that the temperature decrease down to T_0 did not switch on any other process beyond the increase in the glitch rate.

The glitches sourcing phenomenon is not traceable to known events or noise effects that could be quantitatively estimated during operations: they neither occur in correspondence of external episodes, such as micrometeorites colliding with the satellite or cosmic radiation build-ups, nor simultaneously to recurring events happening on the spacecraft, such as the exertion of calibration signals on the TMs. Furthermore, there are no hints that glitches from the cold runs have been triggered by physical phenomena different from the ones of the ambient-T noise runs besides the difference in the occurrence rate.

5.2 Glitches detection and fit

To detect and properly fit the glitches occurring in the differential acceleration data, it is suitable to suppress the lower and higher frequency noise components in $\Delta g(t)$.

The preferred estimation technique to identify and fit spurious signal occurrences would be the Wiener-Kolmogorov optimal filter for the properly shaped impulse. For an impulse of negligible duration, the template in the frequency domain would be

$$h_{\rm W}(\omega) = \frac{\left[S_{\Delta g}(\omega)\right]^{-1}}{\int_{-\infty}^{\infty} \left[S_{\Delta g}(\omega)\right]^{-1} \mathrm{d}\omega}. \tag{5.2}$$

The method that is instead applied to $\Delta g(t)$ data in the course of this work is the following. On one hand, a small data stretch before and after the glitch is detrended with a 4-th order polynomial, with the purpose of removing the long term variations the noise around the signal before fitting.

On the other hand, the presence of high frequency noise in the differential acceleration data makes the spurious events detectable only after applying a lowpass filter. The $\Delta g(t)$ data are filtered with a sliding Blackman-Harris window function of 100 s length, corresponding to a roll-off frequency $f_{\rm c} = 10\,\mathrm{mHz}$: the glitches shape is thus affected by the filter function, and appear as slightly broadened in time.

Such an identification technique appears not to be much worse than the optimal filter (5.2): the uncertainty evaluated with the optimal filter for instantaneous impulses is compatible within a factor 2 with the uncertainty

on the fit parameters evaluated via repeated fits of the same spurious event repeatedly superimposed to glitch-free data stretches of background noise, as described in the following sections.

Naturally, to take into account the lowpass filter effect, the glitch models described in the following are convolved with the same Blackman-Harris filter before being fitted to the lowpass-filtered $\Delta g(t)$.

The fit parameters obtained as outcome are thus unbiased by the convolution with the filter and can then be used to subtract the modeled glitches from the unfiltered high-frequency time-series, where the events would otherwise be undetectable.

The glitches can then be characterized according to the best fitting model used to subtract them from differential acceleration data $\Delta g(t)$. Five different fitting models have been used for the two families distinguished in Figure 5.1:

1. **one-sided glitches**

   - fast one-sided impulses, nominally indistinguishable from a Dirac delta function because their time duration is smaller than the duration of the Blackman-Harris lowpass filter, fitted via

     $$\delta_h(t) = \Delta v \; \delta(t - t_0), \tag{5.3}$$

     where Δv is the total transferred impulse per unit mass of the TM and t_0 is the event arrival time;
   - one-sided signals that have definite time duration and are best fit with a double decaying exponential model, resembling the impulse response of an overdamped oscillator,

     $$h(t) = \frac{\Delta v}{\tau_1 - \tau_2} \left(e^{\left(-\frac{t-t_0}{\tau_1}\right)} - e^{\left(-\frac{t-t_0}{\tau_2}\right)} \right) \Theta(t - t_0), \tag{5.4}$$

     where τ_1 and τ_2 are the rising and decaying time constants of the exponentials;
   - two exceptional cases, corresponding to very energetic events with a duration of several hours, are better fitted to

     $$\begin{aligned} h_3(t) = \Delta v \Bigg(& \frac{e^{\left(-\frac{t-t_0}{\tau_1}\right)} \tau_1}{(\tau_1 - \tau_2)(\tau_1 - \tau_3)} - \frac{e^{\left(-\frac{t-t_0}{\tau_2}\right)} \tau_2}{(\tau_1 - \tau_2)(\tau_2 - \tau_3)} \\ & - \frac{e^{\left(-\frac{t-t_0}{\tau_3}\right)} \tau_3}{(\tau_1 - \tau_3)(\tau_3 - \tau_2)} \Bigg) \Theta(t - t_0), \end{aligned} \tag{5.5}$$

though a fit with (5.4) is not much worse.

2. **double-sided glitches**

   - fast double-sided impulses that transfer zero impulse, compatible with the derivative of the Dirac delta function

$$\delta'_h(t) = \Delta x \; \delta'(t - t_0); \tag{5.6}$$

   - two-sided signals that transfer non-zero impulse and are the sum of two opposite sign decaying exponentials, resulting in a model given by

$$h_A(t) = \left(\frac{\Delta x + \tau_2 \Delta v}{\tau_1(\tau_2 - \tau_1)} e^{\left(-\frac{t-t_0}{\tau_1}\right)} - \frac{\Delta x + \tau_1 \Delta v}{\tau_2(\tau_2 - \tau_1)} e^{\left(-\frac{t-t_0}{\tau_2}\right)} \right) \Theta(t - t_0). \tag{5.7}$$

   Here Δx is the amplitude of the impulse in terms of TM differential displacement: a glitch in $\Delta g(t)$ data fitted with (5.6) is the second derivative of a step in $x_{12}(t) = x_2(t) - x_1(t)$ data, fitted with a step function $\Delta x \; \Theta(t - t_0)$.

The distribution of the spurious events according to the aforementioned fitting functions is summarized in Table 5.1, while the detailed list of detected glitches per noise run, per fitting model is instead listed in Table 5.2.

Table 5.1: Schematic representation of the glitches entire data set.

Total								
513								
Ordinary noise runs					Cold noise runs			
108					405			
One-sided			Two-sided		One-sided		Two-sided	
100			8		337		68	
$\delta_h(t)$	$h(t)$	$h_3(t)$	$\delta'_h(t)$	$h_\mathrm{A}(t)$	$\delta_h(t)$	$h(t)$	$\delta'_h(t)$	$h_\mathrm{A}(t)$
44	54	2	6	2	228	109	64	4

The assessment of the best fitting function between (5.3) and (5.4) for one-sided signals, and between (5.6) and (5.7) for two-sided signals, is done by evaluating the ratio between the squared norm of the residuals obtained from the fit with both functions, that is

$$R = \frac{|\Delta g(t)_{\mathrm{res},\delta(t)}|^2}{|\Delta g(t)_{\mathrm{res},h(t)}|^2}. \tag{5.8}$$

If $R \leq 1.1$, the fit performed via the simpler delta functions $\delta_h(t)$ or $\delta'_h(t)$ is preferable. Notice that the ability to detect a time structure in the glitch depends obviously on the signal to noise ratio, thus a pulse shorter than the filter could still be significantly discriminated from a δ-like signal if the impulse is large enough.

As an example, let us take into account two spurious events detected in best performance noise run #66 of February 2017: in Figure 5.5a, the residual ratio is $R = 1.00$, and the residuals from the two fits are indistinguishable within the noise r.m.s. value, while for the event plotted in Figure 5.5b, $R = 7.36$ and only the fit with $h(t)$ is successful.

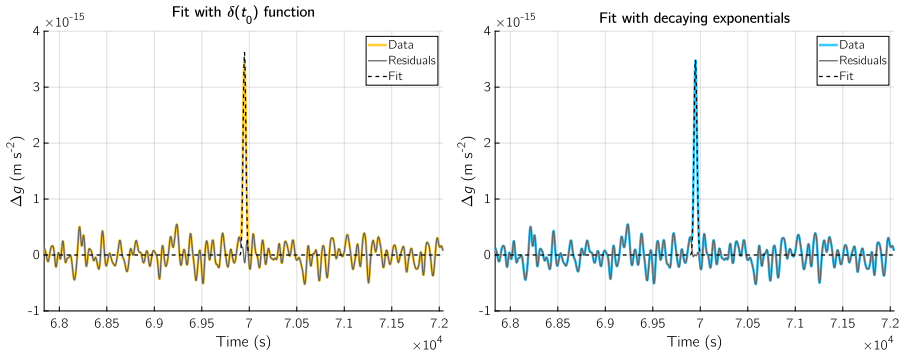

(a) Fit to a spurious signal from the noise run of February 2017 with $R = 1.00$.

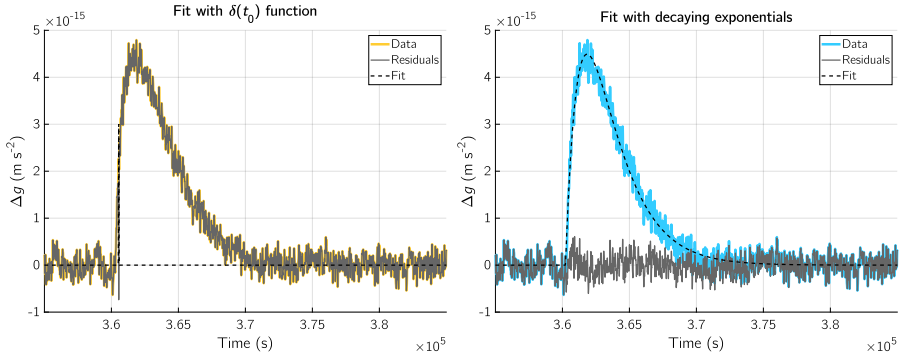

(b) Fit to a spurious signal from the noise run of February 2017 with $R = 7.36$.

Figure 5.5: Comparison between fits to different glitches performed with models (5.3) (left-hand panels) and (5.4) (right-hand panels).

Table 5.2: Detailed list of spurious events occurrences per each noise run. Δg time-series are indexed according to the noise runs total number. One-sided and two-sided events are separated and each of the two families is characterized according to the proper fitting function.

Noise run index	Number of glitches	One-sided			Two-sided	
		$\delta(t)$	$h(t)$	$h_3(t)$	$\delta'(t)$	$h_{\mathrm{A}}(t)$
1	12	12	-	-	-	-
2	1	1	-	-	-	-
3	2	-	2	-	-	-
4	1	1	-	-	-	-
6	2	-	2	-	-	-
8	2	1	1	-	-	-
9	8	4	3	1	-	-
12	3	2	-	-	1	-
13	2	2	-	-	-	-
14	1	-	1	-	-	-
17	3	-	3	-	-	-
18	3	2	1	-	-	-
24	2	-	1	-	1	-
27	1	1	-	-	-	-
35	2	-	1	-	1	-
37	1	-	1	-	-	-
39	1	-	1	-	-	-
41	1	-	1	-	-	-
42	1	1	-	-	-	-
43	1	-	1	-	-	-
44	1	-	-	1	-	-
45	2	-	2	-	-	-
46	1	-	1	-	-	-
58	5	1	4	-	-	-
59	5	1	4	-	-	-
61	13	3	8	-	2	-
64	2	1	1	-	-	-
66	8	3	4	-	-	1
67	6	2	3	-	1	-
70	68	40	11	-	17	-
71	231	137	55	-	37	2
72	65	30	27	-	7	1
73	41	27	19	-	4	1
74	3	3	-	-	-	-
75	7	2	5	-	-	-
76	6	1	4	-	-	1

5.3 Statistics of the spurious events

The statistical investigation of the signals belonging to the wider set of data listed in Tables 5.1 and 5.2 may help in the reducing the number of various hypotheses about the glitches origin.

The key parameter to analyze the glitches distribution are the time of arrival t_0 and the transferred impulse per unit mass Δv, that is, the only two parameters that can be estimated for all four fitting models (5.3)-(5.4)-(5.6)-(5.7). For signals fitted with decaying exponential models (5.4) and (5.7), the distribution of time constants $\tau_{1,2}$ provides additional information on their temporal structure.

5.3.1 Time of arrival t_0

To establish the glitches arrival distribution, one can look at the distribution of time elapsed between the arrival times t_0 of subsequent events, both one-sided and two-sided.

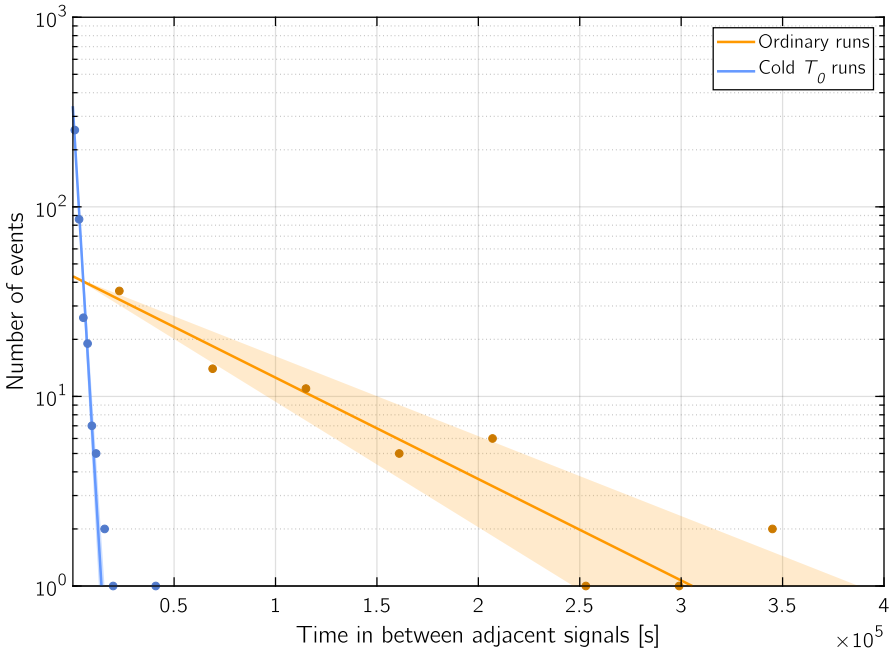

Figure 5.6: Distribution of arrival times of the glitches for both one-sided and two-sided events, divided between the cold T_0 noise runs and the ordinary noise runs. Points represent the number of glitches per time bin, while continuous lines are fit to distribution (5.9) and shaded areas represent the confidence interval of the fit.

This analysis is done per each noise run separately: since the arrival time

is defined with respect to an arbitrary instant in time, for every glitch we are either taking the arrival time of the preceding glitch or, if no preceding glitches exist, the start time T_{start} of the noise run.

This implies that the glitches detected during the available noise runs must be considered as the only valid events for this statistical analysis: signals occurring during science measurements, calibration injections or blind windows on the spacecraft are not taken into account.

The arrival times of the glitches fit to a decaying exponential distribution given by

$$p(t) = \lambda\, e^{-\lambda t}, \tag{5.9}$$

which is the distribution of time elapsed in-between Poisson distributed events with emission rate λ. Thus, within the available resolution, glitches appear to be independent events.

The distribution for the overall glitches data sets is depicted in Figure 5.6, where a significant rate difference is highlighted between ordinary ambient T and cold T_0 noise runs. In the course of the 18 months of operations the events emission rate remained constant at about $\lambda = 1.1\,\mathrm{d}^{-1}$, up until a sharp increase was detected in the emission rate for data belonging to cold noise runs at T_0, when it increased up to $\lambda_0 = 36\,\mathrm{d}^{-1}$.

The emission rate of the signals can be evaluated also for the subsets of one-sided and two-sided events, for each of the models (5.3)-(5.7) and are listed in Table 5.3 with their corresponding confidence intervals.

Table 5.3: Emission rates λ for the glitches detected during the two sets of data, together with the confidence intervals CI_λ that are represented by the shaded areas in Figures 5.6..

	λ (d^{-1})	CI_λ (d^{-1})	λ_0 (d^{-1})	CI_{λ_0} (d^{-1})
	ordinary runs		cold runs	
all signals	1.1	$(0.8 \div 1.3)$	36	$(32 \div 39)$
all one-sided signals	1.0	$(0.8 \div 1.2)$	30	$(27 \div 33)$
$\delta_h(t)$ one-sided signals	0.7	$(0.5 \div 1.0)$	21	$(18 \div 23)$
$h(t)$ one-sided signals	0.6	$(0.4 \div 0.9)$	10	$(8 \div 12)$
$\tau_1 + \tau_2 < 1000\,\mathrm{s}$	0.5	$(0.3 \div 0.8)$	10	$(8 \div 12)$
$\tau_1 + \tau_2 < 100\,\mathrm{s}$	0.3	$(0.1 \div 0.6)$	8	$(7 \div 10)$
$\tau_1 + \tau_2 < 20\,\mathrm{s}$	0.2	$(0.0 \div 0.9)$	4	$(3 \div 5)$
all two-sided signals	n.a.	n.a.	6	$(5 \div 8)$

Moreover, for one-sided events the emission rate is evaluated for different threshold values of the time constants sum $\tau_1 + \tau_2 \leq \tau_{\text{th}}$, both for ordinary and

cold T_0 noise runs, and is listed with the corresponding $C = 0.955$ confidence interval in Table 5.3.

The compatibility among the emission rates at different threshold τ_{th} values is ensured for signals from ordinary noise runs (orange points), not allowing for a distinction among the emission rates of shorter and longer events. For the cold noise runs signals (blue points) the shorter events ($\tau_{\text{th}} = 20\,\text{s}$) emission rate is not compatible with the rate for longer events $\tau_{\text{th}} = 100\,\text{s}, 1000\,\text{s}$.

5.3.2 Transferred impulse per unit mass Δv

The transferred impulse Δv is a direct result of the fit to models (5.3), (5.4), (5.5) and (5.7). In what follows I am going to group the two glitches fitted with (5.5) with events fitted via $h(t)$ (5.4).

In the case of δ'-like glitches the transferred impulse per unit mass Δv is null: the impulse transferred by a spurious force signal is given the integral of the fit curve, which is zero for glitches fitted with the derivative of Dirac's delta.

One-sided events

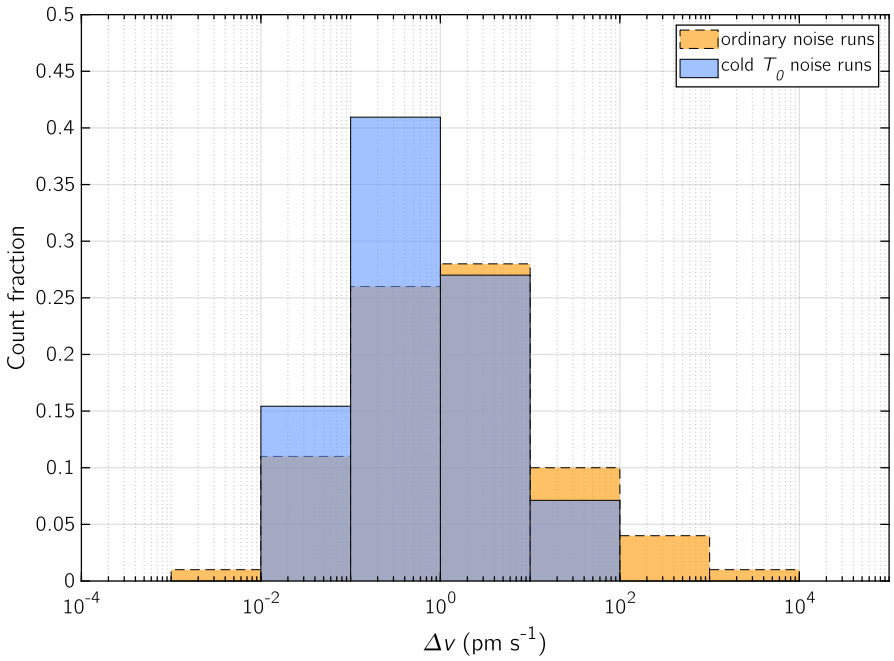

Figure 5.7: Logarithmic histogram of one-sided glitches impulse distribution.

The distribution of impulse per unit mass Δv transferred by all one-sided glitches, without distinction based on their fitting function, is depicted in Figure 5.7 for the signals from ordinary and cold T_0 measurement runs.

The logarithmic histogram shows a distribution peaked around the $\mathrm{pm\,s^{-1}}$ for both data sets, with a tail towards higher impulses in the ordinary glitches data set. Cold signals, instead, primarily transfer impulses Δv of a fraction of $\mathrm{pm\,s^{-1}}$, up to a few $\mathrm{pm\,s^{-1}}$.

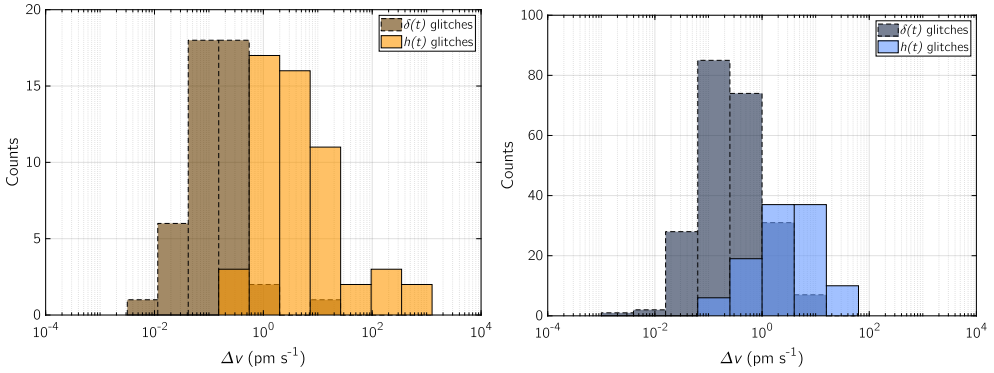

(a) Distribution of glitches detected in the ordinary runs.

(b) Distribution of glitches detected in cold runs.

Figure 5.8: Histograms of impulse distribution for $\delta(t)$ and $h(t)$ glitches, separated between signals detected in ordinary and in cold runs.

The distributions of $\delta_h(t)$ and $h(t)$ glitches can be analyzed for the two data set separately, that is, for glitches detected in the ordinary and for cold T_0 measurements. The comparison is depicted in Figure 5.8.

In the plot it is evident how the $\delta_h(t)$ glitches transfer impulses of few $\mathrm{pm\,s^{-1}}$ and lower in both data sets, while glitches with a defined temporal structure fitted via $h(t)$ populate the distribution from $1\,\mathrm{p\,s^{-1}}$ up.

In the case of ordinary runs, plotted in Figure 5.8a, the populations of instantaneous and time-defined glitches show very little overlap, and $h(t)$ signals show a tail at higher impulses, up to $\sim \mathrm{nm\,s^{-1}}$.

For what concerns the cold T_0 runs, illustrated in Figure 5.8b, the distinction between $\delta_h(t)$ and $h(t)$ glitches is less sharp and the distribution is narrower, with impulses up to a few tens of $\mathrm{pm\,s^{-1}}$.

In both data sets, the occurrence of negative spurious events is a fraction of the total, accounting to about $\sim 21\%$ of the δ-like impulses and $\sim 7\%$ of the decaying exponential signals. In addition to this, their occurrence is slightly non-uniform if looking at the cold and ordinary noise runs separately, as it is depicted in Figure 5.9.

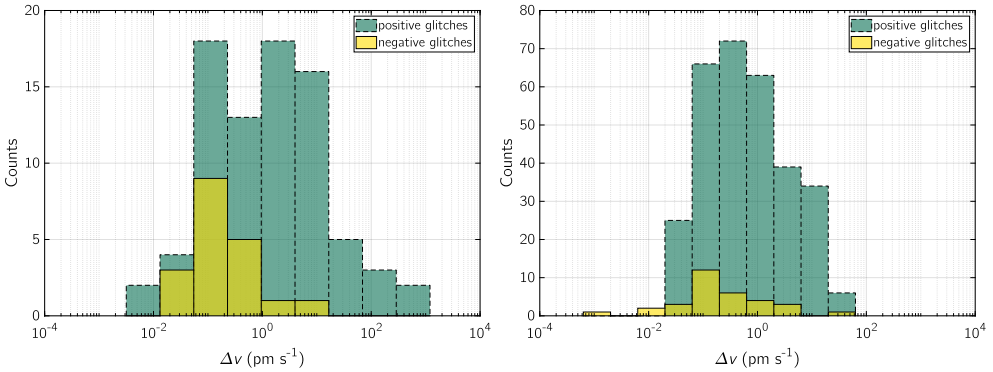

(a) Distribution of glitches detected in the ordinary noise runs.

(b) Distribution of glitches detected in the cold noise runs.

Figure 5.9: Histogram of impulse distribution for positive and negative glitches, separated between glitches detected in the ordinary and cold noise runs.

On the left panel, Figure 5.9a, the distribution of negative Δv glitches is compared to the one for positive signals detected the ordinary noise runs: negative events account for 19% of the sample, their transferred impulse distribution is peaked at $0.1\,\mathrm{pm\,s^{-1}}$, while positive glitches are more uniformly spread between $0.1\,\mathrm{pm\,s^{-1}} \div 10\,\mathrm{pm\,s^{-1}}$.

On the other hand, in the cold T_0 noise runs the incidence of negative signals is 9% and their distribution is illustrated in Figure 5.9b. The shape of the two populations is similar, with positive and negative glitches transferring impulse of similar entity.

The imbalance between the distributions of positive and negative glitches in ordinary and cold noise runs may actually be not significant: the difference in the distributions may be a fluctuation due the reduced number of events in the ordinary noise runs, which are 1/3 of the glitches in the cold T_0 runs.

In Figure 5.10 it is instead depicted the transferred impulse per unit mass Δv over the total mission duration for one-sided glitches in the two data sets, separated among $\delta_h(t)$ and $h(t)$ signals, and every point (either filled or empty) represents a glitch. For δ-like signals (Figure 5.10a) in the ordinary noise runs Δv ranges between 0.1 and $1\,\mathrm{pm\,s^{-1}}$, while glitches of the cold noise runs cover on average a broader Δv range up to $10\,\mathrm{pm\,s^{-1}}$.

On the other hand, in the case of events fitted with the decaying exponential model $h(t)$, depicted in Figure 5.10b, the transferred impulse range is more widely spread between 0.1 and $100\,\mathrm{pm\,s^{-1}}$ both for glitches from the ordinary and cold noise runs.

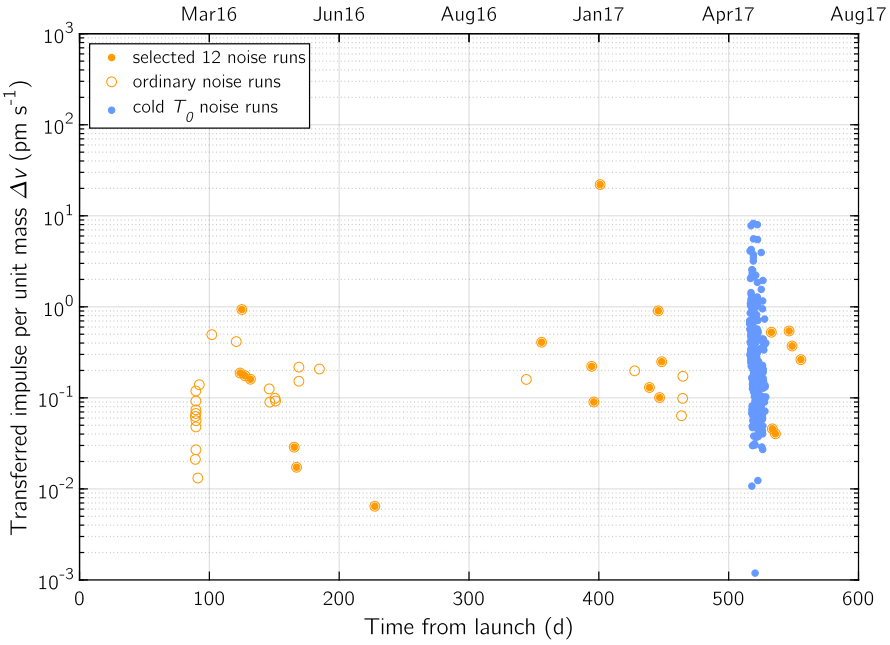

(a) $\delta_h(t)$ signals.

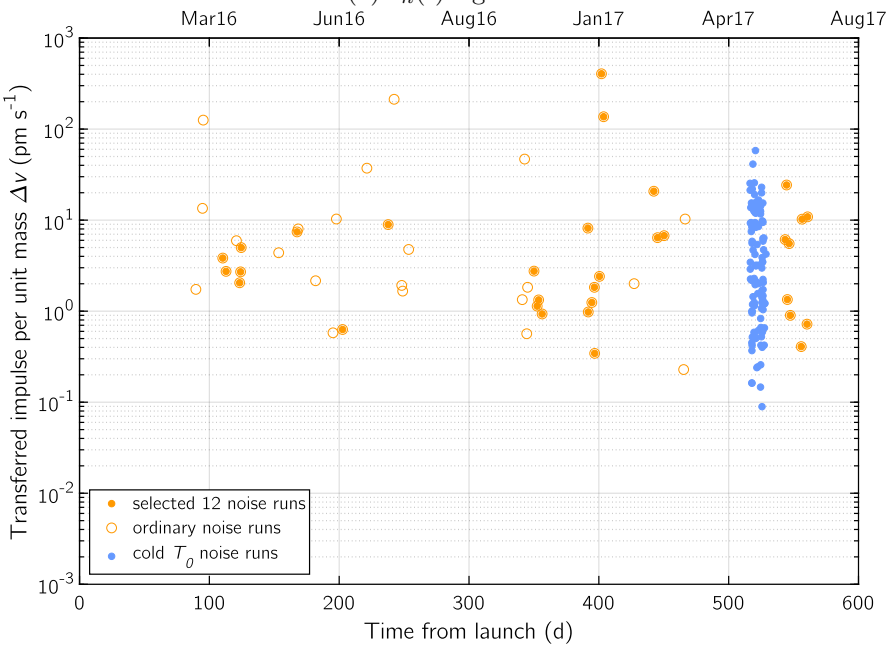

(b) $h(t)$ signals.

Figure 5.10: Scatter plot of the one-sided spurious events transferred impulse Δv over days from launch.

Two-sided signals

The very low occurrence of two-sided signals, which account for about 15% of the total, makes it difficult to evaluate their transferred impulse distribution. In the case of δ'-like signals (5.6), the only fitting parameter available is the width of the step Δx, and they transfer no impulse per unit mass, unlike what happens for decaying exponential signals fitted with model (5.7).

Table 5.4: Transferred impulse per unit mass Δv in $\mathrm{pm\,s^{-1}}$ by the spurious two-sided signals fitted with the decaying exponential model (5.7).

Δx (pm)	Δv ($\mathrm{pm\,s^{-1}}$)	Run
-5.4 ± 0.3	0.092 ± 0.005	66
11 ± 1	0.85 ± 0.01	76
-3.4 ± 0.2	-0.004 ± 0.004	71
16.6 ± 0.6	-0.28 ± 0.02	71
-2.8 ± 0.2	-0.051 ± 0.003	72
-10 ± 1	0.09 ± 0.02	73

The spurious events fitted with $h_{\mathrm{A}}(t)$ are an overall number of 4 signals, 2 out of 8 for the ordinary and 4 out of 68 for the cold T_0 noise runs. Their transferred impulse per unit mass Δv and corresponding step width Δx are listed in Table 5.4.

One of the hypothesis is that two-sided signals transferring impulse are triggered by different physical phenomena with respect to the $\delta'(t)$ events. If that's the case, the $h_{\mathrm{A}}(t)$ signals could be generated by the same physical source of one-sided decaying exponential signals.

5.3.3 Amplitude and duration of the glitches

Spurious signals can also be characterized via their true peak amplitude $\Delta g_{\max}$ in the unfiltered data. The quantity is a combination of the transferred impulse Δv and time constants $\tau_{1,2}$ for models (5.4) and (5.7).

One-sided signals

For what concerns one-sided decaying exponential signals, one could characterize them through their true peak amplitude $\Delta g_{\max}$ in the unfiltered data. That is given by the maximizing value of the fitting model first derivative, that is

$$\Delta g_{\max} = \frac{\Delta v}{\tau_1 - \tau_2}\left(\alpha^{\frac{1}{1-\alpha}} - \alpha^{\frac{\alpha}{1-\alpha}}\right), \quad \alpha = \frac{\tau_1}{\tau_2}. \tag{5.10}$$

The dependence of $\Delta g_{\max}$ on the decaying exponentials time constants $\tau_{1,2}$ can lead to some issues connected to the strong correlation among those parameters.

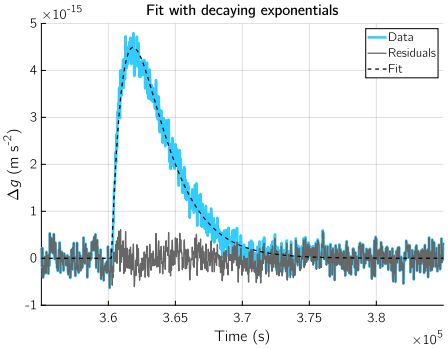

(a) Fit to model (5.4) and subtraction of spurious signal in $\Delta g(t)$ data with residuals.

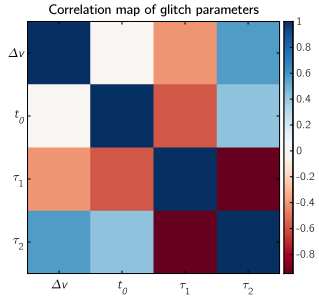

(b) Correlation map of the fit parameters $\Delta v, t_0, \tau_1, \tau_2$ for model (5.4).

Figure 5.11: Third spurious event detected during the best performance noise run of February 2017 published in [17].

By looking at the correlation map of Figure 5.11b among the fit parameters for an exemplifying event, it is clear how the only reasonably uncorrelated parameters of the fit are the arrival time of the event t_0 and the transferred impulse Δv, while the time constants $\tau_{1,2}$ are strongly correlated.

Unfortunately, the strong correlation among the parameters does not allow for a trustful estimation of the error bars, which can be taken as valid only for the low correlation parameters t_0 and Δv.

To get a more empirical grasp of the time duration of the spurious event, one could take into account the Full Width Half Maximum (FWHM) of the signal in the lowpassed data. This choice could however lead to imprecision because of the 100 s lowpass filter constituted by the Blackman-Harris sliding window. The spurious event time duration is spread in time due to the 10 mHz cutoff frequency of the filter, and this would affect the FWHM estimation for events with a duration of the order of the filter duration.

Thus, the best approach is to estimate time constants error bars $\sigma_{\tau_{1,2}}$ via repeated measurements of the same spurious event with different background noise. This is achieved by injecting a single event modeled by (5.4) multiple times in the clean $\Delta g(t)$ time-series of its original noise run.

In this way, the same event can be fitted multiple times with different background noise(depending on the event duration, from about 10 times to several hundreds), allowing for an estimation of the mean $\overline{\tau}_{1,2}$ and standard deviation $\sigma^{\text{std}}_{\tau_{1,2}}$ of the time constants.

Moreover, the sum of the time constants $\tau_1 + \tau_2$ is found to be affected by less deviations from the mean than their separate values: it constitutes therefore the best estimate of the spurious signal duration. As a consequence of this improved error bars estimate, both the signal amplitude $\Delta g_{\max}$ and the time constants $\tau_{1,2}$ distribution can be determined with higher precision.

The distribution of the peak amplitude $\Delta g_{\max}$ for one-sided decaying exponential events is illustrated in Figure 5.12, where a first clear difference between ambient-T and cold noise runs can be observed. Signals distributions from the both data sets runs are peaked at an amplitude $\sim 25\,\mathrm{fm\,s^{-2}}$.

For ordinary noise runs the distribution sharply averages to zero, while cold noise runs events show a broader distribution with a populated tail at higher amplitudes. This implies that glitches from the cold T_0 noise runs where characterized on average by signals with higher amplitudes, while glitches from the ordinary runs show a narrower amplitude distribution, with few exceptions above $100\,\mathrm{fm\,s^{-2}}$.

The distribution of time constants $\tau_{1,2}$ is instead shown in Figure 5.13: in the upper panel 5.13a the separate distributions of τ_1 and τ_2 are depicted for both noise run sets combined together, highlighting a similar behaviour for the two parameters.

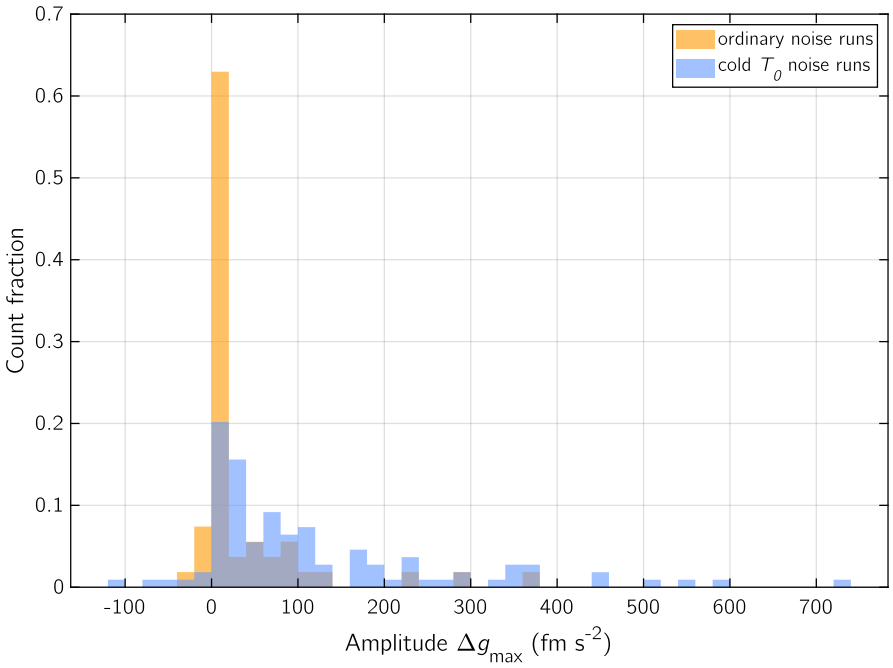

Figure 5.12: Distribution of peak amplitude $\Delta g_{\max}$ of one-sided decaying exponential signals, for the two data sets under investigation.

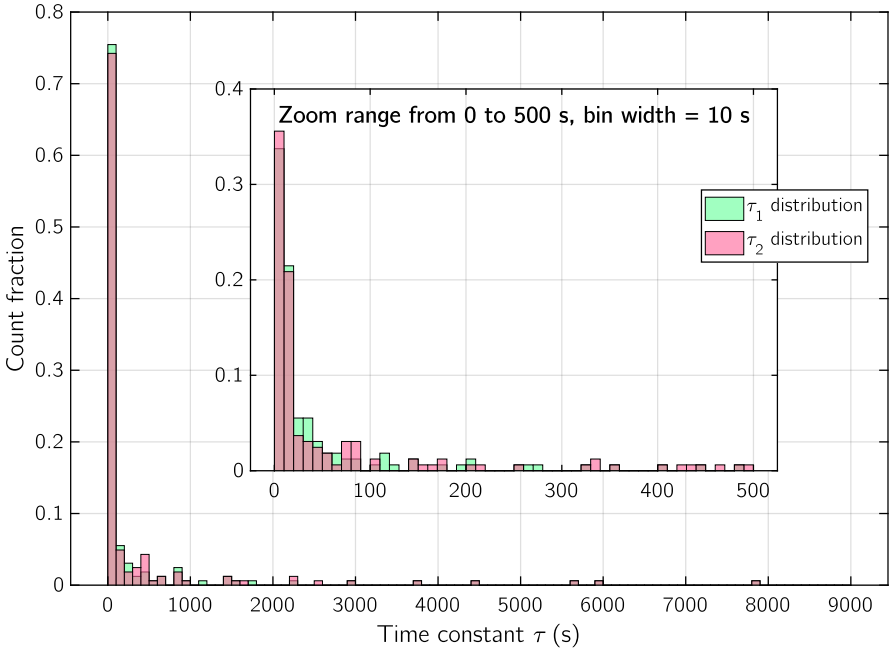

(a) Histogram of time constants τ_1 and τ_2 for the two data sets combined (ordinary and cold noise runs).

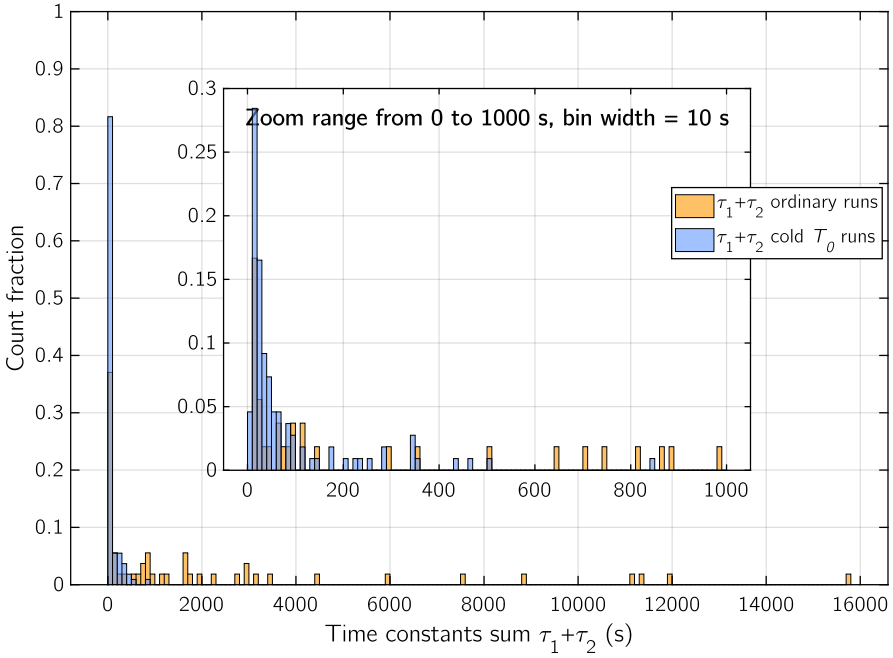

(b) Histogram of time constants $\tau_1 + \tau_2$ for each of the two data sets.

Figure 5.13: Histograms of the $\tau_{1,2}$ distribution for one-sided signals fitted with model (5.4).

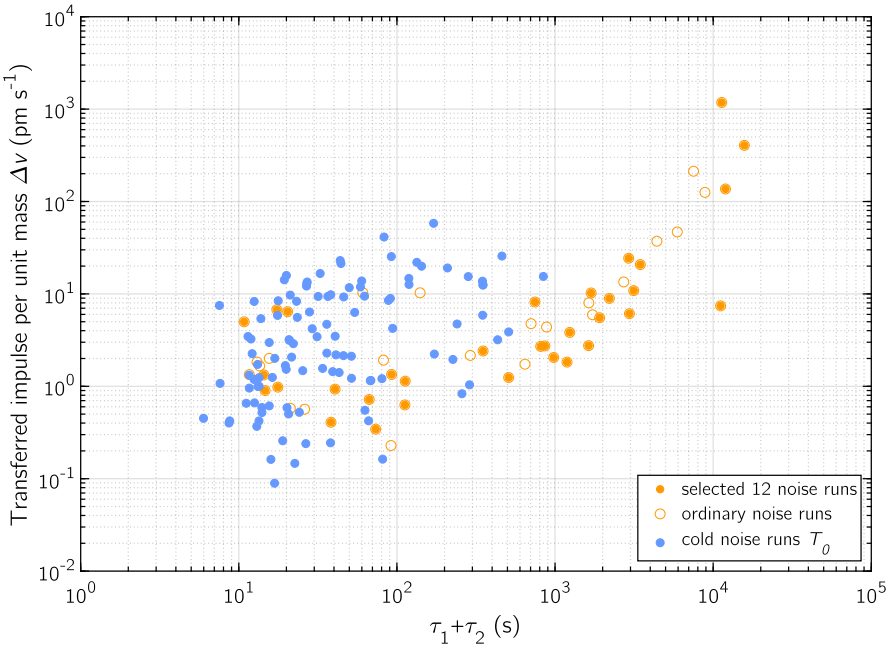

(a) Scatter plot of the glitches transferred impulse $|\Delta v|$ over duration $\tau_1 + \tau_2$.

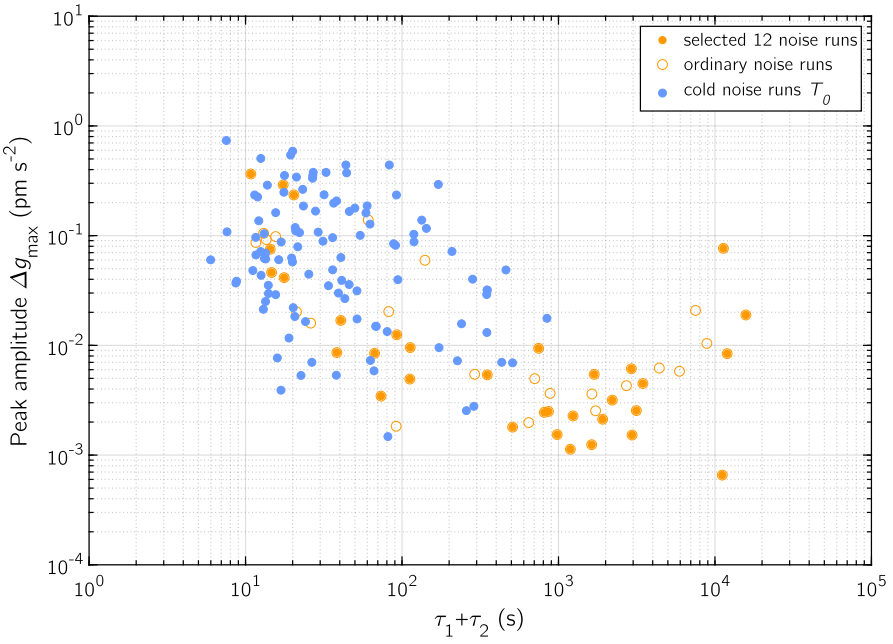

(b) Scatter plot of the glitches peak amplitude $|\Delta g_{\max}|$ over duration $\tau_1 + \tau_2$.

Figure 5.14: Scatter plot of the glitches transferred impulse $|\Delta v|$ and peak amplitude $|\Delta g_{\max}|$ over duration $\tau_1 + \tau_2$. Empty points represent the ordinary noise runs, filled orange points belong to the twelve selected noise runs of Table 2.1 and blue points refer to the cold T_0 noise runs.

In the lower panel 5.13b the sum $\tau_1 + \tau_2$ is shown in the two noise run data sets taken into account in the above. Distribution is peaked at $\tau_1 + \tau_2 = 15\,\mathrm{s}$ for both ordinary and cold T_0 noise runs. Then, the distribution decays smoothly up to $\tau_1 + \tau_2 = 200\,\mathrm{s}$, with a tail that extends at different values depending on the data set: for cold noise runs, he tail extends up to $\tau_1 + \tau_2 \simeq 800\,\mathrm{s}$, while for ordinary noise runs the tail runs up to a duration value of $\tau_1 + \tau_2 \simeq 16\,000\,\mathrm{s} \simeq 4.5\,\mathrm{h}$.

More information about glitches comes from the scatter plot of the transferred impulse absolute value $|\Delta v|$ over the duration estimate $\tau_1 + \tau_2$, plotted in Figure 5.14a. By taking into account both data sets, it becomes evident how the signals duration is distributed with a continuous spectrum spanning from a total duration of few seconds up to several hours.

Instead, by looking at the scatter plot of the peak amplitude absolute value $|\Delta g_{\max}|$ over the duration estimate $\tau_1 + \tau_2$, plotted in Figure 5.14b, one can appreciate how the long duration glitches correspond to low amplitude events, while shorter events from the cold T_0 runs show higher peak amplitude values.

5.4 Torque associated to glitches

To characterize the nature of glitches it is paramount to understand if these pure force events exert some torque on the TMs, and if that's the case, what is the resulting lever arm of the applied force. The presence of any torque transferred to the TMs and associated to the glitches occurrence is evaluated through a linear fit of their shape to the differential angular acceleration data $\Delta\gamma$ (4.3) along the ϕ and η channels, estimated in the previous Chapter §4.

The analysis is performed only on one-sided glitches with definite temporal structure, fitted with (5.4), and detected the ordinary noise runs: the angular dynamics $\Delta\gamma_{\phi,\eta}(t)$ of the cold T_0 noise runs is affected by notable perturbations, due to the spacecraft working outside its normal working conditions. Therefore, it is not possible to quantitatively estimate the lever arm associated to the force applied by glitches detected in the course of T_0 measurements.

The angular amplitude of the glitches is estimated via a linear least-squares fit of the shape of the signal to $\Delta\gamma(t)$ data, where the glitch shape is derived from (5.4) as

$$h^{\mathrm{torque}}(t, t_0, \tau_1, \tau_2) = \Delta v^{\mathrm{torque}}\ \frac{e^{\left(-\frac{t-t_0}{\tau_1}\right)} - e^{\left(-\frac{t-t_0}{\tau_2}\right)}}{\tau_1 - \tau_2}\ \Theta(t - t_0). \qquad (5.11)$$

In (5.11) the transferred impulse per unit mass $\Delta v^{\mathrm{torque}}$ is the only free parameter of the fit, and the glitch shape is determined by the parameters obtained from the fit in the differential acceleration data $\Delta g(t)$: glitch time-base data t, arrival time t_0 and time constants τ_1, τ_2.

The analysis is then realized by following the signal subtraction technique described in Section §5.1: the data stretches used for the fit of the angular amplitude $\Delta v^{\mathrm{torque}}$ are the same used to perform the spurious signal subtraction in $\Delta g(t)$, and each single data stretch stretch is detrended with a 2nd order polynomial to remove the low frequency DC drift.

The angular amplitude $\Delta v^{\mathrm{torque}}$ of the glitch in $\Delta\gamma_{\phi,\eta}$ allows the estimation of the lever arm of the force applied on the TM face, via

$$b_\phi = \frac{\Delta v_\phi^{\mathrm{torque}}}{\Delta v}\frac{\mathcal{I}_{zz}}{M}, \tag{5.12}$$

$$b_\eta = \frac{\Delta v_\eta^{\mathrm{torque}}}{\Delta v}\frac{\mathcal{I}_{yy}}{M}, \tag{5.13}$$

where Δv is the impulse transferred by the glitch in (5.4), $\mathcal{I}_{zz,yy}$ is the moment of inertia of the TM with respect to the rotational axes z, y and M is the TM mass.

The uncertainty σ_{torque} on the angular amplitude of the glitch in $\Delta\gamma_{\phi,\eta}$ is obtained in a similar fashion to the uncertainty in the glitch duration $\tau_1 + \tau_2$: a linear least-squares fit to shape

$$h_\sigma^{\mathrm{torque}}(t, t_0, \tau_1, \tau_2) = \sigma^{\mathrm{torque}}\frac{e^{\left(-\frac{t-t_0}{\tau_1}\right)} - e^{\left(-\frac{t-t_0}{\tau_2}\right)}}{\tau_1 - \tau_2}\Theta(t - t_0) \tag{5.14}$$

is evaluated on all the available $\Delta\gamma_{\phi,\eta}$ data stretches clear from spurious signal occurrences. The stretches i used to estimate $\sigma^i_{\mathrm{torque}}$ have the same length of data stretches used to fit $\Delta v^{\mathrm{torque}}$.

The uncertainty on $\Delta v^{\mathrm{torque}}$ is then given by the root mean square value of the event-free amplitudes $\sigma^i_{\mathrm{torque}}$ evaluated on the i separate clean data stretches for every event, $\sigma^{\mathrm{rms}}_{\mathrm{torque}}$. The uncertainty on the lever arm σ_b is then obtained via uncertainty propagation from $\sigma^{\mathrm{rms}}_{\mathrm{torque}}$, that is

$$\sigma_{b_{\phi,\eta}} = |b_{\phi,\eta}|\sqrt{\left(\frac{\sigma^{\mathrm{rms}}_{\phi,\eta}}{\Delta v^{\mathrm{torque}}_{\{\phi,\eta\}}}\right)^2 + \left(\frac{\sigma_{\Delta v}}{\Delta v}\right)^2}, \tag{5.15}$$

and its comparison with the value obtained for the lever arm $b_{\phi,\eta}$ gives information on the significance of the transferred torque evaluation.

However, the very noisy dynamics of the angular differential acceleration data $\Delta\gamma(t)$ does not allow a proper estimation of the angular amplitude $\Delta v^{\mathrm{torque}}$. In fact, out of the 56 one-sided $h(t)$ glitches detected in the ordinary runs, only 5 of them have a fitted associated lever arm $b_{\phi,\eta}$ that is not compatible with zero within $3\sigma^{\mathrm{rms}}_{\phi,\eta}$, but no noticeable counterpart can be detected in the $\Delta\gamma(t)$ time-series in correspondence of the glitch time of arrival t_0.

Therefore, by looking at the histogram of r.m.s. uncertainty for the arm $\sigma^{\mathrm{rms}}_{b_{\phi,\eta}}$, depicted in Figure 5.15, one can establish the minimum arm b revealability threshold in the data. From the plot, one can see how the distribution of $\sigma^{\mathrm{rms}}_{b}$ is peaked around 1 mm, with width between 0.1 and 10 mm, while the distribution tails account for non significant values (revealability threshold either too large to be physical of too small to be appreciated).

For what concerns the angular dynamics of LPF, the conclusion is that there is no associated torque transferred to the TMs angular dynamics $\Delta\gamma(t)$ by the glitch occurrences detected in $\Delta g(t)$ data. For the majority of the pulses on ϕ the resolution σ_{b_ϕ} is of the order of millimeter or better, and the glitches appear therefore to carry no torque within that resolution.

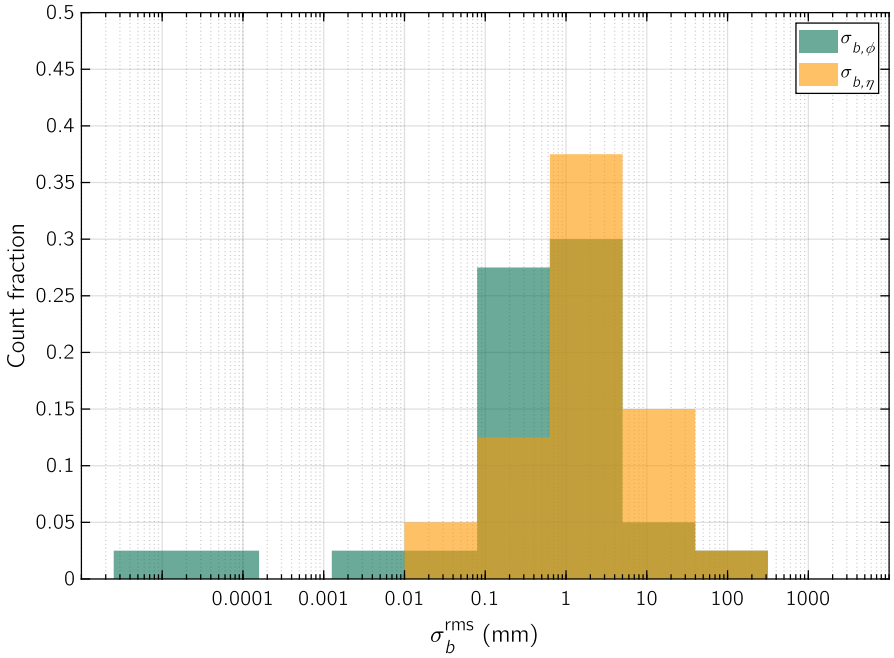

Figure 5.15: Logarithmic histogram of the minimum revealability threshold $\sigma^{\mathrm{rms}}_{b}$ for the associated lever arm to glitches in the ϕ and η channels.

Part II

Discussion

In this Part I will discuss the possible physical origin of the unaccounted disturbances. I will separately discuss the excess power in the low frequency noise in Chapter §6 and glitches in Chapter §7.

6 Sources of low frequency excess noise

The discussion on the low frequency noise behavior of previous Section §3.3 established that the excess power with respect to the expected noise model is neither attributable solely to the actuation noise at low frequency, nor to the correlation with low frequency noise from angular degrees of freedom.

The investigation of other possible sources of the low frequency excess noise is therefore of paramount importance to understand the physical phenomena impacting in the mission performance.

Candidate sources for the excess noise at low frequency, that were not included in the modeled noise of Section §3.4, are:

- non thermal pressure fluctuations;
- gravitational noise;
- frequency-dependent Brownian noise from mechanical dissipation;
- high-frequency magnetic noise fluctuations.

High frequency noise fluctuations from the on-board magnetometers may produce low-frequency noise components when down-converted, if the field amplitude is subjected to modulation.

Despite the absence of on-board high-frequency magnetic sensors, this noise source is considered to be unlikely, due to the on-ground magnetic characterization of the instrument. Moreover, the magnetic environment investigation [35] characterizes the sub-mHz magnetic environment as strongly dominated by the interplanetary magnetic field, and not by magnetic fluctuations from on-board components.

6.1 Non-thermal pressure fluctuations

The possibility that outgassing is a major source of disturbance is discussed in connection to the glitches, in Chapter §7.

Here we just want to highlight the possibility that random outgassing in the proximity of the TM could lead to pressure fluctuations Δp around the TM, and give rise to fluctuations in Δg, via

$$\Delta g(t) = \frac{\Delta p(t)\ S}{m}, \tag{6.1}$$

where S is the TM cubic surface and m is the TM mass.

Hence, the measured excess noise at low frequency may be converted into pressure fluctuations by recalling (3.12) and

$$S_{\Delta g}(\omega) = \frac{S^2}{m^2}\, S_{\Delta p}(\omega), \tag{6.2}$$

which give

$$S_{\Delta p}(\omega) = \frac{4\pi^2 m^2 A}{S^2 \omega^2}. \tag{6.3}$$

This would account for a pressure fluctuation noise $S_{\Delta p}^{1/2} = 8.38 \times 10^{-12}\,\mathrm{Pa\,Hz^{-1/2}}$ at $f = 0.1\,\mathrm{mHz}$, undetectable from pressure readout in orbit.

Further on-ground experimental testing at torsion pendulum facilities are therefore needed to assess the extent of such possible low frequency excess noise source.

6.2 Gravitational noise from mass loss inside the SC

Gravitational noise due to mass loss occurring inside the spacecraft could arise from two different mechanisms:

- mass loss due to depletion of the cold-gas propellant tanks, which is going to be addressed in Section 6.2.1;
- mass loss from SC elements, detailed in Section 6.2.2.

6.2.1 Mass loss from depletion of propellant tanks

The gravitational noise arising from the mass depletion of the propellant tanks located on the spacecraft can be quantitatively assessed. LISA Pathfinder is equipped with four 8.3 L propellant tanks, distributed as in Figure 6.1a. Each of the four propellant tanks present on-board is not directly connected to the µN thrusters, but is piped to a plenum container of capacitance 0.75 L through a pressure transducer flow-meter valve, as depicted in Figure 6.1b.

The plenum container is in turn connected to the cold-gas thruster via another pressure transducer. The whole piping system is referred to as Feed-Branch (FB): tanks 1 and 2 correspond to feed branches FB1 and FB2, while tanks 3 and 4 belong both to FB3. An essentially constant drift is visible in in Δg due to depletion of the propellant tanks to the plenum containers,

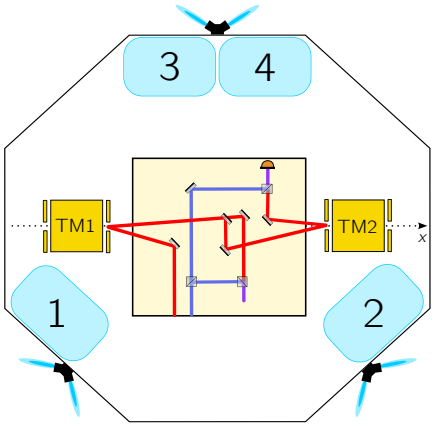

(a) Position of the propellant tanks on-board the spacecraft.

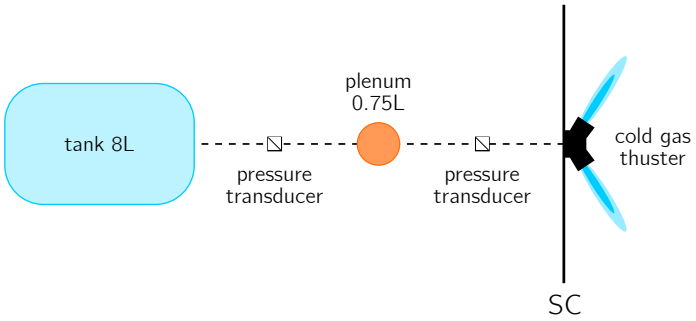

(b) Schematics of the tank to thruster piping system.

Figure 6.1: Schematics of the cold-gas propulsion system on-board LPF.

and amounts to $\sim 4 \times 10^{-18}\,\mathrm{m\,s^{-2}Hz^{-1/2}}$, compatibly with the propellant consumption rate of $\dot{m} = 10\,\mathrm{g\,d^{-1}}$.

If the gas feeding from the tank to the plenum occurs in random steps δm with a Poisson distribution, like for instance if the feeding valves are hysteretic, then the propellant mass, expelled from the tank with a Poisson rate $\lambda = \dot{m}/\delta m$ has a frequency spectrum given by

$$S_m(\omega) = \frac{2\lambda(\delta m)^2}{\omega^2}. \tag{6.4}$$

This can be converted into Δg noise via

$$S_{\Delta g}(\omega) = C_{\mathrm{grav}}^2\, S_m(\omega), \tag{6.5}$$

where $C_{\mathrm{grav}} = (G/r^2)$ is the transfer function from the EH mass m to differential acceleration Δg, with G gravitational constant and r is the distance from the TMs.

Table 6.1: Values of the gravitational coupling coefficient $C_{\rm grav}$ from mass noise fluctuations $S_m(f)$ to Δg noise $S_\Delta g$. Values are expressed in units of $\mathrm{pm\,s^{-2}\,kg^{-1}}$.

FB1	FB2	FB3
-41	-39	44
Plenum 1	Plenum 2	Plenum 3
-2	-65	19

Taking into account the excess noise expression (3.12), this gives, for the low frequency noise slope A,

$$2\pi A = 2\ C_{\rm grav}^2 \dot{m}\ \delta m, \tag{6.6}$$

which holds, for the deployed mass step,

$$\delta m = \frac{2\pi A}{2C_{\rm grav}^2 \dot{m}}. \tag{6.7}$$

Therefore, the amount of ejected mass δm causing a low frequency excess noise compatible with a f^{-2} behaviour can be estimated from the experimental evaluation of A for the twelve noise runs under consideration. The slope value used as a reference in what follows is the lowest A value obtained in the course of the best performance noise run #66 of February 2017.

The mass depletion mechanism from propellant tanks to plenums is characterized by a mass flow $\dot{m} = 10\,\mathrm{g\,d^{-1}} = 1.16 \times 10^{-7}\,\mathrm{kg\,s^{-1}}$ and by a gravitational coupling $C_{\rm grav}$ which is given by

$$C_{\rm grav} = C_{\rm grav}^{\rm FB} - C_{\rm grav}^{\rm plenum} \tag{6.8}$$

where the contributions $C_{\rm grav}$ for the tanks in the three FB and in three plenum containers are listed in Table 6.1.

Hence, to produce a noise spectrum compatible with the excess noise at low frequency observed in the twelve noise runs under analysis, the corresponding height of the depleted mass steps should be

$$\delta m \sim 2 \times 10^{-8}\,\mathrm{kg}, \tag{6.9}$$

with variations depending on the operating FB. The value for δm once inserted in the expression for the mass noise spectrum (6.4), holds

$$S_{\delta m}^{1/2}(f) = \frac{\sqrt{2\dot{m}\delta m}}{2\pi f} \simeq \frac{6 \times 10^{-8}\,\mathrm{kg\,s^{-1/2}}}{2\pi f}, \tag{6.10}$$

corresponding to $S_{\delta m}^{1/2} = 3 \times 10^{-4}\,\mathrm{kg\,Hz^{-1/2}}$ at $f = 0.1\,\mathrm{mHz}$.

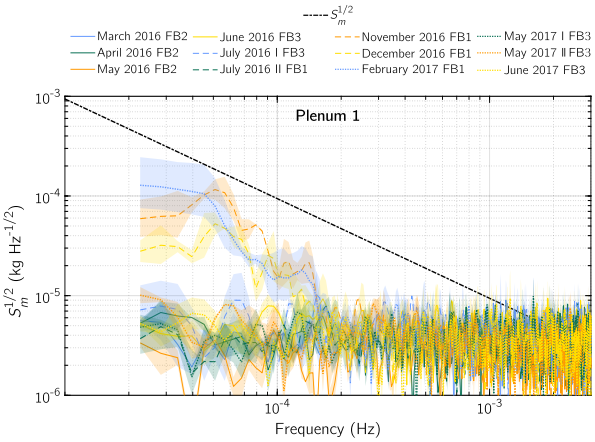

(a) $S_{\delta m}^{1/2}$ for plenum 1.

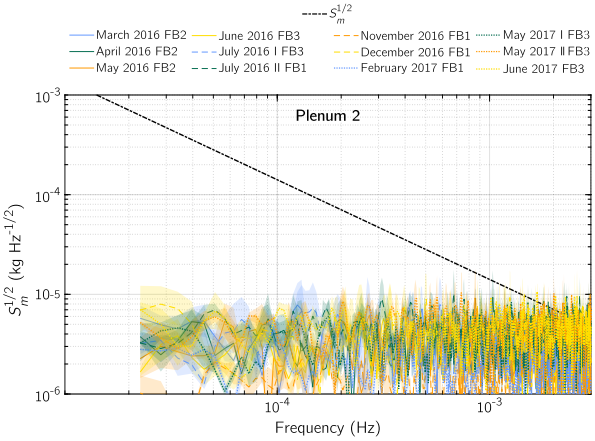

(b) $S_{\delta m}^{1/2}$ for plenum 2.

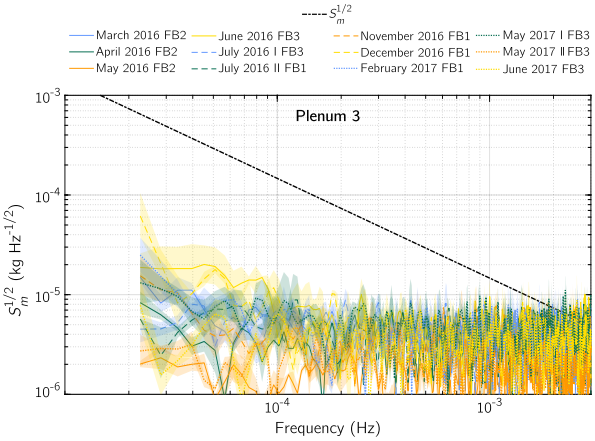

(c) $S_{\delta m}^{1/2}$ for plenum 3.

Figure 6.2: Mass depletion noise spectrum $S_m(f)$ from tanks to the plenum containers, for all noise runs under analysis. The predicted effect of $S_{\delta m}^{1/2}$ (6.10) is illustrated by the dash-dotted black line. (Mass depletion data courtesy of V. Ferroni)

The effect of (6.10) should then be detectable in the depleted mass spectrum $S_m^{1/2}$ of the plenum containers, derived from the pressure readout, as depicted by the dash-dotted line in Figure 6.2. In the plot, the expected behavior of (6.10) the depleted mass noise spectrum is pictured for the twelve noise runs under analysis: the noisier curves in Figures 6.2a and 6.2c represent the noise runs during which the corresponding FB was active.

An effect comparable to the one of (6.10) is visible only in Figure 6.2a, corresponding to the depleted mass spectrum of Plenum 1, active during the most quiet noise runs from the point of view of the excess power in the low frequency noise, ranging from July 2016 to February 2017.

The gravitational effect is negligible in the depleted mass spectra of the other two plenum containers, despite the excess power at low frequency is higher in the respective active noise runs. Moreover, the observed $S_{\delta m}$ does not seem to depend on the feed branch, even if the mass step δm strongly depends on the FB, due to (6.8). Hence, the gravitational noise from propellant tank depletion seems therefore to be unfeasible as low frequency noise source.

6.2.2 Mass leakage from SC elements

As stated in the introductory Chapter §2, LPF is continuously vented to space in order to reduce pressure Brownian noise.

Gravitational noise connected to mass loss may also arise from mass leakage of elements located on-board the spacecraft. SC are known to lose mass for years after launch, since outgassing does not decrease with constant rate, but instead reaches a minimum floor level [36].

If such mass loss is noisy, for instance with Poisson emission of small amount δm of mass due to isotropy, such effect may have very little impact on the low frequency drift of Δg, but would cause low frequency noise.

The mechanical elements from which a consistent percentage mass loss could generate gravitational noise that impacts the Δg measurement are again, the four propellant tanks located on-board and the vacuum housing cylinder. Mass leakage from the GRS is unlikely, but cannot be completely ruled out, and further experimental investigations are needed in order to establish outgassing requirements for the SC elements.

Let's then assume that these components uniformly released gas molecules in the course of the whole mission with a rate λ_m that follows Poisson statistics, and release a varying δm_i amount of gas, per each emission i. The calculation

can be simplified by assuming pores containing an identical mass fraction $\delta m_i \equiv \delta\overline{m}$, such that $\lambda_m = \dot{m}/\delta\overline{m}$.

The gravitational mass-loss noise spectrum for a single step would then amount to

$$S_{\delta\overline{m}}(\omega) = \frac{2(\delta\overline{m})\dot{m}}{\omega^2}. \tag{6.11}$$

Any mass loss model $\dot{m}$, in order to reproduce the slope A for the low frequency excess noise modeled by (3.12), should exist in a parameter space where δm is small and $\dot{m}$ is comparable to the observed mass loss in satellites, for each of the different mechanical elements.

Let us consider the case of uniform mass leakage of the propellant tanks, the quantitative estimation holds a firmer ground. The position of the four propellant tanks, depicted by Figure 6.1a, clarifies the gravitational force exerted on the TMs: tanks 1 and 2 apply a gravitational attraction on the TMs that pulls them apart with respect to the sensitive axis x, while tanks 3 and 4 apply a force on the opposite x direction, pushing the TMs closer.

In the hypothesis of a uniform mass loss occurring homogeneously from all three feed branches, the noise spectrum $S^{1/2}_{\delta\overline{m},j}$ from every FB j would sum incoherently and no net force effect would be visible in the TMs dynamics, giving rise only to incoherent gravitational noise.

The mass leakage from the fill-drain valve at the output of the tanks is $10^{-6}\mathrm{scc\,s^{-1}}$ for gaseous He, per each feed branch, corresponding to $\dot{m} = 3.3 \times 10^{-11}\,\mathrm{kg\,s^{-1}}$ for N cold gas[1].

In order to estimate again the mass leakage spectrum for each $j = 1, 2, 3$ feed branch $S^{1/2}_{\delta\overline{m},j}$, analogously to previous Section, the width of the mass loss steps $\delta\overline{m}$ is estimated via expression (6.7), with $C_{\mathrm{grav}} \equiv C^{\mathrm{tank}}_{\mathrm{grav}}$ of Table 6.1, obtaining $\delta\overline{m} \sim 4 \times 10^{-5}\,\mathrm{kg}$.

Therefore, the expected mass leakage spectrum $S^{1/2}_{\delta\overline{m},j}$ would be directly obtained by (6.11) and can be compared to the mass readout of each Feed Branch. The comparison is pictured in Figure 6.3 for the readout of Feed Branch 1, taken in all the twelve noise runs under analysis.

In the plot it is evident how $S^{1/2}_{\delta\overline{m},j}$ is not visible in the FB mass spectrum, due to the low sensitivity of the tank pressure readout. Therefore, despite the uniform mass leakage from propellant tanks is not considered likely as excess noise source, it is not possible to assess the entity of the phenomenon.

[1]Data courtesy of V. Ferroni, University of Trento

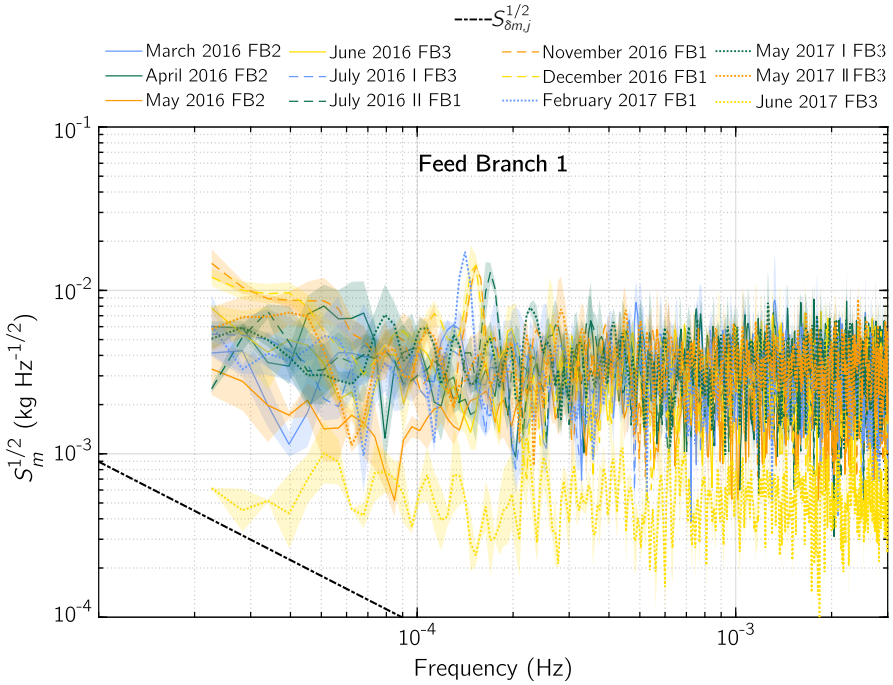

Figure 6.3: Mass loss spectrum of Feed Branch 1, compared to the expected mass leakage spectrum $S^{1/2}_{\delta\overline{m},j}$, depicted as a black dash-dotted line.(Courtesy of V. Ferroni)

6.3 Brownian noise from extra dissipation

The comparatively high stability of the observed noise may also point to some fundamental origin, like Brownian noise from some extra source of dissipation, beside that of gas viscous damping.

The fluctuation-dissipation theorem would predict an extra force PSD given by

$$S_F(\omega) = \frac{4k_{\mathrm{B}}T}{\omega}\mathrm{Im}\left\{\kappa(\omega)\right\} \tag{6.12}$$

where the stiffness $\kappa(\omega)$ has been defined as

$$\kappa(\omega) = \frac{f(\omega)}{x(\omega)}, \tag{6.13}$$

with f the force acting on TM whose coordinate is x.

Therefore, if the excess power in the low frequency noise

$$S_{\mathrm{lowfreq}}(\omega) = \frac{4\pi^2 A}{(2\pi f)^2} \equiv \frac{S_0\omega_0^2}{\omega^2} \tag{6.14}$$

is produced by a frequency dependent Brownian force, the following equality holds

$$\frac{4k_{\mathrm{B}}T}{\omega}\mathrm{Im}\left\{\kappa(\omega)\right\} = M^2 S_0 \frac{\omega_0^2}{\omega^2}. \tag{6.15}$$

The physical implication of the fluctuation dissipation theorem is therefore that the stiffness imaginary part responds to

$$\mathrm{Im}\left\{\kappa(\omega)\right\} = \frac{M^2 S_0 \omega_0^2}{4k_{\mathrm{B}}T}\ \frac{1}{\omega} \equiv \frac{\xi}{\omega}. \tag{6.16}$$

The value of ξ for the best performance noise run#66 of February 2017 is

$$\begin{aligned} \xi_{66} &= 7.9 \times 10^{-15}\,\mathrm{kg\,rad\,s^{-3}}, \\ \text{with confidence interval } &[6.8, 9.1] \times 10^{-15}\ \mathrm{kg\,rad\,s^{-3}}. \end{aligned} \tag{6.17}$$

Therefore, a low frequency noise of Brownian nature would be feasible in the eventuality of a inverse frequency dependence of the imaginary part of the stiffness

$$\mathrm{Im}\left\{\kappa(\omega)\right\} \propto \frac{1}{\omega}. \tag{6.18}$$

A few physical mechanisms that may produce such an imaginary stiffness are discussed below.

Just as an example, if the TM is gravitationally coupled to some movable mechanical part, modeled as a damped harmonic oscillator of coordinate x, the system would obey

$$M\ddot{X}(t) = -k_{\mathrm{c}}(X(t) - x(t)) + f(t), \tag{6.19}$$

$$m\ddot{x}(t) + \beta\dot{x}(t) + k_0 x = -k_{\mathrm{c}}(X(t) - x(t)), \tag{6.20}$$

where m is the oscillator mass, k_{c} is the gravitational gradient created by the TM at the location of the oscillator, β is the viscous damping coefficient and k_0 is the spring constant of the mechanical oscillator.

Solving equations (6.19)-(6.20) in the Fourier domain gives

$$\frac{f(\omega)}{X(\omega)} \equiv \kappa(\omega) = k_{\mathrm{c}} + M\omega^2 - \frac{k_{\mathrm{c}}^2}{-m\omega^2 + i\omega\beta + k_0 - k_{\mathrm{c}}}, \tag{6.21}$$

whose imaginary part is

$$\mathrm{Im}\left\{\kappa(\omega)\right\} = \frac{-k_{\mathrm{c}}^2\,(-\beta\omega)}{\left|-m\omega^2 + i\omega\beta + k_0 - k_{\mathrm{c}}\right|^2}. \tag{6.22}$$

or, by defining

$$\omega_0 = \frac{k_0 - k_{\mathrm{c}}}{m}, \tag{6.23}$$

$$\tau = \frac{m}{\beta}, \tag{6.24}$$

$$\mathrm{Im}\left\{\kappa(\omega)\right\} = \frac{k_\mathrm{c}^2}{m}\frac{\frac{\omega}{\tau}}{\left(\omega_0^2-\omega^2\right)^2+\frac{\omega^2}{\tau^2}}, \tag{6.25}$$

In the case of an overdamped oscillator, for which it holds

$$|\omega_0| \ll \left(\frac{1}{2\tau}\right)^2, \tag{6.26}$$

and re-writing in terms of the roots of (6.25) the imaginary stiffness can be rewritten as

$$\mathrm{Im}\left\{\kappa(\omega)\right\} = \frac{k_\mathrm{c}\frac{\omega}{\tau}}{m(\omega^2+\omega_+^2)(\omega^2+\omega_-^2)}. \tag{6.27}$$

Moreover, the over-damping condition (6.26) implies

$$\omega_+^2 \simeq \frac{1}{\tau^2} \tag{6.28}$$

$$\omega_-^2 \simeq (\omega_0^2\tau)^2 \ll \omega_+^2, \tag{6.29}$$

which, for angular frequency $|\omega_-| \ll \omega \ll |\omega_+|$ translates (6.27) into

$$\mathrm{Im}\left\{\kappa(\omega)\right\} \simeq \frac{k_\mathrm{c}^2\frac{\omega}{\tau}}{m\omega^2\omega_+^2} = \frac{k_\mathrm{c}^2\tau}{m}\frac{1}{\omega}. \tag{6.30}$$

Which would indeed reproduce the observed behaviour if one takes a system satisfying $\xi_{66} = \frac{k_\mathrm{c}^2\tau}{m}$.

Notice that this overdamped case may merge continuously into that of a virtually free particle subject only to viscous damping, with

$$k_\mathrm{c} = -\frac{2GMm}{r^3} \tag{6.31}$$

for a particle located at a distance $r = 10\,\mathrm{cm}$ a mass $m \simeq 0.14\,\mathrm{g}$, and a decaying time of the free particle $\tau \simeq 300\,\mathrm{s}$.

7 Physical origin of the glitches

The glitches manifested in the differential acceleration noise runs along the course of the whole mission, with definite statistical characteristics described in Chapter §5. Several hypotheses about the physical phenomena sourcing the glitches have been ruled out, allowing to focus on few other possible sources that are going to be analyzed in the following.

The glitches do not arise from the gravitational signal of something subject to mechanical relaxation, because no permanent change in force is associated to them. They neither are due to magnetic fields caused by electric transients, because those act on a much slower time-scale. They could arise from amplitude modulation of rapidly changing magnetic fields, but no evidence for this kind of phenomenon has been found in pre-launch on-ground measurements.

Varying electric fields cannot be excluded altogether, but their behavior is largely independent of the charge on the TM. Also, an electrostatically generated force should be generated uniformly on two electrodes located on the same TM side, since no torque is observed in association to the glitches.

The remaining hypotheses about their physical origin are experimentally untested at the time of the writing and may be further explored via on-ground torsion pendulum experiments, with the purpose of investigating the presence of possible sources of the glitches in the GRS apparatus in view of the LISA payload design.

In what follows, the viable physical sources are portrayed with reference to the statistical investigation of the previous Chapter 5. Any feasible common physical origin should be able to explain the two spurious events families, one-sided and two-sided, and also their non-periodic and intensity-varying nature. On the other hand, independent physical sources may be responsible for the different kind of glitches detected in the data.

7.1 One-sided glitches as outgassing phenomena

The glitch source that looks more looks more consistent with the experimental landscape in regard to one-sided events is that they are related to some kind of pressure phenomenon, in particular sudden outgassing events from the various parts that surround the TM. The pressure environment is dominated by outgassing, as is testified by the strong dependence of the pressure on the temperature observed in the Brownian noise data.

Moreover, the distributions Figure 5.14 shows how the continuous spectrum of the glitches duration corresponds to events with varying transferred impulse and peak amplitude. This suggests that the sourcing process for one-sided, high-duration and energetic signals could be a phenomenon that builds up in the proper environment: as if, during the T_0 noise runs, the very high rate of spurious events did not allow the process to build-up and release very long duration signals.

The elements that most likely contribute to desorption are the tungsten W gravitational compensation masses located just outside the Electrode Housing, and the molybdenum Mo EH itself.

By tackling the problem from a theoretical point of view, the single impulse transferred from a gas molecule impacting on the TMs is given by

$$I = 2mv_{\hat{n}}, \quad \text{with} \quad v = \sqrt{\frac{k_{\mathrm{B}}T}{m}}, \tag{7.1}$$

where v is the average Maxwellian velocity of a particle of mass m moving in an ideal gas and $v_{\hat{n}}$ is the velocity component normal to the impacting surface.

Let's take into consideration a water molecule, one of the most common desorbed gas species, with molar mass $M_{\mathrm{H_2O}} = 18\,\mathrm{g}$, mass $m_{\mathrm{H_2O}} = 2.99 \times 10^{-26}\,\mathrm{kg}$ and average ballistic velocity at ambient temperature given by $v = 368\,\mathrm{ms}^{-1}$. Assuming that, on average, the normal component of the velocity is 1/3 of the r.m.s. velocity $v_{\hat{n}} = v/3$ goes into the impact, the impulse transferred in a single direction by a single H_2O molecule is, on average, given by

$$I_{\mathrm{avg}} = 7.33 \times 10^{-12}\,\mathrm{kg\ pm\ s}^{-1}. \tag{7.2}$$

After the impact, the molecule will be re-emitted with a random direction and result into a series of subsequent multiple bounces between the TM and the EH inner walls, up until the molecule exits the EH cage via

To account for the total impulse transferred by one molecule, one needs to take into account the average number of impacts of on the TM face on a single direction n_{bounce}, which would then correspond to

$$I_{\mathrm{tot}} = n_{\mathrm{bounce}} 7.33 \times 10^{-12}\,\mathrm{kg\ pm\ s}^{-1} \tag{7.3}$$

which results in a total impulse per unit TM mass transferred by a single impacting molecule on a single direction given by

$$\Delta v_{\mathrm{tot}} = n_{\mathrm{bounce}} \frac{7.33 \times 10^{-12}\,\mathrm{kg\ pm\ s}^{-1}}{1.928\,\mathrm{kg}} = n_{\mathrm{bounce}}\ 3.80 \times 10^{-12}\,\mathrm{pm\ s}^{-1}, \tag{7.4}$$

This result implies that, to achieve the typical spurious signal transferred impulse of a few pms^{-1}, one would need about $10^{12}/n_{\mathrm{bounce}}$ water molecules entering the EH in a limited amount of time, presumably comparable with the time duration $\tau_1 + \tau_2$ of the spurious signal itself. This rough calculation supports the spontaneous gas desorption hypothesis, at least for the ambient-T noise runs.

A single molecule impacting on the TM would also exert a certain amount of torque $\mathcal{T}$ with every impact, according to

$$\boldsymbol{\mathcal{T}} = \boldsymbol{r} \times \boldsymbol{F}, \tag{7.5}$$

where $\boldsymbol{r}$ is the vector of coordinates of the point where the force $\boldsymbol{F}$ is applied on the TM by the gas molecule, with respect to a reference frame centered in the TM center.

The quantity of interest for our purposes is the transferred impulse per unit mass of the TM, which transforms (7.5) into

$$\boldsymbol{\mathcal{T}}\tau_{\mathrm{abs}} = \boldsymbol{r} \times (\boldsymbol{F}\tau_{\mathrm{abs}}) = \boldsymbol{r} \times \boldsymbol{I}, \tag{7.6}$$

where τ_{abs} is the action time of the force exerted by the gas molecule, which corresponds to the typical absorption and desorption time of a water molecule in a gold-platinum alloy TM. Expression can be reshuffled by taking the vector norm

$$\mathcal{T}\tau_{\mathrm{abs}} = rI\sin\alpha = bI \tag{7.7}$$

where α is the angle between the position and applied impulse vector and $b = r\sin\alpha$ is the lever arm of the applied force.

If the lever arm of the transferred impulse is a quantity compatible with zero, the impact of gas molecules entering the EH from the center of the x laser holes do not transfer any appreciable torque to the TMs, being compatible with what has been observed for glitches in LPF. Since this hypothesis couldn't be tested through dedicated experiments located on board the SC, computational simulations were performed based on previous torsion pendulum studies [37].

The simulation takes into account a single gas molecule ejected from a generic point in space located outside the EH, entering it from the holes located on the x-axis. After entering the EH, the molecule starts a series of impacts between the TM and the housing walls, until it escapes the EH from one of EH holes.

In the simulation, the interaction among particles has been neglected, assuming the particles to be uncorrelated, and the gas molecules are considered

to interact independently with the TM and EH. The average effect of a single molecule is then obtained by repeating the simulation an arbitrary number of times n and averaging all the possible outcomes.

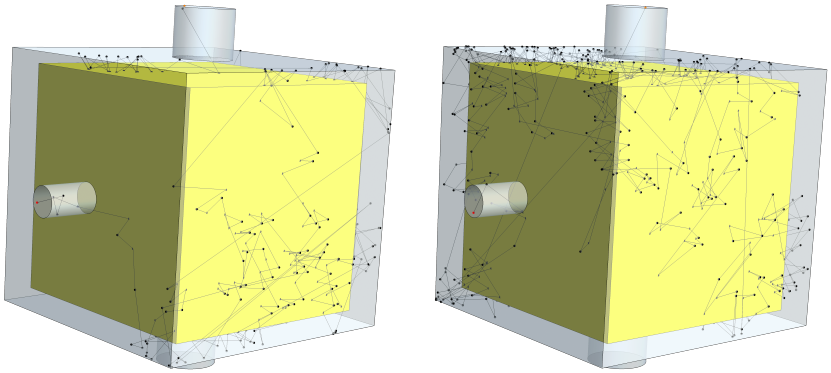

Figure 7.1: Views of the simulated molecule impacts between the TM (yellow) and the EH walls (semi-transparent, gray box). The molecule enters the EH from the x-axis hole (red dot), while the exit point is the z-axis upper hole for both simulations (orange dot).

A 3-dimensional view of two single molecule simulations, with their respective path, is illustrated in Figure 7.1. The parameters obtained from simulations are summarized in Table 7.1, by modeling $n_{\text{tot}} = 1550$ molecules generated at the $-x$ hole. The fraction of molecules successfully entering the EH from the hole on the $-x$ face is 338/1550, and the result is obtained by averaging the result among all the molecules impacting the TM x faces.

Table 7.1: Simulation parameters obtained by simulating $n_{\text{tot}} = 1550$ molecules. Δt is the average time between successive impacts, Δv_{avg} is the average impulse per unit mass of the TM transferred by the single molecule and b is the lever arm of the force applied by the impact of a single gas molecule on the TM x faces.

Δt (s)	Δv_{tot} (pm s^{-1})	n_{bounce}	b (m)
0.0014	$(1.30 \pm 0.18) \times 10^{-10}$	40	0.0 ± 0.1

The mean number of simulated impacts on the x TM faces is $\overline{n}_{\text{bounce}} = 40$, giving for the expected value of Δv_{tot} in (7.4)

$$\Delta v_{\text{tot}} = 1.52 \times 10^{-10}\,\text{pm s}^{-1}, \tag{7.8}$$

which is compatible with the value of Table 7.1 obtained from the simulation.

The impulse per unit mass Δv transferred by the sum in absolute value of all glitches detected during the mission, both in ordinary and cold T_0 noise runs, amounts to

$$\Delta v_{\text{all}} = 3.3\,\text{nm s}^{-1}, \tag{7.9}$$

which, by taking into account the estimated value of impulse per unit mass transferred by a H_2O molecule entering the EH (7.8), would amount to about $N_{\text{all}} = 2 \times 10^{13}$ H_2O molecules transferring impulse, corresponding to a fraction of ng of water.

The sharp increase in the spurious event rate during the cool-down to T_0 noise runs could be explained in the same outgassing framework, by referring to virtual leaks, that is, sources of gas trapped inside a pocket in a physical element of the apparatus.

Virtual leaks release occur when a mechanical stress acts on the low conductance gas pocket, causing the spontaneous emission of vapour in vacuum systems, otherwise clean and tested for presence of other leaks. Their opening could then be compatible with the modification of the working conditions of the LTP during the temperature drop to T_0.

One of the leading hypothesis about the outgassing source is the desorption from mechanical elements located inside the GRS, which is schematized in Figure 7.2, where its horizontal section is depicted with some of its main components: the TM is located inside the EH, which is in turn encapsulated inside the so-called *yellow structure*. On the right-hand side of the picture, the optical window allows the laser beam to reach the OBI and the other TM, while on the left-hand side of it is depicted the W/Cu compensation mass.

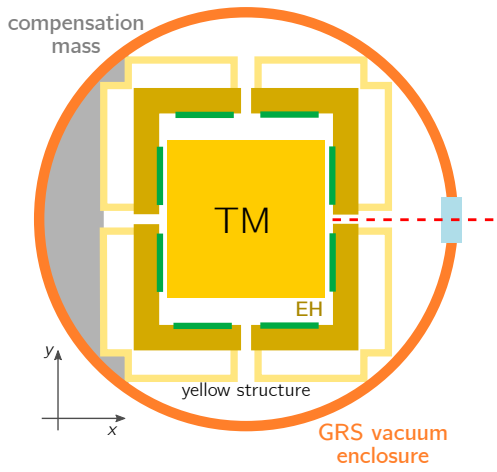

Figure 7.2: Schematic depiction of the GRS horizontal section on the x-y plane. The TM is enclosed by the EH housing (gold box with green electrodes), which is in turn encapsulated inside the *yellow structure* (light yellow). From the gaps on the right-hand side of the EH, the laser beam to reach the OBI and the other TM, while on the left-hand side of it is depicted the W/Cu compensation mass. The orange circle represents the view from above of the GRS vacuum enclosure.

As it is evident from the scheme, desorption of gas from elements inside the GRS vacuum enclosure, such as the molybdenum Electrode Housing or the tungsten gravitational compensation masses, would impact the TM dynamics. Desorption from the Mo EH would release gas directly inside the gaps between the TM and the EH itself, while desorption from the W/Cu compensation mass would release gas both through the $-x$-axis hole (impacting directly on the TM, and in the rest of the vacuum enclosure, possibly entering the EH from holes in other dimensions.

Gaseous desorption from Mo and W/Cu would arise from pre-existing pores inside the materials, created during the production process and containing gas molecule of various species. The pores should then release an amount of gas sufficient to impress on the TM a force per unit mass comparable to the observed glitches. Moreover, the existing pores pores could have varying volume and contain different species and number of gas molecules.

In order to understand this, samples from the EH molybdenum cage (without the Au coating) and the gravitational compensation mass W/Cu 90/10 alloy have been analyzed by the Metallurgy and Micro-structure Laboratory of the Industrial Engineering Department at University of Trento[1], using the Scanning Electron Microscope (SEM).

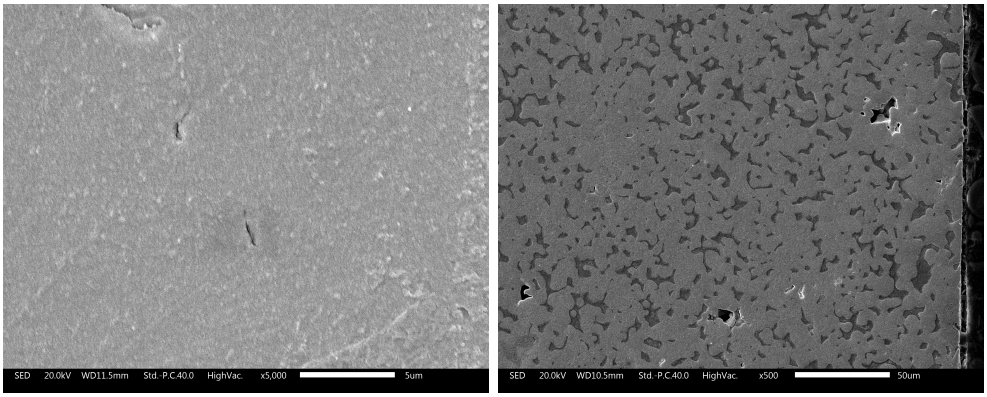

(a) Mo sample from the gravitational compensation masses. Scale is 10 µm.

(b) W/Cu sample from the gravitational compensation masses. Scale is 50 µm.

Figure 7.3: SEM observation scans.

For what concerns the Mo scans, pictured in Figure 7.3a, no pores are visible in the sample. The presence of pores smaller than the available SEM

[1]Laboratorio di Metallurgia e Microstrutture del Dipartimento di Ingegneria dei Materiali, lead by Prof. Alberto Molinari.

resolution cannot be excluded, but if present, they would be closed by the gold-platinum coating of the EH.

The W/Cu sample SEM scans are depicted in Figure 7.3b: heavy elements (W) are represented by light shades of gray, lighter materials (Cu) are pictured as dark gray patches, while black spots represent pores of the sample.

In the compensation mass sample there are pores with diameter of $\sim 5 \div 10\,\mu m$ diameter, which don't appear to be interconnected. A few pores have also been detected close to the original surface of the sample.

Thus, the gravitational compensation mass could give rise to outgassing phenomena compatible with the observed glitches, implying that some production requirements should be established not only for gravitational compensation masses, but for all elements located inside the GRS. A quick-fix solution for the gravitational compensation mass could also be a thick metal coating layer to fill pores.

Further analysis regarding outgassing phenomena are under design at the torsion pendulum facility in the Experimental Gravitation Laboratory at the University of Trento, in order to understand if glitches are detectable during on-ground experimental campaigns.

7.2 Two-sided glitches

As anticipated at the beginning of this Part, the possible sources for two-sided glitches are different and depend on their respective fitting function.

The rare occurrences of two-sided glitches with a temporal structure, that is, the six events fitted with $h_{\mathrm{A}}(t)$ (5.7) and listed in Table 5.4, are the only ones transferring impulse to the TMs.

Because of their complex structure, this type of two-sided signals could originate from outgassing phenomena, just like the one-sided events. Various possible outgassing configurations can produce these glitches as an outcome, and further modeling and simulations are needed to extrapolate more information regarding them.

Instantaneous two-sided glitches fitted with Dirac's delta derivative model $\delta'_h(t)$(5.6) are the most numerous two-sided signals, both in the ordinary and cold T_0 noise runs.

Since δ'-like glitches do not transfer any impulse to the TMs, they may be the result of sources not connected to pressure or force phenomena. Furthermore, being $\delta'_h(t)$ the second derivative of a step of amplitude Δx in the $x_{12}(t)$

time-series, an alternative explanation might be the presence of undetectable steps in $x_{12}(t)$ caused by laser path-length fluctuations.

The step amplitude Δx of the two-sided δ'-like is listed for all events in Table D.3, and spans between 1 pm and 1 pm for ordinary runs, and between 1 pm and 1 pm for cold T_0 runs. Such steps may be connected to laser path-length modifications caused by mechanical deformations of the Zerodur optical bench of which there are no on-board measurements.

This hypothesis would also be coherent with the increase in the rate of two-sided δ'-like signals during the cool-down to T_0 (Table 5.3): they increased from a total number of 6 glitches in all the ordinary runs to events per day in the cold noise runs, compatibly with the mechanical distortion of the elements on the SC caused by the change in operating conditions.

8 Conclusions

In this work I reviewed the experimental results LISA Pathfinder space mission, which flew between December 3rd, 2015 and July 18th, 2017, and discussed the experimental results obtained in the past years.

The first and foremost aspect is the impressive amount of science that has been realized thanks to this mission: for starter, the LISA technological test assessed geodesic motion between free-falling test bodies with a precision better than any past or planned mission apart for LISA and allowed to develop partially original techniques to analyze data. Furthermore, LPF data were used to establish the LISA noise requirements [3, 33] and played a role of primary importance in the LISA mission approval.

In the course of the 18 months of operations, a few noise sources with direct impact on the LISA performance were discovered: the excess power at the low frequency with respect to the modeled noise performance $S_{\Delta g}^{1/2}$, and the presence of spurious force signals, that we call glitches, in the differential acceleration data $\Delta g(t)$. The physical origin of these noise features is of unclear nature, and they have been investigated thoroughly to reduce the number of their possible interpretations.

For both phenomena a few hypotheses have been developed, and their theoretical modeling has been equipped with simulations in order to provide a complete explanation of the process.

On one hand, one of the most likely sources for excess noise at low frequency are be the presence of random outgassing phenomena, giving rise to pressure fluctuations impacting on the TM motion. The assessment of this noise source need though a campaign of dedicated on-ground experiments, in order to assess the presence of such phenomenon.

On the other hand, the stability of the Brownian noise along the course of the mission, up to the engineering maneuvers of April and May 2017, would be consistent with frequency-dependent Brownian noise caused by coupling to a damped mechanical system giving rise to dissipation.

This kind of phenomenon would also be in agreement with the change in the excess behavior observed in the last three noise runs under analysis, after the mechanical distortion caused by the change in operating conditions on-board LPF. In particular, the model of a viscous damped free particle modeled in lays a basis for the investigation of such gravitational coupling model, although not yet providing a physical explanation for the observed excess noise values.

For what concerns the occurrence of uncorrelated, non-periodic, Poisson-distributed glitches in $\Delta g(t)$ data, I have discussed the possibility that their source is a pressure phenomenon due to outgassing phenomena occurring on-board the spacecraft. Being the GRS continuously vented to outer space, any residual gas should be pumped outside of the vacuum enclosure: but other space missions, like Rosetta [36], showed how the outgassing from mechanical elements inside spacecrafts can go on for a long time, even in high vacuum conditions.

Furthermore, SEM observations have established the presence of pores with a diameter of a few µm within the tungsten W gravitational compensation masses, located just outside the EH, inside the GRS vacuum enclosure.

Since the compensation masses are located on EH side opposite to the OBI, this would be compatible with the higher incidence of positive impulse glitches, pushing the TMs closer, with respect to the negative impulse ones, furthering the TMs: as depicted in Figure 7.2 there is a higher probability that gas molecules freed from the compensation mass would enter the EH from the laser hole opposite to the laser beam and the optical window.

The gaseous desorption hypothesis is supported by simulations performed on the TMs dynamics and, once an appropriate model is provided, could also explain the rare occurrence of two-sided signals with time-extended structure.

This thesis work therefore consolidates the experimental framework of LISA Pathfinder, by quantitatively estimating the hypotheses about the noise feature of unclear nature, in order to minimize the number of possible interpretations of these phenomena.

In order to determine the exact nature of the noise features it is necessary to increase the information with a campaign of dedicated on-ground experiments: the only feasible facilities to perform such investigation are the torsion pendulum laboratories, especially for what concerns outgassing phenomena. Hence, the LISA Collaboration is designing experiments to test assumptions and physical models of the sources of glitches and excess noise at low frequency, which, once established, can be translated into requirements for the parameters relevant to LISA.

Appendixes

A Spectral estimation with minimum correlation frequency selection and Bayesian error estimate

In the course of LPF operations the long time-series measurements allowed to cover an extended frequency range, making the development of an adapted spectral estimation technique of paramount importance for data-analysis purposes, with respect to the Weighted Overlapping Segments Average (WOSA) estimate method [29].

The WOSA method for the spectrum estimation is pictorially illustrated in Figure A.1 and consists in the following steps:

1. splitting data in 50% overlapping segments, over all the duration of the noise run;

2. applying a Blackman-Harris window to the data in each segment, to avoid spectrum leakage;

3. performing the Discrete Fourier Transform of each windowed overlapping segment;

4. averaging the spectra obtained separately for the single segments.

Starting from the WOSA method and from previous works [38, 39] this adapted technique takes into consideration both an adjusted frequency resolution and better averaging of the spectrum at the chosen frequencies. This is achieved with minimum-correlation frequency bins equally spaced in the logarithmic space, each accounting for an increasing number of averaging windows in the ASD coefficients estimate.

In addition to the low correlation among frequencies, the method performs the estimate of errors on the ASD coefficients using Bayesian estimation, perfecting the low-frequency error estimation that does not follow the Gaussian statistics.

The minimum-correlation frequencies for spectrum estimation are calculated recursively from the fundamental frequency, initially set to

$$f_0 = \frac{M}{N_{\max}\Delta T}, \tag{A.1}$$

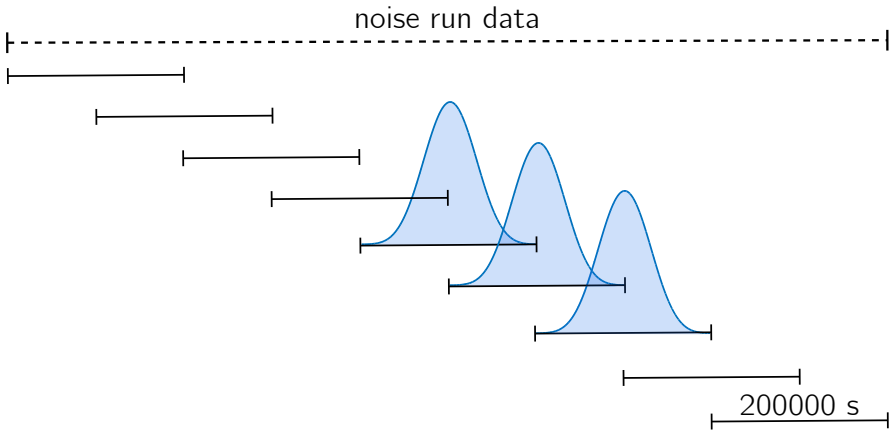

Figure A.1: Schematic depiction of the WOSA method for PSD estimation: a time-series is split in 50% overlapping segments, to whom a Blackman-Harris window is applied in order to avoid spectrum leakage. Then, every windowed segment is Discrete Fourier Transformed, in order to evaluate its noise spectrum. The final spectrum is obtained via averaging the value obtained on all averaging segments.

where $N_{\max}$ is the length of the first averaging window, ΔT is the sampling time of the data, and M is the spacing between frequency bins that allows to avoid spectral leakage from the averaging window among neighboring frequencies.

For a Blackman-Harris window, uncorrelation is obtained by spacing frequencies of a factor $M = 8$, reducible to $M = 4$ without sacrificing too much the coefficients mutual independence [38]. Here the choice was to select $M = 4$ for the fundamental frequency f_0, while a more conservative spacing $M = 8$ was adopted for f_j $(j \geq 1)$.

Higher frequencies values are obtained by progressively reducing the length of each averaging segment following $N_{\max}$ to maintain the same level of uncorrelation between two neighboring frequency bins, with a scaling factor

$$\frac{M - \alpha}{M + \alpha} = \frac{3}{5} \tag{A.2}$$

where $\alpha = 2$ is a numerical factor needed to preserve the uncorrelation among PSD coefficients with a frequency spacing of $\Delta f = 2\alpha\Delta f_0$.

The frequency selection recursive law for $j > 1$ reads

$$f_j = \frac{5}{3} f_{j-1} = \frac{2M}{(3/5)^{(j-1)} N_{\max} \Delta T}, \tag{A.3}$$

by taking into account that the first non-fundamental frequency is given by $f_1 = 2f_0$. Once the minimum-correlation frequency bins have been selected, the ASD estimation is performed at each frequency f_j by progressively reducing the

length $N_j = (3/5)^{(j-1)} N_{\max}$ of the averaging periodograms $N_{\rm w}$ and increasing their number.

The algorithm is graphically described in Figure A.2, where the minimum correlation frequency selection is presented together with the reducing length of averaging periodograms and their increasing number with respect to the same original time-series.

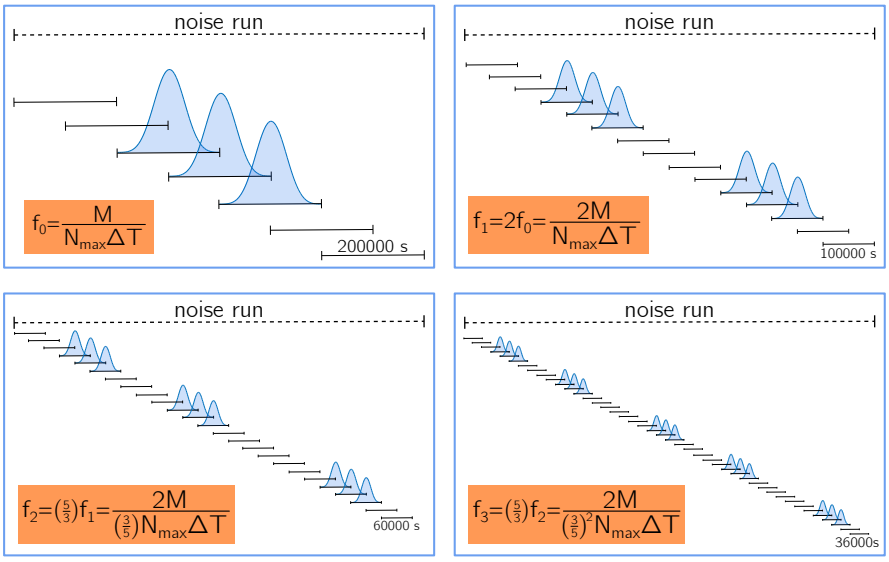

Figure A.2: Minimum correlation frequency selection for frequencies $f_{0,1,2,3}$. As the frequency increases, the number of averaging periodograms also does, progressively reducing their length according to the law (A.3).

Assuming Gaussian noise data the ratio between the experimental power spectrum data X_i (for each periodogram $i = 1, \ldots, N_{\rm w}$) and the theoretical value for the PSD S is a quantity distributed like a χ-square with 2 degrees of freedom

$$\chi^2_k[j] = \frac{2X_i[j]}{S[j]}, \tag{A.4}$$

with probability density function for X_i

$$f_{(X_i[j]|S[j])} = \frac{e^{-2\sum_i^N \frac{X_i[j]}{S[j]}}}{S[j]^N}. \tag{A.5}$$

By applying Bayes theorem,

$$P(X_{i=1,\ldots,N}|S[j]) = \frac{P(S[j]|X_i[j])P(S[j])}{P(X_i[j])}, \tag{A.6}$$

where we assume that the theoretical $S[j]$ prior is flat between 0 and a value much higher of the distribution $P(X_i[j]|S[j])$, nominally ∞. Then, the posterior

probability of obtaining the theoretical value $S[j]$ conditioned to the entire set of experimental data $\{X_i[j]\}$ $(i = 1, \ldots, N_\mathrm{w})$ is

$$f_{S[j]|\{X_i[j]\}}[Z] = \frac{\frac{\exp\left[-\frac{N_\mathrm{w} X_i[j]}{Z}\right]}{Z^{N_\mathrm{w}}}}{\int_0^\infty \frac{\exp\left[-\frac{N_\mathrm{w} X_i[j]}{Z}\right]}{Z^{N_\mathrm{w}}} \mathrm{d}Z}, \tag{A.7}$$

whose cumulative distribution function (CDF) is found to have an analytical expression given by

$$\begin{aligned} \mathrm{CDF}_{S[j]|\{X_i[j]\}} &= \frac{\int_0^X \frac{\exp\left[-\frac{N_\mathrm{w} X_i[j]}{Z}\right]}{Z^{N_\mathrm{w}}} \mathrm{d}Z}{\int_0^\infty \frac{\exp\left[-\frac{N_\mathrm{w} X_i[j]}{Z}\right]}{Z^{N_\mathrm{w}}} \mathrm{d}Z} \\ &= \Gamma_\mathrm{reg}\left(N_\mathrm{w} - 1, \frac{N_\mathrm{w}\overline{X}}{S}\right). \end{aligned} \tag{A.8}$$

The standard estimation of Gaussian relative error underestimates the lower and upper limits of the power spectrum when the number of averaging periodograms N_w is small, as it occurs for the lowest frequency bins. The CDF obtained via (A.8) allows to improve the estimation of S_min and S_max, assuming a confidence level c:

$$S_\mathrm{max}[j] = \frac{N_\mathrm{w} X_i[j]}{\Gamma^{-1}_\mathrm{reg}\left(N_\mathrm{w} - 1, \frac{1+c}{2}\right)}, \tag{A.9}$$

$$S_\mathrm{min}[j] = \frac{N_\mathrm{w} X_i[j]}{\Gamma^{-1}_\mathrm{reg}\left(N_\mathrm{w} - 1, \frac{1-c}{2}\right)}. \tag{A.10}$$

A sample noise spectrum estimated via the technique illustrated here, is depicted in Figure A.3, where every frequency f_j has been selected via the minimum correlation algorithm and every point represents an ASD value $S[j]$ with upper and lower bounds given by $S_\mathrm{max}[j]$ and $S_\mathrm{min}[j]$, with confidence level $c = 0.6827$.

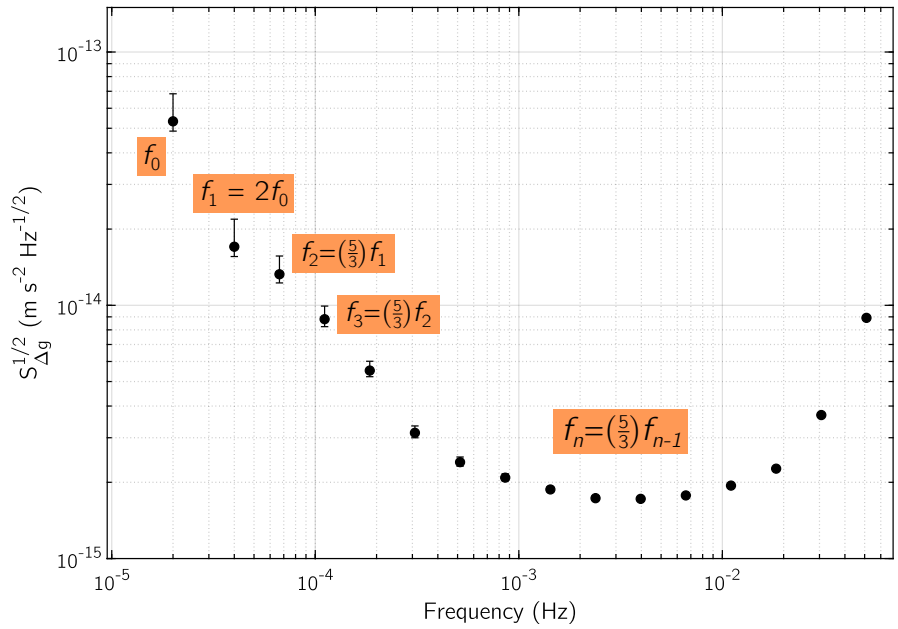

Figure A.3: Spectrum of the best performance noise run #66 of February 2017 evaluated using the Bayesian estimation algorithm illustrated in this section.

A.1 Low frequency excess noise

The low frequency excess noise can be modeled by the simplified model of (3.12), with the assumption that data are Gaussian and the excess noise $S_{\rm lowfreq}(f_j)$ is uniformly distributed between two values $S_{j,\rm min} \leq S_{\rm lowfreq}(f_j) \leq S_{j,\rm max}$ for any selected frequency bin f_j.

Analogously with the considerations about the minimum correlation selection of frequencies, we assume that for different frequency bins f_j, f_l, with $j \neq l$, the excess value $S_k(f_j)$ is independent of $S_k(f_l)$.

The Brownian noise level $S_{{\rm B},k}$ is evaluated separately for each run k, by averaging the spectrum over a frequency interval $f_0 < f_j \leq f_1$, wherein the noise looks frequency independent. We thus limit the fit to values $f_j \leq f_0$, with $f_0 \simeq 1\,$mHz.

The posterior probability density of the excess noise $S_{\rm lowfreq}(f_j)$ for a noise run k and a frequency bin f_j is given by

$$f_{S_{\rm exc}(f_j)}[X] = \frac{\prod_{k=1}^{N_{\rm w}} \frac{\exp\left[-\frac{S_k(f_j)}{S_{{\rm B},k}+X}\right]}{S_{{\rm B},k}+X}}{\int_{S_{j,\rm min}}^{S_{j,\rm max}} \prod_{k=1}^{N_{\rm w}} \frac{\exp\left[-\frac{S_k(f_j)}{S_{{\rm B},k}+X}\right]}{S_{{\rm B},k}+X} {\rm d}X}, \tag{A.11}$$

which holds for $S_{j,\rm min} \leq X \leq S_{j,\rm max}$, while elsewhere is $P_{S_{\rm exc}(f_j)} = 0$.

Here the quantity $\chi^2_{f_j} = \frac{2S_k(f_j)}{S_{\mathrm{B},k}+S_{\mathrm{exc}}(f_j)}$ is distributed like a chi-square with 2 degrees of freedom, as in the case of the PSD estimation discussed in the previous section §A.

The estimation of the upper and lower confidence intervals, $S_{j,\mathrm{min}}$ and $S_{j,\mathrm{max}}$, follows the same mechanisms of the previous section and is therefore numerically searched as

$$\int_0^{S_j,\mathrm{min}} P_{S_{\mathrm{exc}}(f_j)}(X)\mathrm{d}X \leq 1 - \frac{c}{2} \tag{A.12}$$

$$\left(1 - \int_0^{S_j,\mathrm{max}} P_{S_{\mathrm{lowfreq}}(f_j)}(X)\mathrm{d}X\right) \leq 1 - \frac{c}{2}, \tag{A.13}$$

where c is the confidence level.

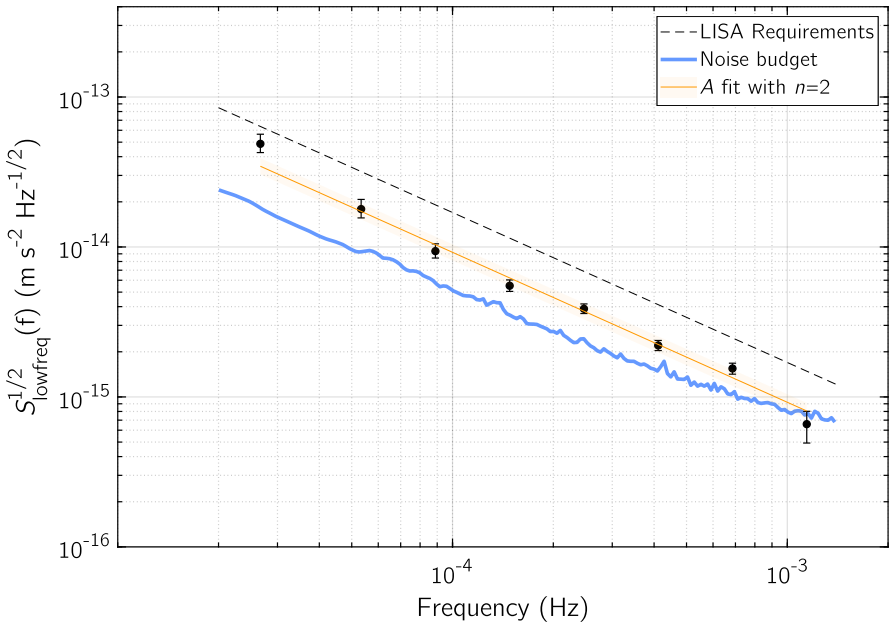

Figure A.4: Evaluation of the low frequency excess noise $S_{\mathrm{lowfreq}}(f_j)$ via marginalization of the Brownian noise $S_{\mathrm{B},k}$.

B List of all differential acceleration noise runs

Table B.1: All noise runs detected in the course of operations

#	Start	Stop	Actuation
1	2016-03-01 08:05:00 UTC	2016-03-03 08:00:00 UTC	NOM
2	2016-03-03 09:00:00 UTC	2016-03-05 08:00:00 UTC	RED
3	2016-03-06 18:15:00 UTC	2016-03-11 07:59:46 UTC	RED
4	2016-03-13 16:30:00 UTC	2016-03-15 07:00:00 UTC	RLA
5	2016-03-16 20:00:00 UTC	2016-03-19 07:59:47 UTC	RLA
6	2016-03-20 18:00:00 UTC	2016-03-26 07:59:45 UTC	URLA
7	2016-03-27 14:00:00 UTC	2016-03-31 07:00:00 UTC	RLA
8	2016-03-31 07:02:00 UTC	2016-04-02 08:00:00 UTC	RED
9	2016-04-03 15:00:00 UTC	2016-04-16 07:30:00 UTC	UURLA
10	2016-04-17 20:40:00 UTC	2016-04-19 07:00:00 UTC	UURLA
11	2016-04-19 07:10:00 UTC	2016-04-23 06:30:00 UTC	RLA
12	2016-04-26 08:00:00 UTC	2016-04-30 08:00:00 UTC	UURLA
13	2016-05-01 08:05:00 UTC	2016-05-02 23:55:00 UTC	UURLA
14	2016-05-03 04:20:00 UTC	2016-05-05 15:30:00 UTC	UURLA
15	2016-05-12 22:55:00 UTC	2016-05-13 07:30:00 UTC	NOM
16	2016-05-13 07:40:00 UTC	2016-05-14 08:00:00 UTC	UURLA
17	2016-05-16 00:00:00 UTC	2016-05-19 08:00:00 UTC	UURLA
18	2016-05-19 08:30:00 UTC	2016-05-21 11:00:00 UTC	NOM
19	2016-05-21 12:30:00 UTC	2016-05-23 14:00:00 UTC	BIG
20	2016-05-23 14:02:00 UTC	2016-05-25 16:44:00 UTC	BIGPlus
21	2016-05-25 20:00:00 UTC	2016-05-28 08:00:00 UTC	RLA
22	2016-05-30 00:10:00 UTC	2016-05-31 12:30:00 UTC	UURLA
23	2016-05-31 20:00:00 UTC	2016-06-01 16:00:00 UTC	UURLA
24	2016-06-01 16:10:00 UTC	2016-06-02 07:00:00 UTC	RLA
25	2016-06-02 07:30:00 UTC	2016-06-03 07:30:00 UTC	NOM
26	2016-06-03 08:00:00 UTC	2016-06-04 16:30:00 UTC	NOM
27	2016-06-04 17:00:00 UTC	2016-06-05 01:00:00 UTC	NOM

Continued on next page

#	Start	Stop	Actuation
28	2016-06-05 03:00:00 UTC	2016-06-05 11:00:00 UTC	BIG
29	2016-06-05 11:30:00 UTC	2016-06-05 19:30:00 UTC	BIGPlus
30	2016-06-05 22:30:00 UTC	2016-06-06 06:30:00 UTC	LargePhi
31	2016-06-06 07:00:00 UTC	2016-06-09 08:00:00 UTC	UURLA
32	2016-06-10 07:37:00 UTC	2016-06-11 07:55:00 UTC	UURLA
33	2016-06-13 00:00:00 UTC	2016-06-13 04:00:00 UTC	UURLA
34	2016-06-13 04:30:00 UTC	2016-06-14 21:30:00 UTC	UURLA
35	2016-06-14 22:00:00 UTC	2016-06-15 10:00:00 UTC	RLA
36	2016-06-15 10:04:00 UTC	2016-06-15 13:04:00 UTC	RLA
37	2016-06-15 13:30:00 UTC	2016-06-18 08:00:00 UTC	UURLA
38	2016-06-18 08:30:00 UTC	2016-06-19 07:00:00 UTC	NOM
39	2016-06-19 11:00:00 UTC	2016-06-25 08:00:00 UTC	UURLA
40	2016-07-10 08:00:00 UTC	2016-07-11 09:55:00 UTC	UURLA
41	2016-07-11 11:40:00 UTC	2016-07-12 09:55:00 UTC	UURLA
42	2016-07-17 12:00:00 UTC	2016-07-20 06:00:00 UTC	UURLA
43	2016-07-24 07:40:00 UTC	2016-07-30 00:00:00 UTC	UURLA
44	2016-07-31 10:10:00 UTC	2016-08-02 06:00:00 UTC	UURLA
45	2016-08-07 07:45:00 UTC	2016-08-08 04:20:00 UTC	UURLA
46	2016-08-12 11:30:00 UTC	2016-08-13 08:00:00 UTC	DURLA
47	2016-08-16 13:15:00 UTC	2016-08-20 05:45:00 UTC	DURLA
48	2016-08-23 14:00:00 UTC	2016-08-27 20:00:00 UTC	DURLA
49	2016-09-05 11:35:00 UTC	2016-09-06 05:05:00 UTC	DURLA
50	2016-09-07 03:09:07 UTC	2016-09-07 04:50:00 UTC	NOM
51	2016-09-11 21:15:00 UTC	2016-09-16 05:15:00 UTC	DURLA
52	2016-09-16 18:36:54 UTC	2016-09-17 08:00:40 UTC	DURLA
53	2016-09-19 01:30:00 UTC	2016-09-22 06:00:00 UTC	UURLA
54	2016-09-28 13:35:00 UTC	2016-10-01 08:00:00 UTC	UURLA
55	2016-10-04 00:00:00 UTC	2016-10-05 07:10:52 UTC	DURLA
56	2016-10-05 17:30:00 UTC	2016-10-08 07:55:00 UTC	UURLA
57	2016-10-21 11:30:00 UTC	2016-10-21 16:39:00 UTC	DURLA
58	2016-11-07 14:20:00 UTC	2016-11-12 08:00:00 UTC	UURLA
59	2016-11-13 21:00:00 UTC	2016-11-26 08:00:00 UTC	UURLA

Continued on next page

#	Start	Stop	Actuation
60	2016-12-02 23:35:00 UTC	2016-12-04 16:35:00 UTC	DURLA
61	2016-12-26 03:30:00 UTC	2017-01-13 19:58:00 UTC	UURLA
62	2017-01-18 15:00:00 UTC	2017-01-20 23:55:00 UTC	UURLA
63	2017-01-27 11:02:00 UTC	2017-01-28 08:00:00 UTC	UURLA
64	2017-02-02 07:00:00 UTC	2017-02-02 20:20:00 UTC	UURLA
65	2017-02-08 23:06:00 UTC	2017-02-11 00:00:00 UTC	UURLA
66	2017-02-13 08:00:00 UTC	2017-03-03 22:00:00 UTC	UURLA
67	2017-03-09 19:20:00 UTC	2017-03-14 09:40:00 UTC	UURLA
68	2017-03-14 09:00:00 UTC	2017-03-17 00:30:00 UTC	UURLA
69	2017-04-21 14:15:00 UTC	2017-04-24 07:45:00 UTC	DURLA
70	2017-04-29 17:35:18 UTC	2017-05-03 19:16:20 UTC	UURLA
71	2017-05-03 19:16:20 UTC	2017-05-09 14:45:00 UTC	UURLA
72	2017-05-10 11:11:20 UTC	2017-05-12 12:02:07 UTC	UURLA
73	2017-05-12 12:02:07 UTC	2017-05-15 08:00:59 UTC	UURLA
74	2017-05-18 18:24:46 UTC	2017-05-23 02:00:00 UTC	UURLA
75	2017-05-28 13:41:00 UTC	2017-06-05 15:04:40 UTC	UURLA
76	2017-06-06 20:19:00 UTC	2017-06-17 02:56:00 UTC	UURLA
77	2017-06-17 16:00:00 UTC	2017-06-20 08:46:00 UTC	UURLA
78	2017-06-22 00:55:00 UTC	2017-06-24 20:00:00 UTC	UURLA
79	2017-06-24 19:52:00 UTC	2017-06-25 16:00:00 UTC	UURLA
80	2017-07-15 00:50:00 UTC	2017-07-17 13:45:00 UTC	UURLA

C LISA Pathfinder experimental results

C.1 Noise performance

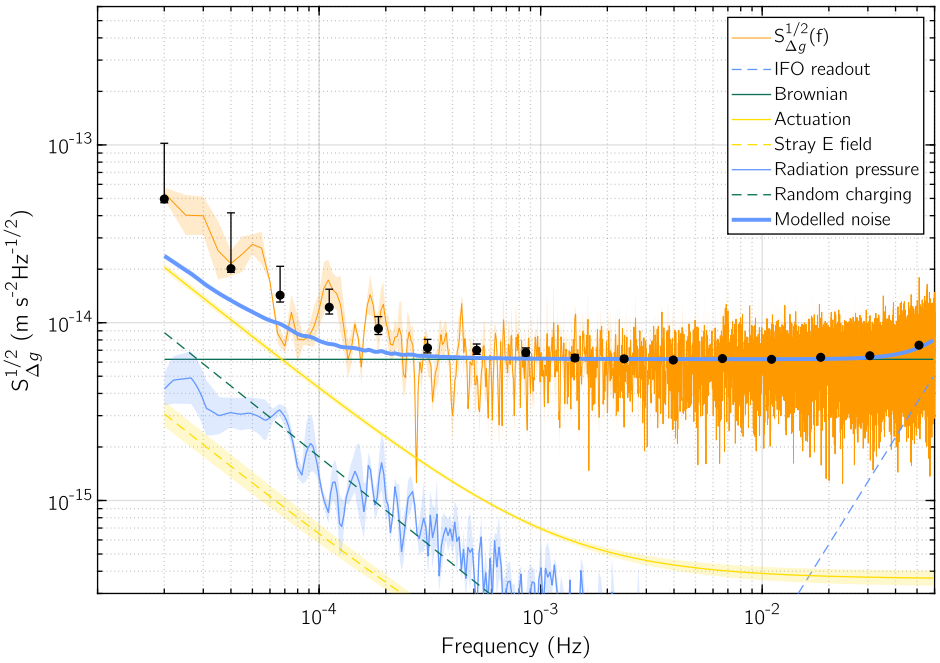

(a) Noise performance of run #6

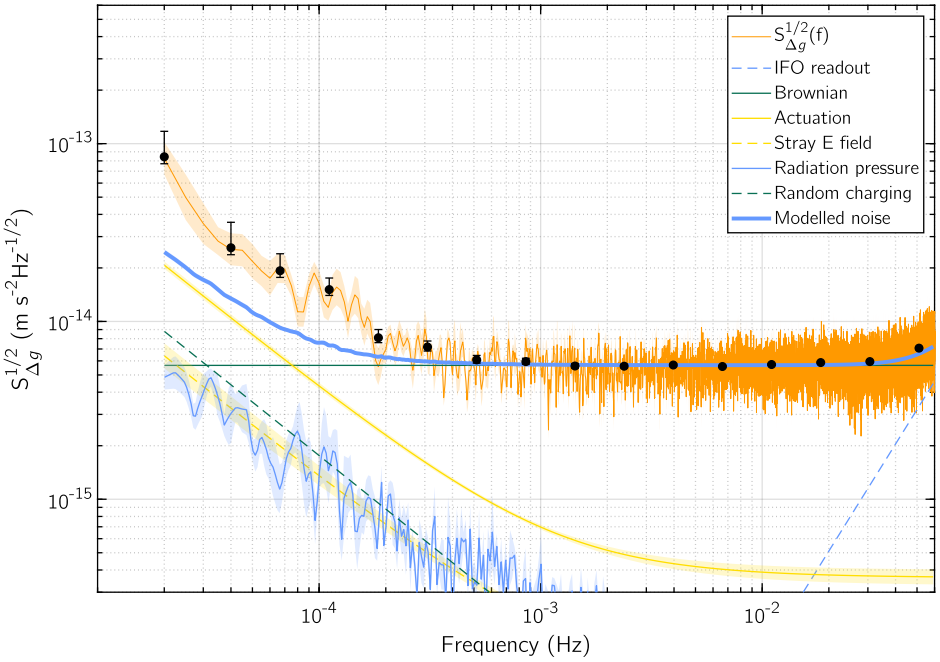

(b) Noise performance of run #9

Figure C.1: ASD of the noise-only runs of Table 2.1, depicted with the evaluated noise budget per each noise run.

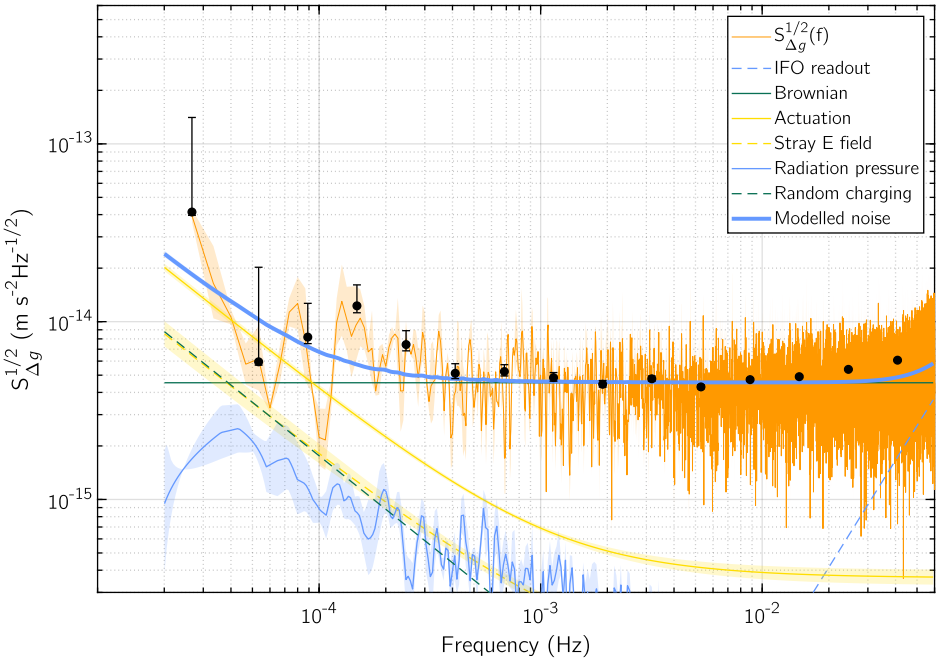

(c) Noise performance of run #17

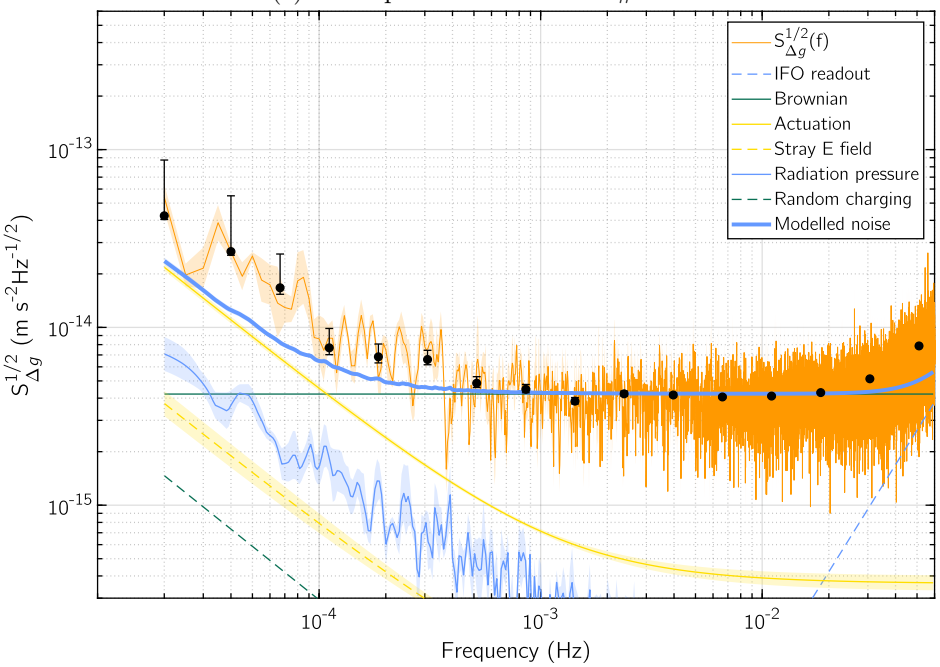

(d) Noise performance of run #39

Figure C.1: ASD of the noise-only runs of Table 2.1, depicted with the evaluated noise budget per each noise run.

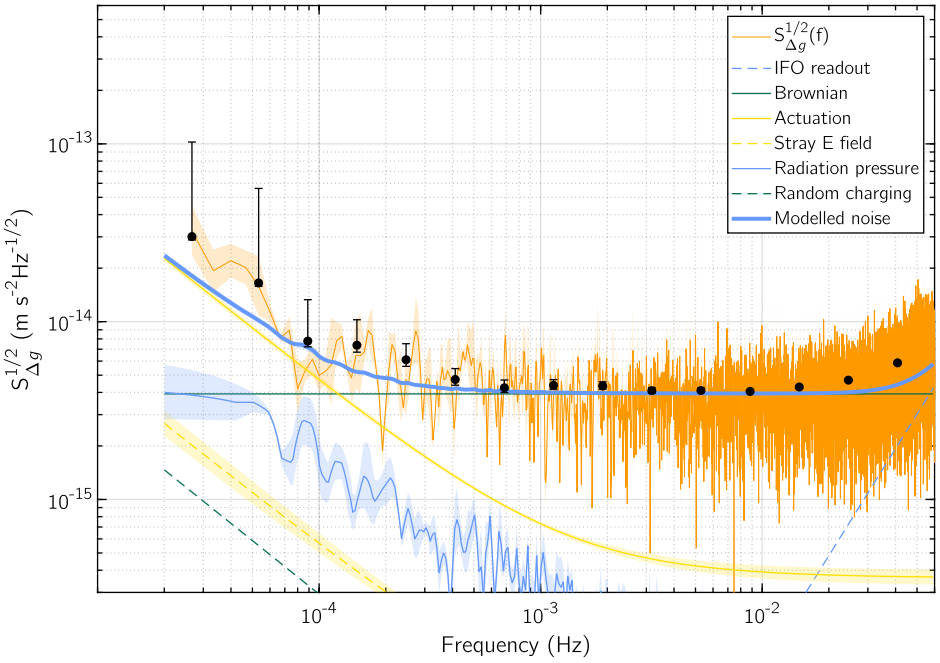

(e) Noise performance of run #42

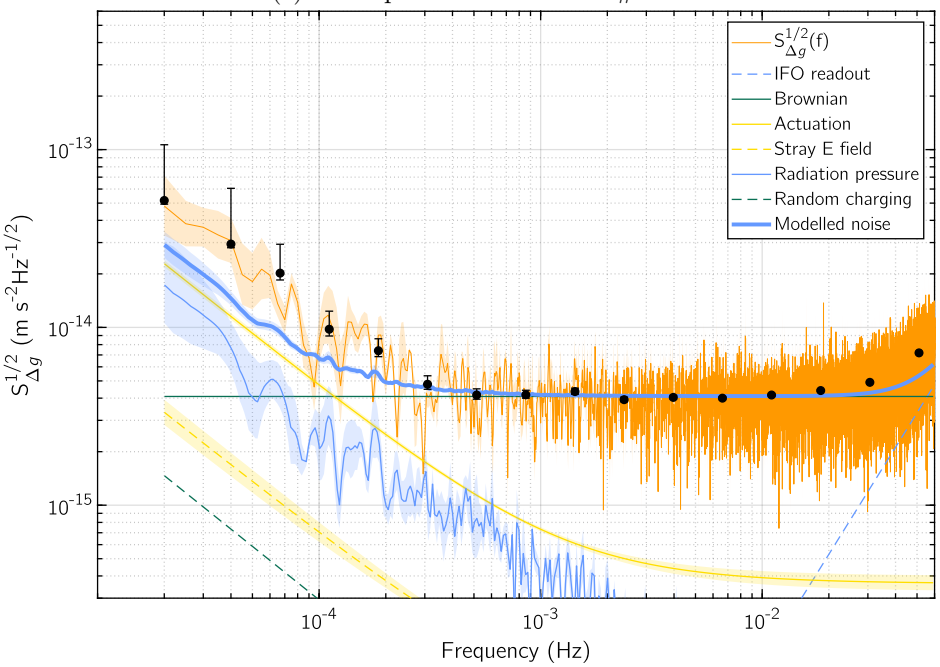

(f) Noise performance of run #43

Figure C.1: ASD of the noise-only runs of Table 2.1, depicted with the evaluated noise budget per each noise run.

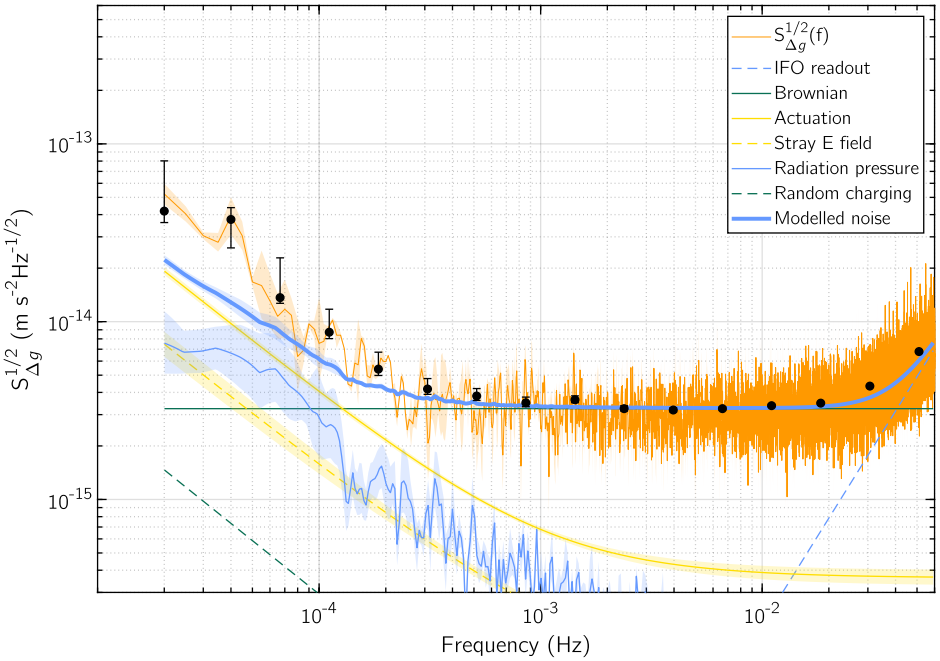

(g) Noise performance of run #59

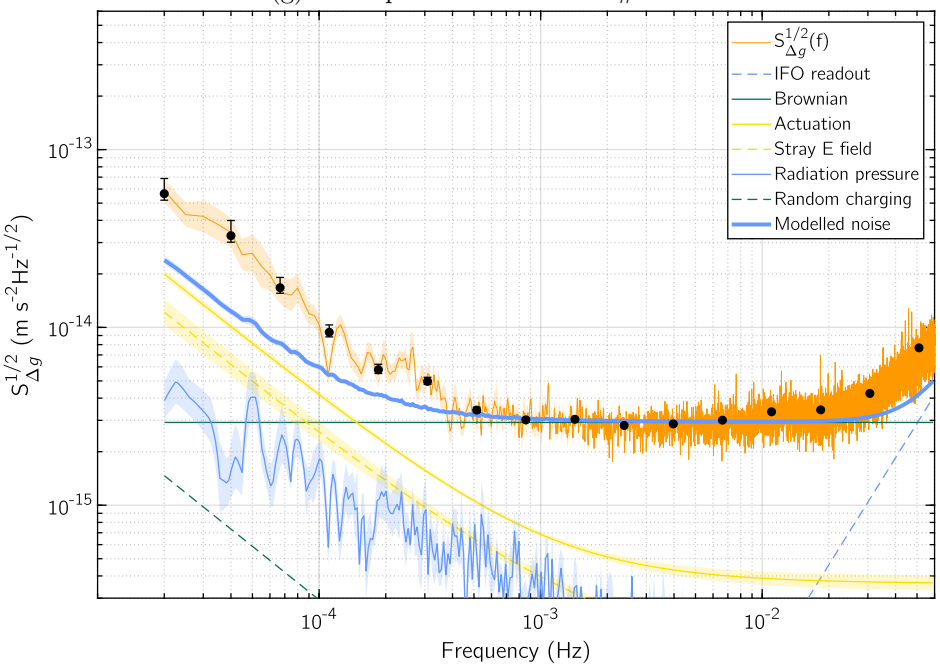

(h) Noise performance of run #61

Figure C.1: ASD of the noise-only runs of Table 2.1, depicted with the evaluated noise budget per each noise run.

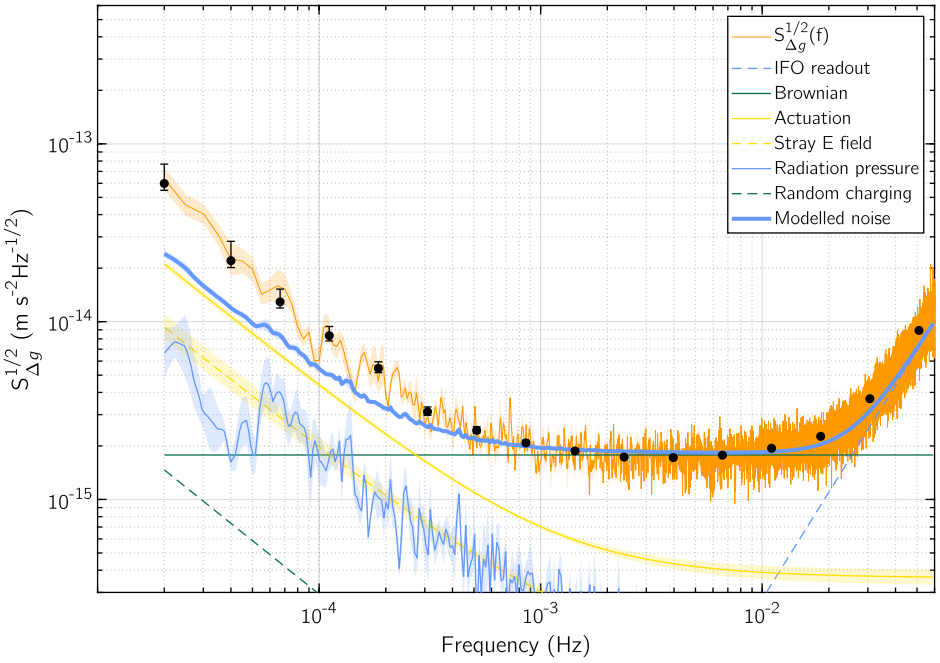

(i) Noise performance of run #66

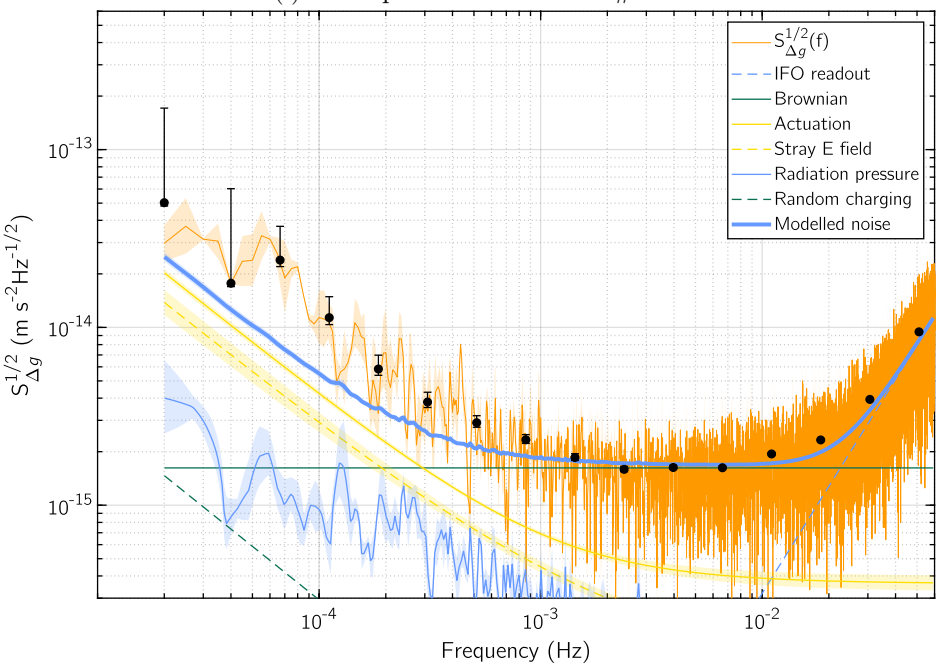

(j) Noise performance of run #74

Figure C.1: ASD of the noise-only runs of Table 2.1, depicted with the evaluated noise budget per each noise run.

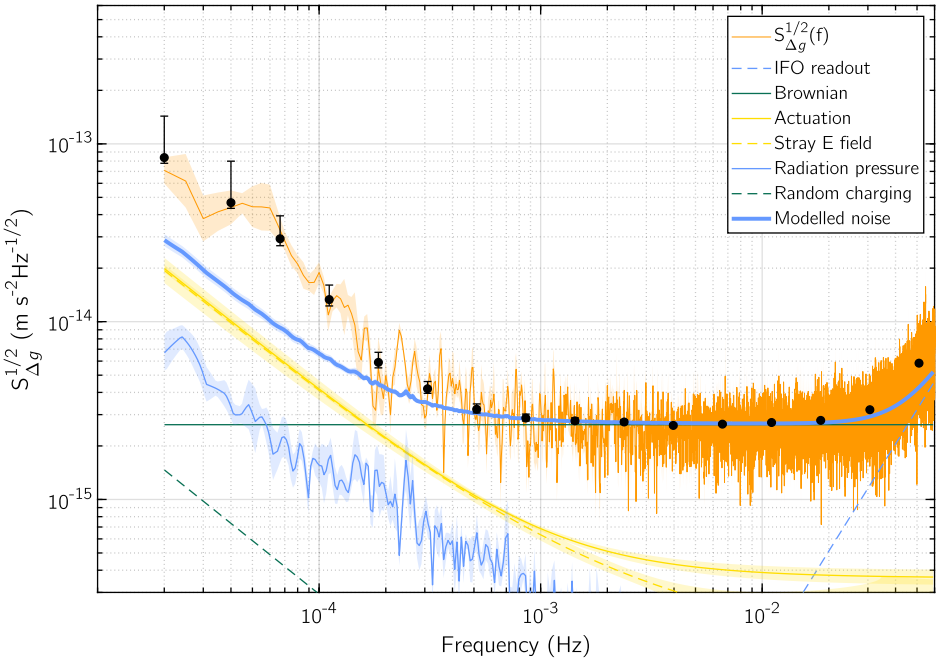

(k) Noise performance of run #75

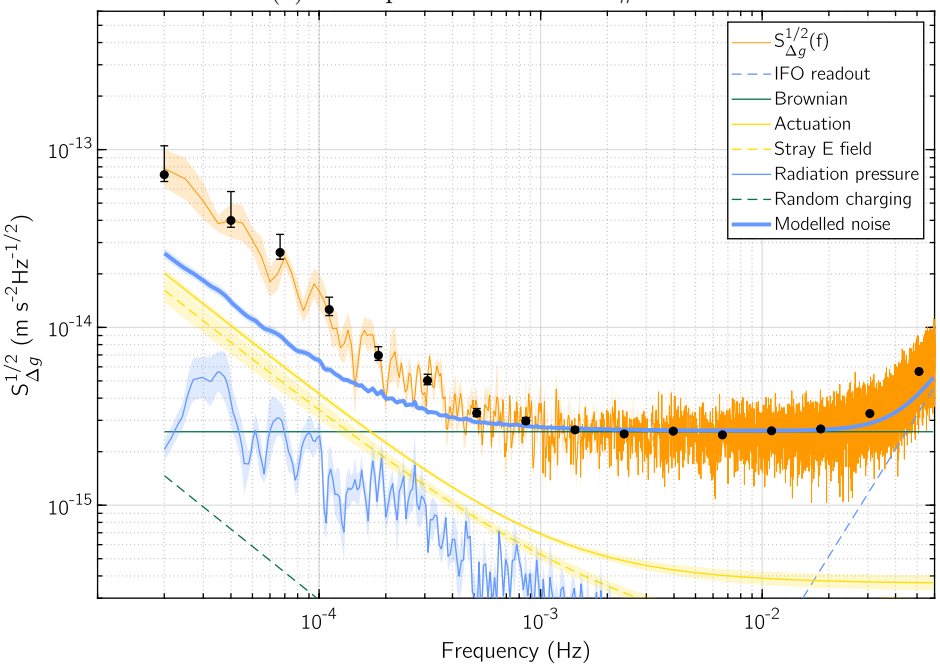

(l) Noise performance of run #76

Figure C.1: ASD of the noise-only runs of Table 2.1, depicted with the evaluated noise budget per each noise run.

C.2 Low frequency excess noise

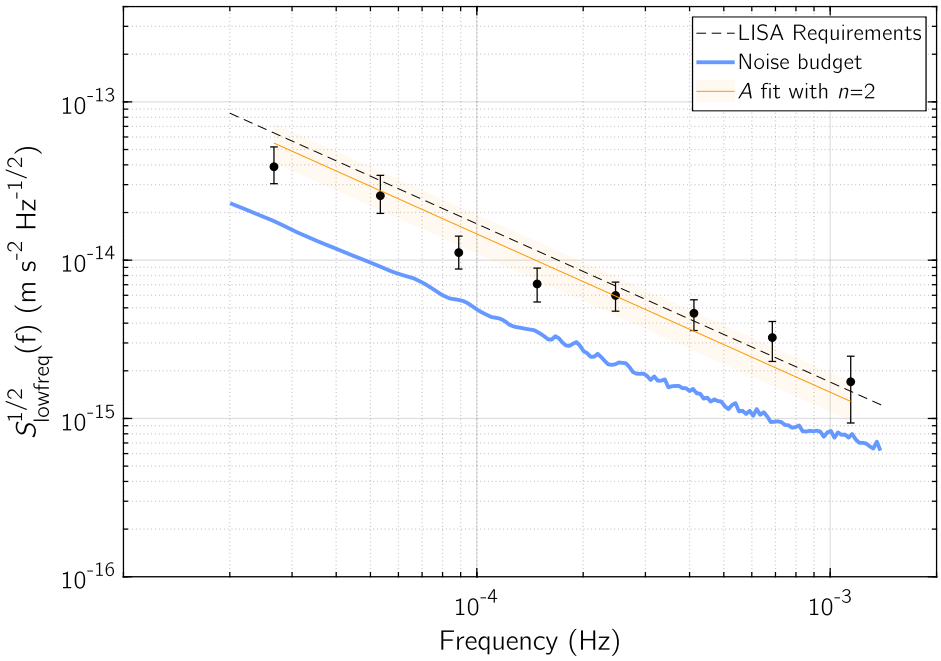

(a) Excess noise at low frequency of run #6

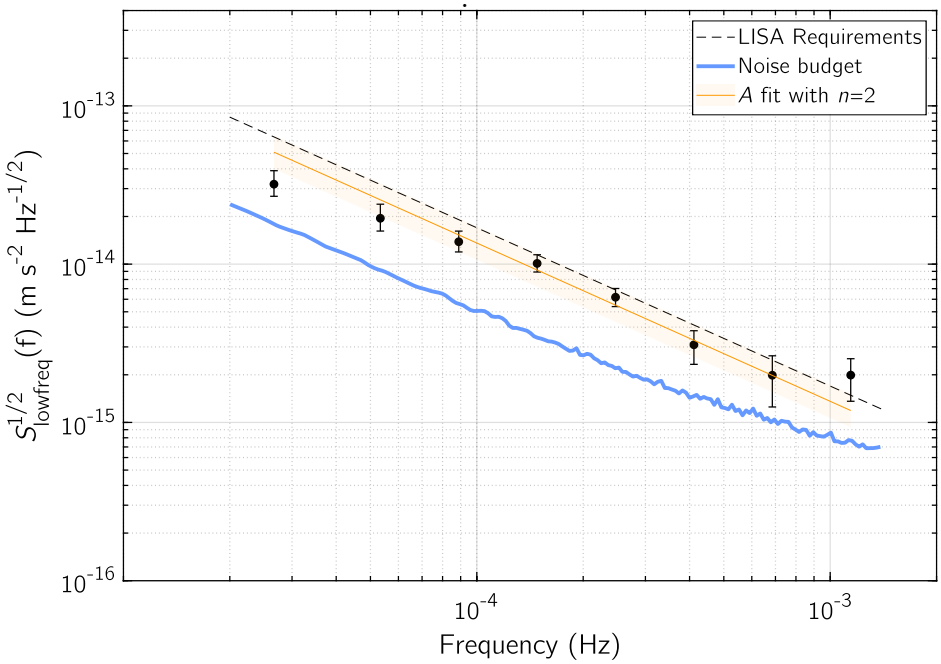

(b) Excess noise at low frequency of run #9

Figure C.2: ASD of the noise-only runs of Table 2.1, depicted with the evaluated noise budget per each noise run.

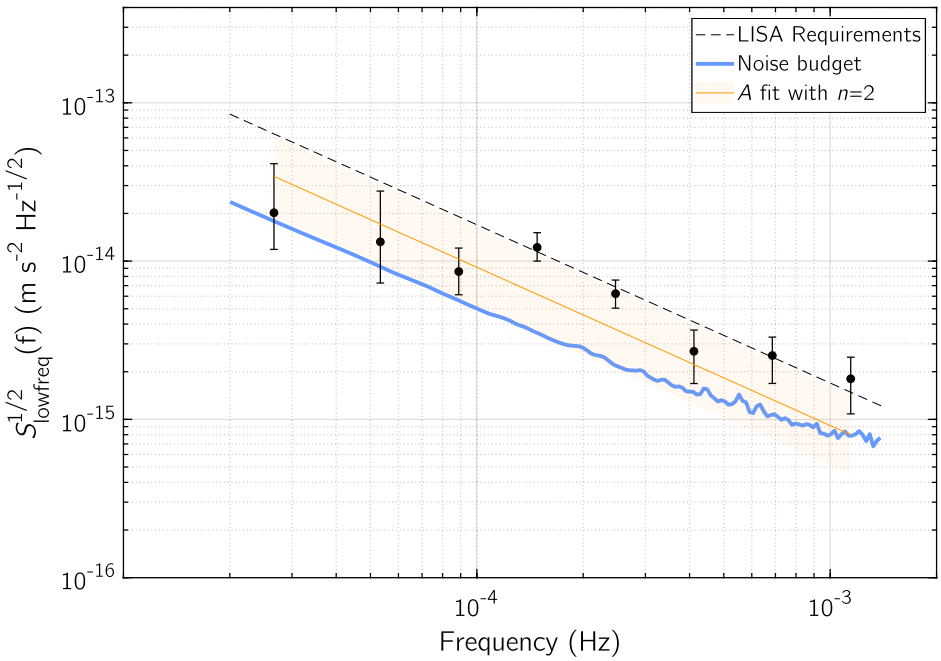

(c) Excess noise at low frequency of run #17.

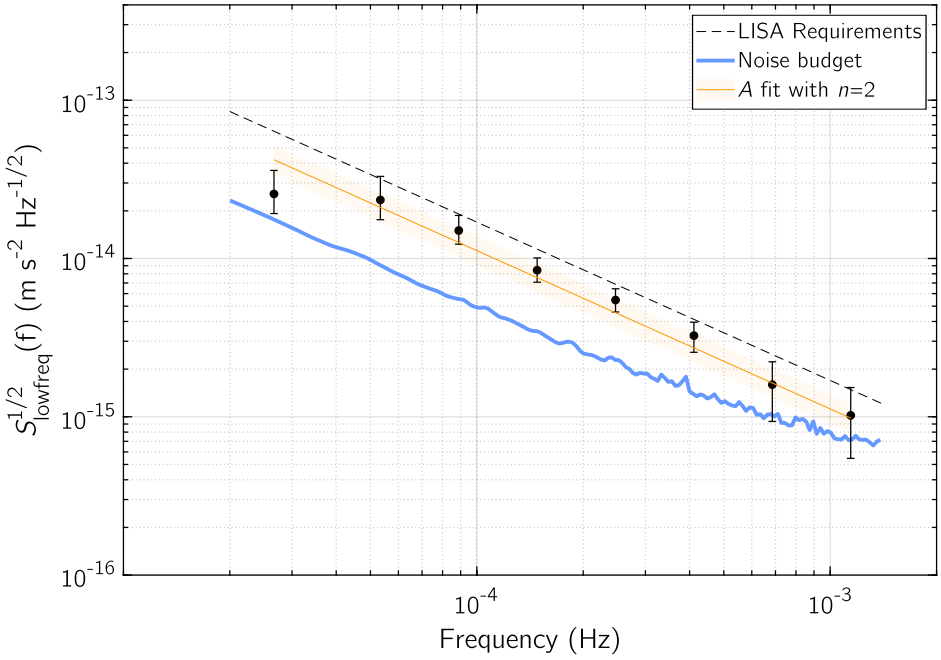

(d) Excess noise at low frequency of run #39.

Figure C.2: ASD of the noise-only runs of Table 2.1, depicted with the evaluated noise budget per each noise run.

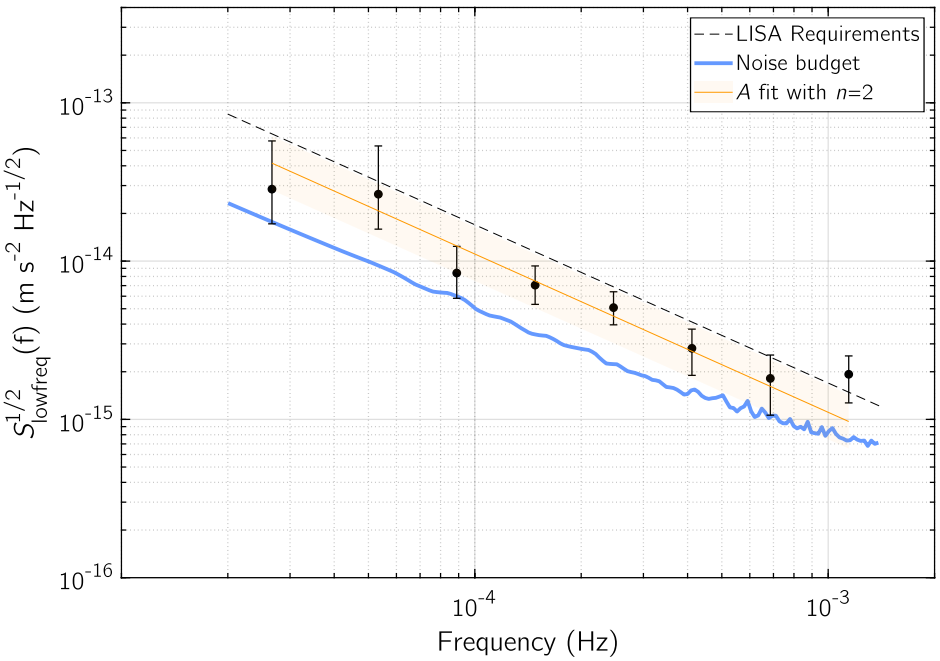

(e) Excess noise at low frequency of run #42.

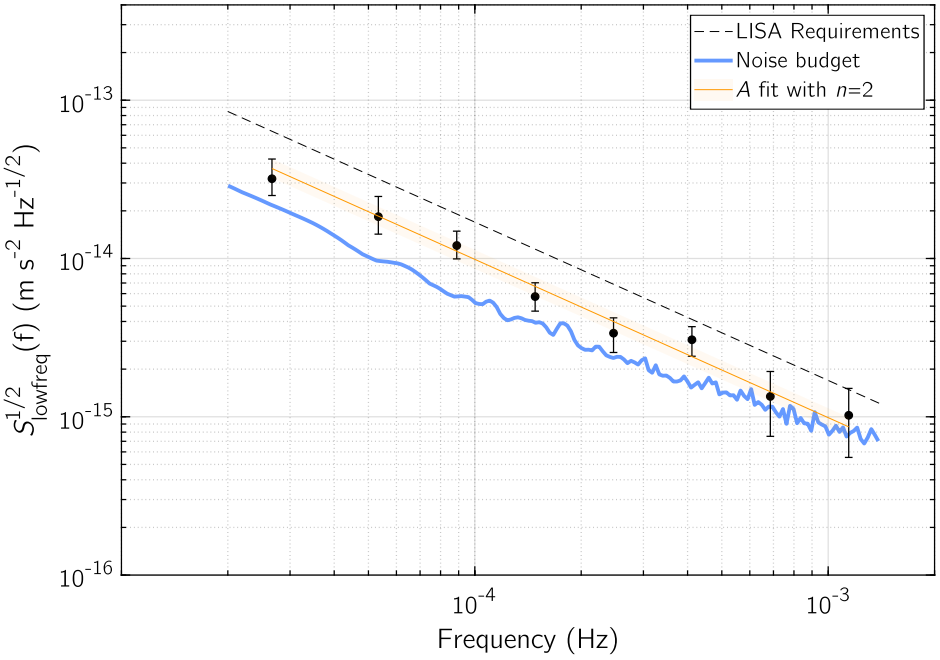

(f) Excess noise at low frequency of run #43.

Figure C.2: ASD of the noise-only runs of Table 2.1, depicted with the evaluated noise budget per each noise run.

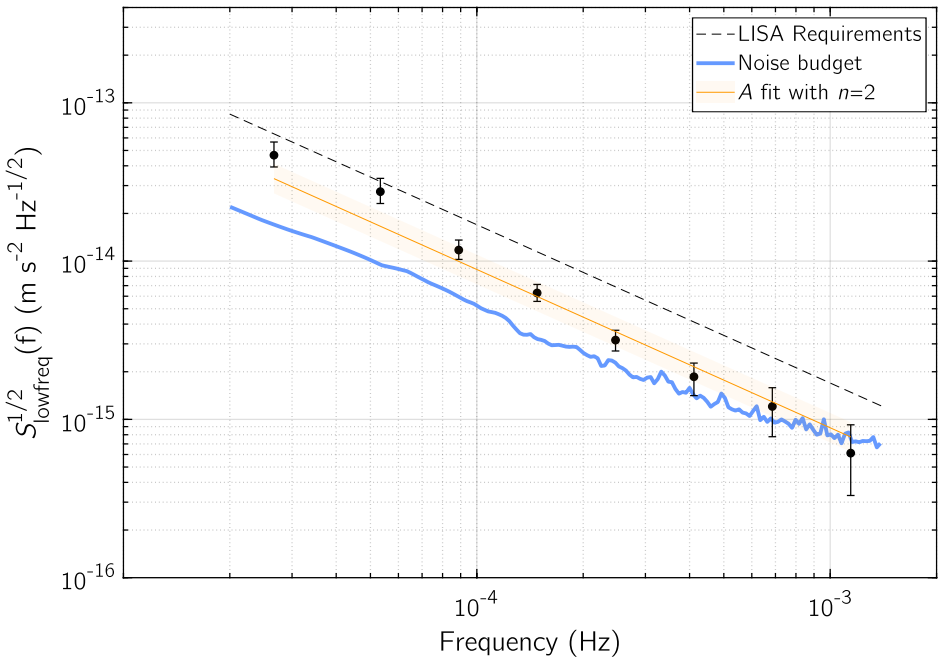

(g) Excess noise at low frequency of run #59.

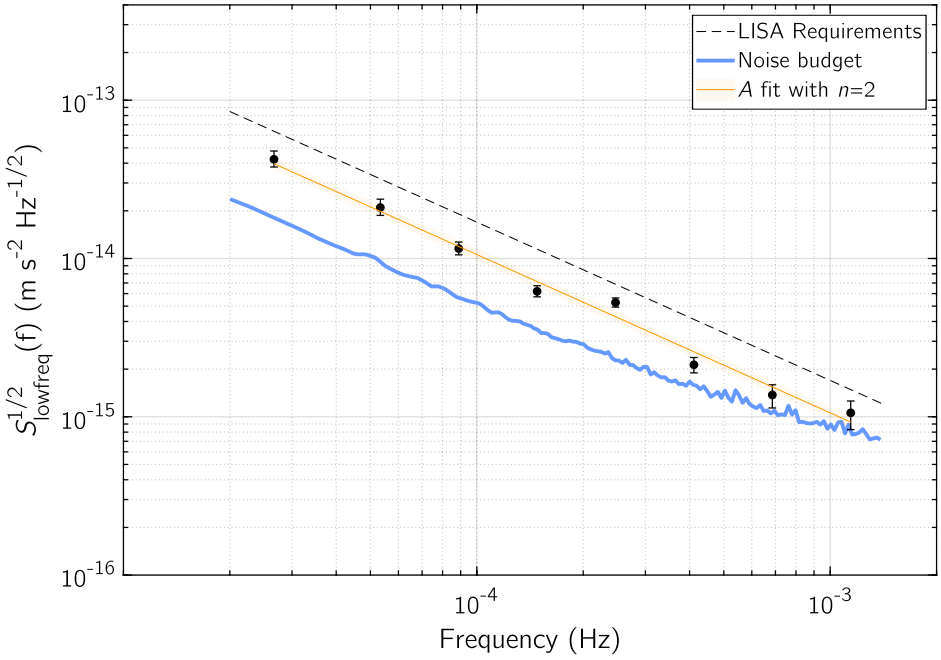

(h) Excess noise at low frequency of run #61.

Figure C.2: ASD of the noise-only runs of Table 2.1, depicted with the evaluated noise budget per each noise run.

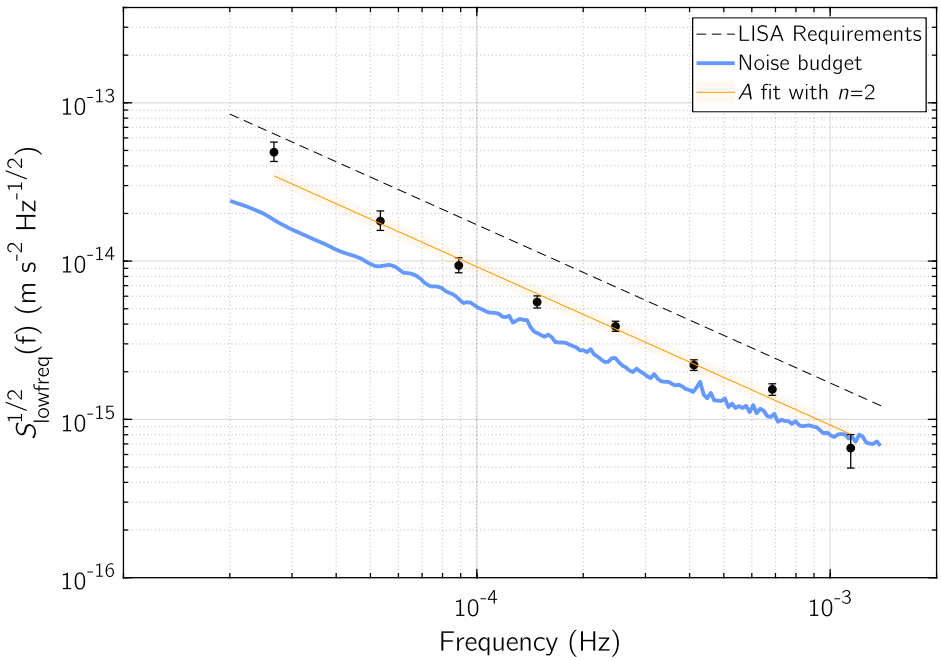

(i) Excess noise at low frequency of run #66.

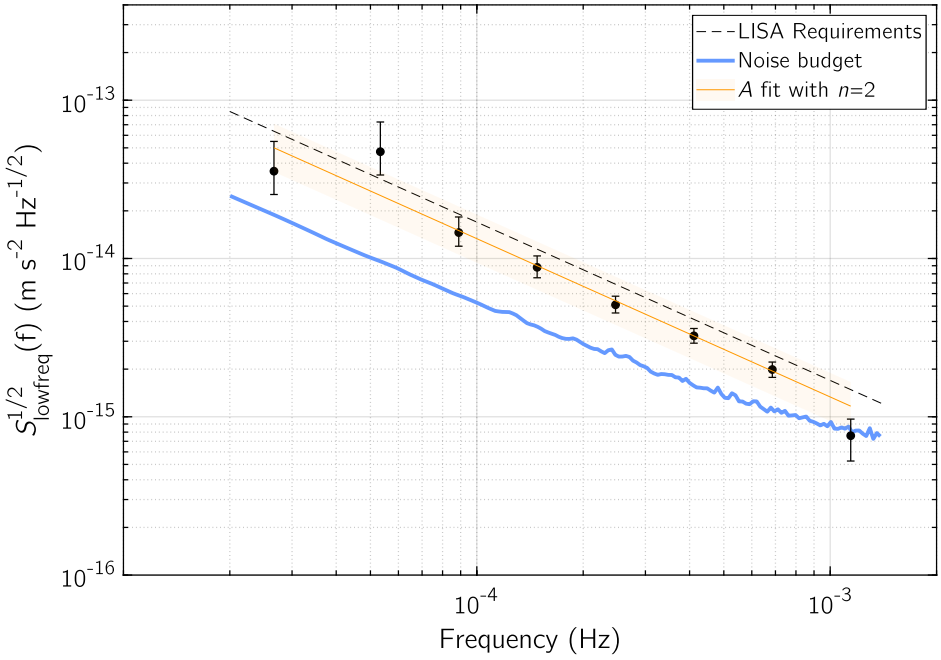

(j) Excess noise at low frequency of run #74.

Figure C.2: ASD of the noise-only runs of Table 2.1, depicted with the evaluated noise budget per each noise run.

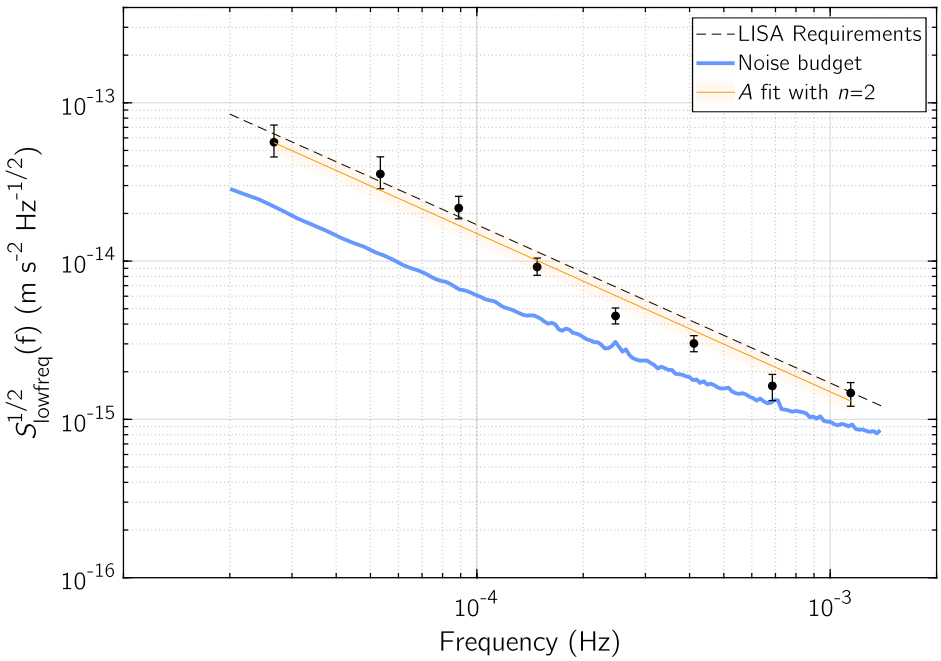

(k) Excess noise at low frequency of run #75.

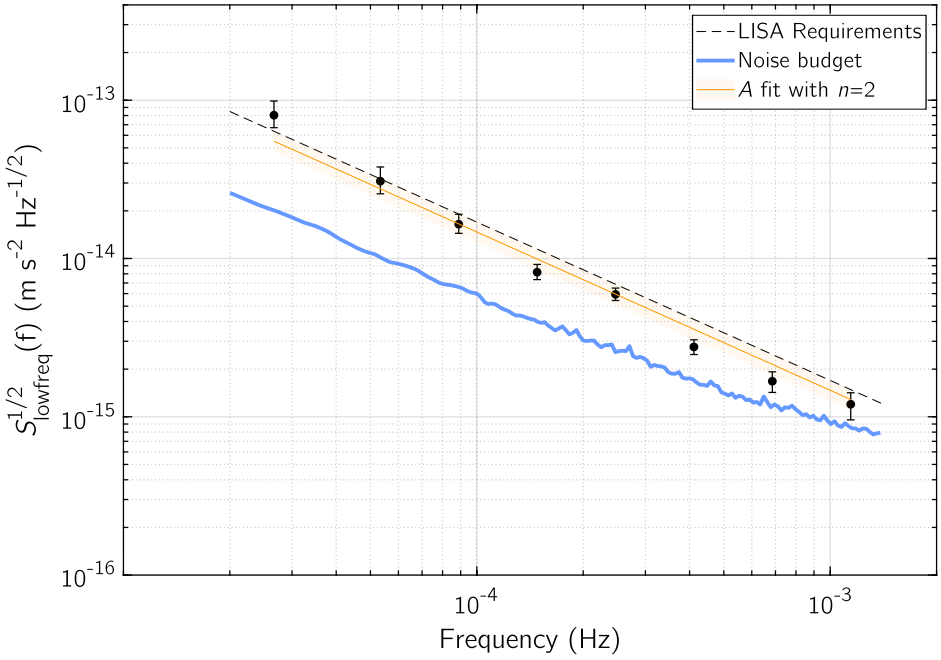

(l) Excess noise at low frequency of run #76.

Figure C.2: ASD of the noise-only runs of Table 2.1, depicted with the evaluated noise budget per each noise run.

C.3 Angular differential acceleration

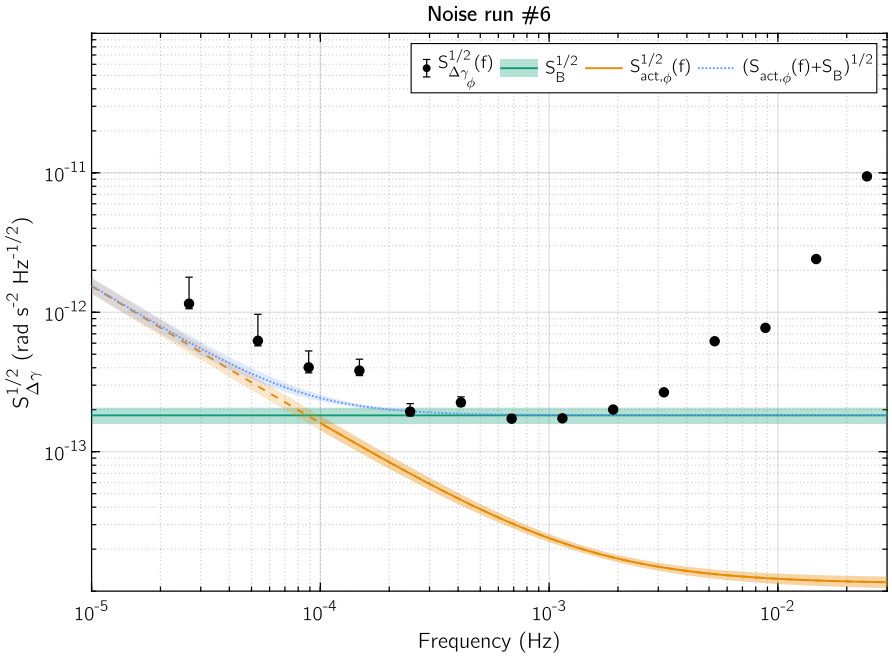

(a) ϕ channel

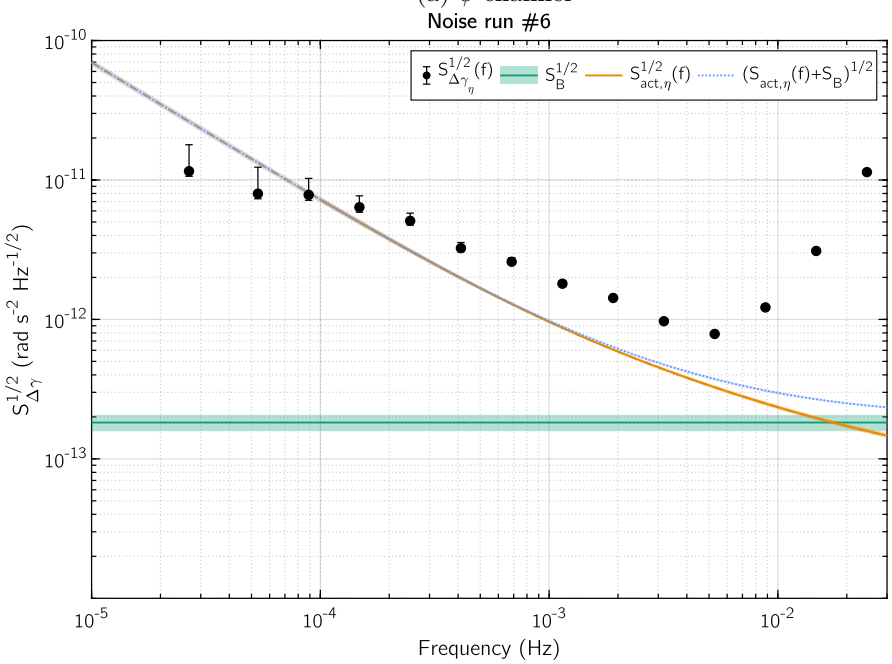

(b) η channel

Figure C.3: ASD of the angular differential acceleration $S^{1/2}_{\Delta\gamma}$ for the two angular degrees of freedom ϕ and η. The angular actuation noise $S^{1/2}_{\mathrm{act}}(f)$ is pictured as a continuous orange line down to 0.1 mHz, while its extension at lower frequencies is dashed. The angular Brownian noise $S^{1/2}_{\mathrm{B}}$ is the green line, and their sum $S_{\Delta\gamma,k}(f)$ is the blue dotted curve.

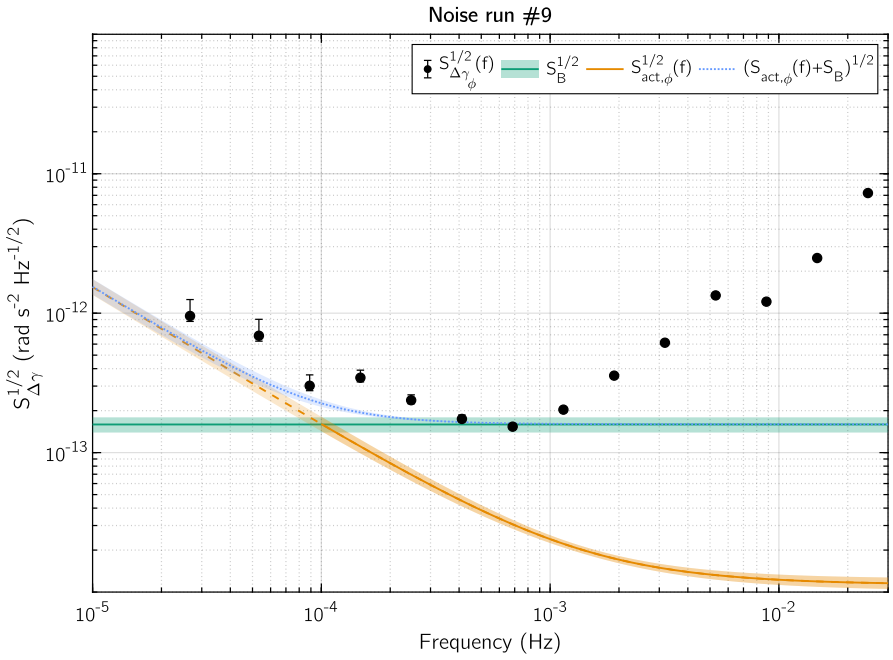

(c) ϕ channel

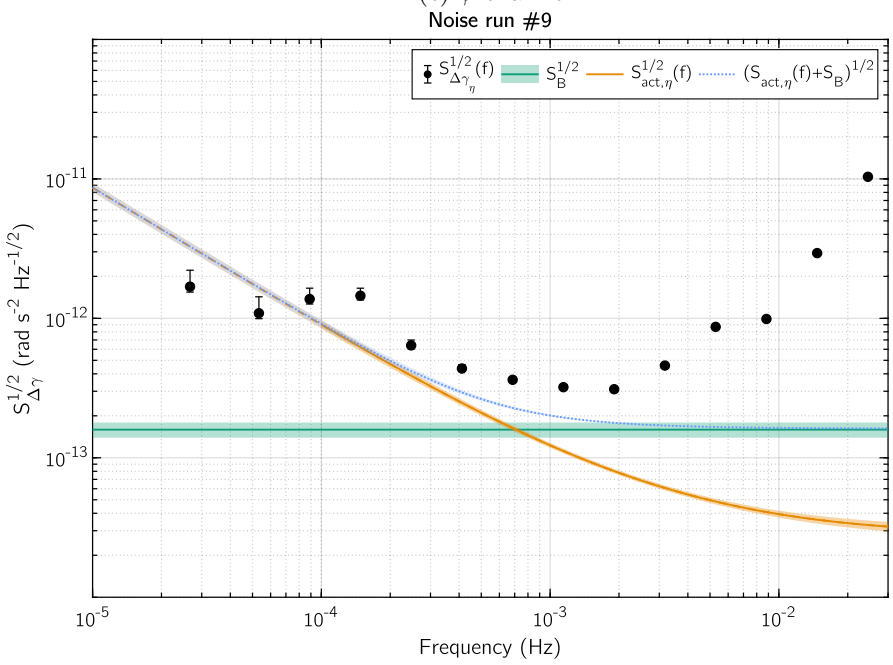

(d) η channel

Figure C.3: ASD of the angular differential acceleration $S^{1/2}_{\Delta\gamma}$ for the two angular degrees of freedom ϕ and η. The angular actuation noise $S^{1/2}_{\mathrm{act}}(f)$ is pictured as a continuous orange line down to 0.1 mHz, while its extension at lower frequencies is dashed. The angular Brownian noise $S^{1/2}_{\mathrm{B}}$ is the green line, and their sum $S_{\Delta\gamma,k}(f)$ is the blue dotted curve.

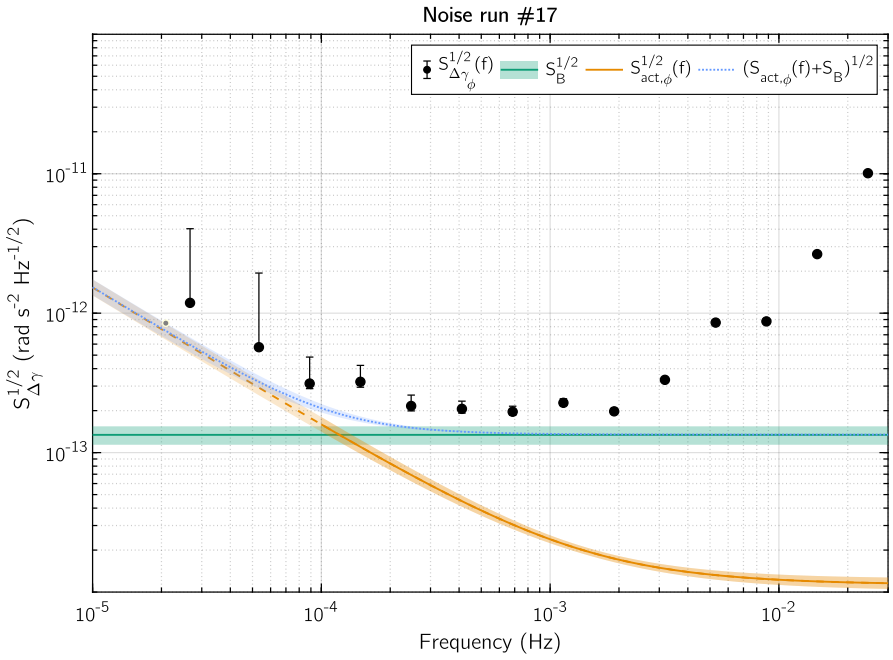

(e) ϕ channel

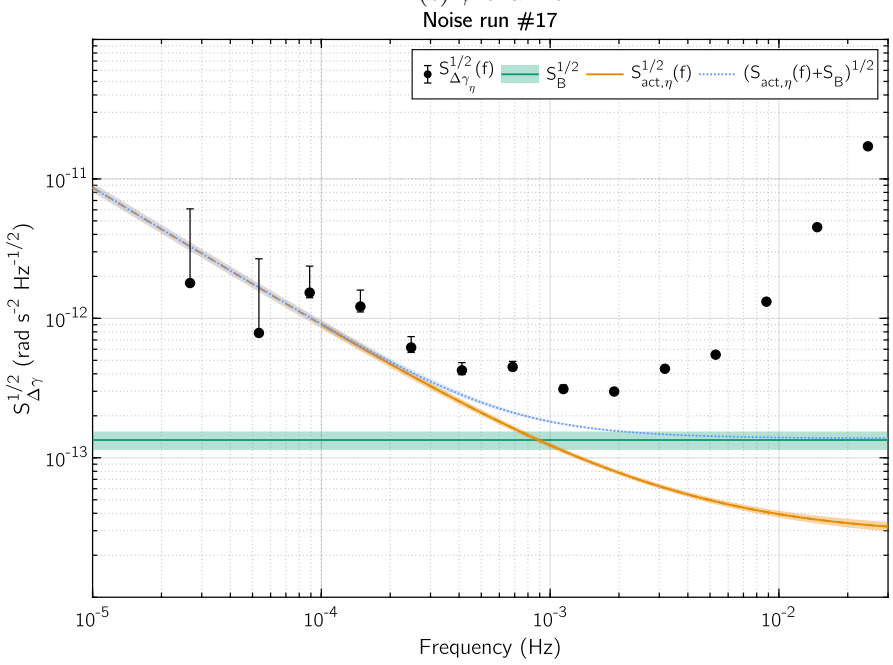

(f) η channel

Figure C.3: ASD of the angular differential acceleration $S^{1/2}_{\Delta\gamma}$ for the two angular degrees of freedom ϕ and η. The angular actuation noise $S^{1/2}_{\mathrm{act}}(f)$ is pictured as a continuous orange line down to 0.1 mHz, while its extension at lower frequencies is dashed. The angular Brownian noise $S^{1/2}_{\mathrm{B}}$ is the green line, and their sum $S_{\Delta\gamma,k}(f)$ is the blue dotted curve.

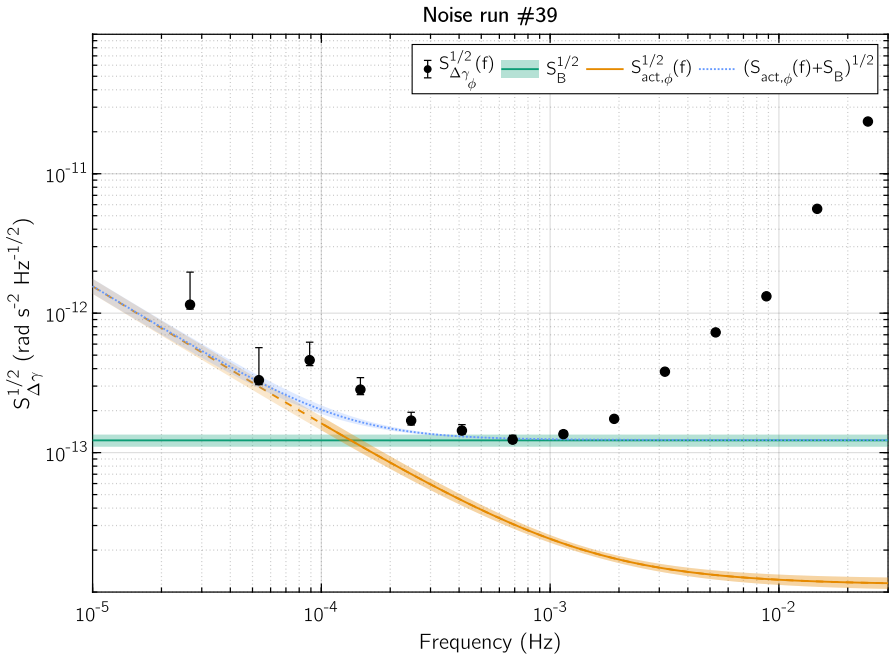

(g) ϕ channel

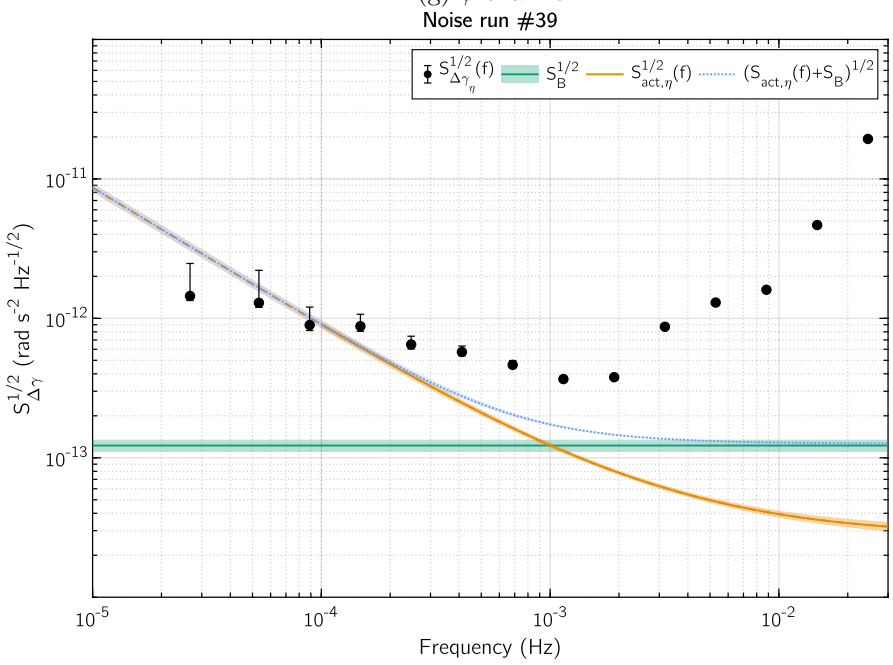

(h) η channel

Figure C.3: ASD of the angular differential acceleration $S^{1/2}_{\Delta\gamma}$ for the two angular degrees of freedom ϕ and η. The angular actuation noise $S^{1/2}_{\mathrm{act}}(f)$ is pictured as a continuous orange line down to 0.1 mHz, while its extension at lower frequencies is dashed. The angular Brownian noise $S^{1/2}_{\mathrm{B}}$ is the green line, and their sum $S_{\Delta\gamma,k}(f)$ is the blue dotted curve.

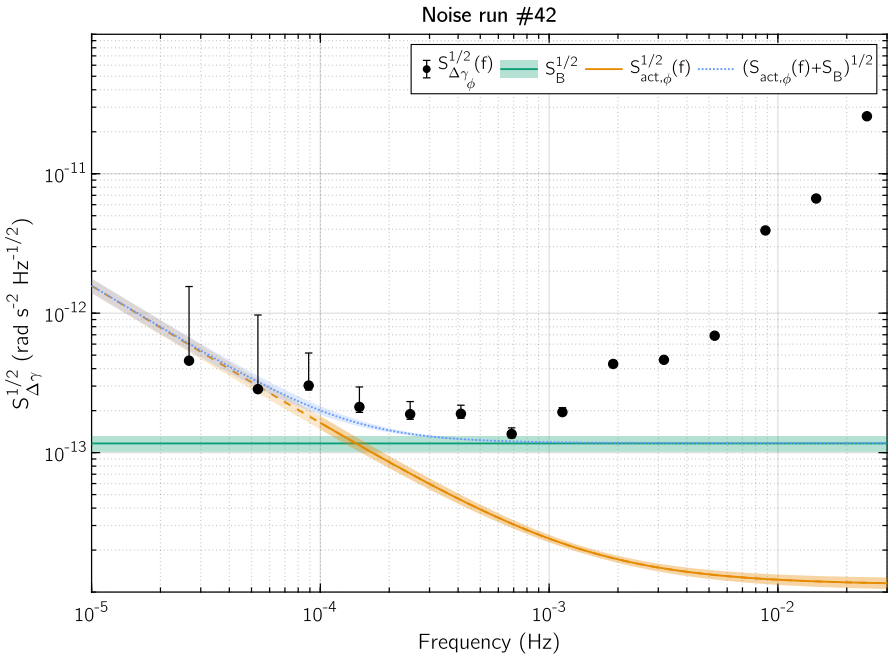

(i) ϕ channel

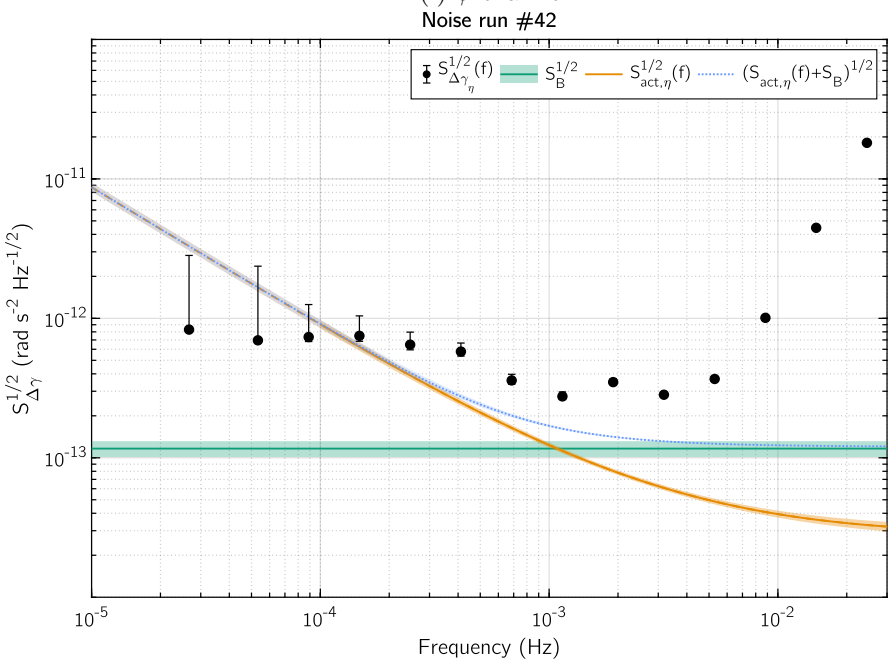

(j) η channel

Figure C.3: ASD of the angular differential acceleration $S^{1/2}_{\Delta\gamma}$ for the two angular degrees of freedom ϕ and η. The angular actuation noise $S^{1/2}_{\mathrm{act}}(f)$ is pictured as a continuous orange line down to 0.1 mHz, while its extension at lower frequencies is dashed. The angular Brownian noise $S^{1/2}_{\mathrm{B}}$ is the green line, and their sum $S_{\Delta\gamma,k}(f)$ is the blue dotted curve.

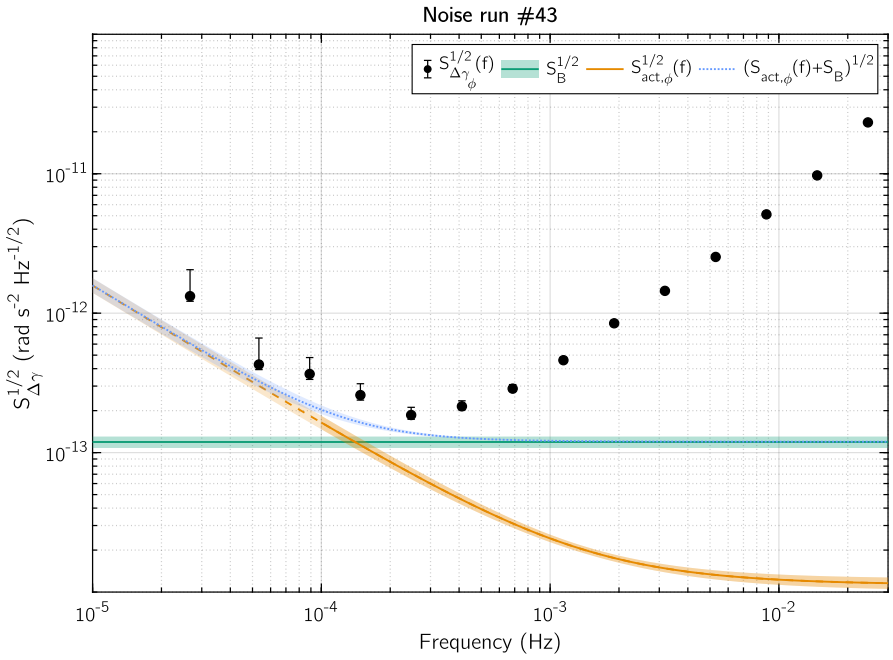

(k) ϕ channel

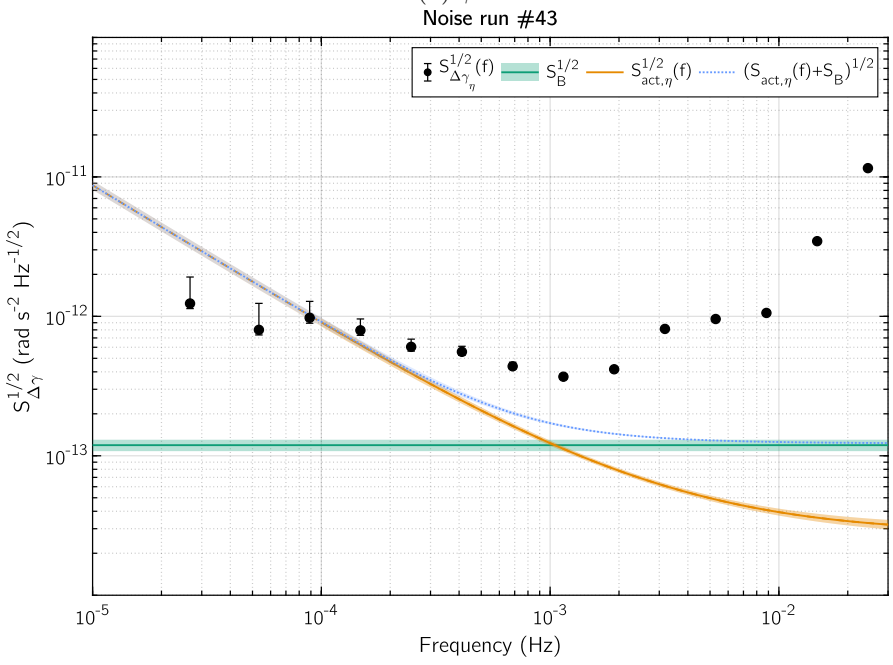

(l) η channel

Figure C.3: ASD of the angular differential acceleration $S^{1/2}_{\Delta\gamma}$ for the two angular degrees of freedom ϕ and η. The angular actuation noise $S^{1/2}_{\mathrm{act}}(f)$ is pictured as a continuous orange line down to 0.1 mHz, while its extension at lower frequencies is dashed. The angular Brownian noise $S^{1/2}_{\mathrm{B}}$ is the green line, and their sum $S_{\Delta\gamma,k}(f)$ is the blue dotted curve.

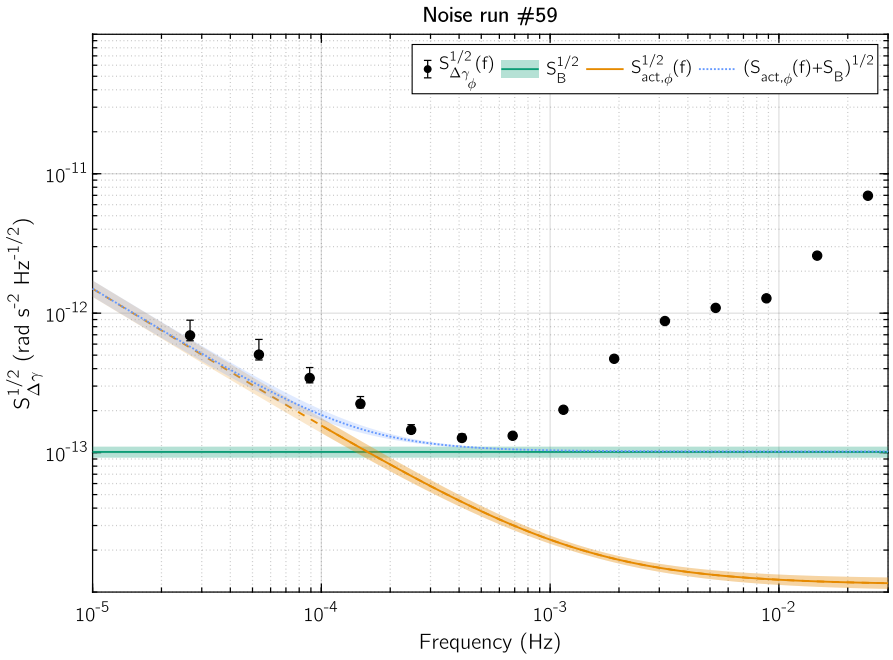

(a) ϕ channel

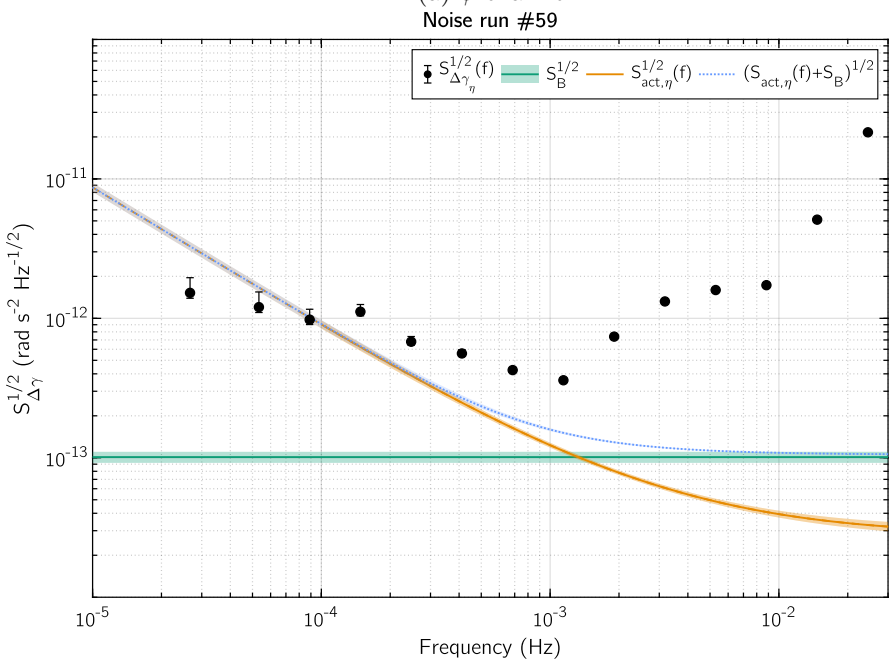

(b) η channel

Figure C.4: ASD of the angular differential acceleration $S^{1/2}_{\Delta\gamma}$ for the two angular degrees of freedom ϕ and η. The angular actuation noise $S^{1/2}_{\mathrm{act}}(f)$ is pictured as a continuous orange line down to 0.1 mHz, while its extension at lower frequencies is dashed. The angular Brownian noise $S^{1/2}_{\mathrm{B}}$ is the green line, and their sum $S_{\Delta\gamma,k}(f)$ is the blue dotted curve.

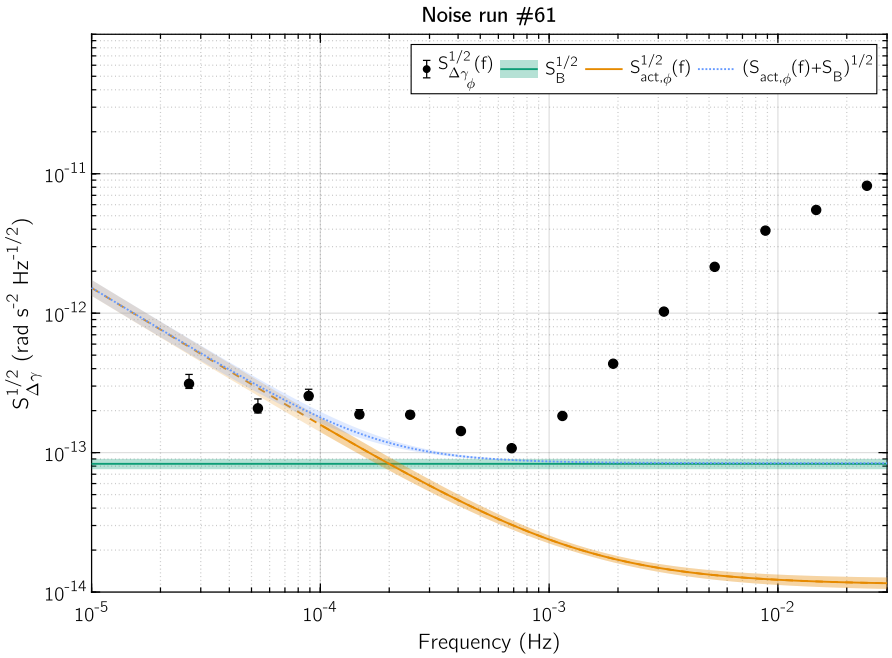

(c) ϕ channel

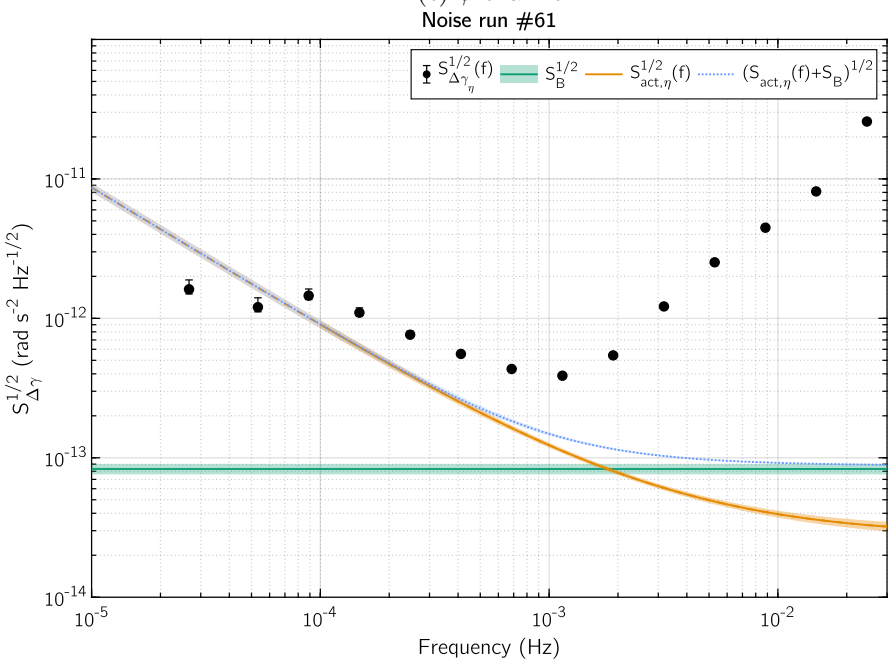

(d) η channel

Figure C.4: ASD of the angular differential acceleration $S^{1/2}_{\Delta\gamma}$ for the two angular degrees of freedom ϕ and η. The angular actuation noise $S^{1/2}_{\mathrm{act}}(f)$ is pictured as a continuous orange line down to 0.1 mHz, while its extension at lower frequencies is dashed. The angular Brownian noise $S^{1/2}_{\mathrm{B}}$ is the green line, and their sum $S_{\Delta\gamma,k}(f)$ is the blue dotted curve.

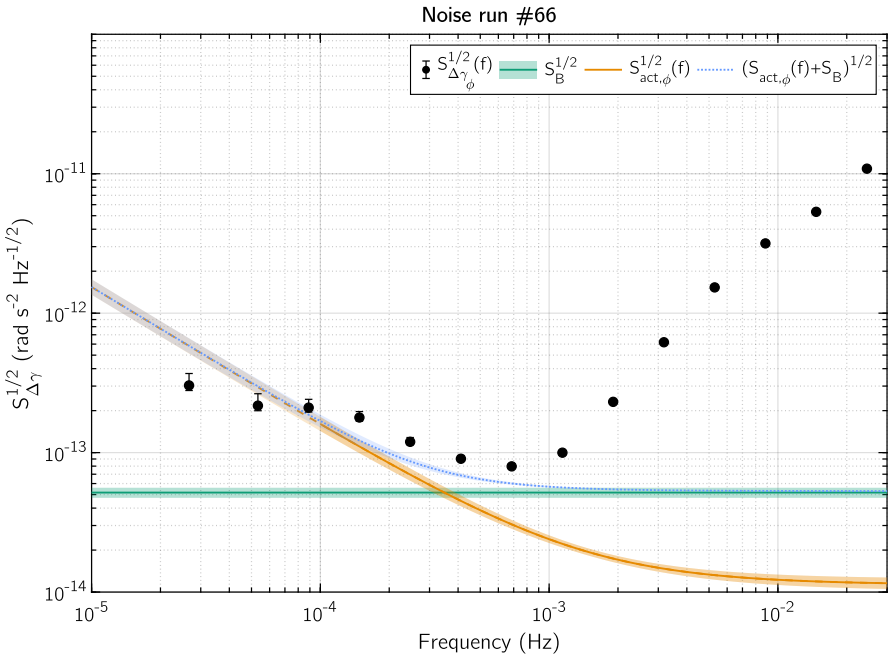

(e) ϕ channel

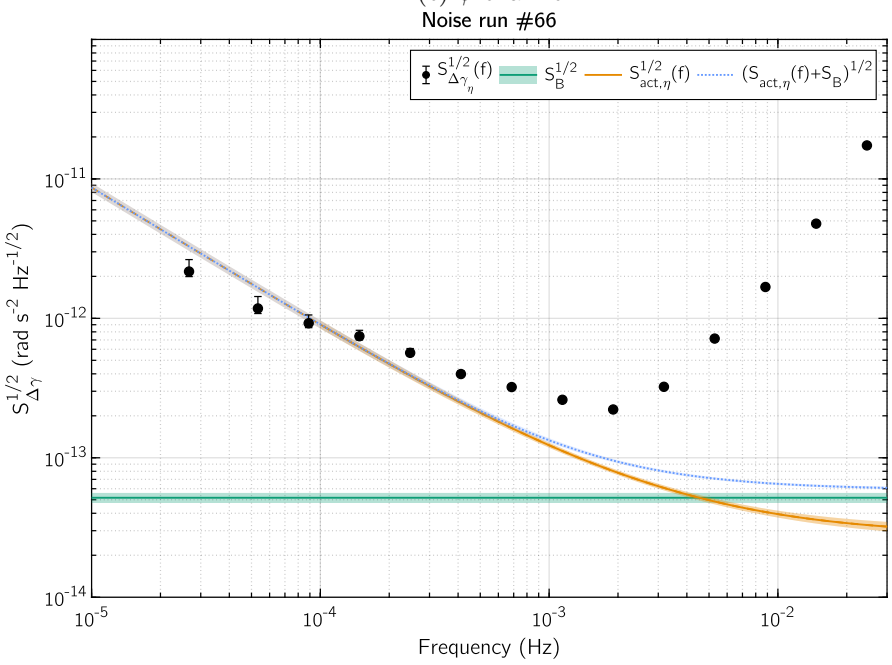

(f) η channel

Figure C.4: ASD of the angular differential acceleration $S^{1/2}_{\Delta\gamma}$ for the two angular degrees of freedom ϕ and η. The angular actuation noise $S^{1/2}_{\mathrm{act}}(f)$ is pictured as a continuous orange line down to 0.1 mHz, while its extension at lower frequencies is dashed. The angular Brownian noise $S^{1/2}_{\mathrm{B}}$ is the green line, and their sum $S_{\Delta\gamma,k}(f)$ is the blue dotted curve.

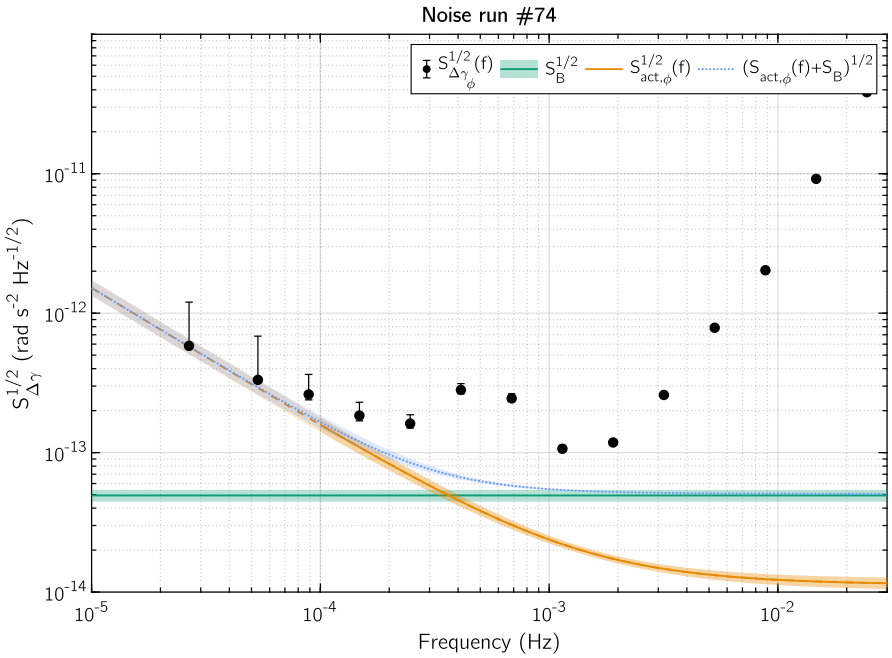

(g) ϕ channel

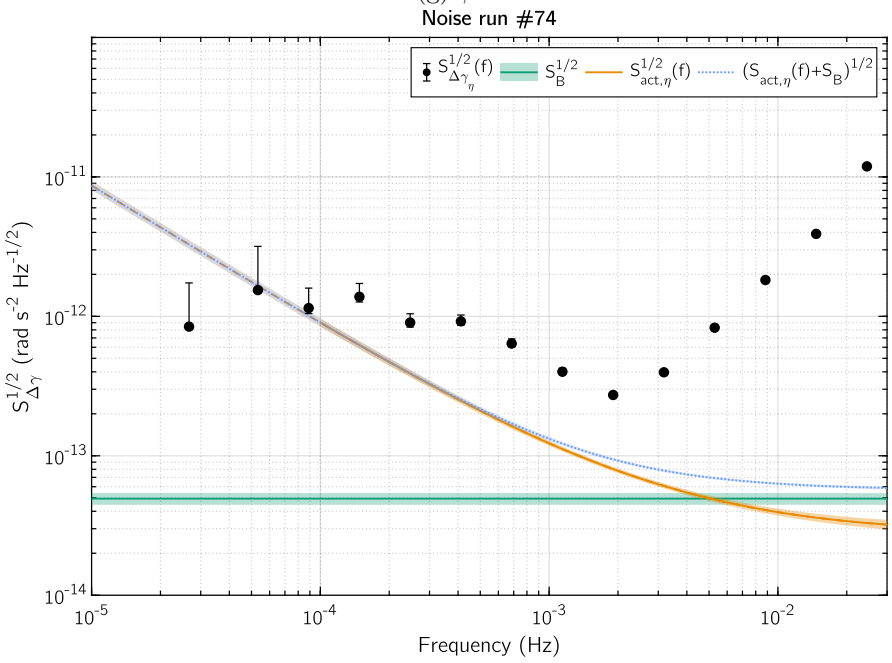

(h) η channel

Figure C.4: ASD of the angular differential acceleration $S^{1/2}_{\Delta\gamma}$ for the two angular degrees of freedom ϕ and η. The angular actuation noise $S^{1/2}_{\mathrm{act}}(f)$ is pictured as a continuous orange line down to 0.1 mHz, while its extension at lower frequencies is dashed. The angular Brownian noise $S^{1/2}_{\mathrm{B}}$ is the green line, and their sum $S_{\Delta\gamma,k}(f)$ is the blue dotted curve.

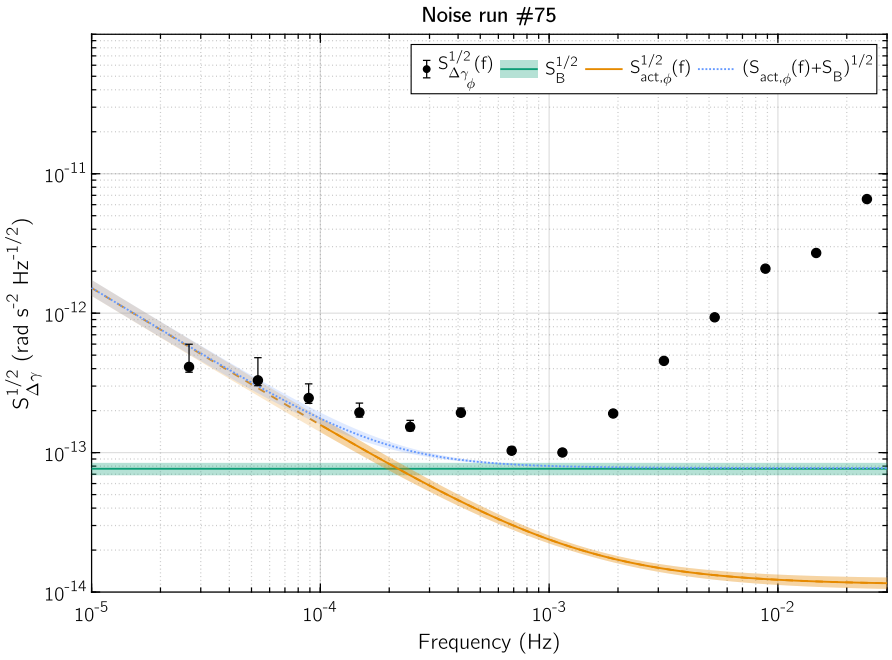

(i) ϕ channel

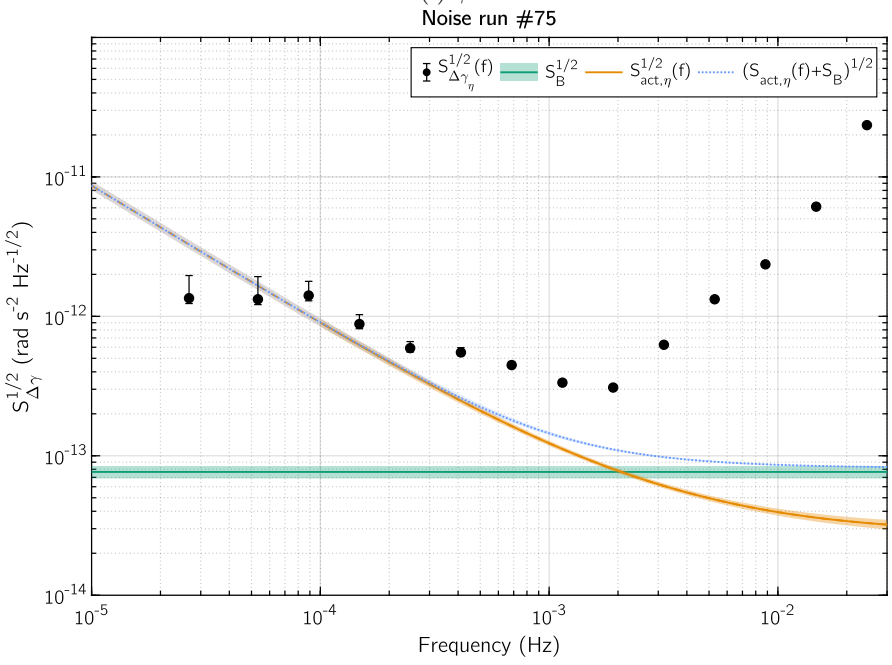

(j) η channel

Figure C.4: ASD of the angular differential acceleration $S^{1/2}_{\Delta\gamma}$ for the two angular degrees of freedom ϕ and η. The angular actuation noise $S^{1/2}_{\mathrm{act}}(f)$ is pictured as a continuous orange line down to 0.1 mHz, while its extension at lower frequencies is dashed. The angular Brownian noise $S^{1/2}_{\mathrm{B}}$ is the green line, and their sum $S_{\Delta\gamma,k}(f)$ is the blue dotted curve.

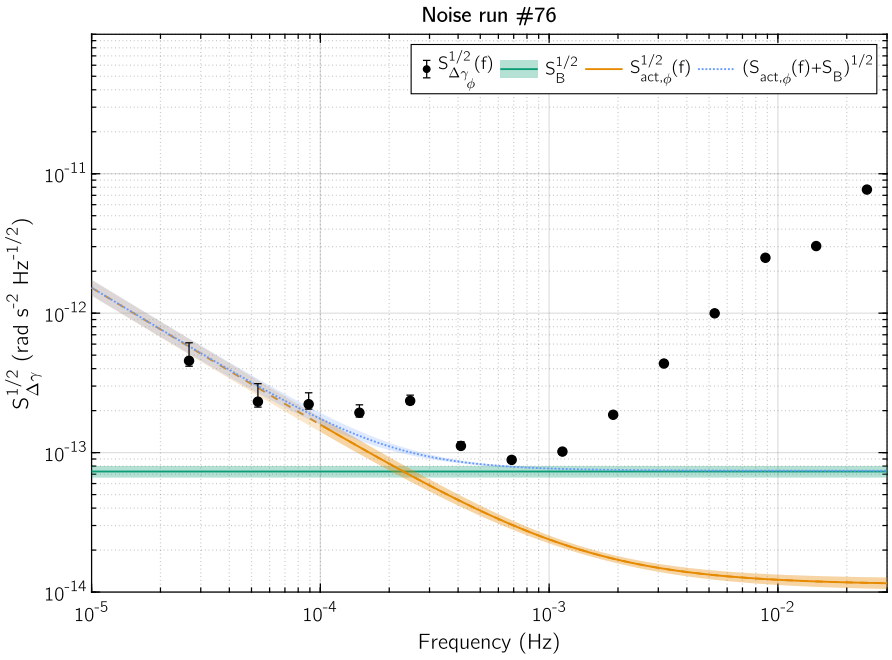

(k) ϕ channel

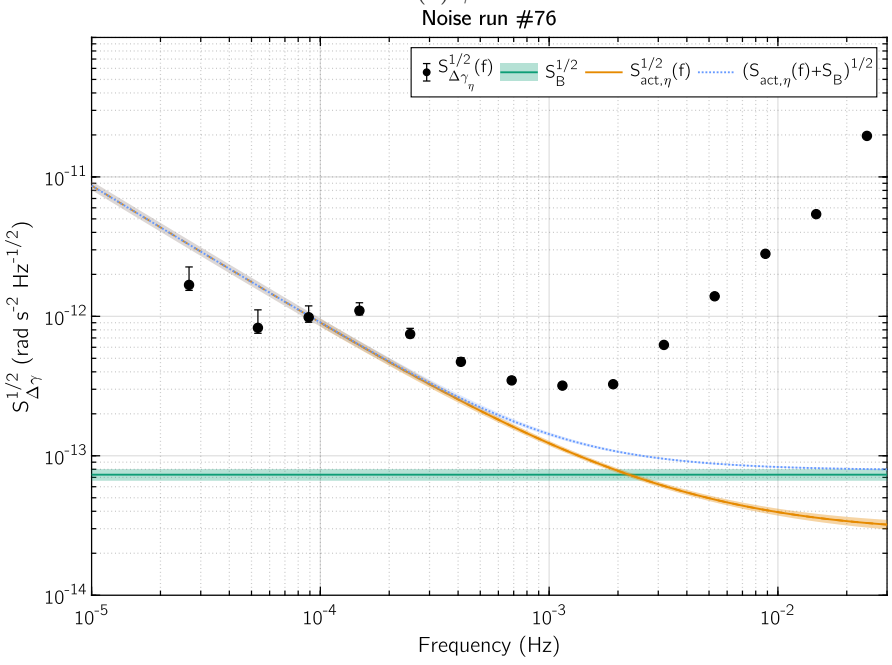

(l) η channel

Figure C.4: ASD of the angular differential acceleration $S^{1/2}_{\Delta\gamma}$ for the two angular degrees of freedom ϕ and η. The angular actuation noise $S^{1/2}_{\mathrm{act}}(f)$ is pictured as a continuous orange line down to 0.1 mHz, while its extension at lower frequencies is dashed. The angular Brownian noise $S^{1/2}_{\mathrm{B}}$ is the green line, and their sum $S_{\Delta\gamma,k}(f)$ is the blue dotted curve.

C.4 Cross correlation of differential angular acceleration with translational differential acceleration

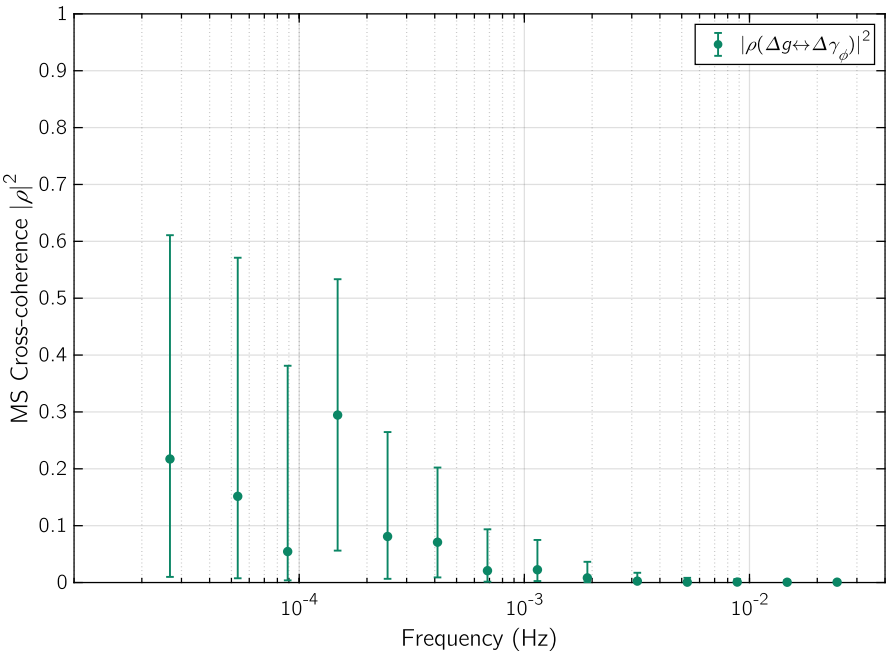

(a) ϕ channel

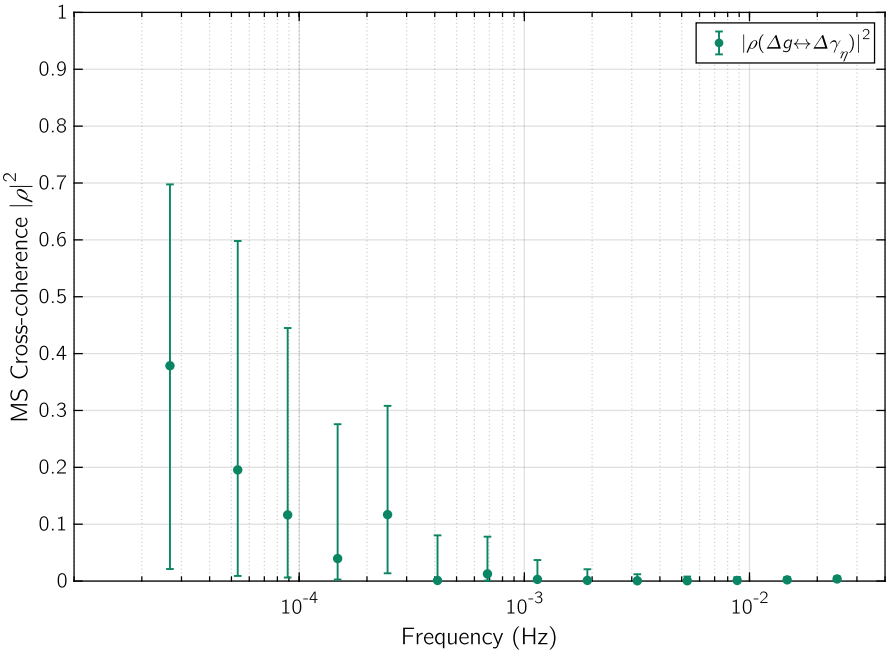

(b) η channel

Figure C.5: ASD of the angular differential acceleration $S_{\Delta\gamma}^{1/2}$ for the two angular degrees of freedom ϕ and η. The angular actuation noise $S_{\mathrm{act}}^{1/2}(f)$ is pictured as a continuous orange line down to 0.1 mHz, while its extension at lower frequencies is dashed. The angular Brownian noise $S_{\mathrm{B}}^{1/2}$ is the green line, and their sum $S_{\Delta\gamma,k}(f)$ is the blue dotted curve.

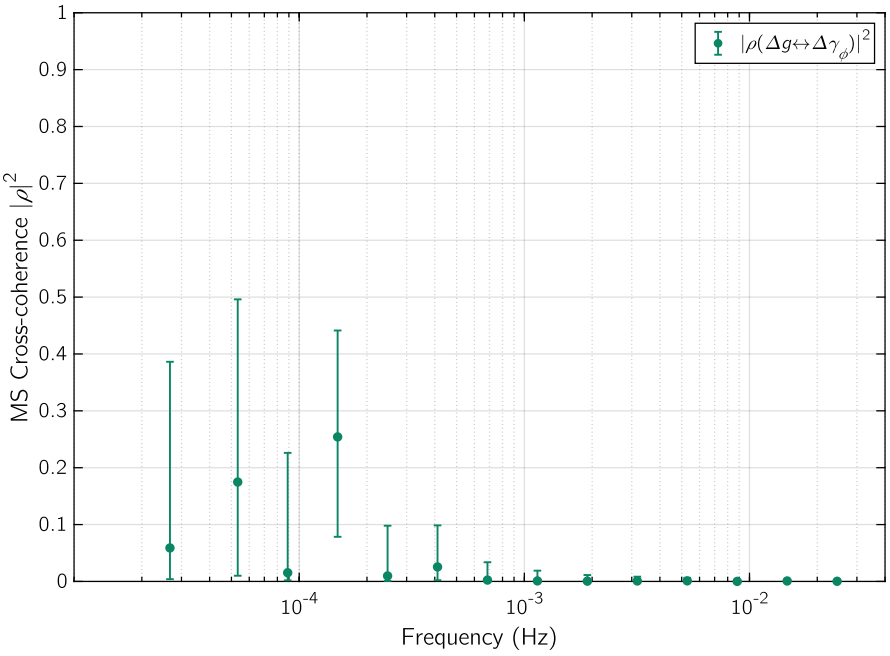

(c) ϕ channel

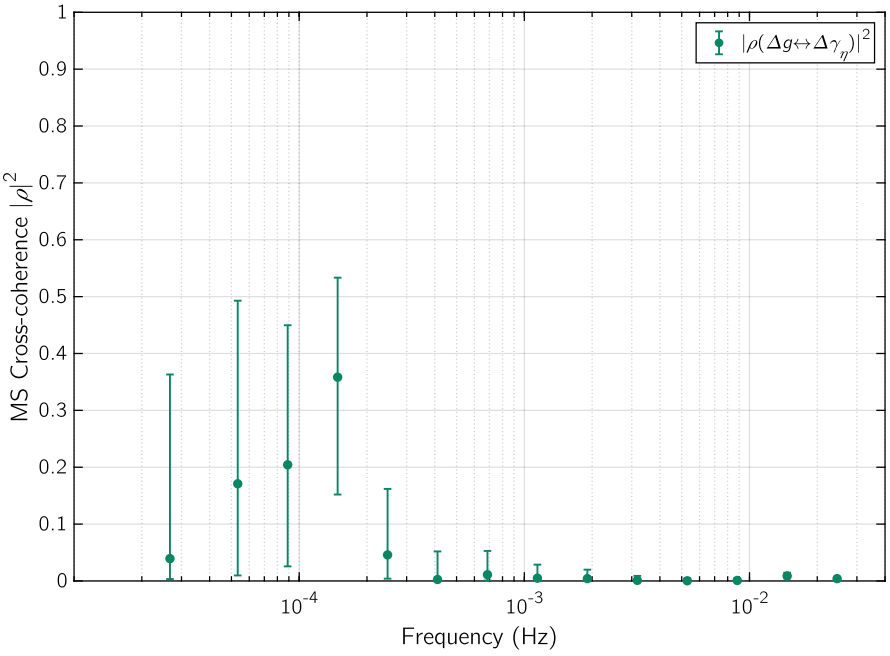

(d) η channel

Figure C.5: ASD of the angular differential acceleration $S_{\Delta\gamma}^{1/2}$ for the two angular degrees of freedom ϕ and η. The angular actuation noise $S_{\mathrm{act}}^{1/2}(f)$ is pictured as a continuous orange line down to 0.1 mHz, while its extension at lower frequencies is dashed. The angular Brownian noise $S_{\mathrm{B}}^{1/2}$ is the green line, and their sum $S_{\Delta\gamma,k}(f)$ is the blue dotted curve.

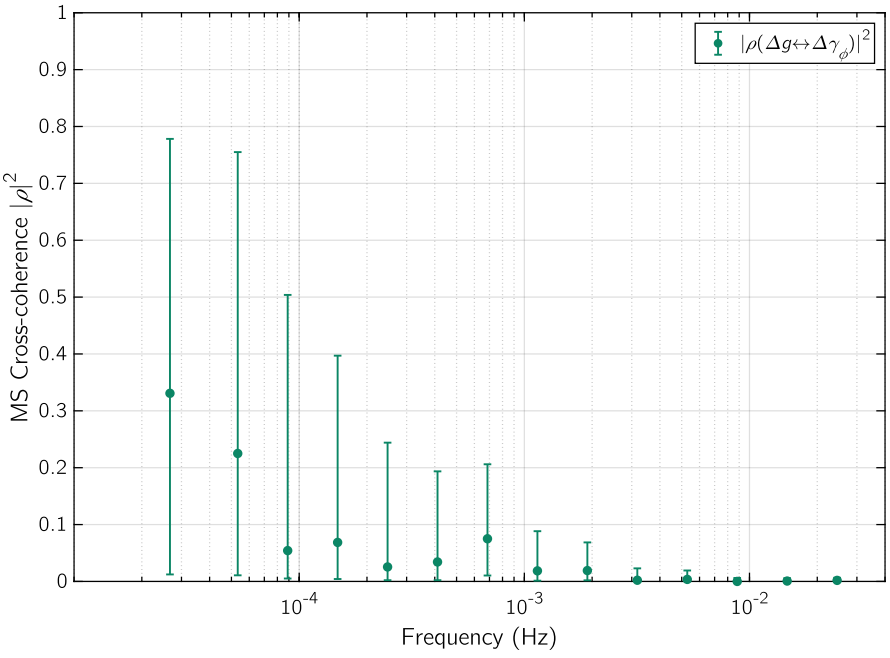

(e) ϕ channel

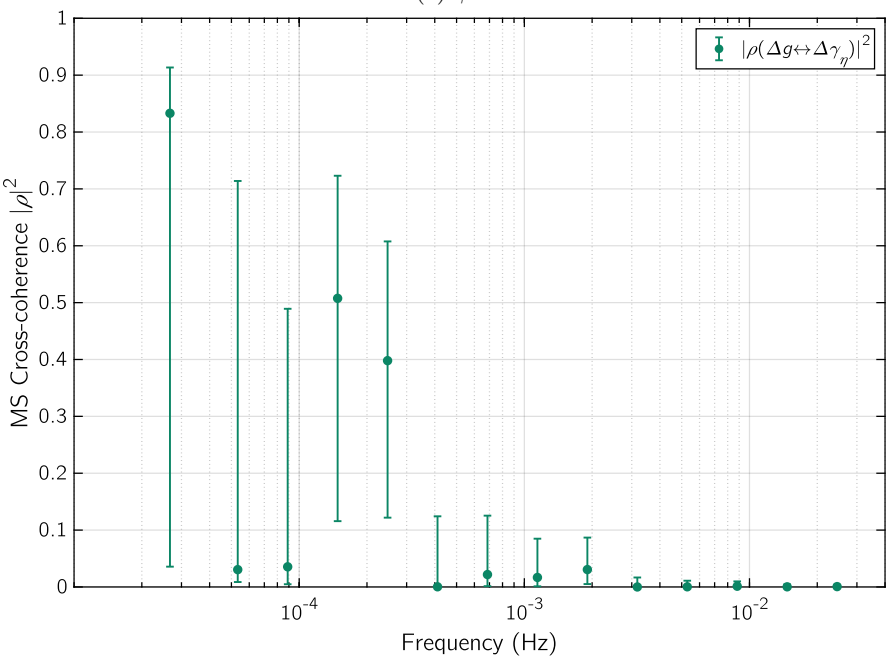

(f) η channel

Figure C.5: ASD of the angular differential acceleration $S_{\Delta\gamma}^{1/2}$ for the two angular degrees of freedom ϕ and η. The angular actuation noise $S_{\mathrm{act}}^{1/2}(f)$ is pictured as a continuous orange line down to 0.1 mHz, while its extension at lower frequencies is dashed. The angular Brownian noise $S_{\mathrm{B}}^{1/2}$ is the green line, and their sum $S_{\Delta\gamma,k}(f)$ is the blue dotted curve.

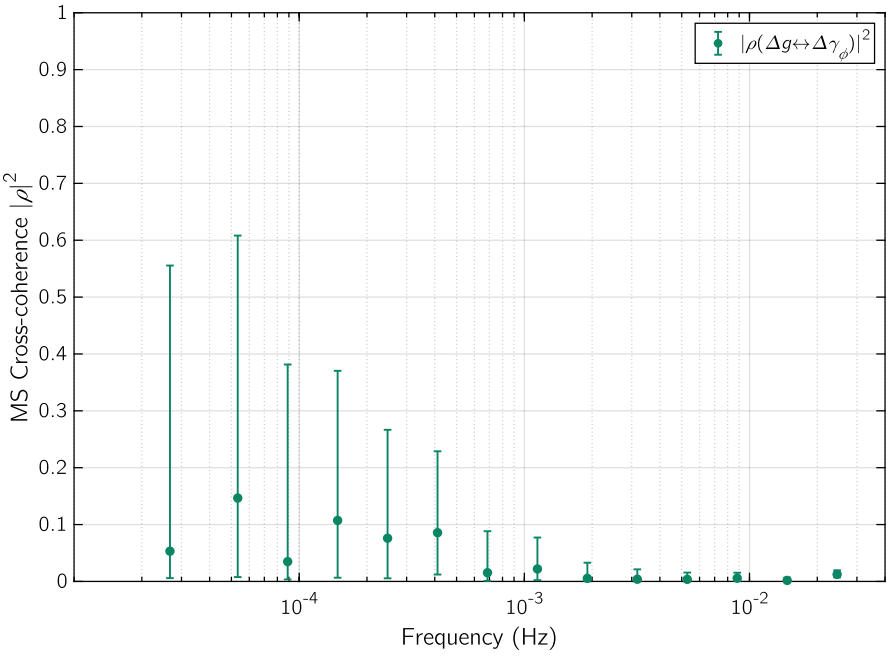

(g) ϕ channel

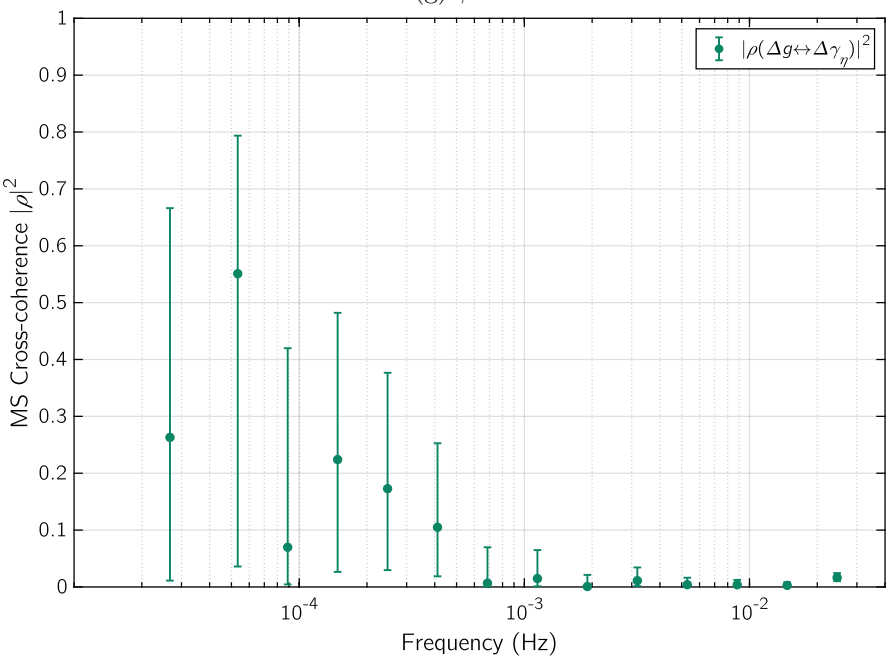

(h) η channel

Figure C.5: ASD of the angular differential acceleration $S_{\Delta\gamma}^{1/2}$ for the two angular degrees of freedom ϕ and η. The angular actuation noise $S_{\mathrm{act}}^{1/2}(f)$ is pictured as a continuous orange line down to 0.1 mHz, while its extension at lower frequencies is dashed. The angular Brownian noise $S_{\mathrm{B}}^{1/2}$ is the green line, and their sum $S_{\Delta\gamma,k}(f)$ is the blue dotted curve.

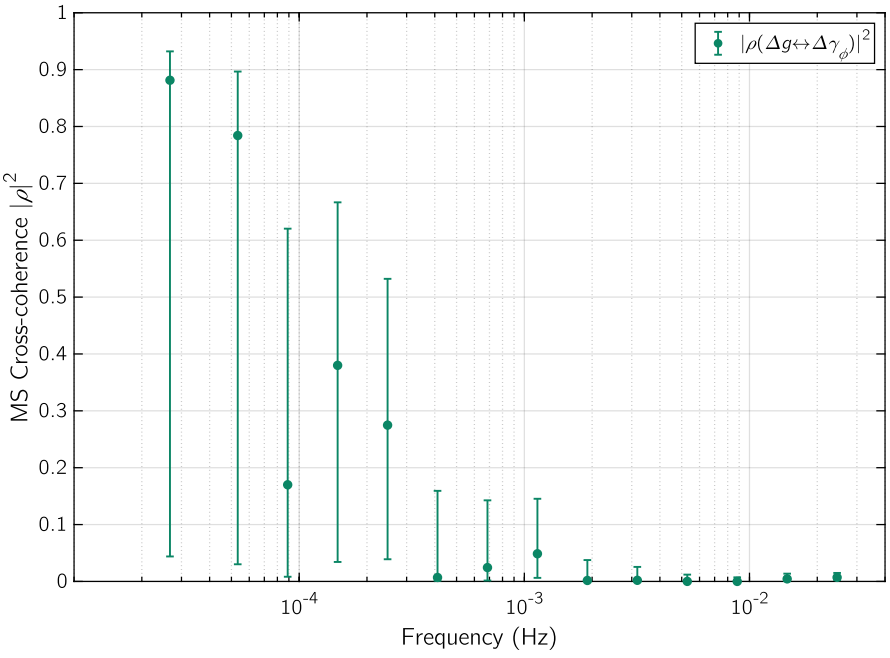

(i) ϕ channel

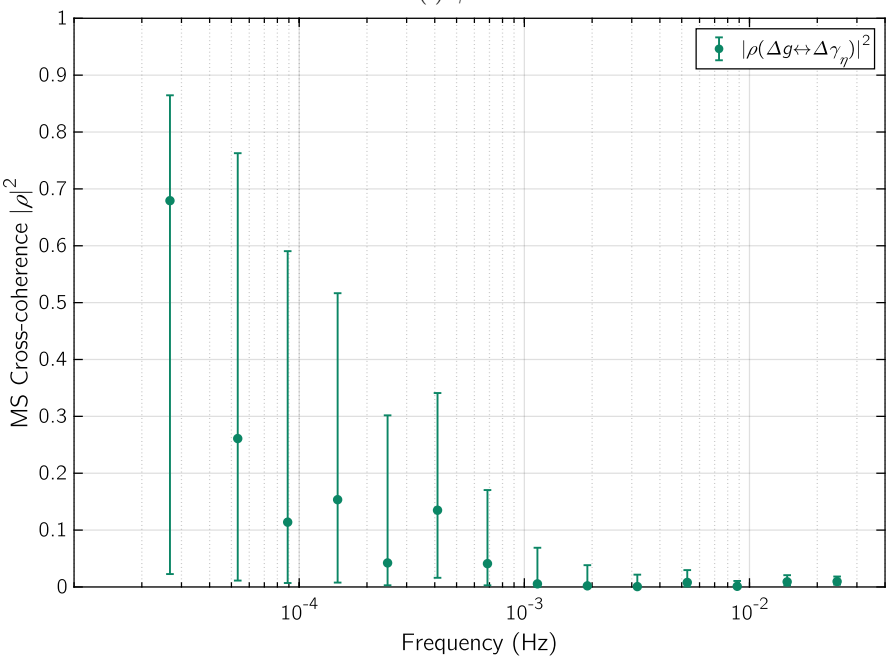

(j) η channel

Figure C.5: ASD of the angular differential acceleration $S_{\Delta\gamma}^{1/2}$ for the two angular degrees of freedom ϕ and η. The angular actuation noise $S_{\mathrm{act}}^{1/2}(f)$ is pictured as a continuous orange line down to 0.1 mHz, while its extension at lower frequencies is dashed. The angular Brownian noise $S_{\mathrm{B}}^{1/2}$ is the green line, and their sum $S_{\Delta\gamma,k}(f)$ is the blue dotted curve.

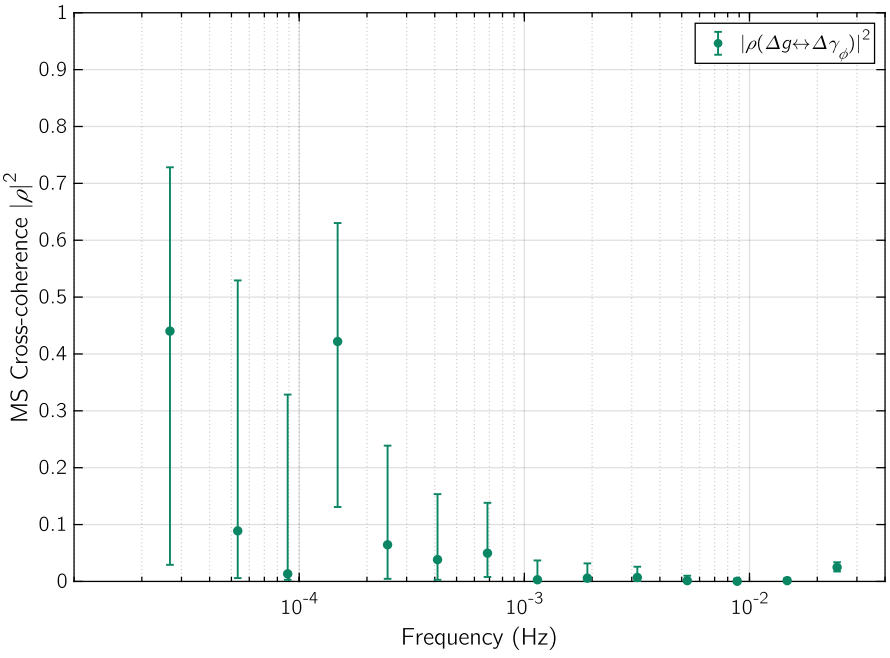

(k) ϕ channel

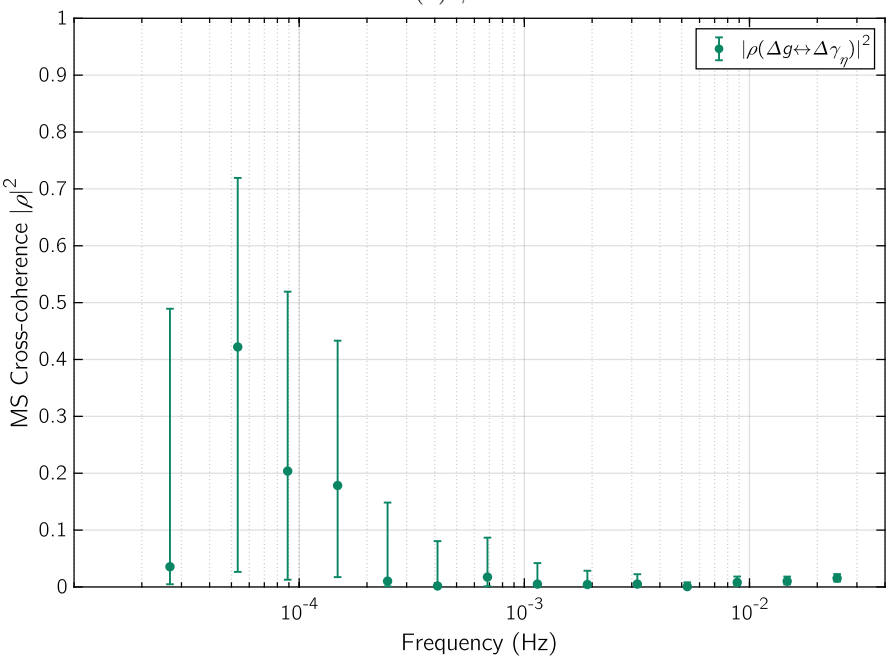

(l) η channel

Figure C.5: ASD of the angular differential acceleration $S_{\Delta\gamma}^{1/2}$ for the two angular degrees of freedom ϕ and η. The angular actuation noise $S_{\mathrm{act}}^{1/2}(f)$ is pictured as a continuous orange line down to 0.1 mHz, while its extension at lower frequencies is dashed. The angular Brownian noise $S_{\mathrm{B}}^{1/2}$ is the green line, and their sum $S_{\Delta\gamma,k}(f)$ is the blue dotted curve.

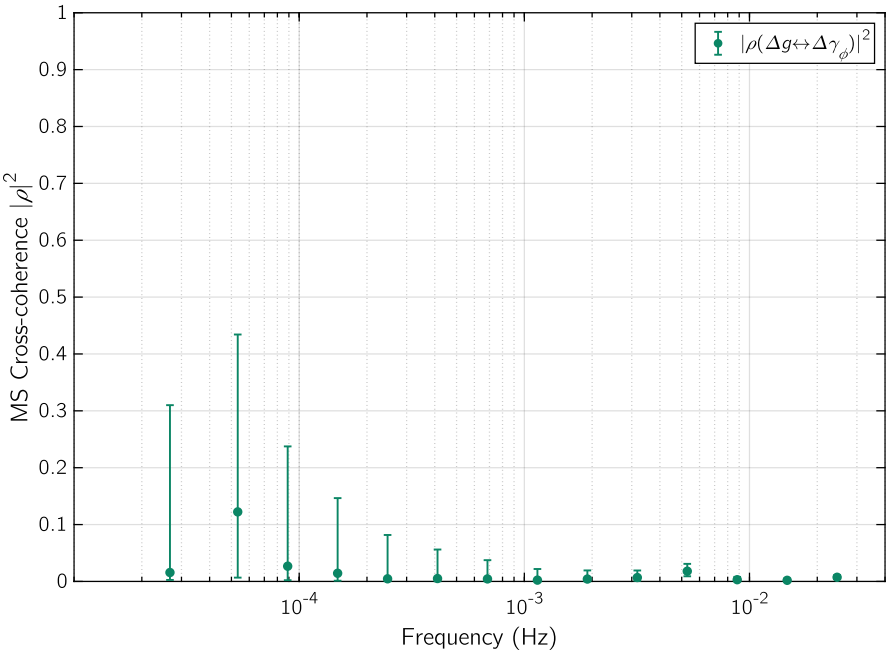

(a) ϕ channel

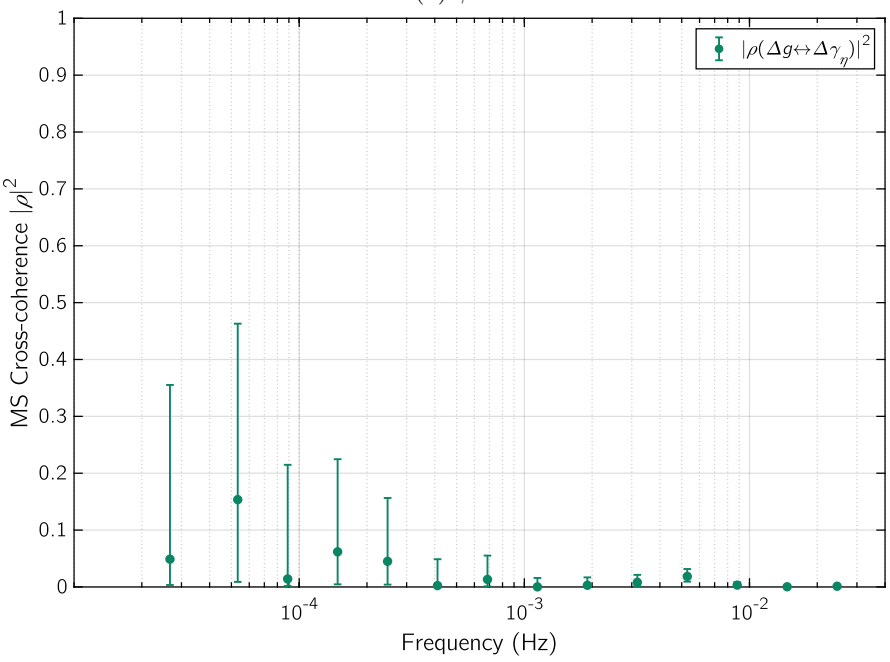

(b) η channel

Figure C.6: ASD of the angular differential acceleration $S_{\Delta\gamma}^{1/2}$ for the two angular degrees of freedom ϕ and η. The angular actuation noise $S_{\mathrm{act}}^{1/2}(f)$ is pictured as a continuous orange line down to 0.1 mHz, while its extension at lower frequencies is dashed. The angular Brownian noise $S_{\mathrm{B}}^{1/2}$ is the green line, and their sum $S_{\Delta\gamma,k}(f)$ is the blue dotted curve.

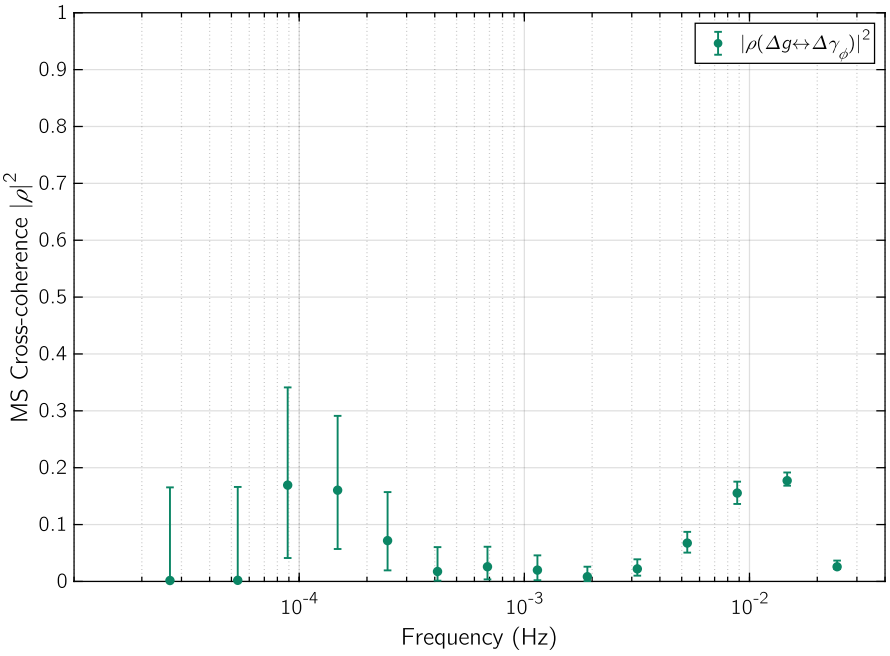

(c) ϕ channel

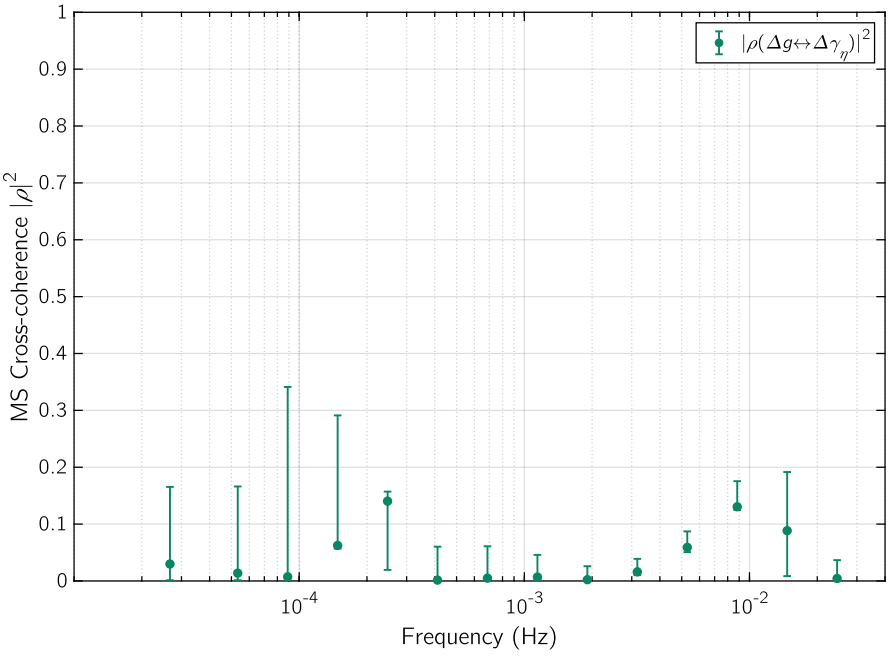

(d) η channel

Figure C.6: ASD of the angular differential acceleration $S_{\Delta\gamma}^{1/2}$ for the two angular degrees of freedom ϕ and η. The angular actuation noise $S_{\mathrm{act}}^{1/2}(f)$ is pictured as a continuous orange line down to 0.1 mHz, while its extension at lower frequencies is dashed. The angular Brownian noise $S_{\mathrm{B}}^{1/2}$ is the green line, and their sum $S_{\Delta\gamma,k}(f)$ is the blue dotted curve.

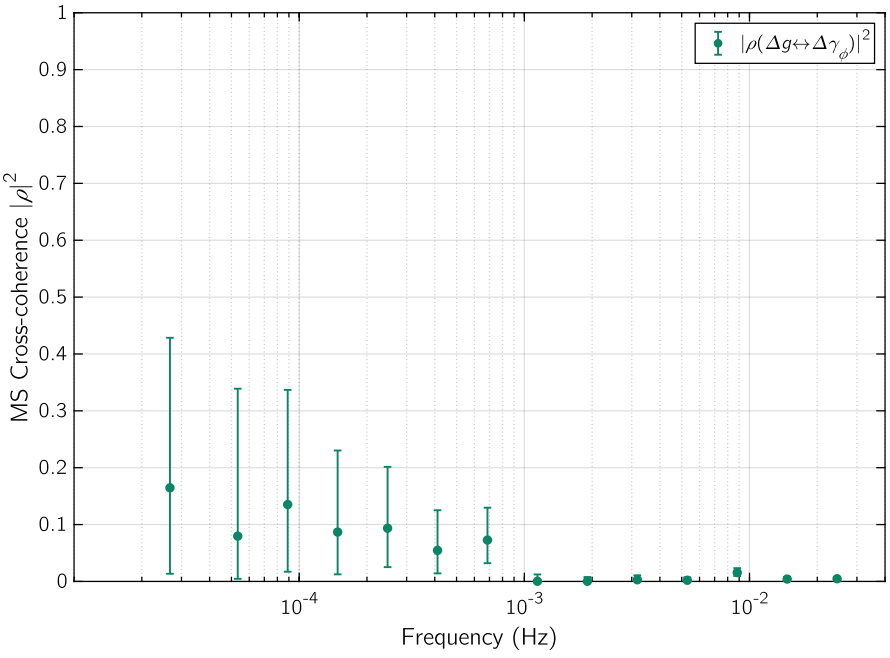

(e) ϕ channel

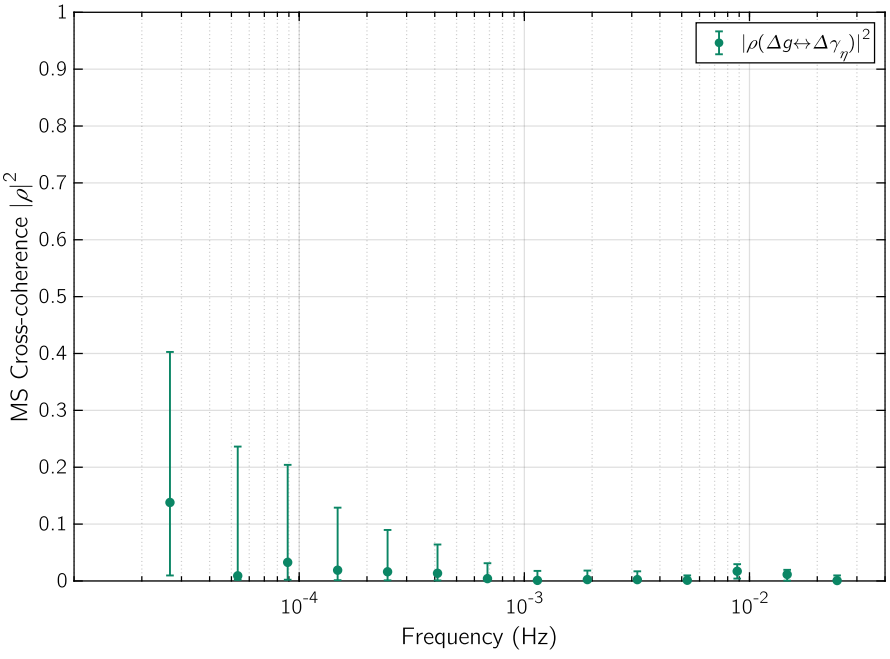

(f) η channel

Figure C.6: ASD of the angular differential acceleration $S_{\Delta\gamma}^{1/2}$ for the two angular degrees of freedom ϕ and η. The angular actuation noise $S_{\mathrm{act}}^{1/2}(f)$ is pictured as a continuous orange line down to 0.1 mHz, while its extension at lower frequencies is dashed. The angular Brownian noise $S_{\mathrm{B}}^{1/2}$ is the green line, and their sum $S_{\Delta\gamma,k}(f)$ is the blue dotted curve.

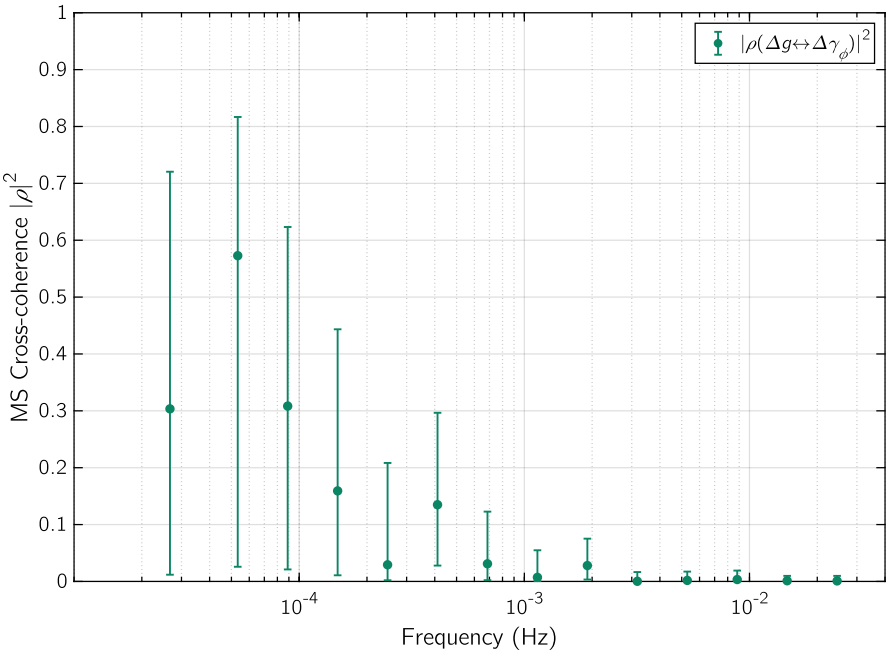

(g) ϕ channel

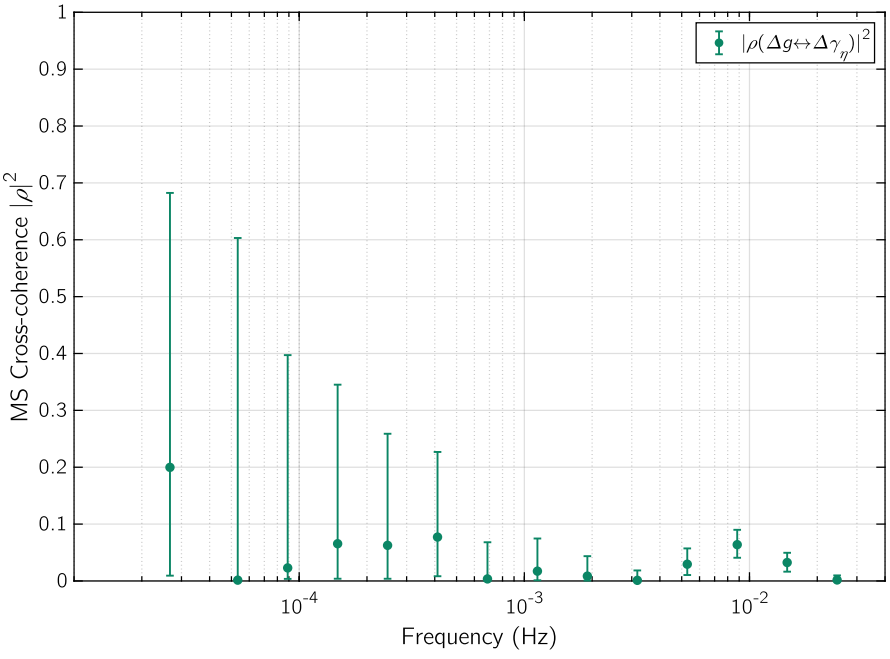

(h) η channel

Figure C.6: ASD of the angular differential acceleration $S_{\Delta\gamma}^{1/2}$ for the two angular degrees of freedom ϕ and η. The angular actuation noise $S_{\mathrm{act}}^{1/2}(f)$ is pictured as a continuous orange line down to 0.1 mHz, while its extension at lower frequencies is dashed. The angular Brownian noise $S_{\mathrm{B}}^{1/2}$ is the green line, and their sum $S_{\Delta\gamma,k}(f)$ is the blue dotted curve.

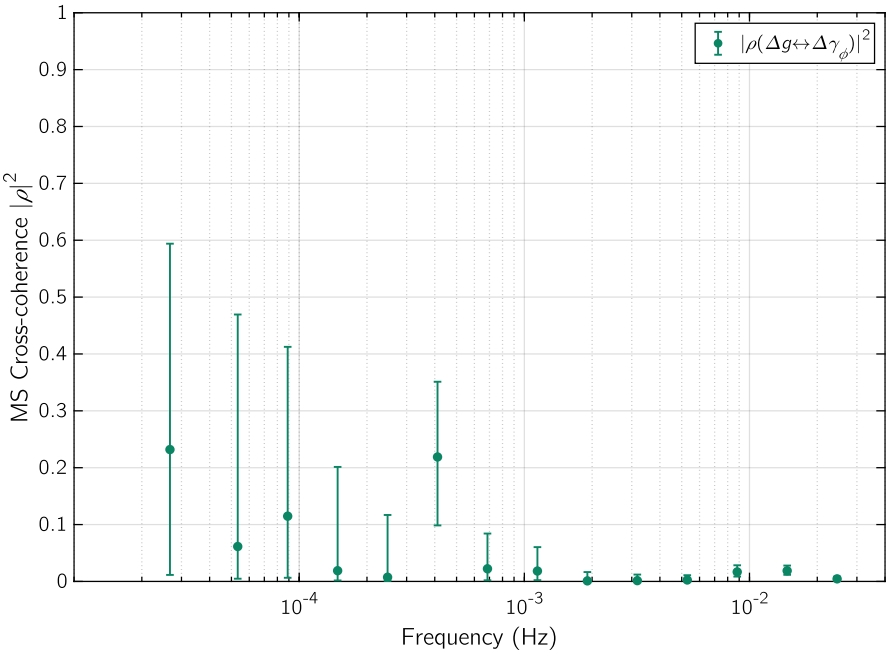

(i) ϕ channel

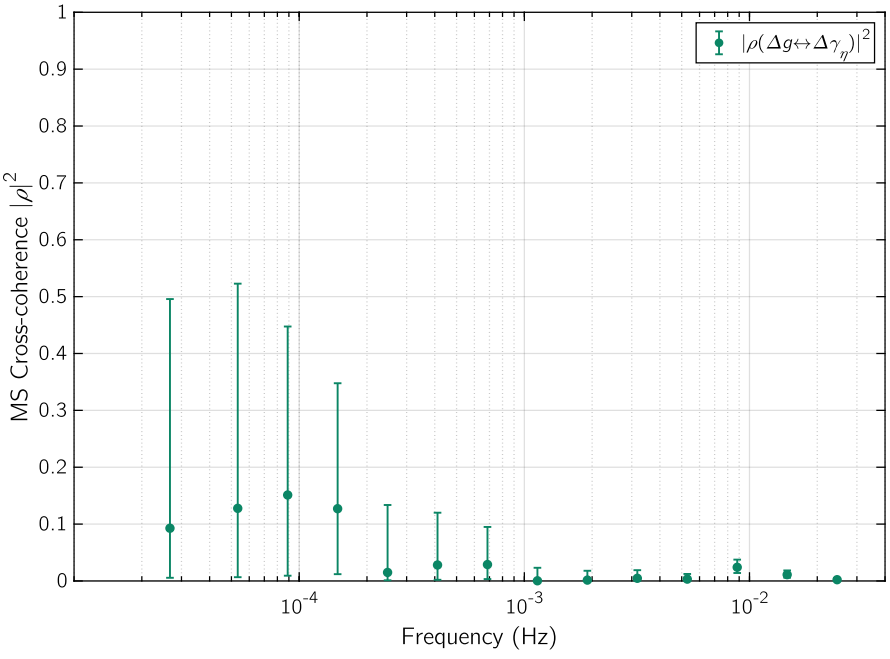

(j) η channel

Figure C.6: ASD of the angular differential acceleration $S_{\Delta\gamma}^{1/2}$ for the two angular degrees of freedom ϕ and η. The angular actuation noise $S_{\mathrm{act}}^{1/2}(f)$ is pictured as a continuous orange line down to 0.1 mHz, while its extension at lower frequencies is dashed. The angular Brownian noise $S_{\mathrm{B}}^{1/2}$ is the green line, and their sum $S_{\Delta\gamma,k}(f)$ is the blue dotted curve.

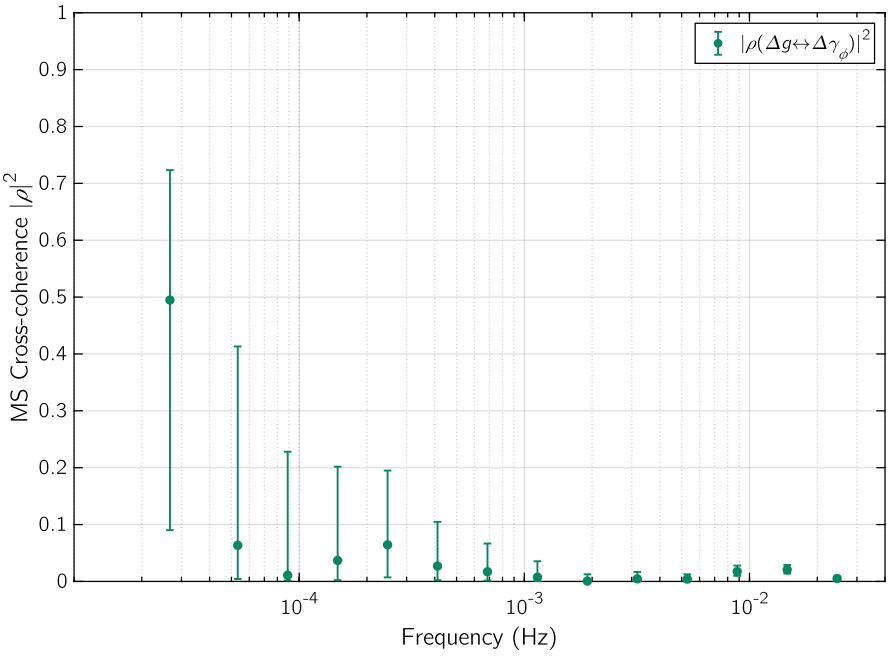

(k) ϕ channel

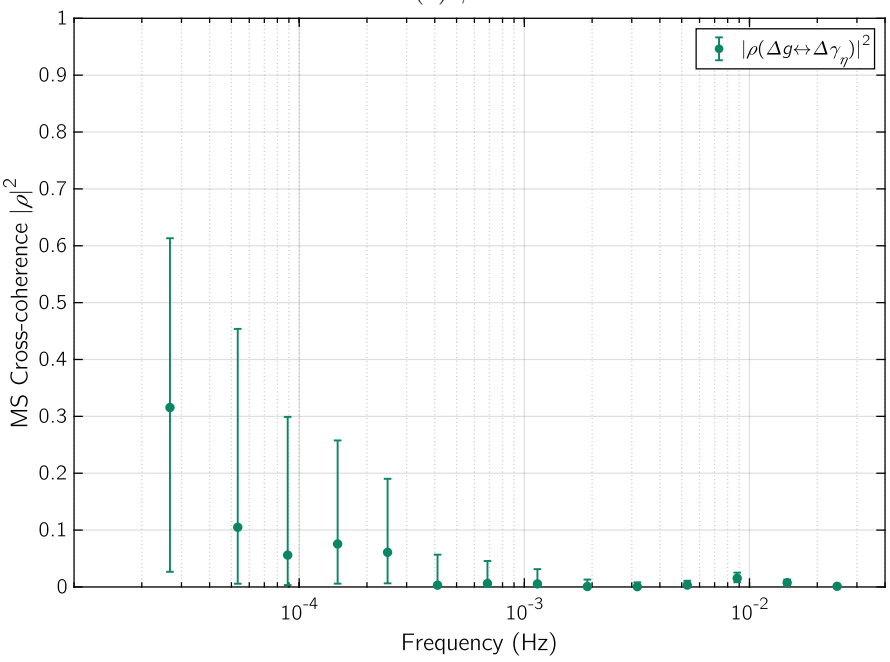

(l) η channel

Figure C.6: ASD of the angular differential acceleration $S_{\Delta\gamma}^{1/2}$ for the two angular degrees of freedom ϕ and η. The angular actuation noise $S_{\mathrm{act}}^{1/2}(f)$ is pictured as a continuous orange line down to 0.1 mHz, while its extension at lower frequencies is dashed. The angular Brownian noise $S_{\mathrm{B}}^{1/2}$ is the green line, and their sum $S_{\Delta\gamma,k}(f)$ is the blue dotted curve.

D List of all detected spurious signals in acceleration data

Table D.1: One-sided glitches fitted with (5.3) and (5.4).

#	Δv	$\sigma_{\Delta v}$	t_0	σ_{t_0}	τ_1	σ_{τ_1}	τ_2	σ_{τ_2}	Run
	($\mathrm{pm\,s^{-1}}$)	($\mathrm{pm\,s^{-1}}$)	(s)	(s)	(s)	(s)	(s)	(s)	
Ordinary ambient-T and T_{low} noise runs									
1	0.06	0.02	7 706 099	5					1
2	0.08	0.02	7 707 177	4					1
3	0.12	0.02	7 738 874	3					1
4	0.07	0.02	7 739 322	5					1
5	1.74	0.14	7 742 675	24	323	201	323	201	1
6	0.05	0.02	7 743 920	9					1
7	0.05	0.02	7 745 283	7					1
8	0.06	0.02	7 746 019	6					1
9	0.002	0.020	7 747 968	173					1
10	0.04	0.02	7 748 280	8					1
11	0.01	0.01	7 875 258	15					1
12	0.14	0.01	7 968 266	2					2
13	13.5	0.2	8 184 092	10	203	636	2516	1165	3
14	125.5	0.5	8 232 294	18	4435	1825	4437	1826	3
15	0.50	0.01	8 801 777.4	0.4					4
16	3.83	0.10	9 531 520	18	621	61	618	50	6
17	2.74	0.08	9 751 297	12	692	185	171	125	6
18	0.415	0.009	10 429 118.5	0.4					8
19	5.95	0.18	10 441 318	18	863	325	864	340	8
20	2.05	0.09	10 656 920	22	489	179	492	159	9

Continued on next page

#	Δv	$\sigma_{\Delta v}$	t_0	σ_{t_0}	τ_1	σ_{τ_1}	τ_2	σ_{τ_2}	Run
	($\mathrm{pm\,s^{-1}}$)	($\mathrm{pm\,s^{-1}}$)	(s)	(s)	(s)	(s)	(s)	(s)	
21	0.19	0.01	10 684 044	1					9
22	2.70	0.08	10 717 418	13	407	113	404	100	9
23	4.99	0.01	10 759 382.9	0.7	9	1	2	1	9
24	0.93	0.01	10 799 743.7	0.2					9
25	−0.19	0.01	11 010 357	9	7	0	7	0	9
26	0.160	0.008	11 371 597	1					9
27	0.126	0.009	12 623 842	1					12
28	−0.15	0.01	12 665 240	7	20	0	21	0	12
29	0.099	0.009	13 009 416	2					13
30	0.020	0.008	13 045 331	6					13
31	4.38	0.09	13 254 171	11	442	190	442	129	14
32	−8.24	0.03	14 286 709.2	0.3	28	0	20	0	17
33	0.45	0.02	14 443 214	5	8	23	71	13	17
34	95.1	0.2	14 475 335	4	2490	143	2487	144	17
35	8.01	0.14	14 549 815	15	818	341	818	325	18
36	0.152	0.02	14 596 749	3					18
37	−0.41	0.02	14 596 834	4	30	0	30	0	18
38	−2.16	0.05	15 710 068	4	146	55	146	57	24
39	0.208	0.009	15 963 377.7	0.9					27
40	−0.59	0.01	16 867 566	2	9	5	13	5	35
41	10.29	0.02	17 092 705.1	0.2	53	22	8	23	37
42	0.63	0.02	17 505 178	5	105	27	7	13	39
43	37.21	0.13	19 123 349	8	2203	139	2203	139	41
44	0.006	0.007	19 652 671	22					42
45	8.94	0.09	20 541 041	9	1736	489	470	188	43
46	1.92	0.02	21 441 995	1	6	3	77	10	45

Continued on next page

#	Δv	$\sigma_{\Delta v}$	t_0	σ_{t_0}	τ_1	σ_{τ_1}	τ_2	σ_{τ_2}	Run
	($\mathrm{pm\,s^{-1}}$)	($\mathrm{pm\,s^{-1}}$)	(s)	(s)	(s)	(s)	(s)	(s)	
47	1.661	0.009	21 505 220.3	0.8	4	1	9	2	45
48	4.76	0.08	21 902 731	7	352	95	353	87	46
49	1.338	0.007	29 464 623	1	8	1	4	1	58
50	46.84	0.12	29 619 653	7	2964	690	2967	690	58
51	−0.206	0.009	29 731 911	4	13	0	13	0	58
52	−0.565	0.009	29 760 254	1.2	13	3	13	4	58
53	1.829	0.008	29 818 009.2	0.6	9	2	4	2	58
54	2.76	0.06	30 245 103	19	815	383	814	399	59
55	1.14	0.02	30 455 779	6	111	33	2	5	59
56	1.329	0.007	30 553 420	1	2	2	12	2	59
57	0.408	0.006	30 747 487.6	0.3					59
58	−0.93	0.01	30 785 023.1	0.8	20	3	20	3	59
59	−8.17	0.04	33 831 552	1	63	11	684	65	61
60	0.979	0.007	33 855 397.3	0.8	6	2	11	2	61
61	0.222	0.004	34 084 189	0.4					61
62	1.24	0.03	34 092 462	8	254	70	255	58	61
63	0.090	0.005	34 226 223.9	1					61
64	1.83	0.06	34 264 044	20	594	404	597	348	61
65	0.34	0.01	34 280 681	3	37	12	37	12	61
66	2.41	0.03	34 600 719	2	277	28	73	24	61
67	22.02	0.01	34 645 097.9	0					61
68	405.1	0.3	34 735 779	5	7881	320	7874	320	61
69	136.7	0.4	34 877 341	17	5982	1625	5982	1103	61
70	2.005	0.004	36 907 896.7	0.3	11	1	4	1	64
71	−0.227	0.006	36 943 385	5	13	0	3	0	64
72	0.130	0.003	37 927 009.5	0.5					66

Continued on next page

#	Δv	$\sigma_{\Delta v}$	t_0	σ_{t_0}	τ_1	σ_{τ_1}	τ_2	σ_{τ_2}	Run
	($\mathrm{pm\,s^{-1}}$)	($\mathrm{pm\,s^{-1}}$)	(s)	(s)	(s)	(s)	(s)	(s)	
73	20.77	0.05	38 217 291	4	1180	65	2283	67	66
74	6.420	0.005	38 466 774.5	0.1	7	0	13	0	66
75	0.904	0.003	38 513 316.5	0.1					66
76	0.101	0.003	38 602 832.9	0.6					66
77	−0.233	0.004	38 740 233	3	6	0	7	0	66
78	6.749	0.004	38 902 038	0.1	11	0	6	0	66
79	0.064	0.003	40 061 127	1					67
80	0.099	0.003	40 135 784.3	0.6					67
81	0.173	0.003	40 153 329.7	0.4					67
82	0.228	0.009	40 203 621	3	45	26	46	26	67
83	10.28	0.01	40 302 448.7	0.1	119	8	21	2	67
84	0.526	0.003	46 039 312.8	0.1					74
85	0.046	0.002	46 103 417.7	0.9					74
86	−0.040	0.002	46 312 833	1					74
87	6.11	0.07	46 960 846	16	1479	384	1476	381	75
88	24.32	0.07	47 054 582	6	1462	81	1460	81	75
89	1.34	0.01	47 106 542	1	85	3	7	5	75
90	0.543	0.004	47 222 178.2	0.2					75
91	5.52	0.05	47 224 574	9	959	130	956	177	75
92	0.900	0.004	47 301 544.2	0.7	10	0	5	0	75
93	−0.392	0.005	47 417 586	2	5	0	5	0	75
94	0.263	0.004	48 005 383.9	0.3					76
95	0.408	0.009	48 028 673	2	6	6	32	14	76
96	10.24	0.06	48 085 790	3	78	47	1613	47	76
97	0.72	0.01	48 414 159	1	53	9	14	6	76
98	10.87	0.07	48 453 420	10	1572	82	1573	81	76

Continued on next page

#	Δv	$\sigma_{\Delta v}$	t_0	σ_{t_0}	τ_1	σ_{τ_1}	τ_2	σ_{τ_2}	Run
	($\mathrm{pm\,s^{-1}}$)	($\mathrm{pm\,s^{-1}}$)	(s)	(s)	(s)	(s)	(s)	(s)	
Cold $T_0 = 0\,^\circ\mathrm{C}$ noise runs									
99	0.65	0.02	44 597 376.3	0.5					70
100	0.70	0.02	44 602 619.3	0.6					70
101	0.57	0.02	44 608 384.9	0.6					70
102	−0.30	0.02	44 611 047	1					70
103	0.70	0.02	44 617 567.2	0.4					70
104	4.1	0.5	44 621 936	3					70
105	25.4	0.5	44 622 220	2	8	1	84	1	70
106	0.41	0.02	44 626 832	1					70
107	21.33	0.05	44 628 880.3	0.2	10	1	34	1	70
108	0.85	0.02	44 632 649	0.5					70
109	−2.90	0.03	44 635 704	2	3	3	19	3	70
110	3.44	0.03	44 639 617	1	26	5	5	5	70
111	9.27	0.04	44 643 231	0.5	40	4	6	1	70
112	1.09	0.09	44 649 961	2					70
113	2.05	0.05	44 650 322.3	0.5					70
114	2.26	0.02	44 651 144	1	6	3	6	2	70
115	1.03	0.02	44 660 535.3	0.3					70
116	0.50	0.02	44 663 549.4	0.7					70
117	0.34	0.02	44 665 102	0.9					70
118	−0.29	0.02	44 668 933	2					70
119	0.33	0.02	44 669 530	1					70
120	13.7	0.2	44 671 024	4	174	0	174	0	70
121	−0.29	0.01	44 673 485	1					70
122	0.24	0.02	44 674 920	1					70
123	0.29	0.02	44 677 837	1					70

Continued on next page

#	Δv	$\sigma_{\Delta v}$	t_0	σ_{t_0}	τ_1	σ_{τ_1}	τ_2	σ_{τ_2}	Run
	($\mathrm{pm\,s^{-1}}$)	($\mathrm{pm\,s^{-1}}$)	(s)	(s)	(s)	(s)	(s)	(s)	
124	0.27	0.02	44 678 355	1					70
125	0.33	0.02	44 680 772	1					70
126	0.33	0.02	44 680 968	1					70
127	0.66	0.06	44 681 903	2					70
128	1.12	0.05	44 683 019.4	0.8					70
129	1.43	0.02	44 685 506.3	0.2					70
130	0.39	0.3	44 687 412	15					70
131	1.2	0.3	44 688 047	5					70
132	0.3	0.3	44 688 583	22					70
133	7.78	0.05	44 689 062.7	0.1					70
134	0.5	0.2	44 691 247	10					70
135	9.40	0.05	44 691 924.5	0.5	28	1	9	1	70
136	0.5	0.2	44 692 092	11					70
137	1.4	0.2	44 697 431	2					70
138	0.2	0.2	44 697 558	15					70
139	4.27	0.06	44 698 063.2	0.3					70
140	7.50	0.02	44 705 296.7	0.9	5	1	3	2	70
141	0.69	0.06	44 708 255	2					70
142	2.19	0.06	44 708 833	2	21	6	20	4	70
143	0.26	0.06	44 711 231	5					70
144	1.23	0.03	44 711 898	0.5					70
145	0.52	0.06	44 712 033	2					70
146	15.4	0.5	44 716 067	12	835	464	8	23	70
147	0.6	0.1	44 718 240	3					70
148	2.15	0.08	44 718 833.3	0.7					70
149	0.7	0.1	44 719 489	3					70

Continued on next page

#	Δv	$\sigma_{\Delta v}$	t_0	σ_{t_0}	τ_1	σ_{τ_1}	τ_2	σ_{τ_2}	Run
	($\mathrm{pm\,s^{-1}}$)	($\mathrm{pm\,s^{-1}}$)	(s)	(s)	(s)	(s)	(s)	(s)	
150	0.163	0.005	44 739 300	2	41	11	41	9	71
151	0.2	0.3	44 739 936	42					71
152	14.72	0.03	44 740 117.5	0.2	14	7	105	52	71
153	0.450	0.003	44 741 826	5	5	2	1	2	71
154	0.0	0.4	44 743 618	769					71
155	−0.1	0.4	44 744 171	123					71
156	8.426	0.007	44 744 619.1	0.1	7	0	11	0	71
157	0.7	0.1	44 745 159	4					71
158	2.56	0.08	44 745 693.7	0.6					71
159	1.1	0.1	44 745 822.5	3					71
160	0.9	0.1	44 746 023	3					71
161	0.369	0.004	44 747 281	3	9	3	4	2	71
162	0.075	0.003	44 750 541.1	0.9					71
163	0.162	0.004	44 752 328	3	11	4	5	5	71
164	1.001	0.009	44 753 830	3	12	1	2	3	71
165	0.996	0.008	44 753 830	3	2	2	11	1	71
166	0.957	0.008	44 753 831	3	10	2	2	2	71
167	5.574	0.005	44 757 054.4	0.1	18	0	5	0	71
168	0.422	0.003	44 758 810	2	2	2	11	3	71
169	0.1	0.2	44 760 639	48					71
170	5.851	0.009	44 761 650.1	0.2	6	1	11	1	71
171	0.1	0.2	44 762 564	55					71
172	0.7	0.2	44 768 690	3					71
173	2.36	0.03	44 769 172.6	0.3					71
174	0.0	0.1	44 769 429	42					71
175	21.970	0.009	44 770 680.9	0.1	120	53	14	6	71

Continued on next page

#	Δv	$\sigma_{\Delta v}$	t_0	σ_{t_0}	τ_1	σ_{τ_1}	τ_2	σ_{τ_2}	Run
	($\mathrm{pm\,s^{-1}}$)	($\mathrm{pm\,s^{-1}}$)	(s)	(s)	(s)	(s)	(s)	(s)	
176	0.520	0.009	44 773 560	4	2	2	12	2	71
177	−0.159	0.003	44 775 262.4	0.4					71
178	−0.141	0.008	44 777 555	1					71
179	0.126	0.009	44 778 355	1					71
180	0.0	0.3	44 785 138	189					71
181	8.289	0.009	44 785 544.7	0.2	3	0	9	0	71
182	1.186	0.004	44 788 822.6	0.5	9	1	4	1	71
183	0.047	0.002	44 793 911.3	0.9					71
184	0.049	0.003	44 797 369	1					71
185	0.41	0.09	44 799 661	4					71
186	−2.51	0.02	44 800 069	0.1					71
187	0.13	0.02	44 803 269	4					71
188	−0.629	0.005	44 803 816.9	0.2					71
189	2.14	0.04	44 806 290.6	0.4					71
190	0.13	0.07	44 806 537	12					71
191	1.04	0.07	44 807 588	1					71
192	0.06	0.07	44 807 776	26					71
193	0.21	0.07	44 808 161	7					71
194	0.06	0.07	44 808 576	24					71
195	0.142	0.005	44 810 983.9	0.8					71
196	41.26	0.07	44 813 696.5	0.3	5	0	78	0	71
197	−1.44	0.01	44 819 337	1	34	17	6	14	71
198	0.16	0.04	44 819 749	5					71
199	4.69	0.03	44 823 305.5	0.4	18	1	18	1	71
200	0.4	0.1	44 824 448	5					71
201	0.1	0.1	44 825 401	29					71

Continued on next page

#	Δv	$\sigma_{\Delta v}$	t_0	σ_{t_0}	τ_1	σ_{τ_1}	τ_2	σ_{τ_2}	Run
	($\mathrm{pm\,s^{-1}}$)	($\mathrm{pm\,s^{-1}}$)	(s)	(s)	(s)	(s)	(s)	(s)	
202	2.148	0.007	44 828 828.4	0.3	12	2	34	1	71
203	0.07	0.05	44 830 037	14					71
204	1.1	0.1	44 836 121	2					71
205	3.2	0.1	44 837 162.3	0.7					71
206	0.1	0.1	44 837 588	19					71
207	−0.8	0.1	44 838 087	4					71
208	0.0	0.1	44 839 815	90					71
209	3.7	0.1	44 840 797.1	0.5					71
210	8.3	0.1	44 843 456.5	0.2					71
211	3.47	0.01	44 846 148.6	0.1					71
212	0.13	0.09	44 847 678	14					71
213	0.42	0.09	44 849 086	4					71
214	5.58	0.09	44 851 420.3	0.3					71
215	0.9	0.2	44 852 918	4					71
216	0.1	0.2	44 853 273	73					71
217	1.0	0.2	44 853 609	4					71
218	0.12	0.02	44 857 074	3					71
219	0.473	0.007	44 858 460.2	0.3					71
220	0.18	0.02	44 859 101	2					71
221	0.54	0.04	44 861 000	1					71
222	1.24	0.02	44 863 152.5	0.3					71
223	0.0	0.2	44 868 925	81					71
224	12.66	0.09	44 870 960.5	0.8	15	0	105	1	71
225	1.0	0.2	44 872 723	3					71
226	0.344	0.002	44 876 306.6	0.1					71
227	0.586	0.004	44 883 983.4	0.7	14	2	6	2	71

Continued on next page

#	Δv	$\sigma_{\Delta v}$	t_0	σ_{t_0}	τ_1	σ_{τ_1}	τ_2	σ_{τ_2}	Run
	($\mathrm{pm\,s^{-1}}$)	($\mathrm{pm\,s^{-1}}$)	(s)	(s)	(s)	(s)	(s)	(s)	
228	0.13	0.02	44 888 348	3					71
229	0.117	0.002	44 893 513.7	0.3					71
230	2.288	0.005	44 897 799.9	0.2	9	9	27	9	71
231	−1.25	0.02	44 903 332	2	3	1	13	1	71
232	1.16	0.03	44 906 968	5	64	4	4	2	71
233	1.15	0.03	44 906 968	5	64	5	4	4	71
234	0.10	0.02	44 907 547	5					71
235	−0.38	0.02	44 908 060	1					71
236	−25.68	0.05	44 909 810.2	0.3	31	1	431	8	71
237	0.073	0.005	44 915 271	1					71
238	0.117	0.003	44 915 808.8	0.6					71
239	0.031	0.002	44 918 023	2					71
240	0.55	0.009	44 920 959	2	55	6	7	3	71
241	19.09	0.08	44 925 612.3	0.5	43	1	166	2	71
242	0.4	0.1	44 926 921	8					71
243	0.7	0.1	44 927 373	4					71
244	0.1	0.1	44 927 977	47					71
245	−0.112	0.002	44 938 450.2	0.4					71
246	0.7	0.3	44 947 172	8					71
247	12.16	0.04	44 948 648.4	0.2	13	1	13	1	71
248	0.13	0.09	44 950 668	14					71
249	0.35	0.09	44 951 048	5					71
250	1.20	0.08	44 952 061	1					71
251	0.09	0.09	44 952 681	20					71
252	4.20	0.06	44 953 070	1	10	1	19	2	71
253	0.24	0.09	44 954 670	8					71

Continued on next page

#	Δv	$\sigma_{\Delta v}$	t_0	σ_{t_0}	τ_1	σ_{τ_1}	τ_2	σ_{τ_2}	Run
	($\mathrm{pm\,s^{-1}}$)	($\mathrm{pm\,s^{-1}}$)	(s)	(s)	(s)	(s)	(s)	(s)	
254	0.05	0.09	44 955 164	37					71
255	0.0	0.2	44 956 816	138					71
256	9.39	0.06	44 957 239.9	0.7	26	0	6	0	71
257	0.2	0.2	44 957 979	19					71
258	0.0	0.2	44 958 110	3523					71
259	0.1	0.2	44 960 163	35					71
260	0.47	0.03	44 961 146	1					71
261	3.2	0.1	44 961 544	11	6	4	427	25	71
262	2.0	0.1	44 961 939	7	25	3	201	15	71
263	13.8	0.1	44 967 629	1	9	0	51	0	71
264	58.10	0.01	44 984 533.6	0.1	14	0	157	0	71
265	0.06	0.03	44 988 021	10					71
266	0.07	0.03	44 989 677	8					71
267	0.980	0.004	44 990 772.4	0.1					71
268	−0.2	0.2	44 992 429	26					71
269	8.321	0.008	44 993 606.9	0.1	12	1	12	1	71
270	0.40	0.02	44 997 454	1					71
271	0.76	0.01	44 997 969.3	0.3					71
272	0.08	0.02	44 998 852	6					71
273	0.11	0.02	44 999 529	4					71
274	2.2	0.2	45 001 697	2					71
275	11.9	0.1	45 004 378	1	11	0	48	0	71
276	0.05	0.01	45 008 254	5					71
277	0.502	0.004	45 009 294.1	0.9	6	2	14	2	71
278	−1.07	0.07	45 012 310	1					71
279	3.14	0.05	45 014 129	1	11	1	10	1	71

Continued on next page

#	Δv	$\sigma_{\Delta v}$	t_0	σ_{t_0}	τ_1	σ_{τ_1}	τ_2	σ_{τ_2}	Run
	($\mathrm{pm\,s^{-1}}$)	($\mathrm{pm\,s^{-1}}$)	(s)	(s)	(s)	(s)	(s)	(s)	
280	2.12	0.03	45 017 138	1	38	1	14	1	71
281	0.33	0.03	45 017 820	2					71
282	0.21	0.03	45 019 506	3					71
283	0.095	0.003	45 027 652.2	0.6					71
284	0.080	0.009	45 030 851	2					71
285	0.340	0.004	45 033 803.2	0.2					71
286	15.846	0.004	45 036 643.7	0.4	12	1	8	2	71
287	−0.069	0.007	45 043 541	2					71
288	0.187	0.005	45 044 041.9	0.5					71
289	0.101	0.004	45 050 658.6	0.9					71
290	0.097	0.005	45 050 943	0.9					71
291	0.037	0.005	45 051 907	3					71
292	0.12	0.02	45 057 452	2					71
293	0.459	0.005	45 059 162.7	0.2					71
294	0.11	0.02	45 063 100	4					71
295	0.818	0.009	45 064 067.5	0.2					71
296	0.28	0.02	45 065 443	2					71
297	0.063	0.006	45 074 345	2					71
298	0.240	0.005	45 075 595	2	6	5	20	11	71
299	8.93	0.01	45 079 648.9	0.1	11	0	80	1	71
300	12.965	0.009	45 081 767	0	13	1	13	1	71
301	3.198	0.003	45 083 844.2	0.1	5	0	16	0	71
302	0.2	0.1	45 086 678	16					71
303	5.402	0.009	45 088 706.9	0.2	7	0	6	1	71
304	0.182	0.003	45 095 519.7	0.3					71
305	0.570	0.002	45 099 409.9	0.1					71

Continued on next page

#	Δv	$\sigma_{\Delta v}$	t_0	σ_{t_0}	τ_1	σ_{τ_1}	τ_2	σ_{τ_2}	Run
	($\mathrm{pm\,s^{-1}}$)	($\mathrm{pm\,s^{-1}}$)	(s)	(s)	(s)	(s)	(s)	(s)	
306	1.07	0.04	45 104 485	0.7					71
307	1.28	0.03	45 104 913.3	0.5					71
308	0.3	0.2	45 108 070	13					71
309	1.9	0.2	45 108 589	2					71
310	0.3	0.2	45 109 079	16					71
311	7.99	0.05	45 110 189	0.1					71
312	0.5	0.2	45 112 713	8					71
313	5.484	0.005	45 123 251	0					71
314	1.06	0.02	45 125 260.5	0.4					71
315	−0.07	0.04	45 127 354	11					71
316	0.71	0.03	45 127 921.7	0.9					71
317	−0.245	0.006	45 132 485	3	34	5	4	11	71
318	0.08	0.02	45 136 339	6					71
319	0.714	0.004	45 137 270.7	0.1					71
320	1.56	0.02	45 138 857.1	0.9	24	2	10	1	71
321	0.33	0.03	45 139 349	2					71
322	0.07	0.03	45 140 066	9					71
323	−0.01	0.03	45 141 537	50					71
324	−0.05	0.03	45 143 352	13					71
325	13.445	0.005	45 151 526	0	19	0	8	0	71
326	0.14	0.02	45 154 148	3					71
327	0.54	0.02	45 155 074	0.6					71
328	0.52	0.02	45 155 862.5	0.7					71
329	0.16	0.02	45 155 976	3					71
330	0.07	0.01	45 159 814	3					71
331	0.331	0.004	45 162 219.8	0.3					71

Continued on next page

#	Δv	$\sigma_{\Delta v}$	t_0	σ_{t_0}	τ_1	σ_{τ_1}	τ_2	σ_{τ_2}	Run
	($\mathrm{pm\,s^{-1}}$)	($\mathrm{pm\,s^{-1}}$)	(s)	(s)	(s)	(s)	(s)	(s)	
332	−0.038	0.005	45 165 810	3					71
333	0.051	0.005	45 166 818	2					71
334	0.121	0.004	45 169 503.5	0.6					71
335	0.614	0.004	45 176 850.8	0.8	8	2	8	3	71
336	0.04	0.02	45 178 087	8					71
337	8.503	0.009	45 184 793.4	0.2	6	3	83	39	71
338	16.631	0.005	45 188 417	0	13	0	20	0	71
339	0.24	0.04	45 195 426	4					71
340	2.01	0.02	45 195 958.9	0.8	9	1	8	0	71
341	0.12	0.04	45 197 026	7					71
342	0.25	0.04	45 198 304	4					71
343	0.144	0.004	45 306 412.2	0.5					72
344	0.059	0.003	45 310 091.7	0.9					72
345	12.5	0.2	45 316 287	2	17	1	333	3	72
346	12.5	0.2	45 316 287	2	17	2	333	1	72
347	0.147	0.003	45 318 817	4	3	5	20	5	72
348	0.078	0.003	45 319 588.9	0.8					72
349	14.203	0.006	45 321 010	0	8	0	12	0	72
350	11.698	0.005	45 321 951	0	36	0	14	0	72
351	0.076	0.002	45 325 855.9	0.6					72
352	0.8	0.01	45 327 850	2	207	25	51	19	72
353	0.257	0.004	45 332 900	5	2	7	17	4	72
354	3.25	0.003	45 334 110.6	0.4	10	0	1	0	72
355	0.06	0.002	45 338 940.2	0.8					72
356	0.423	0.003	45 342 811	3	7	2	2	3	72
357	0.662	0.004	45 344 312	2	11	2	2	3	72

Continued on next page

#	Δv	$\sigma_{\Delta v}$	t_0	σ_{t_0}	τ_1	σ_{τ_1}	τ_2	σ_{τ_2}	Run
	($\mathrm{pm\,s^{-1}}$)	($\mathrm{pm\,s^{-1}}$)	(s)	(s)	(s)	(s)	(s)	(s)	
358	0.068	0.002	45 345 602.8	0.7					72
359	1.528	0.008	45 357 241.8	0.6	7	1	13	2	72
360	0.084	0.003	45 357 952.6	0.7					72
361	0.35	0.008	45 358 994.8	0.5					72
362	−0.17	0.02	45 359 275	2					72
363	1.6	0.2	45 367 014	3					72
364	3.95	0.08	45 367 185.9	0.4					72
365	0.080	0.002	45 371 131.2	0.6					72
366	0.523	0.003	45 380 092.1	0.7	17	3	7	5	72
367	0.214	0.002	45 382 396	0.2					72
368	1.075	0.005	45 383 169	2	2	1	6	1	72
369	22.964	0.007	45 391 846	0	39	2	5	0	72
370	19.94	0.05	45 393 257.7	0.3	127	1	16	0	72
371	0.1	0.4	45 394 042	78					72
372	0.423	0.003	45 403 650.8	0.2					72
373	0.03	0.02	45 404 268	14					72
374	1.676	0.003	45 407 770.4	0.2	10	1	10	1	72
375	1.240	0.003	45 408 966.6	0.4	9	2	5	2	72
376	2.98	0.03	45 409 991	4	14	1	2	0	72
377	0.4	0.1	45 410 094	6					72
378	1.41	0.01	45 413 952	1	37	2	6	1	72
379	0.09	0.05	45 414 799	10					72
380	0.089	0.002	45 418 655	3	8	4	8	7	72
381	3.88	0.02	45 425 306	1	20	3	489	25	72
382	0.401	0.003	45 431 232	3	1	2	7	3	72
383	9.794	0.004	45 432 264.0	0.1	32	0	6	0	72

Continued on next page

#	Δv	$\sigma_{\Delta v}$	t_0	σ_{t_0}	τ_1	σ_{τ_1}	τ_2	σ_{τ_2}	Run
	($\mathrm{pm\,s^{-1}}$)	($\mathrm{pm\,s^{-1}}$)	(s)	(s)	(s)	(s)	(s)	(s)	
384	0.059	0.002	45 439 630.2	0.8					72
385	−0.068	0.004	45 442 251	1					72
386	−0.058	0.004	45 442 517	1					72
387	0.589	0.004	45 444 765	2	12	2	2	2	72
388	0.063	0.002	45 446 035.5	0.8					72
389	0.043	0.003	45 451 373	1					72
390	0.23	0.05	45 454 235.7	5					72
391	0.95	0.01	45 454 573.7	0.3					72
392	0.040	0.002	45 455 083.1	1					72
393	3.483	0.004	45 456 674.0	0.1	23	2	18	2	72
394	3.458	0.003	45 459 168.4	0.2	3	4	9	1	72
395	9.71	0.1	45 462 086	1	8	0	13	0	72
396	1.2	0.4	45 462 256	7					72
397	0.027	0.003	45 463 454	2					72
398	0.199	0.002	45 467 232.4	0.2					72
399	0.049	0.002	45 472 539	1					72
400	15.4	0.3	45 475 477	4	141	2	141	2	73
401	1.32	0.01	45 477 545	4	11	3	1	3	73
402	9.46	0.03	45 478 100.8	0.4	7	1	56	1	73
403	1.9	0.2	45 479 156	2					73
404	6.3	0.2	45 479 227	6	50	1	4	2	73
405	5.88	0.05	45 481 772	2	269	37	80	26	73
406	−2.23	0.04	45 483 098	2	86	46	86	10	73
407	1.48	0.01	45 484 247.6	0.9	7	4	19	4	73
408	1.72	0.02	45 486 780	2	11	2	2	2	73
409	1.04	0.04	45 487 172	6	71	53	217	44	73

Continued on next page

#	Δv	$\sigma_{\Delta v}$	t_0	σ_{t_0}	τ_1	σ_{τ_1}	τ_2	σ_{τ_2}	Run
	($\mathrm{pm\,s^{-1}}$)	($\mathrm{pm\,s^{-1}}$)	(s)	(s)	(s)	(s)	(s)	(s)	
410	0.164	0.007	45 492 196.3	0.9					73
411	0.191	0.007	45 494 754.4	0.8					73
412	2.07	0.01	45 498 433	1	19	2	3	2	73
413	0.443	0.007	45 499 715.8	0.3					73
414	0.206	0.008	45 502 414.0	0.8					73
415	0.13	0.01	45 504 887	2					73
416	0.14	0.01	45 505 350	2					73
417	0.37	0.01	45 516 802	0.7					73
418	0.153	0.008	45 520 048	1					73
419	4.73	0.06	45 522 311	2	198	22	42	16	73
420	0.336	0.007	45 540 042.7	0.4					73
421	6.37	0.01	45 544 358.7	0.2	14	2	14	2	73
422	0.42	0.02	45 565 354	12	2	30	64	18	73
423	0.66	0.01	45 581 497	6	2	3	10	5	73
424	−0.096	0.007	45 590 127	2					73
425	0.090	0.008	45 590 247	2					73
426	0.73	0.01	45 591 524.6	0.3					73
427	1.21	0.01	45 601 076	2	4	19	76	18	73
428	0.389	0.006	45 606 776.5	0.3					73
429	1.22	0.01	45 610 488	0.9	26	8	26	8	73
430	−0.138	0.008	45 614 414	1					73
431	0.07	0.01	45 614 545	3					73
432	−0.132	0.007	45 626 573	1					73
433	0.401	0.008	45 667 944.8	0.4					73
434	0.103	0.009	45 672 033	2					73
435	4.24	0.04	45 684 003	2	6	3	88	3	73

Table D.2: Two-sided glitches fitted with (5.6).

#	Δx (pm)	$\sigma_{\Delta x}$ (pm)	t_0 (s)	σ_{t_0} (s)	Run
Ordinary ambient-T and T_{low} noise runs					
436	4.4	0.2	12 685 190.6	0.4	12
437	−2.9	0.2	15 712 619.5	0.7	24
438	41.1	0.2	16 857 391.3	0.1	35
439	6.8	0.3	33 623 699.3	0.5	61
440	6.0	0.3	33 623 821.2	0.7	61
441	−0.8	0.2	40 152 961	3	67
Cold T_0 noise runs					
442	3.3	0.7	44 596 887	2	70
443	5.4	0.5	44 601 393	1	70
444	−5.4	0.5	44 601 643	1	70
445	−3.8	0.6	44 608 667	2	70
446	−64.4	0.9	44 610 291.4	0.2	70
447	−6.5	0.4	44 629 538.1	0.7	70
448	−7.0	0.7	44 633 452	1	70
449	9.6	0.3	44 661 758.5	0.4	70
450	−3.2	0.5	44 668 605	2	70
451	11	1	44 682 268	1	70
452	12	1	44 682 476	1	70
453	4	6	44 689 165	18	70
454	−15	1	44 699 042	1	70
455	−4	5	44 705 410	14	70
456	3.4	0.5	44 710 496	2	70
457	4.2	0.3	44 713 534.7	0.9	70

Continued on next page

#	Δx	$\sigma_{\Delta x}$	t_0	σ_{t_0}	Run
	(pm)	(pm)	(s)	(s)	
458	−1.29	0.04	44 743 293.9	0.4	71
459	1	3	44 745 487	39	71
460	0.90	0.09	44 750 704	1	71
461	0.5	0.4	44 759 211	10	71
462	−1	4	44 761 190	56	71
463	1	4	44 762 457	49	71
464	−3	2	44 769 738	8	71
465	1.8	0.4	44 772 789	3	71
466	1.74	0.04	44 776 365.4	0.3	71
467	−2.8	0.2	44 778 051.7	0.7	71
468	−3	6	44 784 703	24	71
469	3.84	0.06	44 790 849.6	0.2	71
470	−1.27	0.06	44 795 913.3	0.5	71
471	1	1	44 808 728	17	71
472	−0.9	0.2	44 810 739	2	71
473	−1.1	0.2	44 812 376	2	71
474	−0.6	0.7	44 818 906	14	71
475	−0.5	0.7	44 819 159	16	71
476	2	2	44 847 998	14	71
477	2	2	44 849 851	15	71
478	1	4	44 851 866	33	71
479	−1	3	44 870 417	56	71
480	−7	3	44 870 618	5	71
481	−3.1	0.5	44 890 125	2	71
482	−2.1	0.5	44 890 281	3	71
483	−1.3	0.5	44 906 857	4	71

Continued on next page

#	Δx	$\sigma_{\Delta x}$	t_0	σ_{t_0}	Run
	(pm)	(pm)	(s)	(s)	
484	−2.2	0.2	44 919 902	1	71
485	11	4	44 966 203	4	71
486	−6	4	44 969 017	8	71
487	4	4	44 969 588	13	71
488	42	4	44 969 738	1	71
489	2.02	0.05	44 974 631.5	0.3	71
490	0	12	44 982 153	928	71
491	1	2	45 011 185	24	71
492	−2.3	0.1	45 043 015.9	0.7	71
493	1.7	0.9	45 200 030	6	71
494	−0.50	0.04	45 314 807	1	72
495	6.02	0.06	45 335 153.8	0.1	72
496	−5.26	0.07	45 350 542.1	0.1	72
497	1.69	0.05	45 361 461.8	0.3	72
498	−0.91	0.05	45 400 793.5	0.7	72
499	1.50	0.05	45 443 552	0.4	72
500	−2.02	0.06	45 447 630.8	0.3	72
501	31	8	45 477 841	3	73
502	1.6	0.1	45 699 416.5	0.8	73

Table D.3: Two-sided glitches fitted with (5.7).

#	Δx	$\sigma_{\Delta x}$	Δv	$\sigma_{\Delta v}$	t_0	σ_{t_0}	τ_1	σ_{τ_1}	τ_2	σ_{τ_2}	Run
	(pm)	(pm)	(pm s^{-1})	(pm s^{-1})	(s)	(s)	(s)	(s)	(s)	(s)	
Ordinary ambient-T and T_{low} noise runs											
503	−5.4	0.3	0.092	0.005	38 079 789	2	9	5	9	3	66
504	11	1	0.85	0.01	47 987 259.6	0.5	4.0	0.8	35	7	76
Cold T_0 noise runs											
505	−3.4	0.2	−0.004	0.004	44 764 508	1	10	6	10	4	71
506	16.6	0.6	−0.28	0.02	44 888 261	1	6	3	6	3	71
507	−2.8	0.2	−0.051	0.003	45 336 627	2	5	2	5	2	72
508	−10	1	0.09	0.02	45 529 534	3	16	14	16	8	73

Table D.4: One-sided glitches fitted with (5.5).

#	Δv	$\sigma_{\Delta v}$	t_0	σ_{t_0}	τ_1	σ_{τ_1}	τ_2	σ_{τ_2}	τ_1	σ_{τ_1}	Run
	($\mathrm{pm\,s^{-1}}$)	($\mathrm{pm\,s^{-1}}$)	(s)	(s)	(s)	(s)	(s)	(s)	(s)	(s)	
509	1105.7	0.6	10 924 259	3	750	32	5474	156	5465	437	9
510	217.9	0.4	20 934 409	7	2661	1136	2663	989	2654	1278	44

Acknowledgments

This thesis includes contributions from people working in the LISA Pathfinder collaboration, and I would like therefore to thank the entire LPF community, including the STOC team. In particular, I have to acknowledge the work of the following research groups and institutions:

- Experimental Gravitation Laboratory Group, University of Trento and INFN, Italy;
- European Space Astronomy Centre, European Space Agency, Villanueva de la Cañada, Madrid, Spain;
- European Space Technology Centre, Noordwijk, Netherlands;
- European Space Operations Centre, Darmstadt, Germany;
- Albert Einstein Institut, Max Planck Institut for Gravitational Physics, Hannover, Germany:
- High Energy Physics Group, Imperial College London, UK;
- APC, Université Paris Diderot, CNRS/IN2P3, Paris, France;
- DISPEA, Università di Urbino *Carlo Bo* and INFN, Urbino, Italy;
- School of Physics and Astronomy, University of Birmingham, Birmingham, UK;
- Institut für Geophysik, ETH Zürich, Zürich, Switzerland;
- UK Astronomy Technology Centre, Royal Observatory, Edinburgh, UK;
- Institut de Ciències de l'Espai (ICE, CSIC) and Institut d'Estudis Espacials de Catalunya (IEEC), Barcelona, Spain;
- Physik Institut, Universität Zürich, Switzerland
- SUPA, Institute for Gravitational Research, School of Physics and Astronomy, University of Glasgow, Glasgow, UK;
- Gravitational Astrophysics Lab, NASA Goddard Space Flight Center, Maryland, USA;
- Department of Mechanical and Aerospace Engineering, University of Florida, Gainesville, Florida, USA.

Bibliography

[1] B. P. Abbott et al. "Observation of Gravitational Waves from a Binary Black Hole Merger". In: *Phys. Rev. Lett.* 116 (6 Feb. 2016), p. 061102. DOI: 10.1103/PhysRevLett.116.061102.

[2] B. P. Abbott et al. "GW170817: Observation of Gravitational Waves from a Binary Neutron Star Inspiral". In: *Phys. Rev. Lett.* 119 (16 Oct. 2017), p. 161101. DOI: 10.1103/PhysRevLett.119.161101.

[3] Pau Amaro-Seoane et al. "Laser Interferometer Space Antenna". In: (Feb. 2017). arXiv: 1702.00786. URL: http://arxiv.org/abs/1702.00786.

[4] Davide Castelvecchi. "Japan's pioneering detector set to join hunt for gravitational waves". In: *Nature* (565 2019), pp. 9–10. DOI: doi/10.1038/d41586-018-07867-z.

[5] John Miller et al. "Prospects for doubling the range of Advanced LIGO". In: *Phys. Rev. D* 91 (6 Mar. 2015), p. 062005. DOI: 10.1103/PhysRevD.91.062005. URL: https://link.aps.org/doi/10.1103/PhysRevD.91.062005.

[6] F Acernese et al. "Advanced Virgo: a second-generation interferometric gravitational wave detector". In: *Classical and Quantum Gravity* 32.2 (Dec. 2014), p. 024001. DOI: 10.1088/0264-9381/32/2/024001. URL: https://doi.org/10.1088%2F0264-9381%2F32%2F2%2F024001.

[7] Alberto Sesana. "Prospects for Multiband Gravitational-Wave Astronomy after GW150914". In: *Phys. Rev. Lett.* 116 (23 June 2016), p. 231102. DOI: 10.1103/PhysRevLett.116.231102.

[8] J. E. Faller et al. "Space antenna for gravitational wave astronomy". In: *ESA Colloquium in Kilometric Optical Arrays in Space p 157–163*. JILA Pub. 3012. European Space Agency. European Space Agency, Apr. 1985. URL: http://articles.adsabs.harvard.edu/full/1985ESASP.226..157F.

[9] J.E. Faller et al. "An antenna for laser gravitational-wave observations in space". In: *Advances in Space Research* 9.9 (1989), pp. 107–111. ISSN: 0273-1177. DOI: https://doi.org/10.1016/0273-1177(89)90014-8. URL: http://www.sciencedirect.com/science/article/pii/0273117789900148.

[10] *Report on the Activities of Space Science Department 1995-1996 (SP1211)*. European Space Agency, 1997. URL: https://www.esa.int/esapub/sp/sp1211/funct.htm.

[11] Danzmann K et al. *LISA-Laser Interferometer Space Antenna Pre-Phase A Report, 2nd edition*. Tech. rep. MPQ 233. LISA Study Team, 1998.

[12] eLISA Consortium et al. "The gravitational universe". In: *URL: arxiv. org/abs/1305.5720* (2013).

[13] LISA Pathfinder Science Working Team. *LISA Pathfinder: Einstein's Geodesic Explorer - The Science Case for LISA Pathfinder*. ESA-SCI(2007)1. European Space Agency, 2007.

[14] M. Armano et al. "LISA Pathfinder: the experiment and the route to LISA". In: *Classical and Quantum Gravity* 26.9 (2009), p. 094001.

[15] S. Anza et al. "The LTP experiment on the LISA Pathfinder mission". In: *Classical and Quantum Gravity* 22 (10 May 2005), S125–S138. DOI: 10.1088/0264-9381/22/10/001.

[16] M. Armano et al. "Sub-Femto-g Free Fall for Space-Based Gravitational Wave Observatories: LISA Pathfinder Results". In: *Phys. Rev. Lett.* 116 (23 2016), p. 231101. DOI: 10.1103/PhysRevLett.116.231101.

[17] M. Armano et al. "Beyond the Required LISA Free-Fall Performance: New LISA Pathfinder Results down to 20 μHz". In: *Phys. Rev. Lett.* 120 (6 Feb. 2018), p. 061101. DOI: 10.1103/PhysRevLett.120.061101.

[18] *LISA Assessment Study Report (Yellow Book)*. ESA/SRE(2001)3. ESA, 2011.

[19] LISA Collaboration. *The Gravitational Universe*. White Paper. European Space Agency, 2014.

[20] P. McNamara and G. Racca. *Introduction to LISA Pathfinder*. LISA-LPF-RP-0002. European Space Agency, 2009.

[21] E.T. Elliffe et al. "Hydroxide-Catalysis Bonding for Stable Optical Systems for Space". In: *Classical and Quantum Gravity* 22 (May 2005). DOI: 10.1088/0264-9381/22/10/018.

[22] F. Antonucci et al. "LISA Pathfinder data analysis". In: *Classical and Quantum Gravity* 28.9 (2011), p. 094006.

[23] J Jarrige et al. "Thrust Measurements of the GAIA Mission Flight-Model cold gas thrusters". In: *Journal of Propulsion and Power* 30.4 (2014), pp. 934–943.

[24] M. Armano et al. “Calibrating the system dynamics of LISA Pathfinder”. In: *Phys. Rev. D* 97 (12 June 2018), p. 122002.

[25] F. Antonucci et al. “From laboratory experiments to LISA Pathfinder: achieving LISA geodesic motion”. In: *Classical and Quantum Gravity* 28.9 (2011), p. 094002.

[26] G. Anderson et al. “Experimental results from the ST7 mission on LISA Pathfinder”. In: *Phys. Rev. D* 98 (10 Nov. 2018), p. 102005. DOI: 10.1103/PhysRevD.98.102005. URL: https://link.aps.org/doi/10.1103/PhysRevD.98.102005.

[27] M Armano et al. “Temperature stability in the sub-milliHertz band with LISA Pathfinder”. In: *Monthly Notices of the Royal Astronomical Society* 486.3 (Apr. 2019), pp. 3368–3379. ISSN: 0035-8711. DOI: 10.1093/mnras/stz1017. eprint: http://oup.prod.sis.lan/mnras/article-pdf/486/3/3368/28536406/stz1017.pdf. URL: https://doi.org/10.1093/mnras/stz1017.

[28] Gudrun Wanner and on behalf of the LISA Pathfinder collaboration Nikolaos Karnesis. “Preliminary results on the suppression of sensing cross-talk in LISA Pathfinder”. In: *Journal of Physics: Conference Series* 840 (May 2017), p. 012043. DOI: 10.1088/1742-6596/840/1/012043.

[29] Peter D. Welch. “The use of fast Fourier transform for the estimation of power spectra: a method based on time averaging over short, modified periodograms”. In: *IEEE Trans. Audio and Electroacoustics* 15.2 (1967), pp. 70–73.

[30] LISA Pathfinder science collaboration. “Temperature-induced forces on geodesic reference masses for LISA: results from LISA Pathfinder”. In: *In preparation* (2020).

[31] LISA Pathfinder science collaboration. “Nanonewton electrostatic actuators for femtoNewton small-force measurements: performance of the LISA Pathfinder electrostatic force actuation system”. In: *In preparation* (2020).

[32] A. Cavalleri et al. “Increased Brownian Force Noise from Molecular Impacts in a Constrained Volume”. In: *Phys. Rev. Lett.* 103 (14 Sept. 2009), p. 140601.

[33] LISA Instrument Group. *LISA Performance Model and Error Budget*. Technincal note LISA-LCST-INST-TN-003. LISA Consortium, 2019.

[34] G. C. Carter. “Coherence and time delay estimation”. In: *Proceedings of the IEEE* 75 (1987), pp. 236–255.

[35] M Armano et al. “Spacecraft and interplanetary contributions to the magnetic environment on-board LISA Pathfinder”. In: *Monthly Notices of the Royal Astronomical Society* (). ISSN: submitted.

[36] B. Schläppi et al. “Influence of spacecraft outgassing on the exploration of tenuous atmospheres with in situ mass spectrometry”. In: *Journal of Geophysical Research: Space Physics* 115.A12 (2010). DOI: 10.1029/2010JA015734. eprint: https://agupubs.onlinelibrary.wiley.com/doi/pdf/10.1029/2010JA015734. URL: https://agupubs.onlinelibrary.wiley.com/doi/abs/10.1029/2010JA015734.

[37] R. Dolesi et al. “Brownian force noise from molecular collisions and the sensitivity of advanced gravitational wave observatories”. In: *Physical Review D - Particles, Fields, Gravitation and Cosmology* 84.6 (2011). ISSN: 15507998. DOI: 10.1103/PhysRevD.84.063007. arXiv: 1108.3254.

[38] S. Vitale et al. “Data series subtraction with unknown and unmodeled background noise”. In: *Phys. Rev. D* 90 (4 2014), p. 042003. DOI: 10.1103/PhysRevD.90.042003.

[39] Michael Tröbs and Gerhard Heinzel. “Improved spectrum estimation from digitized time series on a logarithmic frequency axis”. In: *Measurement* 39 (Feb. 2006), pp. 120–129. DOI: 10.1016/j.measurement.2005.10.010.

[40] Shane L. Larson, William A. Hiscock, and Ronald W. Hellings. “Sensitivity curves for spaceborne gravitational wave interferometers”. In: *Phys. Rev. D* 62 (6 Aug. 2000), p. 062001. DOI: 10.1103/PhysRevD.62.062001. URL: https://link.aps.org/doi/10.1103/PhysRevD.62.062001.

[41] Wen-Rui Hu and Yue-Liang Wu. “The Taiji Program in Space for gravitational wave physics and the nature of gravity”. In: *National Science Review* 4.5 (2017), pp. 685–686. DOI: 10.1093/nsr/nwx116.

[42] Jun Luo et al. “TianQin: a space-borne gravitational wave detector”. In: *Classical and Quantum Gravity* 33.3 (Jan. 2016), p. 035010. DOI: 10.1088/0264-9381/33/3/035010. URL: https://doi.org/10.1088%2F0264-9381%2F33%2F3%2F035010.

[43] Claudio Maccone. *Deep Space Flight and Communications: Exploiting the Sun as a Gravitational Lens.*

[44] R. Dolesi et al. *LISA Pathfinder on-orbit investigations: scientific justification, implementation guidelines, and scientific products*. S2-UTN-TN-3109 Iss. 1/Rel. 0. Università degli Studi di Trento, 2015.

[45] S. Vitale. *Measurement of LTP dynamical coefficients by system identification*. S2-UTN-TN-3045 Iss.3/Rel. 1. Università degli Studi di Trento, 2015.

[46] S. Vitale et al. *Recommendation for an algorithm for Power Spectral Density estimation for LISA Pathfinder*. S2-UTN-TN-3040 Issue/Rev. 1.0. Università degli Studi di Trento, 2006.

[47] P. Amaro-Seoane et al. "Low-frequency gravitational-wave science with eLISA/NGO". In: *Class. Quant. Grav.* 29 (2012), p. 124016.

[48] P. McNamara. *Overview of LISA Pathfinder*. LISA-LPF-RP-0001(1). European Space Agency, 2009.

[49] G. Congedo et al. "Time domain maximum likelihood parameter estimation in LISA Pathfinder data analysis". In: *Phys. Rev. D* 85 (12 2012), p. 122004. DOI: 10.1103/PhysRevD.85.122004.

[50] Michele Maggiore. *Gravitational Waves: Volume 1: Theory and Experiments*. Oxford University Press, USA, 2007.

[51] M. Nofrarias et al. "Bayesian parameter estimation in the second LISA Pathfinder mock data challenge". In: *Phys. Rev. D* 82 (12 2010), p. 122002. DOI: 10.1103/PhysRevD.82.122002.

[52] C J Moore, R H Cole, and C P L Berry. "Gravitational-wave sensitivity curves". In: *Classical and Quantum Gravity* 32.1 (2015), p. 015014.

[53] Giuseppe Congedo et al. "Space-borne gravitational-wave detectors as time-delayed differential dynamometers". In: *Phys. Rev. D* 88 (8 2013), p. 082003. DOI: 10.1103/PhysRevD.88.082003.

[54] M. Armano et al. "Precision charge control for isolated free-falling test masses: LISA pathfinder results". In: *Phys. Rev. D* 98 (6 Sept. 2018), p. 062001. DOI: 10.1103/PhysRevD.98.062001.